ESCOLA DE DOUTORAMENTO
INTERNACIONAL DA USC

Martín
Senande Rivera

Tese de doutoramento

Wildfire-atmosphere interactions in a changing climate

Santiago de Compostela, 2023

Programa de Doutoramento en Enerxías Renovables e Sustentabilidade Enerxética

USC
UNIVERSIDADE
DE SANTIAGO
DE COMPOSTELA

TESE DE DOUTORAMENTO

WILDFIRE-ATMOSPHERE INTERACTIONS IN A CHANGING CLIMATE

Martín Senande Rivera

ESCOLA DE DOUTORAMENTO INTERNACIONAL DA UNIVERSIDADE DE SANTIAGO DE COMPOSTELA

PROGRAMA DE DOUTORAMENTO EN ENERXÍAS RENOVABLES E SUSTENTABILIDADE ENERXÉTICA

SANTIAGO DE COMPOSTELA

ANO 2023

USC
UNIVERSIDADE
DE SANTIAGO
DE COMPOSTELA

AUTORIZACIÓN DO DIRECTOR / TITOR DA TESE

Wildfire-atmosphere interactions in a changing climate

D./Dna. Gonzalo Míguez Macho

INFORMA/N:

Que a presente tese, correspóndese co traballo realizado por D/Dna. Martín Senande Rivera, baixo a miña dirección/titorización, e autorizo a súa presentación, considerando que reúne os requisitos esixidos no Regulamento de Estudos de Doutoramento da USC, e que como director desta non incorre nas causas de abstención establecidas na Lei 40/2015.

De acordo co indicado no Regulamento de Estudos de Doutoramento, declara tamén que a presente tese de doutoramento é idónea para ser defendida en base á modalidade de Monográfica con reprodución de publicacións, nos que a participación do/a doutorando/a foi decisiva para a súa elaboración e as publicacións se axustan ao Plan de Investigación.

En Santiago de Compostela, 11 de maio de 2023

USC
UNIVERSIDADE
DE SANTIAGO
DE COMPOSTELA

Agradecementos

Primeiramente, grazas a miña nai e a meu pai por educarme e coidarme do xeito en que o fixeron, fan e seguirán facendo. Grazas tamén ao resto da miña familia. Especialmente ás miñas avoas e aos meus avós, por tódalas aprendizaxes e por todo o agarimo que deles recibín, e que conservarei para sempre.

Tamén debo agradecer ás miñas amizades todo o tempo que compartiron comigo. A Guille, por medrar a canda min. A Damián, por aprender comigo. A todas e todos, en xeral, por compartir momentos de festa, conversa, emocións, música e vida.

Grazas ás compañeiras e compañeiros do Grupo de Física Non Lineal, de quen sinto que recibín moita mais axuda da que conseguín ofrecer.

Grazas a Gonzalo por dirixir esta tese dende a experiencia, o coñecemento e a vontade de ensinar.

Grazas por último á miña parella, Lucía, polo amor e os coidados. Con ela aprendo sobre empatía, emocións e sensibilidade. Tamén que aos sentimentos non se lle aplican medias aritméticas.

USC
UNIVERSIDADE DE SANTIAGO DE COMPOSTELA

USC
UNIVERSIDADE
DE SANTIAGO
DE COMPOSTELA

Contents

Abstract **13**

Resumo **15**

Resumo extenso **17**

1 General introduction **23**
1.1 Fire in the Earth System . . . 23
1.1.1 Interactions with humans . . . 24
1.1.2 Interactions with vegetation . . . 24
1.1.3 Interactions with the atmosphere . . . 25
1.1.4 Interactions with other elements of the Earth System . . . 26
1.2 Anthropogenic climate change . . . 27
1.2.1 The radiative balance . . . 27
1.2.2 Radiative forcing agents . . . 28
1.2.3 Climate change evidences and climate system response . . . 29
1.2.4 Future climate change . . . 33
1.3 Fires and climate change . . . 34
1.4 Objectives and thesis outline . . . 35

2 Methodology **37**
2.1 Rothermel's fire spread model . . . 37
2.1.1 Heat sink . . . 37
2.1.2 Heat source . . . 38
2.1.3 Wind and slope coefficients . . . 41
2.1.4 Final form . . . 41
2.1.5 Fuel models . . . 42
2.2 Numerical simulation of the atmosphere . . . 45
2.3 Coupled atmosphere-wildfire modelling . . . 45
2.3.1 Fire propagation . . . 46
2.3.2 Fire fluxes into the atmosphere . . . 46
2.3.3 Case study: October 2017 Hurricane Ophelia fires . . . 47
2.3.4 Case study: June 2017 Pedrógão Grande fire . . . 50

3 Present global fire-prone regions and their expected alterations due to climate change **55**
3.1 Introduction . . . 55

USC UNIVERSIDADE DE SANTIAGO DE COMPOSTELA

3.2 Methods . . . 56
3.2.1 Burned area data . . . 56
3.2.2 Climate data . . . 56
3.2.3 GCM data . . . 56
3.2.4 Threshold selection . . . 58
3.3 Results and discussion . . . 63
3.3.1 Present fire-climate classification . . . 63
3.3.2 Future fire-climate classification . . . 67
3.3.3 Future changes in global fire activity . . . 68
3.4 Conclusions . . . 71
Supplementary Figures . . . 72

4 The influence of climate change on wildfire behaviour in the Iberian Peninsula 93
4.1 Introduction . . . 93
4.2 Methods . . . 94
4.2.1 Fire and climate data . . . 94
4.2.2 Rate of spread calculation . . . 95
4.2.3 Attribution method . . . 95
4.3 Results and discussion . . . 97
4.3.1 The role of the different factors . . . 97
4.3.2 Spatial and temporal patterns . . . 98
4.3.3 Event-scale analysis . . . 100
4.3.4 Energy released to the atmosphere . . . 100
4.4 Conclusions . . . 102
Supplementary Figures . . . 104
Supplementary Tables . . . 114

5 Analysis of the atmospheric risk of deep pyroconvection in Europe 123
5.1 Introduction . . . 123
5.2 Methods . . . 124
5.3 Results and discussion . . . 127
5.3.1 Present firestorm risk in Europe . . . 127
5.3.2 Future trends under different climate change scenarios . . . 129
5.3.3 An ongoing process . . . 131
5.4 Conclusions . . . 132
Supplementary Figures . . . 133
Supplementary Tables . . . 156

6 Wildfire-atmosphere interactions in Galicia 159
6.1 Climate scale . . . 160
6.2 Synoptic scale . . . 161
6.3 Local scale . . . 163

7 General conclusions 167

List of Figures 169

USC UNIVERSIDADE DE SANTIAGO DE COMPOSTELA

List of Tables **185**

List of publications **187**

Copyright Permissions **189**

Funding information **191**

Bibliography **193**

USC
UNIVERSIDADE DE SANTIAGO DE COMPOSTELA

USC
UNIVERSIDADE
DE SANTIAGO
DE COMPOSTELA

Abstract

Wildfire activity is controlled by different factors such as meteorology, climate, vegetation characteristics and human activity. At the same time, fires can alter the state of the atmosphere, produce important impacts on vegetation and have consequences on the economy and human health. Fires are therefore considered to be part of the Earth System. Anthropogenic climate change is triggering important changes in the atmosphere and the biosphere, so it is expected to affect wildfires as well, modifying their role within the Earth System. The aim of this thesis is to analyse how the interactions between the atmosphere and wildfires are being altered.

By comparing global burned area data with climate data, a classification of global climates associated with high fire activity was developed. Using climate projections from general circulation models, the expected future variation in fire activity was calculated, finding a clear increase in boreal regions. These regions contain a great amount of the terrestrial carbon stocks, so an increase in the frequency of fires there can lead to a significant emission of carbon dioxide to the atmosphere.

Applying a meteorological event attribution methodology to the equations that solve the spread of wildfires, the influence of climate change on the behaviour of fires in the Iberian Peninsula between 2001 and 2021 was quantified. With this methodology, it is possible to calculate the increase in the rate of spread attributable to the increasing evaporative demand of the atmosphere, as well as to estimate the influence of vegetation alterations caused by anthropogenic global warming.

Finally, using a coupled atmosphere-fire numerical model, we identified the atmospheric conditions that favour the development of deep pyroconvection, a phenomenon by which fires modify the local meteorology through the release of sensible and latent heat. Analysing future projections from different regional climate models, it was found that the risk of deep pyroconvection is increasing in southern Europe.

Based on the results of these studies, we can conclude that anthropogenic climate change is intensifying the interactions between wildfires and the atmosphere over different spatio-temporal scales.

USC
UNIVERSIDADE DE SANTIAGO DE COMPOSTELA

USC
UNIVERSIDADE
DE SANTIAGO
DE COMPOSTELA

Resumo

Os incendios forestais están condicionados por diferentes factores como a meteoroloxía, o clima, as características da vexetación ou a actividade humana. Paralelamente, os incendios poden alterar o estado da atmosfera, supoñen importantes impactos na vexetación e teñen consecuencias na economía e saúde das persoas. Por iso considérase que os incendios forman parte do sistema terrestre. O cambio climático antropoxénico está producindo importantes cambios na atmosfera e biosfera, co cal é de esperar que tamén afecte á ocorrencia de incendios forestais, modificando o seu rol dentro do sistema terrestre. O obxectivo desta tese é analizar de que xeito se están alterando as interaccións entre a atmosfera e os incendios forestais.

Comparando datos globais de área queimada con datos climáticos elaborouse unha clasificación dos climas do planeta asociados a unha alta actividade de incendios. A través de proxeccións climáticas de modelos de circulación xeral, calculouse a variación esperada para o futuro da actividade de incendios, atopando un claro aumento en rexións boreais. Nestas rexións atópanse gran parte das reservas de carbono terrestre, polo que o aumento na frecuencia de incendios pode supoñer un importante aporte de dióxido de carbono á atmosfera.

Aplicando unha metodoloxía de atribución de eventos meteorolóxicos ás ecuacións que resolven a propagación de incendios forestais, cuantificouse a influencia do cambio climático no comportamento dos incendios da Península Ibérica entre 2001 e 2021. Con esta metodoloxía conséguese calcular o aumento na velocidade de propagación atribuíble á crecente demanda evaporativa da atmosfera, así como estimar a influencia dos cambios na vexetación producidos polo quecemento global antropoxénico.

Por último, empregando un modelo numérico acoplado atmosfera-incendio, identificáronse as condicións atmosféricas que favorecen o desenvolvemento de piroconvección profunda, fenómeno polo cal os incendios conseguen modificar a meteoroloxía local a través da liberación de calor sensíbel e latente. Analizando proxeccións futuras de diferentes modelos climáticos rexionais púidose comprobar que o risco de piroconvección profunda está aumentando no sur de Europa.

De acordo cos resultados destes estudos, podemos concluír que o cambio climático antropoxénico está intensificando as interaccións entre os incendios forestais e a atmosfera ao longo de diferentes escalas espazo-temporais.

USC
UNIVERSIDADE DE SANTIAGO DE COMPOSTELA

USC
UNIVERSIDADE
DE SANTIAGO
DE COMPOSTELA

Resumo extenso

Os incendios forestais son un elemento do sistema terrestre, xa que interaccionan coa antroposfera, biosfera e atmosfera en diferentes escalas espaciais e temporais. Os humanos exercemos unha influencia directa nos incendios, tanto por ser unha importante fonte de ignicións como por intervir na súa extinción, mais as consecuencias na saúde e na economía dos incendios son tamén significativas, especialmente durante os eventos extremos. Os réximes dos incendios forestais están tamén influenciados pola vexetación, que conforma o combustible. Ao mesmo tempo, os lumes producen impactos importantes nos bosques e nas características das plantas, así como na produtividade dos ecosistemas. O clima determina fortemente a ocorrencia de incendios a escala global, e a meteoroloxía influencia a propagación a menor escala. Mais os efectos da combustión da biomasa teñen capacidade para alterar as condicións atmosférica, tanto a escala climática mediante a modificación do ciclo do carbono ou do balance da radiación, como a escala local a través da liberación de calor.

Como parte do sistema terrestre, as características ou a ocorrencia de incendios forestais é sensíbel ás perturbacións que ocorran nos outros elementos do sistema. Os humanos estamos alterando o clima a través, principalmente, da combustión de combustibles fósiles, que liberan grandes cantidades de dióxido de carbono á atmosfera, potenciando así o efecto invernadoiro e aumentando a temperatura global do planeta. Este fenómeno, coñecido como quecemento global ou cambio climático antropoxénico, ten un efecto non lineal no sistema climático, xa que o aumento da temperatura atmosférica acaba alterando outras variables ou características climáticas, que ao mesmo tempo poden potenciar ou reducir o propio aumento de temperatura nun proceso coñecido como retroalimentación. O sexto informe do Grupo Intergubernamental de Expertos sobre o Cambio Climático (IPCC, polas súas siglas en inglés) determina que o actual rango de aumento na temperatura da superficie global dende o período pre-industrial (1850-1900) está entre 0.8°C e 1.3°C. Outras variables climáticas, como a cantidade de humidade na atmosfera, a produtividade da vexetación, a cobertura de xeo ou o nivel do mar, experimentaron tamén cambios significativos atribuíbles á actividade humana.

Así, o cambio climático antropoxénico constitúe unha importante perturbación no sistema terrestre, coa capacidade de alterar cada un dos elementos que o conforman, entre eles os incendios forestais. O principal obxectivo desta tese é demostrar e cuantificar a influencia que o cambio climático antropoxénico está a ter nos incendios forestais, poñendo o foco nos diferentes procesos de interacción entre os incendios e a atmosfera, dende a escala climática até a escala local.

Para levar a cabo este obxectivo foi preciso o desenvolvemento dun traballo previo de revisión e adaptación dunha serie de ferramentas que nos permitisen estudar a propagación dos incendios forestais dende unha óptica físico-matemática. As ecuacións de Rothermel resolven a propagación dunha fronte de incendio a través dun combustible en superficie. Están baseadas no principio de conservación de enerxía, considerando o combustible en combustión como

USC DE SANTIAGO

unha fonte de enerxía e o combustible sen queimar como un sumidoiro. A enerxía necesaria polo combustible que actúa como sumidoiro depende da cantidade de combustible e da calor requirida para levar unha unidade de masa deste combustible á ignición, que se calcula a través dunha expresión física na que interveñen principalmente a temperatura de ignición e a cantidade de auga contida no combustible. No caso da fonte de enerxía, esta depende da taxa de perda de masa de combustible, do seu contido calorífico e da eficiencia da propagación desta calor ao combustible que non está ardendo. Neste cálculo interveñen multitude de parámetros estruturais do combustible, así como a velocidade do vento e a pendente do terreo, que varían a eficiencia da propagación do fluxo de calor ao reducir a separación entre a chama e o combustible que non está ardendo. As propiedades e parámetros estruturais do combustible están agrupadas en diversas categorías ou clases definidas na literatura (denominados modelos de combustible) coa fin de representar a variedade de tipoloxías de combustible que podemos atopar na natureza. As ecuacións de Rothermel son a base de multitude de modelos de propagación de incendios, e foron tamén incluídas como un módulo adicional no modelo atmosférico rexional WRF, coa posibilidade de simular a evolución da atmosfera e da propagación de incendios forestais de xeito acoplado. Así, os fluxos de calor sensíbel e calor latente procedentes do incendio son incorporados nas variables atmosféricas, influenciando a meteoroloxía local, que ao mesmo tempo condiciona a propagación do incendio. Probamos o rendemento deste modelo simulando dous eventos reais de incendios na Península Ibérica: dous incendios da vaga de outubro de 2017 en Galicia e o incendio de xuño de 2017 de Pedrógão Grande en Portugal. Para o primeiro caso, foi preciso elaborar un mapa de categorías de combustible a partir de datos da cobertura vexetal e de uso do solo. Os incendios da vaga de outubro de 2017 en Galicia tiveron unha rápida propagación pola presenza do Furacán Ophelia, que ocasionou unhas condicións de fortes ventos que advectaron aire cálido e seco dende o sur, reducindo así a humidade do combustible. Comprobouse que o modelo acoplado atmosfera-incendio reproduce axeitadamente a área queimada observada dende o satélite. Realizouse tamén un pequeno estudo da sensibilidade da propagación de estes incendios ante diferentes condicións de humidade do combustible. Para o caso do incendio de Pedrógrão Grande puido corroborarse a capacidade do modelo para reproducir un evento de piroconvección profunda, xa que na simulación o incendio xerou unha nube convectiva que influenciou as condicións meteorolóxicas en superficie, algo que tamén foi observado na realidade segundo diferentes relatorios de expertos que analizaron o evento.

Dende unha escala global, a distribución da ocorrencia de incendios está fortemente determinada polo clima de cada rexión. Partindo desta hipótese, elaborouse unha metodoloxía para inferir as características climáticas de cada unha das rexións do planeta cunha alta incidencia de incendios forestais. Para isto cruzamos datos de área queimada obtidos por satélite con datos climáticos. Avaliando o cambio nas distribucións estatísticas da precipitación e temperatura entre pontos espazo-temporais asociados á ocorrencia de incendios con pontos sen rexistros de incendios, puidemos establecer unha serie de categorías climáticas asociadas ás rexións propicias á ocorrencia de incendios do planeta, definidas unicamente por limiares de precipitación e temperatura. Ademais, analizando o número de veces que se rexistran estas determinadas condicións climáticas podemos cuantificar a duración da estación de incendios, así como a recursividade inter-anual das condicións asociadas a incendios. Nas zonas tropicais, a ocorrencia de incendios está fortemente ligada á estacionalidade da precipitación, rexistrando unha alta actividade de incendios durante os meses secos. Os climas de sabana concentran case a totalidade dos incendios deste clima, mais algunhas zonas onde a falta de precipitación está asociada á presenza do fenómeno de El Niño no Pacífico tamén son clasificadas como

propicias a ter incendios, aínda que cunha menor recursividade. Os climas boreais teñen pola contra unha actividade de incendios asociada á estacionalidade da temperatura, con presenza de incendios unicamente durante os meses do verán. A recursividade inter-anual dos incendios é moito menor neste clima, xa que a cantidade de precipitación no verán pode variar moito entre uns anos e outros, con maior actividade de incendios nos anos máis secos. Nas zonas temperadas do planeta, existe unha forte presenza de incendios forestais nas rexións con climas mediterráneos, onde a estación cálida coincide coa estación seca, como é o caso de Galicia ou a costa oeste dos Estados Unidos. Nos climas desérticos os incendios forestais ocorren só a partir dun certo limiar de precipitación, que garante a presenza de combustible. A estación de incendios varía en función da temperatura de cada rexión: nas zonas áridas máis frías coincide cos meses cálidas, nas rexións máis cálidas como o Sahel cadra xusto despois dos meses de chuvia, e nas área con temperaturas máis intermedias os incendios ocorren á fin da estación seca. As categorías de climas propicios a ter incendios creadas están definidas unicamente por variables climáticas, polo que utilizando as saídas de diferentes modelos de circulación xeral para o final do século 21 segundo o escenario de emisións RCP8.5, podemos proxectar como variará a extensión destas rexións e a duración da estación de incendios. Atopamos un aumento xeral da área global con frecuentes condicións climáticas asociadas a incendios, especialmente nos climas boreais, que son os que rexistrarán un aumento máis pronunciado da temperatura. O aumento na ocorrencia de incendios nestas latitudes é algo que pode ter implicacións importantes para o sistema climático. Nestas rexións atópase gran parte do solo rico en carbono, como é o caso das turbeiras. Unha maior incidencia de incendios neste tipo de solos podo aumentar considerablemente as emisións netas de dióxido de carbono á atmosfera, amplificando o aumento de temperatura. Un alongamento da estación de incendios é tamén notable tanto nos climas boreais como nos temperados de acordo coas proxeccións climáticas empregadas. Para o caso concreto de Galicia, a estación de incendios pasará de durar entre 2 e 3 meses no presente a entre 4 e 5 ao final do século 21 segundo o escenario de emisións RCP8.5. En relación aos incendios forestais, as rexións tropicais son as menos sensibles ao cambio climático, debido a que a recursividade das condicións favorables aos incendios é xa moi alta no clima presente, cunha menor dependencia da temperatura. Estes resultados foron publicados nun artigo científico na revista *Nature Communications* [1].

Para analizar a relación entre as perturbacións climáticas e o comportamento dos incendios forestais con maior detalle, utilizouse unha metodoloxía baseada nos estudos de atribución de eventos meteorolóxicos, pero adaptada para o estudo de incendios forestais. Mediante as ecuacións de Rothermel, calculamos a velocidade de propagación característica de tódolos incendios forestais de máis de 500 ha entre 2001 e 2021 da Península Ibérica. Para isto foi preciso tamén utilizar outros conxuntos de ecuacións que nos permitiron calcular a humidade dos combustibles mortos e vivos. Así, obtivemos un conxunto de velocidades de propagación destes incendios para varios tipos de combustible, partindo unicamente de variables meteorolóxicas obtidas dunha reanálise climática. Podemos estimar como serían estas velocidades de propagación baixo unhas condicións pre-industriais (sen cambio climático) ou baixo unhas condicións futuras de quecemento global perturbando os nosos datos meteorolóxicos de entrada coas anomalías climáticas obtidas de diferentes modelos de circulación xeral para cada escenario. Esta aproximación é útil para cuantificar a influencia da compoñente termodinámica do cambio climático, que no caso dos incendios forestais correspóndese co aumento de demanda evaporativa da atmosfera, o cal facilita o secado dos combustibles. Os cambio na dinámica inducidos polo quecemento global non poden ser

avaliados con esta metodoloxía, polo que as variables máis vinculadas á dinámica atmosférica, como a velocidade do vento ou a precipitación, non son perturbadas no noso experimento. Mais os incendios forestais non son un fenómeno meteorolóxico, polo que a influencia do cambio climático no seu comportamento non responde unicamente ás interaccións directas co estado da atmosfera. É coñecido que unha maior concentración de dióxido de carbono na atmosfera e o aumento da temperatura potencian a fotosíntese, incrementando o crecemento da vexetación globalmente. Isto inflúe no comportamento dos incendios forestais ao aumentar a cantidade e a continuidade do combustible. Avaliamos a influencia desta compoñente da vexetación ao multiplicar a carga de combustible (un parámetro definido para cada categoría de combustible) nas nosas ecuacións polo factor de aumento da produtividade en cada escenario, obtido tamén dos modelos de circulación xeral. Os resultados demostran un aumento significativo, de entre o 2.5% e o 11%, na velocidade de propagación do conxunto de incendios analizados atribuíble á compoñente termodinámica do cambio climático dende a época pre-industrial. O aumento atribuíble á compoñente da vexetación estímase que é incluso máis pronunciado, mais a incerteza asociada a esta compoñente é maior. No caso das proxeccións para o final do século 21, considerando un escenario de emisións intermedias (SSP2-4.5), o incremento da velocidade de propagación asociado á compoñente termodinámica espérase que sexa máis intenso que o experimentado dende a época pre-industrial. Pola contra, espérase unha relaxación do efecto da compoñente da vexetación, evidenciando que a resposta do comportamento dos incendios ante o aumento de temperatura non é lineal. Considerando os diferentes incendios rexistrados por separado, obtense un aumento significativo da velocidade de propagación dende o período pre-industrial atribuíble á compoñente termodinámica en máis do 50% de eventos, e unha diminución significativa en menos do 3% de eventos. A zona máis sensíbel a este incremento é o norte de Portugal e o sur de Galicia, sendo esta unha das rexións europeas máis afectada polos incendios na actualidade. Este patrón espacial é debido a unha resposta non lineal do contido de humidade da vexetación viva co aumento da demanda evaporativa. Ademais da resposta da velocidade de propagación, analizouse tamén a variación da enerxía liberada polos incendios, para a cal tamén se atopou un aumento significativo asociado a ambas compoñentes (termodinámica e vexetación) e para ambos escenarios (presente-pasado e futuro-presente). Estes resultados indican que o cambio climático está aumentando a capacidade dos incendios forestais de alterar as condicións atmosféricas locais. Estes resultados están a ser revisados para a súa posterior publicación nun artigo científico na revista *Science of the Total Environment* [2].

Coa fin de ampliar o noso entendemento sobre os posibles impactos na meteoroloxía sinóptica do esperado aumento da área queimada na Península Ibérica, realizamos un experimento co modelo rexional atmosférico WRF no que analizamos a influencia dos incendios do 2017 (un dos anos con maior área queimada dende que hai rexistros) na meteoroloxía dos seguintes meses. Para isto realizamos dous conxuntos de simulacións dos meses da primavera de 2018: un conxunto partindo das variables de solo sen perturbar (como se non se tivesen dado os incendios do 2017), e o outro conxunto introducindo as perturbacións na vexetación asociadas aos incendios do 2017 obtidas mediante observacións do satélite. A hipótese de partida é que a gran área afectada polos incendios puidese ter unha influencia tanto na temperatura como na precipitación, xa que a vexetación pode actuar como unha importante fonte de humidade atmosférica durante os meses de primavera e verán. Aínda que si atopamos unha influencia significativa na temperatura e na humidade relativa en superficie, o impacto na precipitación queda reducido a menos do 1% segundo este estudo.

O principal proceso de interacción entre un incendio forestal e a atmosfera a escala local

prodúcese a través da piroconvección, no que os fluxos de calor sensible e humidade liberados pola combustión de biomasa orixinan correntes ascendentes de aire, que eventualmente pode chegar a condensar o seu vapor de auga formando unha nube. Nos casos de piroconvección profunda, o incendio pode chegar a formar unha tormenta, e as intensas correntes ascendentes e descendentes alteran por completo as condicións atmosféricas na superficie, afectando á propagación do incendio. Este acoplamento entre incendio e atmosfera pode provocar un comportamento moi errático do incendio, ademais de favorecer a inxección de fume nas capas máis altas da troposfera e chegando incluso á estratosfera, o cal pode ter grandes implicacións no balance de radiación e na química atmosférica. O desenvolvemento da piroconvección profunda non depende unicamente das características do incendios, senón que tamén son precisas unha serie de condicións ambientais ou meteorolóxicas que posibiliten a convección orixinada polos fluxos de calor procedentes do incendio. Analizamos estas condicións ambientais asociadas a este fenómeno utilizando o modelo acoplado atmosfera-incendio WRF-Fire, co cal simulamos varios incendios idealizados baixo 6000 perfís atmosféricos reais, obtidos de diferentes localizacións do sur de Europa. Os resultados das simulacións amosan que os procesos de piroconvección profunda desenvólvense unicamente para unha certa carga de combustible en superficie e para un certo grao de inestabilidade atmosférica. Ademais, puidemos ver que entre os índices de inestabilidade atmosférica empregados, o índice K é o que mellor identifica as condicións asociadas á piroconvección, o que nos permitiu establecer un limiar de risco de piroconvección empregando este índice en conxunto con o índice FWI de risco de incendios en superficie. Así, puidemos avaliar en que medida está o cambio climático alterando as condicións atmosféricas asociadas ao desenvolvemento da piroconvección profunda. Para iso empregamos diferentes proxeccións futuras de modelos climáticos rexionais para Europa, e analizamos as tendencias de ambos índices. O risco de incendio en superficie está experimentando un maior aumento co cambio climático nos países do sur de Europa. Pola contra, os días por ano cunha inestabilidade atmosférica axeitada para o desenvolvemento de piroconvección profunda aumentan máis acentuadamente nos países do norte de Europa. En xeral, cruzando os dous índices atopamos un aumento significativo do risco de piroconvección profunda en todo o sur de Europa, especialmente acentuado no nordeste da Península Ibérica, onde pasarán de ter entre 10 e 20 días por ano de alto risco de pirconvección por ano a entre 30 e 50 a finais do século 21, segundo o escenario de emisións RCP8.5. Porén, segundo os resultados das simulacións numéricas, o desenvolvemento da piroconvección profunda é fortemente dependente da cantidade de combustible dispoñible, polo que rexións cunha alta produtividade, como o noroeste da Península ou a costa oeste dos Balcáns teñen un maior potencial de experimentar este fenómeno baixo unhas mesmas condicións atmosféricas. Estes resultados foron publicados nun artigo científico na revista *Environmental Research Letters* [3]. Posteriormente á publicación destes resultados, puidemos comprobar que os limiares seleccionados para representar as condicións atmosféricas favorables ao desenvolvemento de piroconvección profunda cumpríanse durante o evento piroconvectivo de Galicia en xullo de 2022.

A xeito de resumo, podemos dicir que analizamos a relación entre os incendios forestais e a atmosfera en diferentes escalas, estudando como varían estas interaccións por causa do quecemento global antropoxénico. Nunha escala global, determinouse que áreas do planeta con un clima pouco favorable á presenza de incendios forestais pasarán a ter un clima asociado a unha alta actividade de incendios, algo especialmente importante no caso de algunhas rexións boreais con solos ricos en carbono, nas que esta maior incidencia de incendios pode

USC UNIVERSITAT DE CATALUNYA

retroalimentar o aumento de temperatura. Nunha escala máis rexional, cuantificouse o aumento da velocidade de propagación dos incendios da Península Ibérica atribuíble ao aumento da demanda evaporativa da atmosfera e ao aumento do crecemento da vexetación producidos polo cambio climático, comprobando tamén que efectos podería ter na meteoroloxía sinóptica. En canto ás interaccións locais entre atmosfera e incendios, identificáronse as condicións ambientais que poden favorecer o desenvolvemento de procesos de piroconvección profunda, analizando o aumento deste risco no futuro por causa do cambio climático. A conclusión xeral desta tese é que a importancia dos incendios forestais dentro do sistema climático está aumentando por causa do cambio climático, xa que se demostrou que as interaccións entre atmosfera e incendios intensifícanse ao longo de diferentes escalas ante o aumento de temperatura.

USC
UNIVERSIDADE DE SANTIAGO DE COMPOSTELA

Chapter 1

General introduction

Wildfires - also referred as wildland fires or vegetation fires - are the result of the combustion of vegetative fuels. Combustion is an exothermic chemical reaction between a fuel and a oxidizer that produces a different set of chemical products and heat [4]. Part of the Earth's surface is covered by plant organic matter (the fuel) under an atmosphere that contains 21% of oxygen (the oxidizer), which enables the existence of wildfires if an initial high-temperature heat source occurs (the ignition) [5].

The combustion of vegetation organic compounds can be expressed in a general way by the following chemical equation:

$$\text{Biomass} + O_2 + \text{Heat} \longrightarrow CO_2 + H_2O + \text{Thermal Energy} \tag{1.1}$$

Combustion can be considered as the reverse chemical process of photosynthesis, where carbon dioxide (CO_2) and water (H_2O) coupled with the sun's energy, are combined to produce organic matter and oxygen (O_2) [6].

Part of the heat released is transferred to the adjacent fuels, which allows combustion to continue as a spreading fire [7]. The wind and the terrain slope can enhance the propagation of the heat flux by reducing the resulting angle between the flame and the fuel [8]. The amount of heat required by the fuel to sustain combustion also depends on its water content, since part of the energy may be dissipated by the need to evaporate water. As a result, three conditions are required for a wildfire to occur: an ignition, sufficient fuel and suitable fuel dryness conditions [6]. Climate dynamics, vegetation patterns and human activity are involved in the occurrence of these three conditions, influencing wildfire activity. Through the biomass consumption and the release of different combustion products (smoke, heat, CO_2, etc.), wildfires can in turn affect the biosphere, atmosphere, hydrosphere, geosphere and cryosphere [9]. As a result of these two-way interactions, fire is considered an important component of the Earth System [9, 10, 11].

1.1 Fire in the Earth System

In order to achieve a better understanding of the role of wildfires on Earth, it is essential to analyse how they directly interact with the Earth System components.

USC
UNIVERSIDADE DE SANTIAGO DE COMPOSTELA

1.1.1 Interactions with humans

Human activity is an important source of fire ignitions in many ecosystems like tropical forests or savannas [12]. Humans ignite wildfires either intentionally, for land management purposes, or accidentally [13]. Humans also exert direct control on fire activity through active fire suppression and preventive fuel management, specially in densely populated regions and during recent decades due to fire-fighting and fire management advances [14].

Wildfires can result in large losses of house properties, infrastructure and even human lives. These damages are mostly associated with extreme wildfire events [15] reaching the wildland-urban interface (WUI) [16]. Smoke from wildfires can substantially degrade air quality [17], becoming an important contributor to global mortality [18, 19]. In addition to direct impacts on human health and economic losses, wildfires also affect society through indirect post-fire effects (increasing flooding risks, soil erosion, pollution of water bodies, etc.) [20].

1.1.2 Interactions with vegetation

Vegetation is a key factor for fire activity because it constitutes the necessary fuel for combustion [21]. Thus, the continuity [22] and structure [23, 24, 25] of the fuel enable and influence fire spread. Fuel availability can also influences the fire–climate relationship, since it also determines the climatic factors required for switching to fire-prone conditions [26, 27, 28].

But the relationship between wildfires and vegetation reaches far beyond that. Fire regimes, defined as the combination of wildfire characteristics in an area (such as frequency, intensity, size, season, etc.) [29], have shaped local ecosystems for centuries [30], co-evolving with plant-traits [31]. Consequently, fire regime transitions can have significant impacts on ecosystems and biodiversity [11, 30, 32].

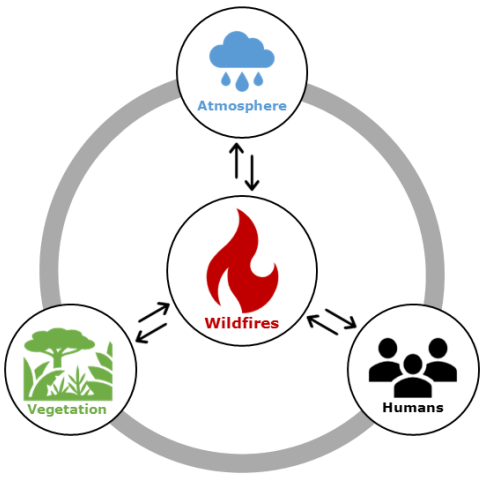


Figure 1.1: Schematic representation of the interactions between wildfires, humans, vegetation and the atmosphere.

USC
UNIVERSIDADE DE SANTIAGO DE COMPOSTELA

1.1.3 Interactions with the atmosphere

Interactions between wildfires and the atmosphere span across different spatial and temporal scales, that can be categorised into climate, synoptic and local scales.

Climate scale

Climate exerts two major impacts on global wildfire activity. In a direct way, climate drives global temperature and precipitation patterns, thus determining the occurrence of dry or hot seasons that control fuel dryness [21, 33, 34, 35]. In fact, inter-annual climate variability substantially contributes to burned area variability [36, 37, 38, 39, 40, 41]. In addition, climate also indirectly influences fire activity by controlling vegetation productivity and thus fuel availability [36, 42, 34].

Conversely, climate is affected by wildfire activity in multiple ways. Since biomass combustion is the reverse chemical process of photosynthesis [6], wildfires emit CO_2 into the atmosphere (equation 1.1) affecting the global carbon cycle and the greenhouse effect [43]. Fire-induced atmospheric CO_2 emissions are balanced by post-fire vegetation recovery carbon uptake [11, 44, 45], but this balance is disturbed by deforestation-related wildfires [11, 43], peatland fires [46] and different fire-induced shifts in the state of the carbon pools [47, 48]. It has been estimated that about 20% of the global fire emissions represent a net source of CO_2 that cannot be recovered by vegetation regrowth in decadal or centennial time scales [11, 49, 50]. Model simulations indicate that atmospheric CO_2 concentrations would be about 40 ppm lower in the absence of fires [51], an amount that is similar to the difference in observed mean annual CO_2 concentrations between 2022 (418.56 ppm) and 2004 (377.70 ppm), as measured in the Mauna Loa Observatory [52].

Smoke from wildfires contain aerosols that can affect the radiative balance of the Earth by directly scattering or absorbing shortwave radiation, by influencing cloud properties acting as cloud condensation nuclei, and by changing the surface albedo (either locally by altering the vegetation cover or remotely by black carbon deposition on glaciers, snow or ice sheets) [51, 53, 54, 55, 56, 57]. In addition, it has recently been demonstrated that fire smoke injections into the stratosphere can affect stratospheric chemistry, contributing to ozone depletion [58, 59, 60, 61].

Synoptic scale

Specific meteorological synoptic events or configurations can bring conditions of wind, temperature, precipitation or humidity that lead to favourable fire spread conditions (strong winds or low fuel moisture contents) [62, 63, 64, 65, 66]. Sustained droughts [40, 67], heat waves [68, 69] or Santa Ana [70, 71] or Foehn winds [72, 73] are some examples widely analysed in the scientific literature. In addition, weather can also be related to wildfire ignitions by lightning strikes, that can be most important ignition source for extreme wildfires [74, 75], even in the Iberian Peninsula [76, 77].

Wildfires are also able to modify the meteorological conditions on a synoptic scale. Fire burned areas involve abrupt changes in land cover that have climate and meteorological implications. Apart from the aforementioned effect on the radiative balance due to surface albedo changes [51], fire-induced vegetation disturbances can affect the hydrological cycle. Vegetation takes up soil water through its roots [78] and releases it into the atmosphere through evapotranspiration processes [79]. It has been estimated that up to 40% of precipitation over

UAB UNIVERSITAT AUTÒNOMA DE BARCELONA

land has its origin in terrestrial evapotranspiration [80] and that the contribution of vegetation to precipitation can surpass the 50% in some events [81]. Post-fire vegetation losses can significantly reduce local evapotranspiration depending on the burn severity [82, 83], leading to regional precipitation decreases in high fire activity areas like Africa, where fire season burned areas produce precipitation reductions of up to 10% during the wet season [84, 85].

In addition, regional precipitation patterns can be also altered by the influence of smoke aerosols in cloud microphysics and atmospheric radiation. The increased radiative absorption of the aerosol layer leads to modifications of vertical profiles of temperature that can alter atmospheric stability and synoptic dynamics [86, 87]. On the other hand, high concentrations of fine aerosols that can act as Cloud Condensation Nuclei (CCN) can lead to strong impacts on cloud microphysics [87, 88, 89]. The combination of both factors can result in a positive or negative effect on precipitation depending on the specific conditions of each event. Using meteorology-chemistry coupled simulations, Huang *et al.* [86] showed that smoke emissions from extreme wildfires in Southeastern Asia have modified the atmospheric temperature profile in the region, causing a mid-tropospheric heating and a surface dimming that result in a weakened convection and altered monsoon circulation, thereby suppressing rainfall in the region. Contrary, Zhang *et al.* [90] showed that 2018 wildfires in the western United States led to increased occurrences of heavy precipitation rates and large hail in the central United States, both by the smoke aerosol effects on cloud microphysics and by the altered synoptic circulation pattern. When large amounts of smoke from wildfires are injected into the stratosphere, as during the 2019/20 Australian wildfires, the increased aerosol radiation absorption can induce a persistent stratospheric warming [91] that alters the stratospheric synoptic circulation [92, 93].

Local scale

On a local or event scale, atmosphere influences fire behaviour predominantly through the wind. The combined effect of local topography and wind determines the spread of fires by changing the distance between the flame and the unburned fuel [94]. In addition, wind also influences fire behaviour by carrying burning particles (firebrands or embers) that can start new fires downwind where they reach the ground, a process known as spotting [95].

Wildfires can also substantially modify local atmospheric conditions through sensible and latent heat fluxes, creating their own weather [96]. The main mechanism by which a fire modifies atmospheric conditions is pyroconvection. The air above the fire warms due to the sensible heat emissions, rises and expands, forming a fire plume. As the air ascends, moisture can condense releasing latent heat, which enhances convection and results in the formation of pyrocumulus (pyroCu) or pyrocumulonimbus (pyroCb) clouds [97]. In cases of deeper convection, the fire may form a firestorm, leading to (a) intense updrafts and downdrafts that can modify surface winds and affect fire spread [98, 99, 100], (b) lightning activity that can spark new ignitions [101], (c) the formation of tornados [102, 103] and (d) stratospheric smoke injections [102, 104, 105]. The feedbacks between deep pyroconvection and surface atmospheric conditions may lead to an unpredictable and hazardous fire behaviour.

1.1.4 Interactions with other elements of the Earth System

Apart from the aforementioned interactions with the atmosphere, the biosphere and the anthroposphere, fires can also affect the hydrosphere through fluvial or marine sediment

USC

deposition [106], the cryosphere through black carbon deposition on snow or ice sheets [107, 108] and the geosphere by increasing the potential for soil erosion [109].

1.2 Anthropogenic climate change

In 1896 Svante Arrhenius [110], being aware of the importance of the chemical composition of the atmosphere into the global energy balance, prove that increased atmospheric CO_2 concentrations would result in long-term variations in surface temperature. But it wasn't until the late 1950s that Revelle and Suess [111] and Charles Keeling [112] found that the CO_2 concentration was increasing due to the burning of fossil fuels. In 1967 Manabe and Wetherald [113] developed the first numerical climate model, being able to predict that a doubling of the current CO_2 level would result in a 2°C increase in global temperature [113, 114]. Since then, scientific evidence that anthropogenic CO_2 emissions have warmed the climate has been mounting [115].

1.2.1 The radiative balance

The solar energy flux at the Earth (called the solar constant, S_0) depends on the distance between the Sun and the Earth (d), and on the rate at which the Sun emits energy (Q):

$$S_0 = \frac{Q}{4\pi d^2}. \tag{1.2}$$

Due to variations in the Earth's orbit S_0 is not really constant, but on average the incoming solar energy flux is $S_0 = 1367$ Wm^{-2} [116].

Given that the cross-sectional area of the Earth receiving the solar energy flux is πr^2 (where r^2 is the Earth's radius) and that part of the solar radiation is reflected according to the planetary albedo (with an average fraction value of $\alpha_p = 0.3$), the solar radiation absorbed by the Earth is [116]:

$$R_a = (1-\alpha_p) S_0 \pi r^2. \tag{1.3}$$

Considering that the Earth radiates in all directions like a spherical ($4\pi r^2$) blackbody of uniform temperature T_e, and following the Stefan-Botzmann law, the emitted terrestrial radiation is:

$$R_e = 4\pi r^2 \sigma T_e^4, \tag{1.4}$$

where σ is the Stefan-Boltzmann constant, $\sigma = 5.67 \cdot 10^{-8}$ Wm^{-2}K^{-4} [116].

In equilibrium, the emitted terrestrial radiation (R_e) must balance the absorbed solar radiation (R_a), so the emission temperature of the Earth is :

$$T_e = \left[\frac{S_0 (1-\alpha_p)}{4\sigma} \right]^{\frac{1}{4}} = 255 \text{ K}, \tag{1.5}$$

a value that is nearly 40K cooler than the globally averaged observed surface temperature. This difference is due to the fact that the atmosphere absorbs and re-emits downwards part of the radiation that receives from the Earth [116].

Wien's displacement law states that the wavelength of maximum energy emission from a black body is inversely proportional to the emission temperature, which indicates that solar radiation has its maximum energy in the visible spectrum (shortwave radiation) and that the Earth has its maximum in the infrared spectrum (longwave radiation) [117]. Although the atmosphere is almost completely transparent in the visible spectrum, much of the longwave radiation is absorbed within the atmosphere by some molecules (primarly H_2O, CO_2, CH_4 and N_2O) that can be excited by infrared radiation [116]. This absorbed radiation will be radiated downward and upward within the different layers of the atmosphere, so the surface receives more incoming radiation than if the atmosphere were not present. This effect is known as the greenhouse effect [117].

Higher atmospheric concentrations of these greenhouse gases (H_2O, CO_2, CH_4, N_2O and O_3) would lead to increases in incoming surface radiation and thus to a surface warming. The phase changes of water vapour, controlled by the hydrological cycle, mean that the residence time of H_2O in the atmosphere is much shorter than that of other greenhouse gases. So humans do not directly control the concentration of water vapour in the atmosphere. However, due to the longer time scales of the carbon cycle, human emissions of CO_2 and CH_4 into the atmosphere as a result of fossil fuel can significantly impact the atmospheric concentration of greenhouse gases, contributing to global warming [117].

1.2.2 Radiative forcing agents

Effective radiative forcing (ERF) quantifies the energy gained or lost by the Earth system as a result of an imposed perturbation, expressed in watts per square meter. ERF is determined by the change in the net downward radiative flux at the tropopause after the system has adjusted to the perturbation while maintaining the surface temperature unchanged [118]. The main radiative forcings that affect the Earth's climate can be grouped into anthropogenic and natural forcings.

The largest contribution to the Earth's radiative balance change comes from the modification of the atmospheric CO_2 concentration as a result of the burning of biomass and fossil fuels, with an ERF of 2.16 Wm^{-2} between 1750 and 2019 (Figure 1.2) [118]. Other human-induced changes in the concentration of well-mixed greenhouse gases present lower ERFs: 0.54 Wm^{-2} for CH_4 and 0.21 Wm^{-2} for N_2O (Figure 1.2) [118]. In 2019, concentrations of CH_4 and N_2O were higher than at any time in at least 800,000 years, and atmospheric CO_2 concentrations were unprecedented in at least 2 million years [119].

In addition, increased methane CH_4 concentrations can lead to higher H_2O concentrations in the stratosphere (through methane oxidation) that can also influence the radiative balance, since water vapour has a longer residence time in the stratosphere than in the troposphere. The estimated ERF of stratospheric water vapour is 0.05 Wm^{-2} (Figure 1.2) [118].

Tropospheric ozone (O_3) has a shorter atmospheric residence time, so the associated radiative forcing depends on the region considered [117]. Halocarbons, apart from inducing a positive forcing by acting as greenhouse gases, they can contribute to stratospheric ozone depletion, thus inducing a negative radiative forcing [117]. The overall effect is a positive ERF of 0.41 Wm^{-2} (Figure 1.2) [118].

Anthropogenic biomass and fossil fuels burning has also led to a significant increase in aerosol emissions. These human-induced changes in the atmospheric concentration of aerosols can change the radiative balance by absorbing and scattering shortwave and longwave radiation and by interacting with cloud formation [117]. The effective radiative forcing of aerosols

is negative, but not large enough to counterbalance the CO_2 radiative forcing alone (Figure 1.2). Other anthropogenic radiative forcings are surface albedo modifications associated with land-use changes or particle deposition on snow and ice surfaces, or aviation-induced cirrus and contrails [118].

The two main natural forcings are variations in the total solar irradiance and explosive volcanic eruptions. Changes in solar activity and Earth's orbital cycles can alter the total solar irradiance. It has been estimated that between the Maunder Minimum (1645–1715, a period of reduced solar activity) and the second half of the 20th century, the total solar irradiance increased by 0.7 to 2.7 Wm^{-2}, implying an ERF of 0.09 to 0.35 Wm^{-2} [120]. Over the last 9000 years, the reconstructed variability in total solar irradiance is of the order of 1.5 Wm^{-2} [121]. Major volcanic SO_2 injections into the stratosphere might persist for months in the atmosphere, reducing the incoming short-wave radiation and acting as a negative radiative forcing. Since 1750 the volcanic eruptions were episodic with no significant effect on the radiative balance [118].

The total anthropogenic effective radiative forcing between 1750 and 2019 is 2.72 Wm^{-2}, while the natural solar ERF is lower than 0.08 Wm^{-2} with a 95% of confidence [118]. The estimated contribution of all the forcing agents to 2019 temperature change relative to 1750 is 1.27°C (Figure 1.2), with a range between 0.96°C and 1.64°C as a 5%–95% confidence interval according to the IPCC Sixth Assessment Report [118].

1.2.3 Climate change evidences and climate system response

In response to the anthropogenic radiative forcings, all the climate system will adjust until an equilibrium is reached. The Intergovernmental Panel on Climate Change (IPCC) is a group of experts created by the United Nations that periodically prepare detailed reports about the state of scientific and socio-economic knowledge on climate change, its impacts and future risks. Some of the most important changes in the state of the climate system according to recently published IPCC Sixth Assessment Report are the following:

- *Temperature.* Global surface temperature has increased by $[0.84°C - 1.10°C]$ from 1850–1900 to 2001–2020, and by $[0.95°C - 1.20°C]$ from 1850–1900 to 2011–2020 [126]. Temperatures as high as during the 2011-2020 decade were likely unprecedented in the past 125,000 years [126]. The likely range of human-induced change in global surface temperature in 2010–2019 relative to 1850–1900 is 0.8°C to 1.3°C, while only –0.1°C to +0.1°C is attributable to natural forcings [126]. Figure 1.3, created by Kaufman *et al.* [125], shows different global mean surface temperature reconstructions for the last 12000 years. Figures 1.4a and 1.4b show the 2m air temperature trend for 1940-2022 and 1980-2022 periods respectively.

- *Atmospheric water-vapour.* The total atmospheric water vapour has increased since the 1970s, at a rate that was consistent with the Clausius-Clapeyron relationship (about 7% per °C) given the observed temperature trend [127]. Contrary, surface relative humidity has decreased over land in mid-latitude Northern Hemisphere continents (Figure 1.4d), possibly due to the larger warming rates over land than over the ocean and to reduced evapotranspiration by the drying of soils, specially during summertime [127].

USC UNIVERSIDADE DE SANTIAGO DE COMPOSTELA

- *Precipitation.* Human influence has contributed to an increase in high latitude land precipitation over the Northern Hemisphere and a strengthening of the zonal mean wet

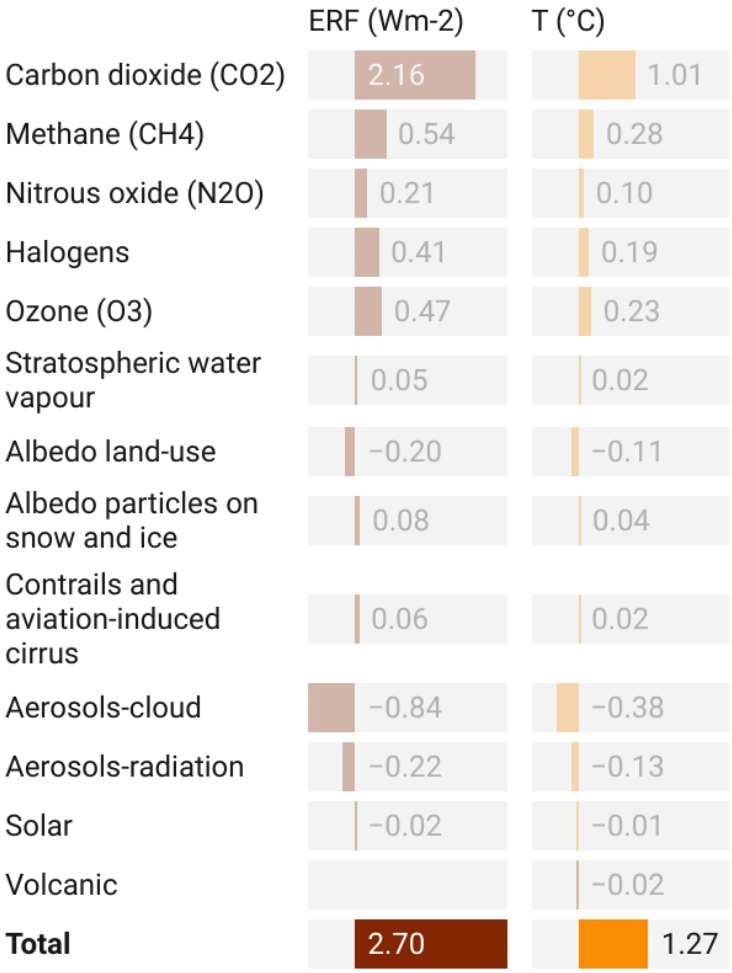


Figure 1.2: Contribution of different forcing agents to changes in effective radiative forcing (ERF) and global surface air temperature (T) from 1750 to 2019. Data from ref. [118].

tropics - dry subtropics contrast (Figure 1.4e) [127].

- *Atmospheric circulation.* It is likely that human influence has contributed to the poleward expansion of the Hadley cell in the Southern Hemisphere in recent decades [127]. By contrast, the Hadley cell expansion in the Northern Hemisphere may be within the range of internal variability [127].

- *Cryosphere.* Anthropogenic forcing is the main driver of Arctic sea ice loss, observed reductions in Northern Hemisphere springtime snow, general retreat of glaciers and observed surface melting of the Greenland Ice Sheet over recent decades [127].

- *Carbon cycle.* Vegetation greenness has increased over the last decades (Figure 1.4f). As CO_2 is the substrate for photosynthesis, rising atmospheric CO_2 concentration enhance photosynthesis, leading to an increased vegetation growth (CO_2 fertilization) [128]. Although CO_2 fertilization is the main driver of global greening, anthropogenic warming, regional trends in precipitation and land-use changes also contribute to vegetation greening [128].

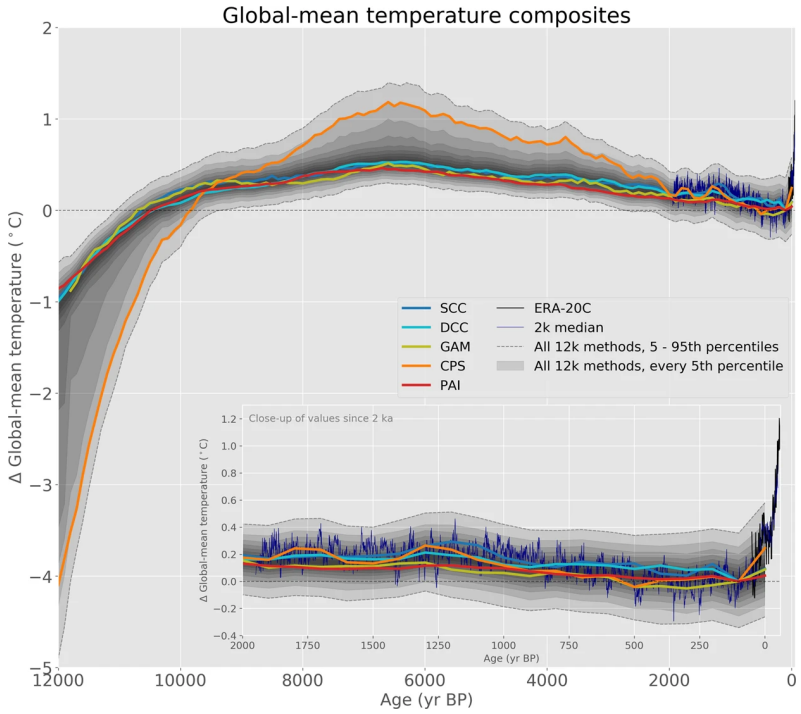


Figure 1.3: Global mean surface temperature from the Temperature 12k database using different reconstruction methods. Coloured lines are the ensemble medians of each of the five reconstruction methods (Standard Calibrated Composite (SCC), Dynamic Calibrated Composite (DCC), Composite Plus Scale (CPS), Pairwise Comparison (PAI) and Generalized Additive Model (GAM)). Gray shading represents every 5th percentile of the 2500 ensemble members from all methods; the 5th and 95th percentiles are indicated by dotted lines. The fine blue line is the median latitude-band 2000-year, multi-model temperature field reconstruction from Neukom *et al.* [122], which was based on data from PAGES 2k Consortium [123]. The fine black line is instrumental data for 1900–2010 from the ERA-20C reanalysis product [124]. The inset displays an enlarged view of the past 2000 years. Adapted with permission of Springer Nature from Kaufman *et al.*, ref. [125].

These modifications of the climate system variables can in turn alter the radiative fluxes, inducing feedbacks that can amplify (positive feedback) or dampen (negative feedback) the direct influence of the perturbation [117]. The most important positive and negative feedbacks of the climate system in response to a increase in surface temperature can be summarized as:

- *The longwave feedback.* As surface temperature increases, the emitted terrestrial radiation also augment according to equation 1.4, leading to the most basic negative feedback.
- *Water-vapour feedback.* A warmer atmosphere is able to host more water vapour according to the Clausius–Clapeyron relationship. An increased H_2O concentration results in enhanced absorption of longwave radiation and reduced outgoing radiation, leading to a positive feedback [118].
- *Lapse-rate feedback.* Vertical differences in the tropospheric warming can lead to a negative feedback. If the upper troposphere is affected by a larger temperature increase than the lower troposphere, the total emission of outgoing longwave radiation will be

USC UNIVERSIDADE DE SANTIAGO DE COMPOSTELA

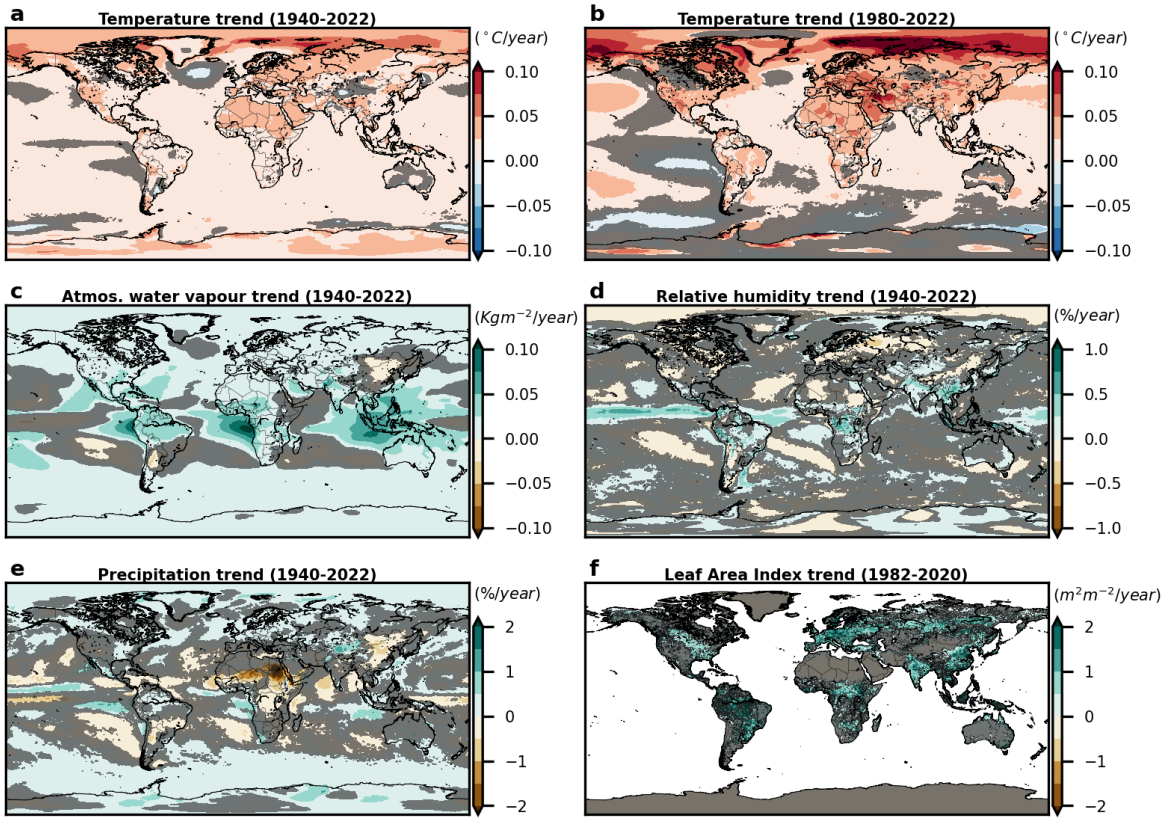


Figure 1.4: Historical trends of different environmental variables. **a**, 1940-2022 2 m temperature trend, **b**, 1980-2022 2 m temperature trend, **c**, 1940-2022 total column atmospheric water vapour trend, **d**, 1940-2022 2 m relative humidity trend, **e**, 1940-2022 annual precipitation trend and **f**, 1982-2020 leaf area index trend. Data for panels **a**, **b**, **c**, **d** and **e** were obtained from ERA5 reanalysis [129] and data for panel **f** were obtained from GIMMS LAI4g dataset [130].

higher, since upper levels provide a large contribution to the total vertical emission [117]. This vertical pattern of temperature increase dominates in the tropics, leading to a negative global mean lapse-rate feedback [118]. In high latitudes the temperature increase vertical pattern is reversed, leading to a positive feedback that partly causes the exacerbated temperature increase in the Artic region (Figure 1.4b), known as polar amplification [131].

- *Surface albedo feedback.* The temperature increase induce albedo changes primarily by reducing the extent of sea ice and snow cover, as these surfaces are highly reflective [118]. A less reflective surface implies an increase in solar radiation absorbed by the Earth, leading to a positive feedback. This feedback is also a major contributor to the polar amplification [131].

- *Cloud feedbacks.* The presence of clouds tends to reduce the longwave emission from Earth, but also the incoming shortwave radiation [117]. Therefore, the induced changes in cloud formation can lead to a positive or negative feedback depending on the type of cloud and on the region [118].

- *Soil moisture feedbacks.* When the temperature rises, the water demand of the atmosphere increases due to the Clausius–Clapeyron equation, leading to enhanced evapotranspiration that cools the surface. Eventually, this enhanced evapotranspiration can dry the soils, reducing the water exchange and finally leading to a positive feedback [117].

- *CO_2 fertilization feedback.* Increased vegetation growth due to CO_2 fertilization leads to a larger carbon sequestration by the biosphere, thus inducing a negative feedback [118].

1.2.4 Future climate change

Intergovernmental Panel on Climate Change (IPCC) Assessment Reports (AR) assess results from multiple General Circulation Models (GCMs). The implementation of these models is carried out by different institutions and it is coordinated by the World Climate Research Programme (WCRP) under different projects named Coupled Model Intercomparison Project (CMIP). IPCC Sixth Assessment Report analyses model outputs of the Coupled Model Intercomparison Project Phase 6 (CMIP6).

Future climate change impacts are assessed by forcing global climate models with different projections of greenhouse gases emissions, aerosols or land-use patterns. These projections are grouped in different scenarios: descriptions of how the future may develop, based on a set of assumptions about demography, economic processes, technological innovation, governance and lifestyles [115]. Scenarios in CMIP6 [132] were developed using the Shared Socio-economic Pathways (SSP) framework, with five different SSPs representing 'sustainability' (SSP1), a 'middle-of-the-road' path (SSP2), 'regional rivalry' (SSP3), 'inequality' (SSP4) and 'fossil fuel-intensive' development (SSP5). These scenarios are usually labelled with the approximate radiative forcing value reached by 2100, spanning from 1.9 to 8.5 Wm^{-2}: SSP1-1.9, SSP1-2.6, SSP2-4.5, SSP3-7.0 and SSP5-8.5.

Scenarios in CMIP5 [133], the Coupled Model Intercomparison Project Phase 5 developed for the Fifth Assessment of the IPCC, were grouped under different Representative Concentration Pathways, also labelled with the approximate radiative forcing value reached by 2100: RCP2.6, RCP4.5, RCP6.0 and RCP8.5. In CMIP3 [134], the Coupled Model Intercomparison Project Phase 5 developed for the Fourth Assessment of the IPCC, three scenarios were consider: a low low forcing scenario (B1), a medium forcing scenario (A1B) and a high forcing scenario (A2).

USC UNIVERSIDADE DE SANTIAGO DE COMPOSTELA

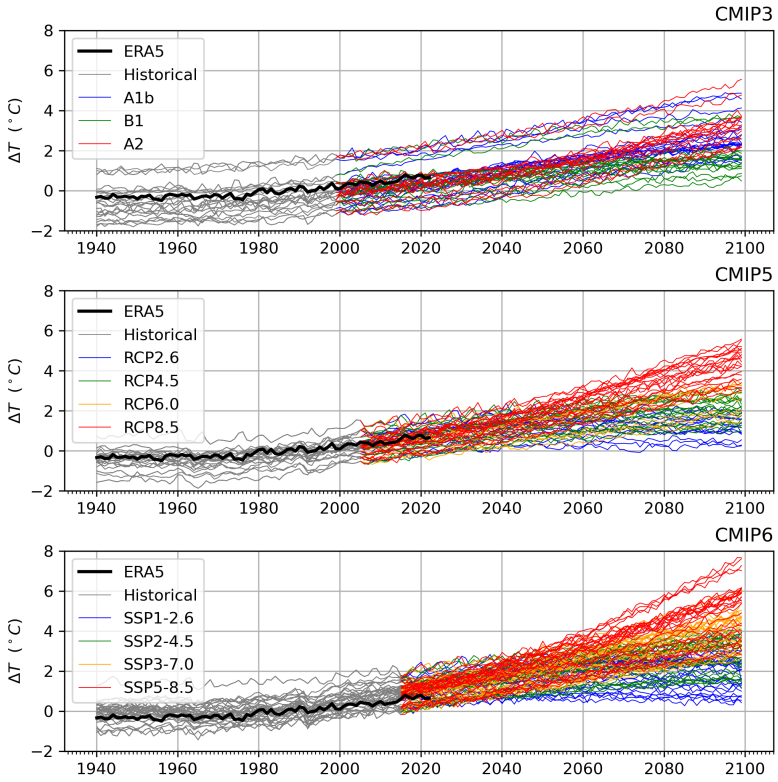


Figure 1.5: Global mean surface temperature anomaly for multiple models of CMIP3 [134], CMIP5 [133] and CMIP6 [132]. Historical period of each CMIP is coloured in grey. Each colour of the future projections represent a different scenario. ERA5 global mean surface temperature (1940-2020) is shown in black [129]. Temperature anomalies were obtained from ERA5 1940-2020 mean surface temperature [129].

1.3 Fires and climate change

Fires interact with the atmosphere at different spatial and temporal scales. As anthropogenic climate change alters atmospheric conditions, it is expected that fire activity will be affected, thus modifying the interactions between fires and the atmosphere as well as the role of fires in the Earth system.

The issue of how climate change affects wildfires has already been addressed in multiple studies. In general, higher fire risk is expected under a warmer climate as a result of fuel dryness increase [13, 135, 136, 137, 138, 139, 140], but there is a lot of spatial variability depending on precipitation and vegetation patterns [9, 141]. Fire risk or fire weather increases can lead to longer fire seasons [38, 142, 143] and to larger burned areas [22, 144, 145, 146, 147, 148, 149, 150], although trends in burned area are also highly dependent on human activity [12]. Due to the occurrence of highly devastating fires in recent years (such as the Australian 2019-2020 fire season [151], the 2021 Boreal fires [50], the October 2017 wildfires in the Iberian Peninsula [152] or the 2020 California fire season [153]) the link between climate change and extreme wildfire events is also being extensively studied [69, 154, 155, 156, 157, 158, 159].

However, despite the increased interest in fire and climate change within the scientific community, there are still many uncertainties regarding the impact of climate change on fire-atmosphere interactions. The large number of involved factors [160] (such as human

ignitions, suppression efforts, vegetation dynamics, etc.) and the complex interactions among these factors [31, 161] are usually referred as the main sources of uncertainty concerning the study of the relation between climate change and fire activty. In addition, the relatively brief fire records [9], the large spatial heterogeneity in fire controls and fire activity [141], and the number of different spatial and temporal scales involved [148] also hinder our understanding on how the fire-atmosphere relation is changing due to global warming.

1.4 Objectives and thesis outline

The main objective of this thesis is to identify and quantify the influence of climate change on different fire-atmosphere interactions. Our analysis aims to cover the different scales of the fire-atmosphere relationship, thus the specific objectives at each scale are different.

On a global scale, we focus on determining which regions that are not exposed to fire activity at present are likely to become fire-prone in the future, posing a threat to soil carbon stocks. To achieve this goal, we define these two objectives:

1. To identify the climate indicators that define the global pattern of fire-prone regions by comparing satellite-derived burned area data and climate variables.

2. To assess future potential changes in the extent of fire activity by analysing climate change projections of different General Circulation Models.

From a synoptic to a local scale, our goal is to identify which effects of climate change are influencing fire behaviour and to what extent. To do so, these objectives were defined:

3. Quantify the influence of ongoing climate change on the rate of spread and the energy released of multiple recent fire events by using a climate change attribution approach.

4. For these same events, compare the relative contribution of enhanced vegetation growth and increased fuel dryness on fire behaviour.

On a local scale, we aim to assess if climate change is favouring extreme fire events associated with deep pyroconvection, thus defining these specific objectives:

5. Identify the environmental conditions that enable deep pyroconvection by using a fire-atmosphere coupled model.

6. Analyse the trend in the risk of deep pyroconvection using different climate change scenarios.

The main results obtained throughout the thesis are included in Chapters 3, 4 and 5, with each chapter focusing on a different scale. Chapter 3 covers objectives 1 and 2, Chapter 4 objectives 3 and 4 and Chapter 5 objectives 5 and 6. Chapter 2 contains a detailed description of some of the equations and methods used in this thesis, including two case studies of coupled fire-atmosphere simulations. Chapter 6 summarises the results obtained throughout the thesis with a focus on Galicia, complemented with some specific analyses not included in the previous chapters. The main conclusions of the thesis are provided in Chapter 7.

USC UNIVERSIDADE

USC
UNIVERSIDADE
DE SANTIAGO
DE COMPOSTELA

Chapter 2

Methodology

The following is a detailed description of some of the physical background and mathematical expressions used to represent fire behaviour and their interactions with the environment. Some coupled fire-atmosphere simulations of two recent extreme fire events are presented at the end of this chapter.

2.1 Rothermel's fire spread model

The Rothermel's fire spread model [94] is based on the conservation of energy described by a heat source (burning fuel) and a heat sink (unburned fuel) [162], and it calculates spread rate of a head fire with or without wind and slope. The model is categorized as quasi-empirical, since it combines physical relations representing heat transfer and conservation of energy with empirical relations obtained from wind tunnel experiments in artificial fuel beds and data from real wildfires [163]. The model has been used since its origins as a quantitative index of fire risk and as a tool for fire spread prediction.

Heat is released from the fire to the potential fuel, so the surface is dehydrated and further heating raises the surface temperature until the fuel begins to pyrolyze, releasing combustible gases [94]. When the gas evolution rate from the potential fuel is sufficient to support combustion, the gas is ignited by the flame and the fire advances [94].

The steady rate of spread (R) equation is equal to the heat received by the fuel ahead of the fire divided by the heat required for the ignition of this fuel [163]:

$$R = \frac{I_P}{\rho_{be} \cdot Q_{ig}}, \tag{2.1}$$

where I_P is the heat flux absorbed by a unit volume of fuel (whose SI units are $\mathrm{J \cdot m^{-2} \cdot s^{-1}}$), ρ_{be} is the effective bulk density (i.e. the amount of fuel per unit volume of the fuel bed that burns, with units $\mathrm{kg \cdot m^{-3}}$) and Q_{ig} is the heat required to bring a unit weight of fuel to ignition (also known as heat of preignition, with units $\mathrm{J \cdot kg^{-1}}$).

2.1.1 Heat sink

USC

The heat required for ignition, or heat sink, depends on the ignition temperature, the moisture content of the fuel and the amount of fuel involved in the ignition process. Considering cellulosic fuels, the energy per unit mass required for ignition (Q_{ig}) is defined as:

$$Q_{ig} = c_{pd} \cdot \Delta T_{ig} + M_f \left(c_{pw} \cdot \Delta T_v + L_v \right), \tag{2.2}$$

where c_{pd} is the specific heat of dry wood with units $\mathrm{kJ} \cdot \mathrm{K}^{-1} \cdot \mathrm{kg}^{-1}$, ΔT_{ig} is the temperature range to ignition in Kelvin, M_f is the fuel moisture expressed as a fraction between mass of water and mass of dry wood, c_{pw} is the specific heat of water with units $\mathrm{kJ} \cdot \mathrm{K}^{-1} \cdot \mathrm{kg}^{-1}$, ΔT_v is the temperature range to vaporization in Kelvin and L_v is the water specific latent heat of vaporization with units $\mathrm{kJ} \cdot \mathrm{kg}^{-1}$. An approximate version of this expression is commonly used, assuming that the ignition temperature ranges from 20°C to 320°C and that the boiling temperature is 100°C, then equation 2.2 becomes:

$$Q_{ig} = 581 + 2.59 \cdot M_f. \tag{2.3}$$

The amount of fuel involved in the ignition process is expressed as the effective bulk density (ρ_{be}), that depends on the amount of fuel per unit volume of the fuel bed (the actual bulk density, ρ_b) and the efficiency of the combustion process (the effective heating number, ε), since not all the available fuel is completely burned:

$$\rho_{be} = \varepsilon \rho_b. \tag{2.4}$$

The bulk density (ρ_b) is a fuel property that depends on the oven-dry fuel load (w_0) and the fuel bed depth (δ):

$$\rho_b = w_0 / \delta. \tag{2.5}$$

The effective heating number (ε) was determined experimentally as a function of the surface-area-to-volume ratio of the fuel (σ):

$$\varepsilon = \exp\left(-\frac{4.528}{\sigma} \right), \tag{2.6}$$

This relation indicates that combustion efficiency is higher in fuels consisting of thin structures, with a high ratio of surface are to volume σ. The units of the σ fuel property are cm^{-1}.

2.1.2 Heat source

The propagating flux (I_P) is the heat per unit area and per unit time transferred from the burning fuel to the adjacent potential fuel. It has two components, an horizontal term (I_x) and a vertical term (I_z). The vertical flux is more important during wind-driven and upslope fires, in which the flames tilt over the fuel, increasing radiation and convective heat transfer and causing direct flame contact (Figure 2.1). For convenience, the propagating flux is usually expressed as a no-wind no-slope flux (I_{P0}) and two wind and slope dependent terms (Φ_w and Φ_s):

$$I_P = I_{P0} \cdot \left(1 + \Phi_w + \Phi_s \right). \tag{2.7}$$

The propagating flux (I_P) is expected to be closely related to the rate of energy released by the fire front, produced by burning gases coming from the organic matter in the fuel. Therefore, the heat release rate per unit area of the front (named the reaction intensity, I_R) is equal to the rate of change of organic matter from solid to gas and the heat content of the fuel:

USC DE SANTIAGO DE COMPOSTELA

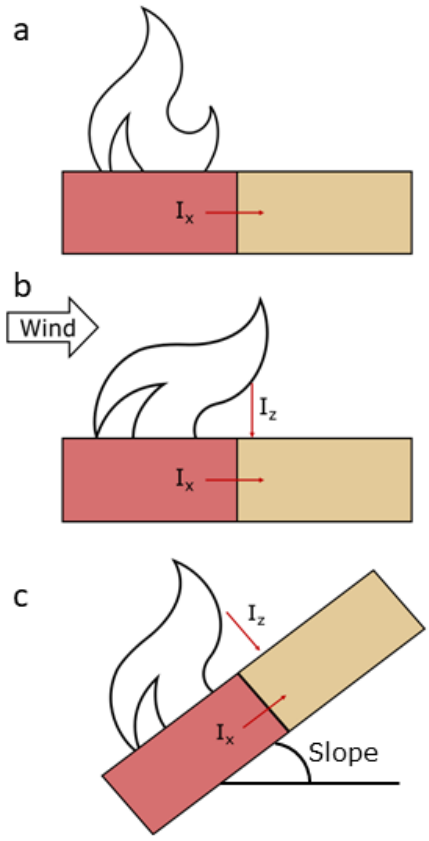


Figure 2.1: Schematic representation of a no-wind and no-slope spreading fire (**a**), a wind-driven fire (**b**) and a slope driven fire (**c**), with arrows I_x and I_z representing the horizontal and vertical term of the propagating flux.

$$I_R = -\frac{dw}{dt} \cdot h, \tag{2.8}$$

where dw/dt is the mass loss per unit area in the fire front (with units $\mathrm{kg \cdot m^{-2} \cdot s^{-1}}$) and h is the heat content of the fuel (with units $\mathrm{J \cdot kg^{-1}}$). We can rearrange equation 2.8 by using the net initial fuel load (w_n), the residue load after passage of the reaction zone (w_r) and the time taken for the fire to travel the reaction zone (t_R):

$$I_R = \frac{w_n - w_r}{t_R} \cdot h. \tag{2.9}$$

The net fuel load w_n can be obtained by subtracting the mineral content (S_T) to the oven-dry fuel load (w_0): $w_n = w_0 \cdot (1 - S_T)$.

We can define the reaction velocity (Γ) as the fraction of the initial fuel loading (w_n) consumed during the time taken for the fire to travel the reaction zone (t_R):

$$\Gamma = \frac{\frac{w_n - w_r}{w_n}}{t_R}. \tag{2.10}$$

Combining equations 2.10 and 2.10 we obtain:

USC UNIVERSIDADE DE SANTIAGO

$$I_R = \Gamma \cdot w_n \cdot h. \tag{2.11}$$

Four fuel parameters have a major effect on Γ: moisture content, mineral content, surface-area-to-volume ratio and the fuel bed bulk density. The effect of fuel moisture and mineral content is represented by two damping coefficients (η_M and η_S). The moisture damping coefficient equation represents the decrease in intensity caused by the combustion of fuels that initially contained moisture. It was determined by Anderson [164], who tested identical fuel beds over a wide moisture range:

$$\eta_M = 1 - 2.59\frac{M_f}{M_e} + 5.11\left(\frac{M_f}{M_e}\right)^2 - 3.52\left(\frac{M_f}{M_e}\right)^3, \tag{2.12}$$

where M_f is the fuel moisture content and M_e is the moisture content of the fuel at which fire will not be able to spread (moisture content of extinction). The relation of the fuel moisture content with the fire rate of spread at constant wind and slope is shown in Figure 2.2a, representing fuel models with different moisture contents of extinction.

The mineral content damping coefficient was evaluated from thermogravimetric analysis data of natural fuels by Philpot [165]:

$$\eta_S = 0.174 \cdot S_e^{-0.19}, \tag{2.13}$$

where S_e is the fractional mineral content of the fuel.

Other fuel properties that affect reaction velocity (Γ) are contained in one relation that was experimentally obtained by Rothermel [94]. He defined the potential reaction velocity (Γ') so that $\Gamma = \Gamma' \eta_m \eta_s$, obtaining the following expression for Γ' in terms of fuel properties:

$$\Gamma' = \Gamma'_{max}\left(\frac{\beta}{\beta_{op}}\right)^A \exp\left[A \cdot \left(1 - \frac{\beta}{\beta_{op}}\right)\right]. \tag{2.14}$$

Here, Γ'_{max} is the maximum reaction velocity, calculated from the surface-area-to-volume ratio:

$$\Gamma'_{max} = \left(3.546 + 175.56\sigma^{-1.5}\right)^{-1}, \tag{2.15}$$

The packing ratio or fuel bed compactness (β) in equation 2.14 is calculated from the bulk density (ρ_b) and the fuel particle density (ρ_p):

$$\beta = \frac{\rho_b}{\rho_p}. \tag{2.16}$$

The optimum packing ratio (β_{op}) in equation 2.14 is calculated from the surface-area-to-volume ratio (σ):

$$\beta_{op} = 0.20395\sigma^{-0.8189}, \tag{2.17}$$

The term A in equation 2.14 is also related to the surface-area-to-volume ratio (σ):

$$A = 8.9033\sigma^{-0.7913}, \tag{2.18}$$

USC UNIVERSIDADE DE SANTIAGO DE COMPOSTELA

Therefore, the final equation for the reaction intensity (I_R) is:

$$I_R = w_0(1-S_T)\cdot h\cdot \eta_M \cdot \eta_S \cdot \Gamma'_{max}\left(\frac{\beta}{\beta_{op}}\right)^A \exp\left[A\cdot\left(1-\frac{\beta}{\beta_{op}}\right)\right]. \tag{2.19}$$

But as mentioned before, the reaction intensity (I_R) is the total heat release rate per unit area in all directions, not only in the direction of the adjacent fuel (I_P). Therefore, the proportion of the total reaction intensity (I_R) that actually heats adjacent fuel must be considered, and it is defined as the propagating flux ratio (ξ), so that: $I_{P0} = I_R \cdot \xi$. Rothermel [94] found the following equation for ξ as a function of β and σ:

$$\xi = \frac{\exp\left[\left(0.792+3.7597\sqrt{\sigma}\right)(\beta+0.1)\right]}{192+7.9095\sigma}. \tag{2.20}$$

Combining the heat source and heat sink expressions, we get the final no-wind no-slope rate of spread equation:

$$R_0 = \frac{I_R\xi}{\rho_b \varepsilon Q_{ig}}. \tag{2.21}$$

2.1.3 Wind and slope coefficients

Rate of spread measurements in the presence of wind or different slopes, combining laboratory experiments by Rothermel [94] and field data by McArthur [166], were used to determine the wind and slope coefficients of equation 2.7. The equation obtained for the wind coefficient (Φ_w) as a function of the surface wind (U) in $\mathrm{m}\cdot\mathrm{s}^{-1}$ is:

$$\Phi_w = C\cdot(196.85U)^B\cdot(\beta/\beta_{op})^{-E}, \tag{2.22}$$

where:

$$C = 7.47\exp\left(-0.8711\sigma^{0.55}\right) \tag{2.23}$$

$$B = 0.15988\sigma^{0.54} \tag{2.24}$$

$$E = 0.715\exp\left(-0.01094\sigma\right). \tag{2.25}$$

The slope coefficient equation is a function of slope steepness ($\tan\varphi$) and packing ratio (β):

$$\Phi_s = 5.275\cdot\beta^{-0.3}(\tan\varphi)^2. \tag{2.26}$$

A comparison of the relative importance of the wind and slope coefficients is shown in Figure 2.2b, which shows for different wind intensities the slope angle that equals the contribution of the wind and slope coefficients to the rate of spread.

2.1.4 Final form

The final form of the rate of spread R, with units $\mathrm{m}\cdot\mathrm{s}^{-1}$, is:

$$R = \frac{I_R\xi\left(1+\Phi_w+\Phi_s\right)}{\rho_b\varepsilon Q_{ig}}, \tag{2.27}$$

USC UNIVERSIDADE DE SANTIAGO DE COMPOSTELA

where I_R is the reaction intensity with units $\mathrm{kJ \cdot s^{-1} \cdot m^{-2}}$ (equation 2.19), ξ is the propagating flux ratio (unitless, equation 2.20), Φ_w is the wind factor (unitless, equation 2.22), Φ_s is the slope factor (unitless, equation 2.26), ρ_b is the oven-dry bulk density with units $\mathrm{kg \cdot m^{-3}}$ (equation 2.5), ε is the effective heating number (unitless, equation 2.6) and Q_{ig} is the heat of preignition with units $\mathrm{kJ \cdot kg^{-1}}$ (equation 2.3).

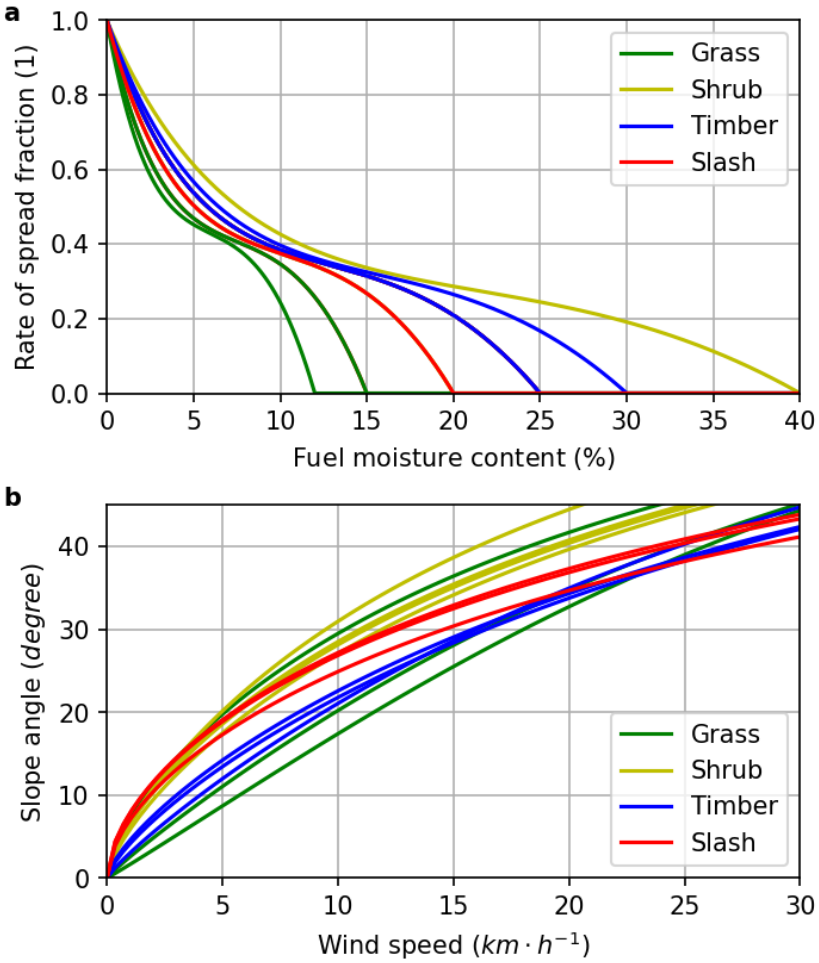


Figure 2.2: Rate of spread relations. **a**, Rate of spread decline with dead fuel moisture, expressed as a fraction between the rate of spread at different fuel moisture contents and the rate of spread at zero moisture content. **b**, Correlation of wind speeds and slope angles with identical effect on the rate of spread. Results are shown for the 13 Anderson fuel models [167], with different colours representing fuel model groups (grass, shrub, timber and slash).

2.1.5 Fuel models

The Rothermel's rate of spread model requires 11 input parameters grouped into three categories: fuel particle properties, fuel array arrangements and environmental variables (Table 2.1).

Fuel particle properties are parameters that are intrinsic to the fuel particle, and they are often held constant [163]. Fuel array properties related to the fuel bed are instead defined under

Table 2.1: Input parameters for the Rothermel's rate of spread model.

Type	Symbol	Units	Definition
Fuel particle	h	$kJ \cdot kg^{-1}$	Fuel heat content
	S_T	fraction	Total mineral content
	S_E	fraction	Effective mineral content
	ρ_p	$kg \cdot m^{-3}$	Oven-dry particle density
Fuel array	σ	cm^{-1}	Surface-area-to-volume ratio
	w_0	$kg \cdot m^{-2}$	Oven-dry fuel load
	δ	m	Fuel bed depth
	M_x	fraction	Moiture content of extinction
Environmental	M_f	fraction	Moisture content
	U	$kJ \cdot kg^{-1}$	Wind speed
	$\tan\varphi$	fraction	Slope steepness

different fuel models, that contain a complete set of inputs for the mathematical fire spread equations. These fuel models are composed of heterogeneous mixtures of fuel sizes and include both dead and live fuels.

The described rate of spread equations apply to a single size class of fuel, named as the basic fire spread model. In order to apply the model to heterogeneous fuels (fuel models), a weighting method was developed based on the surface area of the fuel within each size class [94]. The average surface area per unit fuel cell of each size class (A_{ij}) is obtained from the fuel load of each size class ($(w_0)_{ij}$), the surface-area-to-volume ratio (σ_{ij}) and the particle density (ρ_p):

$$A_{ij} = \frac{\sigma_{ij} \cdot (w_0)_{ij}}{\rho_p}, \tag{2.28}$$

where subscripts j are used to indicate the fuel size class and subscripts i are used to indicate the fuel type ($i = 1$ for dead fuels and $i = 2$ for live fuels) [163]. Therefore, weighting factors f_{ij} and f_i are defined as following:

$$f_{ij} = \frac{A_{ij}}{\Sigma_j A_{ij}} \qquad , \qquad f_i = \frac{\Sigma_j A_{ij}}{\Sigma_{ij} A_{ij}}. \tag{2.29}$$

Dead fuel components of fuel models are organized by size or time lag: fine (1-h), medium (10-h) large (100-h) and extra-large (1000-h). Finer dead fuels have shorter time lag and higher surface-area-to-volume ratio, and its moisture responds faster to changes in the environment [168]. Moisture content of dead fuels can be estimated from environmental variables through a time-lag equation, considering that moisture m approaches an equilibrium E with a time lag t_L:

$$\frac{dm}{dt} = \frac{E - m}{t_L}. \tag{2.30}$$

If coefficients E and t_L are constant in time, the solution of equation 2.30 is [168]:

$$m(t) = E + (m(0) - E)\, e^{-t/t_L}. \tag{2.31}$$

USC UNIVERSIDADE DE SANTIAGO DE COMPOSTELA

The moisture equilibrium E is defined from surface temperature (T) and relative humidity (RH) according to the Van Wagner and Pickett approach [169, 170]:

$$E = a \cdot RH^b + c \cdot \mathrm{e}^{\frac{RH-100}{10}} + d(21.1 - T)(1 - \mathrm{e}^{-f \cdot RH}), \tag{2.32}$$

where a, b, c, d and f are constants. By using two different sets of values of these constants, a drying (E_d) and a wetting (E_w) equilibrium moisture contents were defined based on laboratory tests [169]. E_d is then used as equilibrium moisture if $m > E_d$ and E_w is used as equilibrium moisture if $m < E_w$. Moisture change is zero when $E_d \geq m \geq E_w$ [168]. When rainfall occurs, the equilibrium moisture content (E) is equal to the saturation fuel moisture content (S) and the time lag depends on the rain intensity (r):

$$\frac{dm}{dt} = \frac{S - m}{t_r} \left(1 - \exp\left(-\frac{r}{r_s} \right) \right), \tag{2.33}$$

where r_s is the saturation rain intensity and t_r is the minimum rain-wetting time lag [168]. The effective time lag is longer for low rain intensities and reaches t_r asymptotically for heavy rainfall [168]. These equations for determining dead fuel moisture are based on both physical and empirical relations. There are other approaches available in the literature, either physical or empirical [171, 172, 173].

Fuel models may also include two live fuel components, labelled as herbaceous and woody live fuels. The fuel moisture content of live fuels depends on the phenological state of vegetation, with a seasonal variation throughout the year determined by the vegetation growing season. Although vegetation greenness can be estimated from satellite observations, an index based on environmental variables can also be used to assess live fuel moisture. The Growing Season Index [174] considers daylength, evaporative demand and suboptimal temperature thresholds to identify the state of the vegetation, and it can be employed as a live fuel moisture predictor. This index varies between 0 (inactive vegetation) and 1 (unconstrained vegetation activity), and it is defined as the product of three environmental indicators:

$$GSI = iT_{min} \cdot iVPD \cdot iPhoto, \tag{2.34}$$

where iT_{min} is the daily indicator for minimum temperature (T_{min}) and varies from 0 when $T_{min} \leq -2$°C to 1 when $T_{min} \geq 5$°C, $iVPD$ is the daily indicator for vapour pressure deficit (VPD) and varies from 0 when $VPD \geq 4100$ Pa to 1 when $VPD \leq 900$ Pa, and $iPhoto$ is the daily photoperiod indicator and varies from 0 when the daylength is shorter than 10 hours to 1 when the daylength is longer than 11 hours [174]. Live fuel moisture is set to a minimum value (30% for herbaceous and 60% for woody fuels) when $GSI = 0$. When $GSI > 0.5$, live fuel moisture increases linearly up to a maximum value (250% for herbaceous and 200% for woody fuels) when $GSI = 1$.

Eleven fire behaviour fuel models were initially described by Rothermel [94]: short grass, tall grass, brush, chaparral, timber (grass and understory), timber (litter), timber (litter and understory), hardwood litter, light logging slash, medium logging slash and heavy logging slash. Anderson [167] expanded these fuel models to 13, and Scott and Burgan [175] developed a set of 40 fuel models organized into 6 categories: grass, grass-shrub, shrub, timber-understory, timber litter and slash-blowdown.

USC UNIVERSIDADE DE SANTIAGO DE COMPOSTELA

2.2 Numerical simulation of the atmosphere

Atmospheric motions are governed by three fundamental physical principles: mass conservation, momentum conservation and energy conservation [176]. Newton's second law (the conservation law for momentum) relates the rate of change of absolute velocity of the fluid (U) to the sum of forces acting on the fluid:

$$\frac{d\mathbf{u}}{dt} = -2\Omega \times \mathbf{u} - \frac{1}{\rho}\nabla p + \mathbf{g} + \mathbf{F}, \tag{2.35}$$

where $\frac{1}{\rho}\nabla p$ is the pressure gradient force term, $\mathbf{g}$ is the gravity term, $\mathbf{F}$ is the frictional force and $-2\Omega \times \mathbf{u}$ is the Coriolis force term.

By applying the mass conservation law to an air parcel, an expression is obtained that relates the rate of change of the fluid density (ρ) with the velocity divergence, known as the continuity equation:

$$\frac{1}{\rho}\frac{d\rho}{dt} + \nabla \cdot \mathbf{u} = 0. \tag{2.36}$$

The conservation of energy applied to a moving parcel of fluid leads to the thermodynamic energy equation, that relates the latent and radiative heating rate (J) with temperature (T) and density changes of the fluid parcel:

$$c_v \frac{dT}{dt} + p\frac{d\alpha}{dt} = J, \tag{2.37}$$

where α is the inverse of the fluid density $\alpha = \rho^{-1}$.

Equations 2.35, 2.36 and 2.37 determine the atmospheric circulation. Since they do not have an analytical solution, atmospheric models solve these differential equations from a set of initial and boundary conditions through numerical methods, that can be divided into finite difference methods (which solve the equations by approximating derivatives with finite differences in a discretized domain) and spectral methods (in which the solution is written as a sum of basis functions). Some physical processes occur at scales too small, or they are too complex, so they cannot be physically represented in atmospheric models. These processes (such as cloud microphysics or turbulence) are thus parametrised, so they are represented using other resolved variables.

Both climate and weather modelling consist mainly of solving the same equations and representing the same processes. However, weather modelling is said to be an initial conditions problem, since the short-term evolution of the atmosphere depends mainly on its initial state [176]. In contrast, climate modelling is a boundary conditions problem, since on longer time scales, the average circulation depends on external forcings [176].

2.3 Coupled atmosphere-wildfire modelling

In this thesis we used a coupled wildfire-atmosphere numerical model to analyse the local coupling of fires and atmospheric conditions. This model (WRF-Fire) is based on a wildfire behaviour module integrated into a regional numerical weather prediction model [177, 178], the Weather Research and Forecasting model (WRF) [179]. The wildfire behaviour module is

USC UNIVERSIDADE DE SANTIAGO DE COMPOSTELA

based on the Rothermel's rate of spread equations, computed from the surface conditions given by the atmospheric model at each time step. Heat and water vapour fluxes from the fire are also integrated into the atmospheric model, resulting in a two-way coupling between the two modules.

2.3.1 Fire propagation

The fire propagation is resolved from one or more initial ignition points through the level-set method [96, 178]. A level set function $\psi = \psi(\mathbf{x},t)$ is defined for the whole domain, so that the burned region at time t corresponds to negative values ($\psi < 0$), the no-fire region corresponds to positive values ($\psi > 0$) and the fireline is at $\psi = 0$ [96]. An outside normal vector at the fireline is thus defined as:

$$\mathbf{n} = \frac{\nabla\psi}{\|\nabla\psi\|}. \tag{2.38}$$

By considering a point $\mathbf{x}$ that moves with the fireline, the rate of spread R can be defined as:

$$R = \mathbf{n} \cdot \frac{\partial \mathbf{x}}{\partial t}. \tag{2.39}$$

Considering that $\psi = 0$ in the fireline, we obtain:

$$\frac{d}{dt}\psi(\mathbf{x},t) = \frac{\partial\psi}{\partial t} + \frac{\partial\psi}{\partial x} + \frac{\partial\psi}{\partial y} = 0. \tag{2.40}$$

By substituting equations 2.38 and 2.39 in 2.40 we have:

$$\frac{\partial\psi}{\partial t} + \|\nabla\psi\|\left(\mathbf{n}\cdot\frac{\partial\mathbf{x}}{\partial t}\right) = \frac{\partial\psi}{\partial t} + R\|\nabla\psi\| = 0. \tag{2.41}$$

Therefore, the time evolution of the level set function is determined by the following partial differential equation (the level set equation [180]):

$$\frac{\partial\psi}{\partial t} + R\|\nabla\psi\| = 0. \tag{2.42}$$

The level set equation is resolved by a finite differences method in a discretized grid [96]. The rate of spread R is computed from equation 2.27 and the initial conditions are determined by the coordinates of one or more fire ignition points defined by the user.

2.3.2 Fire fluxes into the atmosphere

Once a grid point is ignited ($\psi = 0$) at time t_i, the fuel fraction decreases exponentially:

$$F(t) = \exp\left(-\frac{t - t_i}{T_f}\right), \tag{2.43}$$

where $F(t)$ is the no-burned fuel fraction at time t and T_f is the characteristic fuel burn time, a coefficient that is determined for each existing fuel model.

The average sensible heat flux density released by the fire between time t and $t + \Delta t$ in $\mathrm{W \cdot m^{-2}}$ is expressed as:

$$\phi_h = \frac{F(t) - F(t+\Delta t)}{\Delta t} \frac{w}{1+M_f} h, \tag{2.44}$$

where w is the total fuel load in $\mathrm{kg} \cdot \mathrm{m}^{-1}$, M_f is the fuel moisture content expressed as a fraction of the total fuel load and h is the fuel heat content of dry fuel with units $\mathrm{J} \cdot \mathrm{kg}^{-1}$ [96].

Similarly, the average latent heat flux density is computed as:

$$\phi_q = \frac{F(t) - F(t+\Delta t)}{\Delta t} \frac{w}{1+M_f} L\left(M_f + 0.56\right), \tag{2.45}$$

where L is the specific latent heat of condensation of water and the coefficient is the estimated mass portion of water (to the dry fuel mass) released during combustion (see equation 1.1) [96]. The sensible and latent heat fluxes are introduced into the potential temperature and water vapour concentration equations of the atmospheric model respectively, considering an exponential decay with altitude of the forcing terms [96].

2.3.3 Case study: October 2017 Hurricane Ophelia fires

Between the 14th and the 17th of October 2017, hurricane Ophelia (which reached category 3 in the Saffir–Simpson hurricane wind scale) moved from the south of the Azores archipelago to Ireland (Figure 2.3a). Ophelia approached the coast of the Iberian Peninsula on the 15th of October, advecting warm and dry air from the south (Figure 2.3bc), resulting in extremely favourable conditions for the spread of fires on the Iberian Peninsula. These extreme fire conditions were enhanced by the prolonged dry conditions during the year 2017 in Spain and Portugal [152].

We reproduced the spread of some of the October 2017 wildfires in Galcia with the WRF-Fire model. To do so, we undertook two previous tasks: (1) to obtain the burned area map of several fire events from Sentinel-2 high-resolution satellite images [182] (by computing the Normalized Burn Ratio [183] with spectral bands 8 and 12), and (2) to produce a fuel map from the Spanish Land Cover Information System (SIOSE) by comparing the descriptions of the existing vegetation type with the descriptions of the 13 Anderson fuel models [167] (Figure 2.4b).

We used 5 model nested domains, with resolutions ranging from 8100 m to 100 m (Figure 2.4). Initial and boundary conditions were obtained from ERA5 reanalysis [129]. The two higher resolution domains were run with explicit resolution of turbulence in Large-Eddy Simulation (LES) mode. The fire module runs at a refined grid with a resolution of 10 m, interpolating the atmospheric variables from the 100 m resolution domain.

In order to quantify the degree of similarity between the modelled and real fire spread, we define an accuracy index by using the burned grid points burned in the simulation (*Sim*) and the grid points contained in the burned area observed in the satellite (*Obs*). This index is defined as the percentage of burned grid points correctly modelled (the intersection between *Sim* and *Obs*, $Sim \cap Obs$) from the total burned grid points (the union of *Sim* and *Obs*, $Sim \cup Obs$):

$$Accuracy = \frac{Sim \cap Obs}{Sim \cup Obs} \cdot 100. \tag{2.46}$$

Similarly, we define a detection index as the percentage of burned grid points correctly modelled (the intersection between *Sim* and *Obs*, $Sim \cap Obs$) from the total observed burned grid points

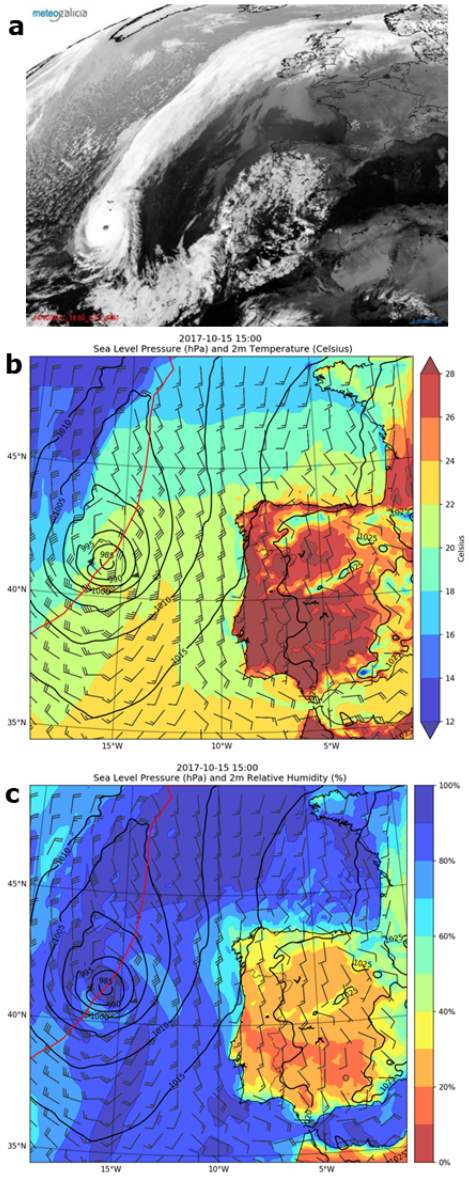


Figure 2.3: Hurricane Ophelia near the Iberian Peninsula. **a**, Infrared satellite image of the day 2017-10-14 at 1800Z from the Meteosat Second Generation (MSG) [181] satellites, obtained from the Galician meteorological service (MeteoGalicia) website. **b**, Mean sea level pressure, 10 m wind barbs and 2 m air temperature from ERA5 reanalysis data. **b**, 2 m air temperature on 2017-10-15 at 1500Z. **c**, 2 m relative humidity on 2017-10-15 at 1500Z. Panel **b** and **c** also show the mean sea level pressure (black lines), 10 m wind speed (wind barbs) and the trajectory of the hurricane center (red line). Data for panels **b** and **c** were obatained from the first domain of the WRF-Fire simulations.

(just *Obs*):

$$Detection = \frac{Sim \cap Obs}{Obs} \cdot 100. \tag{2.47}$$

Two wildfires from different Galician municipalities were simulated: As Neves wildfire

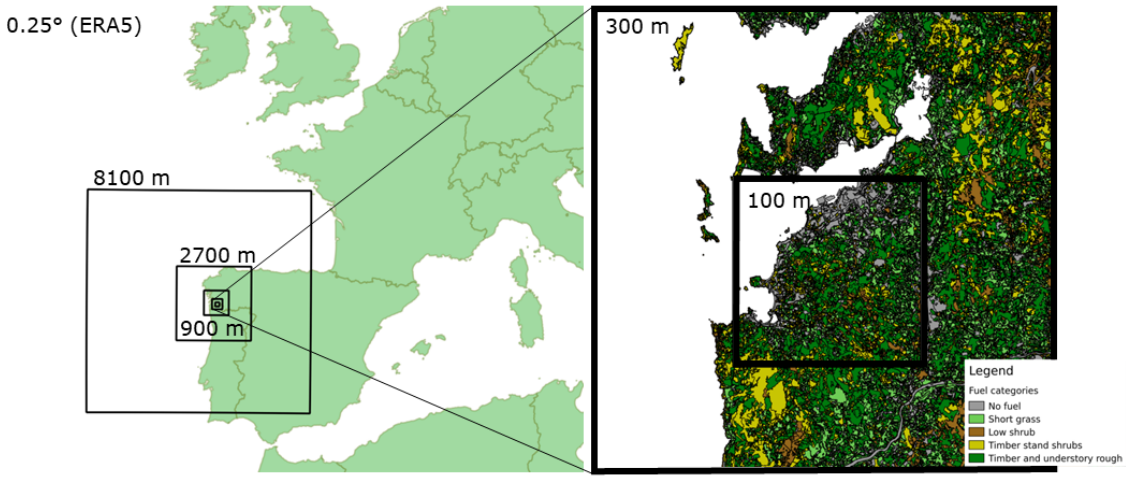


Figure 2.4: WRF-Fire model domain configurations used to reproduce 2017-10-15 wildfire in Nigrán, consisting of 5 models of resolutions 8100 m, 2700 m, 900 m, 300 m and 100 m.

Table 2.2: Accuracy and detection index for the teste fuel moisture contents in As Neves and Gondomar fires. Shaded cells indicate maximum accuracy and detection index values.

	As Neves		Gondomar	
Moisture	Accuracy	Detection	Accuracy	Detection
0 %	51.33 %	76.07 %	53.11 %	90.75 %
2 %	54.54 %	82.53 %	54.58 %	83.41 %
4 %	54.12 %	80.98 %	55.66 %	82.52 %
6 %	54.38 %	80.67 %	56.54 %	82.82 %
8 %	55.04 %	82.05 %	56.69 %	84.45 %
10 %	52.70 %	76.31 %	56.72 %	85.39 %
12 %	15.34 %	16.29 %	47.54 %	86.15 %
14 %	19.44 %	20.74 %	47.18 %	87.44 %

(2017-10-15, 2818.49 ha burned) and Gondomar wildfire (2017-10-15, 1384.92 ha burned). A sensitivity test was conducted in order to check how fuel moisture content affects fire spread and model performance. Eight constant values of dead fuel moisture content, ranging from 0% to 14%, were analysed. Live fuels were not considered for this test. The accuracy index (equation 2.46) and the detection index (equation 2.47) are shown in Table 2.2 for each fuel moisture content. While the detection index is generally higher for low fuel moistures (because the fire spreads more easily), the accuracy index is higher for a fuel moisture content of 8% in the As Neves wildfire and 10% in the Gondomar wildfire. By computing fuel moisture contents from ERA5 reanalysis data through equations 2.30 to 2.33, we obtain values ranging from 8.46% to 8.84% for As Neves wildfire location (the variation depends on the fuel model considered) and values from 10.81% to 11.14% for Gondomar wildfire event. As expected, fire simulation performance depends on fuel moisture determination.

As an example of the strong dependence of fire spread on fuel moisture, we show in Figure 2.5 the modelled burned area associated with different fuel moisture contents for the As Neves wildfire. The burned area at 00:00h in the 4% moisture content simulation ($fmc = 0.04$) is

approximately twice the burned area of the 10% moisture content simulation.

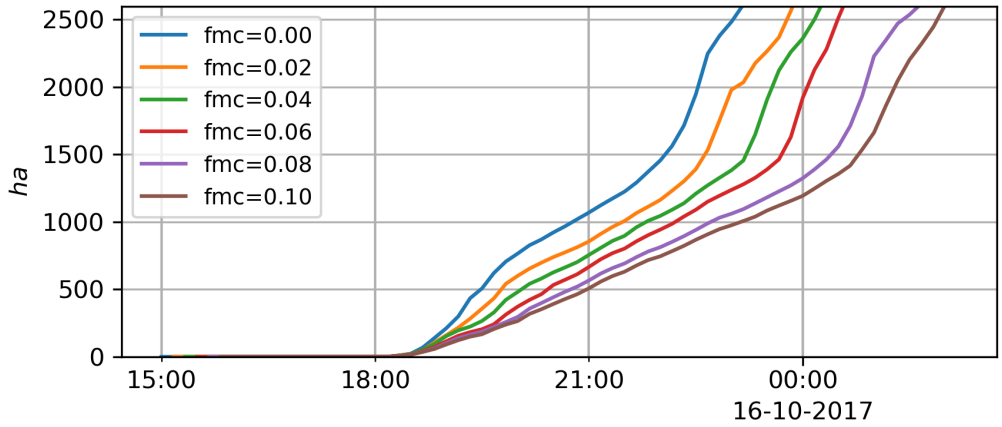


Figure 2.5: Bunrned area dependence on fuel moisture content. Time series of the modelled fire burned area increase for the As Neves wildfire. Each line represents each of the simulations with different fuel moisture contents (fmc) expressed as a fraction.

Figure 2.6 shows the comparison between the simulated and observed burned area for the most accurate simulation of each wildfire and at the instant of maximum accuracy. The percentage of well detected burned area by the model is 82.05% in the As Neves wildfire, and the accuracy index is 55.04%. For the Gondomar wildfire, the detection index is 85.39% and the accuracy is 56.72%. Part of the reduction in this accuracy index (relative to the detection index values) is due to the fact that some of the interior areas that did not burn inside the outer perimeter of the fires were burned in the simulation. During the first hours of simulation, the detection and accuracy values are very similar, indicating a good performance of the model. The lack of more detailed information on the actual evolution of the fires hampers a more in-depth analysis of the model's performance.

The As Neves fire simulation shows an explosive fire spread at 01:00h on 2017-10-16 (Figure 2.6). In Figure 2.7a we observe that the fire causes a significant increase in air temperature due to the sensible heat flux from combustion, inducing strong updrafts and downdrafts. The intensity of these vertical drafts is up to 8 $m \cdot s^{-1}$ at 200 m above the surface, as shown in Figure 2.7b and in the vertical cross section of Figure 2.7c. We ran a control simulation with exactly the same model configuration but without the spreading fire in order to analyse the influence of the fire on the wind. In Figure 2.7d we show the difference between the 20 m wind speed of the simulation with the fire and the 20 m wind speed of the simulation without the fire. A clear wind surface intensification is observed in the vicinity of the active fireline.

2.3.4 Case study: June 2017 Pedrógão Grande fire

On the 17th of October 2017 a devastating fire was started near the Portuguese village of Pedrógao Grande. This wildfire had a rapid spread, which was later attributed to the strong downdrafts caused by a pyrocumulonimbus (pyroCb) originated by the fire itself [152, 184, 185, 186]. We made a simulation of this wildfire with the WRF-Fire model [177, 178]

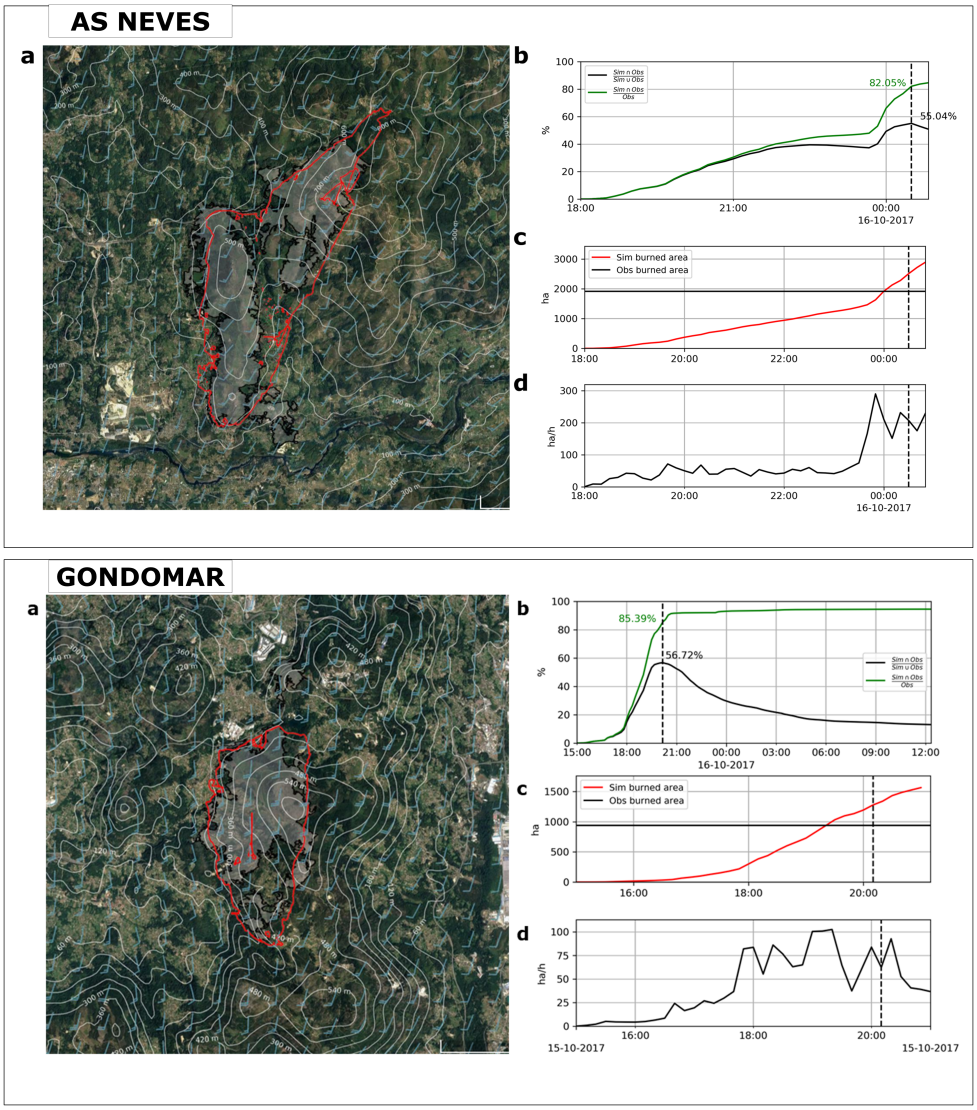


Figure 2.6: As Neves (top) and Gondomar (bottom) fire simulation. **a**, Simulated fire burned area (in red) at instant of maximum accuracy, observed final burned area (black contour filled in grey), terrain height in white contours and 10 m wind speed in wind barbs, represented over a Google Earth image. **b**, Simulation accuracy time series (equation 2.46) in black and simulation detection time series (equation 2.46) in green. **c**, Total simulated burned area time series in red and final observed burned area in black. **d**, Time series of fire burning rate, expressed in burned area per hour ($\mathrm{ha} \cdot \mathrm{h}^{-1}$). A vertical dashed line indicates the instant of maximum accuracy in the time series.

to test whether the model is able to reproduce the deep pyroconvection associated with this event. The fuel data and the burned area perimeter were obtained from the public Portuguese forestry service (Instituto da Conservação da Natureza e das Florestas, ICNF). Information about the time evolution of the fire perimeter is available in the technical report prepared by a multidisciplinary group of experts and requested by the Portuguese parliament [184], from

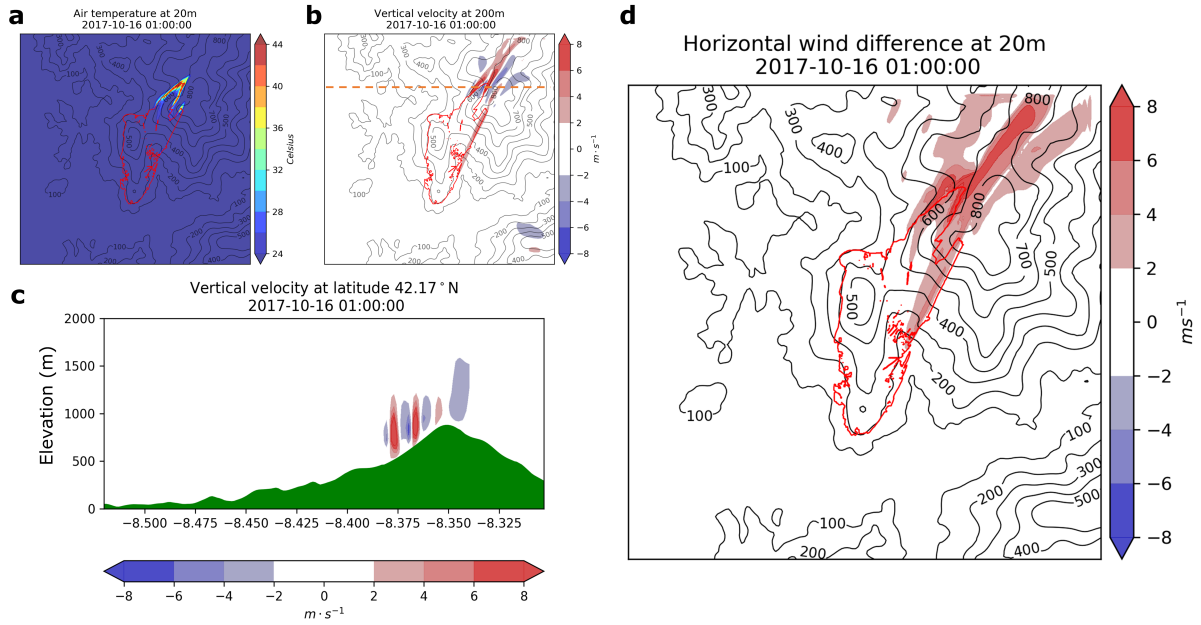


Figure 2.7: As Neves fire influence on atmospheric conditions. **a**, 20 m air temperature (in °C) on 2017-10-16 at 01:00h. **b**, 200 m vertical component of wind (in $\mathrm{m \cdot s^{-1}}$) on 2017-10-16 at 01:00h. **c**, Vertical cross section of the vertical component of wind (in $\mathrm{m \cdot s^{-1}}$) on 2017-10-16 at 01:00h. The location of the cross section is indicated in panel **b** with a horizontal orange dashed line. **d**, Horizontal wind speed anomaly at surface originated by the fire (in $\mathrm{m \cdot s^{-1}}$) on 2017-10-16 at 01:00h. The wind speed anomaly is computed by subtracting the wind intensity of the control simulation (a simulation without the fire) from the wind intensity of the fire simulation.

which we have created the scheme shown in Figure 2.8a.

The model is able to accurately reproduce the actual southward wind-driven fire spread during the first hours, from 14:00h (ignition) to 17:00h (Figure 2.8b). Around this time, a pyrocumulus is formed from the head of the fire with a vertical development tilted to the northwest (Figure 2.8b), following the wind direction between 4000 m and 8000 m (Figure 2.8c). This pyrocumulus causes strong vertical air currents that reach altitudes of up to 8000 m above the ground, as shown in the vertical cross section of Figure 2.8c. Surface winds are also altered, as revealed by the comparison between the fire simulation and the non-fire control simulation (Figure 2.8c).

According to the available information on the actual behaviour of the fire [184], from 17:00h onwards the fire started to rapidly spread to the west. This behaviour is probably associated with the influence of the fire-generated storm on the surface wind, as no significant change in wind direction is observed in the non-fire control simulation. However, the model fails at reproducing this windward rotation to the west in the fire simulation. Instead, it enhances the southward wind component, as shown in Figure 2.8d.

We proved that WRF-Fire model is able to simulate a deep pyroconvective fire event and reproduce the formation of a fire-generated cloud (pyrocumulus or pyrocumulonimbus). However, properly resolving the influence of such storms on the spread of the fire is a challenging task, due to the highly chaotic behaviour of these processes.

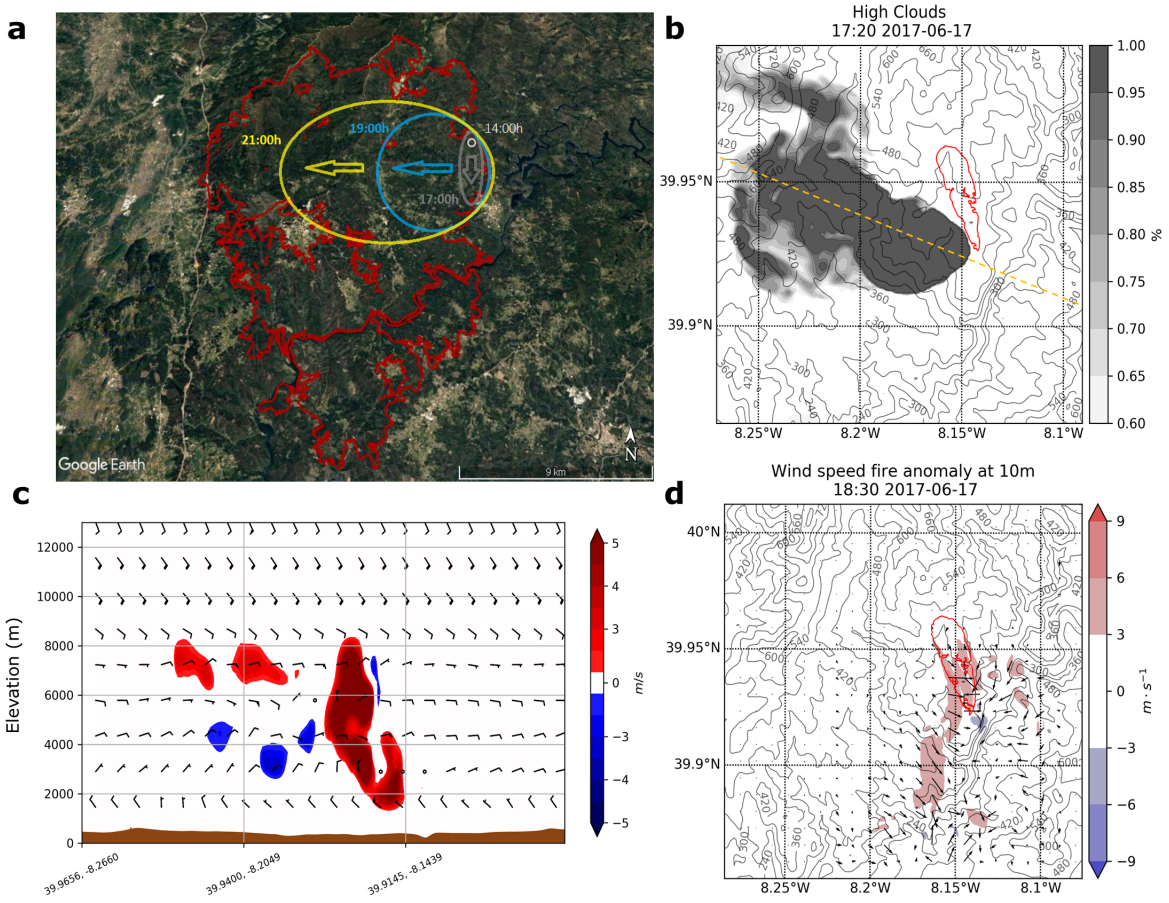


Figure 2.8: Pedrógão Grande fire simulation. **a**, Observed burned area perimeter of the fire in red and schematic representation of the actual fire spread from 14:00h to 17:00h (grey perimeter), 17:00h to 19:00h (blue perimeter) and 19:00h to 21:00h (yellow perimeter), according to ref. [184]. **b**, High cloud cover percentage in the fire simulation at 17:20h and modelled fire burned area in red. **c**, Vertical cross section of the vertical wind component in $m \cdot s^{-1}$ and horizontal wind barbs. The location of the cross section is indicated in panel **b** with a horizontal orange dashed line. **d**, Horizontal wind speed anomaly at surface originated by the fire (in $m \cdot s^{-1}$) at 18:30h. The wind speed anomaly is computed by subtracting the wind intensity of the control simulation (non-fire simulation) from the wind intensity of the fire simulation. Wind anomaly directions are indicated though horizontal arrows.

USC
UNIVERSIDADE DE SANTIAGO DE COMPOSTELA

USC
UNIVERSIDADE
DE SANTIAGO
DE COMPOSTELA

Chapter 3

Present global fire-prone regions and their expected alterations due to climate change

* The results from this chapter have already been published as Senande-Rivera, M.[1], Insua-Costa, D.[1] & Miguez-Macho, G.[1]. Spatial and temporal expansion of global wildland fire activity in response to climate change. *Nature Communications* **13**, 1208 (2022). https://doi.org/10.1038/s41467-022-28835-2.

[1] CRETUS, Non-linear Physics Group, Universidade de Santiago de Compostela, Galicia, Spain

3.1 Introduction

There is evidence of a greater influence of climate than of human activities on global biomass burning during the Holocene across multiple spatial and temporal scales [34]. Many studies have focused on quantifying the impact of different climatic and human factors controlling global fire activity [38, 26, 35]. The variability in global interannual fire response to climate variables has also been previously analysed [36, 37]. The general conclusion emerging from these investigations is that climate related, rather than human factors, are the major controls on global fire activity on a broad spatiotemporal scale, and in particular fuel availability (usually quantified by net primary production, NPP) and precipitation [35, 21]. However, on a smaller, regional scale, the drivers of wildfire activity are more varied, and human activity can be the major factor in some areas [187]. Given the strong relationship between fire and climate, climate change resulting from increased greenhouse gas emissions is expected to alter the spatial distribution of fire activity. Some studies point to increases in the severity of the fire season [142] and the wildfire potential [188], and a gradual shift to a global fire regime dominated by temperature [189], rather than precipitation or human factors, at the end of the 21st century. However, the magnitude and location of change is still debated for many parts of the world [42].

This study aims at (1) demonstrating that through simple climate indicators we can reproduce and explain the present global pattern of fire-prone regions and (2) subsequently use the trends in these indicators to infer future potential changes in the extent of fire activity. We focus on the climate-fire relationship, disregarding interannual variability, ignition elements and

human factors (when not related to climate, e.g. some agricultural practices). The underlying hypothesis is that, on broad spatial and decadal scales, there is a high probability of observed fire occurrence wherever a favourable climatic fire setting exists.

3.2 Methods

3.2.1 Burned area data

To study how climate influences fires at the global scale we use the Global Fire Emissions Database (GFED) [43]. The fourth generation of the GFED burned area data set (GFED4) provides global monthly burned area at the 0.25° spatial resolution from mid-1995 to 2016 [190]. This dataset is obtained from the Collection 5.1 MODIS direct broadcast (DB) burned area product (MCD64A1), now generated globally using the MODIS DB burned-area mapping algorithm [191].

The GFED4 dataset [190] contains information about the land cover distribution within the burned area. Supplementary Figure S3.1b shows the percentage of the mean annual burned area (BA) associated to croplands (one of the land cover categories of the GFED4 data). Fires on agricultural land can correspond to human-controlled agricultural practices, with minimal relationship to weather or climate conditions.

Supplementary Figure S3.2a shows the mean annual burned area. There are regions (e.g. boreal regions) with a high difference between mean and maximum annual burned area for the period (Figure 3.1a), implying that there is large variability, with years when fire activity is particularly high among many other years with low burned area. Conversely, the more similar mean and maximum values in the tropical regions suggest that there the annual burned area is regularly high for most of the years. Similar conclusions can be inferred from Supplementary Figure S3.2b for the number of years per decade with an annual burned area higher than 100ha. The frequency of fires is much higher in the Tropics than anywhere else.

3.2.2 Climate data

Climate datasets are acquired from WFDE5 [192], WATCH Forcing Data methodology applied to ERA5 [129], the fifth generation ECMWF reanalysis for the global climate. This is a meteorological forcing dataset for land surface and hydrological models. The dataset was derived applying sequential elevation and monthly bias correction methods [193] to 0.5° aggregated ERA5 reanalysis products [194]. The monthly observational datasets used for bias correction are the Climate Research Unit gridded station observations CRU TS4.03 [195] and the Global Precipitation Climatology Centre gridded station precipitation observations GPCCv2018 [196] for rainfall and snowfall rates. From this climate dataset we calculated the annual and monthly temperature and total precipitation (rainfall and snowfall) climatology for the same 1996-2016 period. We downscale these variables to a 0.25 ° grid using a bilinear interpolation.

3.2.3 GCM data

USC DE SANTIAGO

For analysing future variations in fire activity, we use the Coupled Model Intercomparison Project Phase 5 CMIP5 [197] historical and future projections from 22 climate models. The

GCMs are ACCESS1-0, ACCESS1-3, bcc-csm1-1, bcc-csm1-1-m, BNU-ESM, CMCC-CMS, CNRM-CM5, GFDL-CM3, GFDL-ESM2G, GFDL-ESM2M, GISS-E2-H, GISS-E2-H-CC, GISS-E2-R, GISS-E2-R-CC, HadGEM2-CC, inmcm4, IPSL-CM5A-LR, IPSL-CM5A-MR, IPSL-CM5B-LR, MPI-ESM-LR, MPI-ESM-MR and NorESM1-M. We use the RCP8.5 [198] greenhouse gas concentration model outputs for the future period. The Representative Concentration Pathway RCP8.5 assumes a scenario in which greenhouse gas emissions continue to increase throughout the 21st century, which leads to a radiative forcing of 8.5 $W \cdot m-2$ by 2100 [199]. For each model, we only consider the main ensemble member (r1i1p1). We analyse two periods, present (1996-2016) and future (2070-2099). The present period is obtained by concatenating precipitation and temperature historical data (1996-2006) and projected data until 2016 (2006-2016). Future climatology values are obtained with the anomaly method [200] for each one of the 22 CMIP5 global models, we calculate temperature anomalies and precipitation ratios between 1996–2016 and 2070–2099 and interpolate them from their native model resolution to 0.25° using bilinear interpolation. Finally, future values of the variables of interest were derived from present values by adding the temperature anomalies to present temperatures and by multiplying the present precipitation by the precipitation ratios.

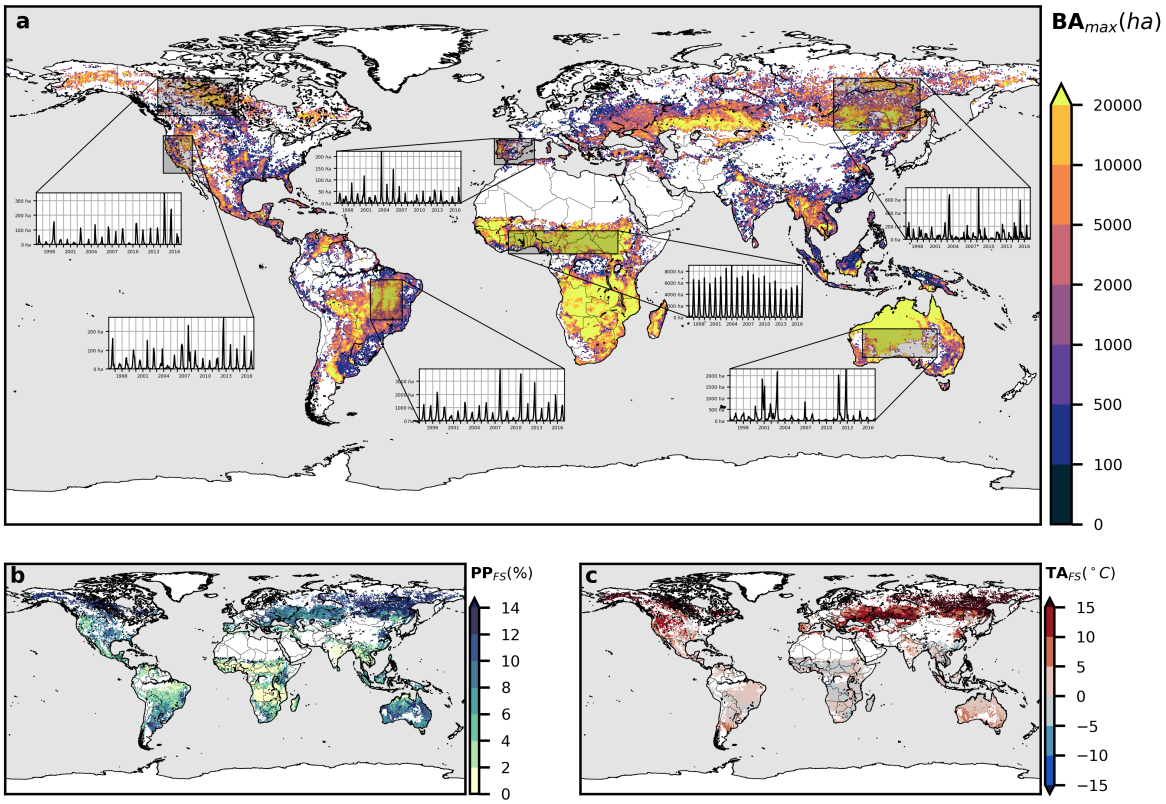


Figure 3.1: Burned area observations and climate drivers. **a**, 1996-2016 maximum annual burned area (*BAmax*) and monthly burned area time series for selected regions. **b** Average monthly precipitation percentage from the annual total for the fire season (PP_{FS}). **c** Average monthly temperature anomaly from the annual mean for the fire season (TA_{FS}).

USC UNIVERSIDADE DE SANTIAGO DE COMPOSTELA

3.2.4 Threshold selection

We examine the statistical distribution of different climatic variables at fire-impacted and fireless pixels within the Köppen-Geiger main categories, to find the conditions that are suitable for fire activity. The objective is to obtain sets of climatic thresholds that univocally identify the different classes of burned areas in actual fire occurrence data, both in extent and duration of the FS. Precisely, for each grid cell we obtain the mean value of each annual variable (Pa, Ta, Pmin and Tmax) for the years with an annual burned area (BA) greater or equal than 100 ha (we will refer to all these data values as fire "points"), and the mean value for the years with BA$<$100 ha (which we will refer to as non-fire "points"). Once the data values are separated into fire and non-fire groups, we compare for each main Köppen-Geiger category (Supplementary Figure S3.3) the statistical density function for BA$\geq$100 ha values against BA$<$100 ha values.

We sort out global grid points with burned area data into 5 different groups according to their main Köppen-Geiger climate class [201]: tropical (A), arid (B), temperate (C), cold (D) and polar (E). We follow the classification criteria used by Beck *et al.* [202] and Peel *et al.* [203], but with a new threshold between temperate (C) and cold (D) climates. Since the definition of the Köppen-Geiger climate classification several authors proposed changes, and most of these proposals were aimed at improving the C-D boundary [204], such as redefining the coolest-month isotherm at 0°C [202, 203, 205] or -3°C [206]. We modified the C-D boundary to associate the cold climate (D) to the boreal forest (taiga), so we set the threshold between temperate and cold climates at 2°C of mean annual temperature (MAT). This threshold is consistent with Whittaker [207] and Woodward *et al.* [208], who determine the temperate-boreal forest transition to occur below 5°C of mean annual temperature. Supplementary Figure S3.3 shows the Köppen-Geiger world classification with this modification, computed from WFDE5 climate data [194].

We next identify the fire season (FS), defined as the minimum number of months that contain more than 80% of the annual burned area. A similar definition, considering only consecutive months, is widely used [36, 29, 209]. We allow non-consecutive months in our definition to accurately identify bi-modal fire seasons. To calculate the fire season length (FSL), we employ monthly means of burned area computed over years with total BA$\geq$100 ha. We start from the month with highest value and progress to lower BA months until 80% or more of the total area is covered. Supplementary Figure S3.1a shows the FSL obtained from GFED4 burned area data.

For the monthly variables (Pm and Tm) we make two different comparisons. We first contrast their average magnitude during each FS month for years with BA$\geq$100 ha (fire "points") against average values in months out of the FS for all years (non-fire "points"). At grid cells with no fire incidence (BA$<$100 ha in all years), there is no FS, and means for each and every month, computed over all years, are added to the non-fire "points". With this analysis we assess the seasonal variability of the monthly variables, determining the values that characterize the FS. We then make a second comparison using the monthly variables aiming at analysing the interannual variability of the fire season. Here, we compare average Pm and Tm values for the FS months of the years with BA$\geq$100 ha (fire "points"), against averages for FS months in years with BA$<$100 ha (non-fire "points"). By doing so, we check whether the FS months present precipitation or temperature differences between years with fire activity and years with no fire activity. These interannual differences are only detectable if variability is an intrinsic characteristic of the climate. Supplementary Figure S3.4 shows a scheme of the three comparisons of statistical distributions: the annual variables, the seasonal analysis and the

interannual variability analysis.

We note that we exclude from the statistical distributions data from fire-prone regions with a percentage of mean annual burned area corresponding to cropland land cover of more than 90% (Supplementary Figure S3.1b), due to the likely relation of fires with agricultural practices in these grid cells [210, 211].

The thresholds are selected automatically for each distribution at the value that maximizes the area enclosed between the density function of the fire points and the density function of the non-fire points (coloured minus grey areas in Supplementary Figures S3.5, S3.6, S3.7, S3.8, S3.9, S3.10, S3.11 and S3.12). The only prior consideration is that the thresholds work as an upper limit for Pmin and Pm variables (looking for seasonal dry conditions), and as a lower limit for the other variables (looking for warm conditions and fuel availability). Distributions with a big area difference evidence that the considered variable is a good indicator of fire incidence, since the values associated with fire activity are clearly distinct from the values that are not. In an ideal scenario where the data points associated with fire activity, or fire points, were perfectly separated from the remaining points, this area would be equal to 1. In most cases, however, it is the simultaneous meeting of the conditions for two variables that determines fire risk; thus, there can be a sizeable amount of non-fire data points satisfying either of them. The objective is then that fire points, and especially those representing locations and months with more burned area, fulfil all the conditions simultaneously in the highest percentage possible, while non-fire points that do so are a minority.

Once we have a threshold for each distribution, we select the variables and thresholds for the classification according to the area difference and classified fire-point percentage criteria. The final threshold is chosen as a rounded value inside the obtained uncertainty range.

Table 3.1 and 3.2 show all defining criteria for the four classes, including the Köppen-Geiger-based general classification of climates zones and the specific fire classification thresholds. One grid cell is classified as fire-prone if at least one month in the time series meets all the conditions. For each cell, we define fire-prone year (FPY) as a year with at least one month meeting all the conditions in Table 3.1. The months that meet the thresholds during a particular FPY conform the potential fire season (PFS). The categories of Table 3.1 are sub-divided into: recurrent (r), occasional (o) and infrequent (i) depending on the number of FPY per decade: recurrent (FPY$>$7 years/decade), occasional (3$<$FPY$<$7 years/decade) and infrequent (0$<$FPY$<$3 years/decade). More information about the threshold selection method for each general climate is provided below.

Tropical dry season fire category

Fire activity in the Tropics is confined to relatively dry months, in which the mean monthly precipitation (Pm) is less than 90 mm (Supplementary Figure S3.6a). This variable is the one presenting more differences between the fire-prone and the non-fire probability density functions (area difference of 0.55, see Supplementary Figure S3.6a). As many as 83.7% of the points with high fire activity, but only 28.4% of the non-fire points, are to the left of the threshold, accounting for 96.8% of the tropical burned area. The statistical distribution of Pmin (Supplementary Figure S3.5c), with an area difference of 0.30, indicates that under tropical climates fire activity occurs in places where at least one month is extremely dry ($<$6 mm). This implies that places where the dry season consists of months with mean monthly precipitations ranging between 6 mm and 90 mm, will not be classified as fire-prone. A stronger precipitation

USC DE COMPOSTELA

Table 3.1: Fire classification defining criteria. Fire-climate classes (Tr-ds, Ar-fl, Te-dhs and Bo-hs) must meet general Köppen-Geiger climate criteria (Tr, Ar, Te and Bo, in bold) and the specific fire-climate thresholds. Fire-climate classes are subdivided into three sub-classes according to the number of years classified per decade: r-reccurrent (FPY>7 years/decade), o-occasional (7>FPY>3 years/decade) and i-infrequent (3>FPY>0 years/decade). All variables are defined in Table 3.2.

Tr	$MAP \geq 10 \cdot P_{threshold} \& Tcold \geq 18°C$
Tr - ds	$Pa \geq 220mm \& Pmin \leq 6mm \& Pm \leq 90mm$
Ar	$MAP < 10 \cdot P_{threshold}$
Ar - fl	$Pa \geq 220mm \& Tm \geq 19.5°C \& Pm \leq 60mm$ if $MAT < 18.5°C$, all months analysed if $18.5°C \leq MAT < 27.5°C$, months with $7 \leq dm_{Pmax} \leq 10$ analysed if $MAT \geq 27.5°C$, months with $2 \leq dm_{Pmax} \leq 4$ analysed
Te	$MAP \geq 10 \cdot P_{threshold} \& Tcold < 18°C \& MAT \geq 2°C$
Te - dhs	$Pa \geq 220mm \& Pmin \leq 13mm \& Tm \geq 12°C \& Pm \leq 42mm$
Bo	$MAP \geq 10 \cdot P_{threshold} \& MAT \leq 2°C$
Bo - hs	$Pa \geq 220mm \& Tmax > 15°C \& Tm \geq 7°C \& Pm \leq 67mm$

seasonality is needed, where at least one month has a mean precipitation under 6 mm. If this Pmin threshold is satisfied, the number of months with Pm<90 mm is defined as the potential fire season (PFS) under tropical climates.

The Pa statistical distribution (Supplementary Figure S3.5a) shows that fire-prone areas have relatively lower annual precipitations than the non-fire-prone regions; however, since this is likely due to the aforementioned rainfall seasonality, we find that we do not need to use an upper Pa limit to characterize the fire-prone regions in the Tropics. Neither we need to employ temperature variables in the fire-climate classification, as they do not show any distinct behaviour in the fire season (Supplementary Figure S3.5b,d and S3.6b,d). The strong link between fires in the Tropics and rainfall seasonality has been widely studied [212, 213, 214]. The location of the Inter-Tropical Convergence Zone (ITCZ) generally determines precipitation patterns in the Tropics, and consequently fire activity [214].

Arid fuel limited fire category

An arid fuel limited fire category (Ar-fl) is initially defined through a Pa (Supplementary Figure S3.7a) and a Tm threshold (Supplementary Figure S3.8b), with area differences of 0.44 and 0.23 respectively. Fires are observed in regions with an annual precipitation that is sufficient to enable the existence of a certain amount of vegetation, so fire in dry climates is more limited by fuel amount than by fuel moisture [215, 28]. The Pa arid threshold is applied to all other categories to analyse a possible future desertification due to climate change. High monthly temperatures are also related to fire activity. Supplementary Figure S3.8b shows that most of the fire season months in arid climates have temperatures above $19.5°C$. Despite monthly precipitation distributions not showing significant differences between fire-prone and

USC DE COMPOSTELA

Table 3.2: Variable definitions

Variable	Units	Definition	Temporal dimension
MAT	$^{\circ}C$	Mean annual 2m air temperature	-
Ta	$^{\circ}C$	Annual 2m mean air temperature	Years
$Tcold$	$^{\circ}C$	Mean 2m air temperature of the coldest month	-
$Tmax$	$^{\circ}C$	Maximum monthly 2m mean air temperature of the year	Years
Tm	$^{\circ}C$	Monthly 2m mean air temperature	Months
MAP	mm	Mean annual precipitation	-
Pa	mm	Annual precipitation	Years
$Pmin$	mm	Minimum monthly precipitation of the year	Years
Pm	mm	Monthly precipitation	Months
$P_{threshold}$	mm	$2 \times MAT$, if $P_{winter} > 70\%$ $2 \times MAT + 28$, if $P_{winter} < 30\%$ $2 \times MAT + 14$, otherwise	-
P_{winter}	%	Percentage of MAP that falls during the colder six-month period between April-September and October-March	-
dm_{Pmax}	-	Month distance to the wettest month of the year, ranging from 0 to 11	Months

non-fire-prone data, we also include a Pm threshold of 60 mm (corresponding to the 90th percentile of the fire points distribution) in order to detect a possible fire season shortening due to a future precipitation increase. Above this monthly precipitation value, the number of months belonging to a fire season anywhere with arid climate is almost negligible.

However, these three thresholds (Pa, Tm and Pm) are not enough to characterize the fire season in certain regions. We checked the monthly values of burned area, precipitation and temperature in different fire-prone arid regions (Supplementary Figures S3.13, S3.14, S3.15 and S3.16) and found that the fire season is associated with a hot season in midlatitude arid areas where no clear wet period is observed, e.g. Kazakhstan and North America (Supplementary Figures S3.13 and S3.14), but closer to the tropics where it is warm year-round, it can be also determined by the existence of a pronounced annual wet and dry season cycle, with fires occurring sometime during the dry season, in places just at the beginning (e.g. Sahel region, Supplementary Figure S3.15) while in others, more toward the end of it (e.g. Botswana and Australia, Supplementary Figure S3.15 and S3.16).

Supplementary Figure S3.17 shows the distance in months between the month of maximum burned area and the wettest month (Supplementary Figure S3.17a), and between the month of maximum burned area and the hottest month (Supplementary Figure S3.17b). The values of the latter variables indicate that the maximum burned area in the cool arid regions (e.g. Kazakhstan and North America) is reached during the hottest months, so that the Tm threshold can be sufficient to define the fire season. However, in warmer regions with more tropical monsoonal climatic features, additional variables must be considered. Supplementary Figure S3.18a compares the mean annual temperature (MAT) probability density function of areas

where the month of maximum burned area precede the wettest month, i.e., it is at the end of the dry season (yellow distribution) vs. areas where the month of maximum burned area follows the wettest month, i.e., it is at the beginning of the dry season (orange distribution). According to this, we define three different arid fire-prone regions:

- $MAT < 18.5°C$. Due to the practical absence of precipitation seasonality (Supplementary Figures S3.13 and S3.14), the fire season coincides with the hot season (Supplementary Figure S3.18b).
- $18.5°C \leq MAT < 27.5°C$. The fire season occurs at the end of the dry months, just before the wet season, when the fuel moisture reaches the lowest values (Supplementary Figure S3.18c). For this MAT interval we will constrain the fire season to the five months at the end of the dry season.
- $MAT \geq 27.5°C$. The high temperatures rapidly dry the fuel, so the fire season occurs at the beginning of the dry season, right after the wet season (Supplementary Figure S3.18d). Two more factors enhance the rapid fuel drying in the Sahel region, the low soil water retention [210] and the grass-dominated vegetation [216] in contrast with other arid regions covered mostly by shrubs or hummock grasses, as in Australia. The herbaceous vegetation desiccates early in the dry season [217], favouring fires, while the severe drought suppresses grass production at the end of the dry season, limiting fires [217]. In addition, fires in the early dry season are used as preventive burning strategies in order to hinder later destructive fires in Mali [218] and Senegal [219]. Therefore, for these MAT values we will constrain the fire season to the three months at the beginning of the dry season.

Temperate dry and hot season fire category

The Temperate dry and hot season fire category (Te-dhs) is defined by setting a Pm and a Pmin threshold, indicating a precipitation seasonality dependence as in the Tropics. The fire season months are relatively dry; most of the Pm values are concentrated below a 42 mm threshold (Supplementary Figure S3.10a), with a pronounced peak close to 0 mm, meaning a totally dry month. The Tm seasonal distribution (Supplementary Figure S3.10b) shows also significant differences between fire season months and non-fire-prone months, indicating that cooler monthly temperature values below 12°C tend to hamper fire activity. Therefore, the fire season in temperate climates occurs during dry and hot conditions. As we see in Supplementary Figures S3.9 and S3.10, Pm, Tm and Pmin are the three variables that show the highest area differences (0.34 and 0.33 and 0.29, respectively), with the fire points classified representing more than the 88% of the burned area data.

Unlike in ever warm tropical climates, where fire risk is largely determined by the lack of precipitation in the dry season, in midlatitude temperate climates with temperature seasonality, fires occur when dry conditions coincide with the warm season [220, 221, 222, 223, 224, 40], as cold temperatures diminish fire risk. Thus, the use of simultaneous monthly precipitation and temperature thresholds are needed. The annual Ta and Pa statistical distributions (Supplementary Figure S3.9a,b) do not show any important distinction in temperate fire-prone regions. With regard to interannual variability, the years of high burned area show slightly drier fire seasons (Supplementary Figure S3.10c), but the differences at this broad spatial scale of analysis are so small that we choose not to modify the Pm threshold.

Boreal hot season fire category

The Boreal hot season fire category (Bo-hs) is mainly defined through a Tmax and a Tm threshold, given that the fire season is characterized by the warmest conditions along the year. Supplementary Figure S3.12b clearly shows how most fire season months have monthly temperatures above 7°C. In a similar way as we did for the precipitation thresholds in Tropical climates, we combine this monthly threshold with a maximum monthly temperature threshold of 15°C (Supplementary Figure S3.11d). This indicates that boreal regions with a warm season with more moderate monthly temperatures ranging between 7°C and 15°C are not classified as fire prone.

It is typical of boreal climates to present higher precipitation in warm months, as the very cold air masses in winter contain little moisture and precipitation amounts are commonly small, especially in regions away from the coast. This is the reason why the monthly precipitation seasonal statistical distribution (Supplementary Figure S3.11a) does not show a drier fire season than the rest of the year under Boreal climates. However, Supplementary Figure S3.11c clearly indicates that the fire season in the particular years with burned area is noticeable drier than in years with no fires, which means that boreal fires, in addition to the need of warm conditions to occur, easily achieved almost every year, are enhanced when the warm season coincides with a dry period. This explains why boreal fires have the lowest annual frequency among all main fire classes (Figure 3.2b), and suggests the need of an additional threshold for monthly precipitation to better characterize the climate setting in which they develop. Because the obtained threshold from the distributions of Supplementary Figure S3.11c is too restrictive (with only 49.7% of the fire points meeting the condition) we use the 75th percentile of the fire point distribution, corresponding to 67 mm, which still includes a sizeable amount of non-fire points, but discards many, nevertheless.

Due to the practical absence of polar (E) fires, as cold temperatures are registered year around and vegetation consists of tundra, we excluded this general climate class from our analysis.

3.3 Results and discussion

3.3.1 Present fire-climate classification

To identify the different regions of the planet with suitable climatic conditions for fire activity, we compare the global distribution of climate indicators based on temperature and precipitation, with satellite-derived GFED4 burned area data [190] (Figure 3.1). Starting from four general climates (Tr-tropical, Ar-arid, Te-temperate and Bo-boreal) based on the Köppen-Geiger climate classification main categories [201], we create four fire-prone classes using climate thresholds to define the patterns observed in Figure 3.1. Each category is characterized by the element that boosts fire activity during the fire season (FS): low precipitation, high temperatures or a combination of both. The classification is made by contrasting the probability distribution of the climatic variables at data points associated with high fire activity vs. points with low fire activity within the main Köppen-Geiger categories.

The environmental conditions associated with fire occurrence emerge more clearly in this comparison, yielding the different threshold sets in Table 3.1 that determine the fire-prone months at any location. We define those years with at least one month meeting the thresholds, as

fire-prone years. Depending on the number of fire-prone years at each location, the categories of Table 3.1 are sub-divided into: recurrent (r), occasional (o) and infrequent (i). The average number of fire-prone months during the fire-prone years is defined as the potential fire season length (PFSL), i.e. the season with climatic characteristics prone to fire activity.

Figure 3.2a depicts the global map of burned area classified according to the selected thresholds (Table 3.1). Savanna fires are responsible for the largest proportion of burned area at the global scale [190]. The FS in these areas is longer than in other climates (Supplementary Figure S3.1) and, despite savanna fires being also dependent on ignition patterns and human policies and practices, the FS is tied to a pronounced seasonal cycle of precipitation [212, 213, 214], with fire occurring mainly during the dry part of the cycle. Because of this, the Tropical - dry season fire class (Tr-ds) coincides with the distribution of the tropical savanna climate.

Fires in the Tropics occur with a very high annual frequency (Supplementary Figure S3.2b). Lying close the equator, South-eastern maritime Asia (Indonesia, Malaysia and Papua New Guinea) is a region that is regularly not fire-prone, except when fire activity is favoured by the appearance of marked dry seasons associated with El Niño events, as suggested by the coincidence of low precipitation periods and high fire activity during the El Niño episodes of 1997/1998, 2002/2003, 2009/2010 and 2015/2016 [190, 225, 226] (Supplementary Figure S3.19). Figure 3.2b shows this region classified as Tr-ds-i, indicating that climate conditions are prone to fire activity with a frequency of 1 to 3 years per decade (a frequency interval consistent with El Niño episodes).

In Figure 3.2, boreal fires are represented as hot season fires (Bo-hs) due to the large positive temperature anomaly existing in those locations during the FS (Figure 3.1c). In fact, temperature variations explain much of the variability in boreal burned area [144, 227].

Temperate fires are classified as dry and hot season (Te-dhs) because they affect regions where the dry season coincides with the warm season (Figure 3.1b,c). Here, high temperatures and precipitation seasonality determine fire activity and inter-annual burned area variability, e.g. in Western North America [220, 221, 222, 223] and Southern Europe [224, 40].

Fire activity in arid regions occurs during warm months, but the relation with precipitation is more complex. The fire season is associated with a hot season in cooler ($MAT < 18.5°C$) midlatitude arid areas where no clear wet period is observed, e.g. the Western US and Central Asia (Supplementary Figures S3.13 and S3.14), but closer to the tropics where it is warm year-round, it can be also determined by the existence of a marked annual wet and dry season cycle, with fires occurring sometime during the dry season. In the warmest arid regions ($MAT > 27.5°C$), the fire season starts right at the beginning of the dry season (e.g. the Sahel, Supplementary Figure S3.15) while where MATs are more moderate, between $18.5°C$ and $27.5°C$, it takes longer to develop (e.g. Central Australia and the Kalahari desert, Supplementary Figures S3.15 and S3.16). Due to the dependency between fires and the existence of fuel in arid climates, we named this class as Arid fuel limited (Ar-fl).

In Figure 3.2b we classify every spatial point and not only those with burned area observations as in Figure 3.2a. The four groups in Fig 2a show observed fire locations that share some specific climate conditions, and the classification in Figure 3.2b shows the world areas were these conditions occur for at least one month. The correspondence between these two maps is quantified in Supplementary Figure S3.20b, with more than 70% of the land area well classified as either fire prone ($BA > 0ha$) or fireless ($BA = 0ha$). This reveals a two-way relation between fires and climate: fires take place under specific climatic conditions, and most places

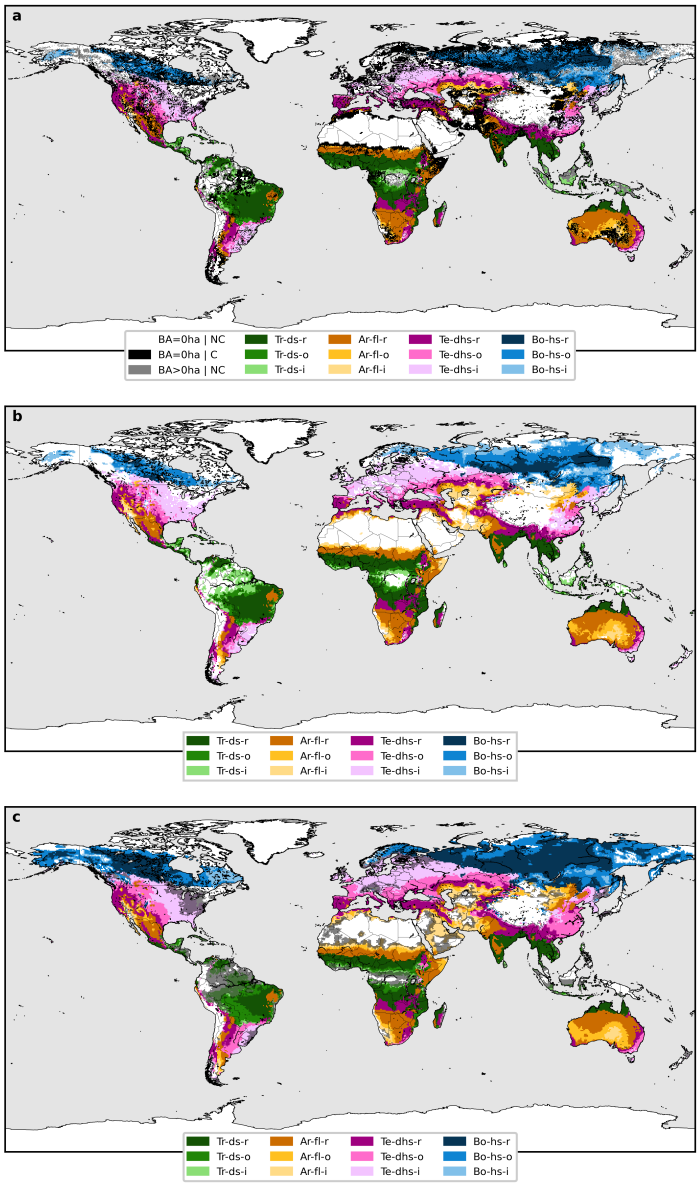


Figure 3.2: Fire-prone region classification. **a**, With observed burned area data as a reference: Not classified (NC, white) and misclassified (C, black) areas with $BAmax = 0ha$, unclassified (NC, grey) and classified (Tr-ds, Ar-fl, Te-dhs and Bo-hs) areas with $BAmax > 0ha$. Each class is subdivided into 3 subcategories depending on the recurrence of the fire-prone conditions: recurrent (r), occasional (o) and infrequent (i). **a**, Present (1996-2016) fire-prone climatic regions. **c**, Future (2070-2099) fire-prone climatic regions with shaded grey representing a ¡75% confidence percentage, estimated as the percentage of CMIP5 Global Circulation Models (GCMs) agreeing on the result.

with these climatic conditions are indeed fire prone, which supports our earlier hypothesis. Fire activity is controlled by weather, resources to burn and ignitions, as represented through the fire regime triangle [26, 42]. On broad temporal scales and large spatial scales, temperature and precipitation have an important impact on fire because these climate variables influence vegetation type and the abundance, composition, moisture content, and structure of fuels [161].

USC DE SANTIAGO

Although ignitions may be driving fires to a greater extent than temperature or precipitation at specific locations or events [70], they do not seem to limit fire activity at coarse spatial and temporal resolutions, implying that, where fuels are sufficient and atmospheric conditions are conducive to combustion, the potential for ignition exists, either by lightning or human causes [21, 42]. For all these reasons, we can identify specific climates that are prone to fires.

The areas classified as fire-prone in Figure 3.2b comprise 99.26% of the observed global mean annual burned area in Supplementary Figure S3.2. This percentage is above 85% for all four general climates (Supplementary Figure S3.20). The percentage of land area with non-zero burned area data classified as fire-prone is 91.22%. Considering for each location only the obtained fire-prone years (FPY), the percentage of the observed burned area classified is 90.36%. Furthermore, the PFS obtained in the fire-climate classification (Figure 3.3b) also correlates well with the timing of observed fire incidence, as globally 87.91% of the observed mean burned area occurs during the identified months of PFS at classified fire-prone locations.

We note that some fire-impacted areas have not been classified (in grey in Figure 3.2a). These areas represent the 8.78% of the total fire-impacted global land area (points with $BAmax > 0ha$), as shown in Supplementary Figure S3.20a. Notwithstanding, they correspond for the most part to areas with relatively low fire incidence, as combined they only account for less than 1% of the global mean annual burned area (Supplementary Figure S3.20a). The climate with the lowest amount of burned area observed at classified grid cells is the Boreal climate (89.08%, Supplementary Figure S3.20a). In addition, as the classification is conceived from a climatic point of view, locations with fire activity associated with specific meteorological conditions that are not appreciable at the monthly temporal resolution, are probably not well identified. For example, a week of extremely high temperatures could be almost unnoticeable in the monthly mean temperature, but not in fire activity. Similarly, months with the same total precipitation may have different fire activity if the precipitation falls concentrated in a few days or is distributed throughout the month. Furthermore, the short temporal sampling period of the burned area data could also be influencing our results. Locations with long fire cycles may not be well represented in the data.

On the contrary, some regions with $BAmax = 0ha$ are classified as fire-prone, represented as black points in Figure 3.2a of the main text and Supplementary Figure S3.20b. Even though the percentage of these black points could seem very large (Supplementary Figure S3.20b), this is mostly due to the discontinuous nature of the observed burned area data (Figure 3.1). In addition, a large percentage of these missclassified regions with observed $BAmax = 0ha$ (49.03%) are classified as infrequently fire-prone (Tr-ds-i, Ar-fl-i, Te-ds-i and Bo-hs-i). Few broad regions are represented in black in Figure 3.2a of the main text. Most of them correspond to boundaries between arid fire-prone areas (Ar-fl) and deserts (e.g. Afghanistan, Ethiopia, Niger or Australia), which are difficult to define based solely on annual precipitation. In the Scandinavian Peninsula the burned area data do not reflect high fire activity. However, our classification identifies a fire-prone region from Northwest Russia towards the North of Sweden. The mismatch between our results and the burned area data in this case could be due to the effective fire suppression system in Nordic countries like Finland [228]. In terms of the global land area, 71.91% of area is well classified (classified $BA > 0ha$ points and non-classified $BA = 0ha$ points, Supplementary Figure S3.20b).

Although there may be coincidences between our climate classification and fire regimes, e.g. infrequent fires in Boreal regions (Bo-hs) or frequent fires in the Tropics (Tr-ds) [29], our classification is not related to fire regimes because these are strongly dependent on other factors

such as vegetation traits [229] or human action [230].

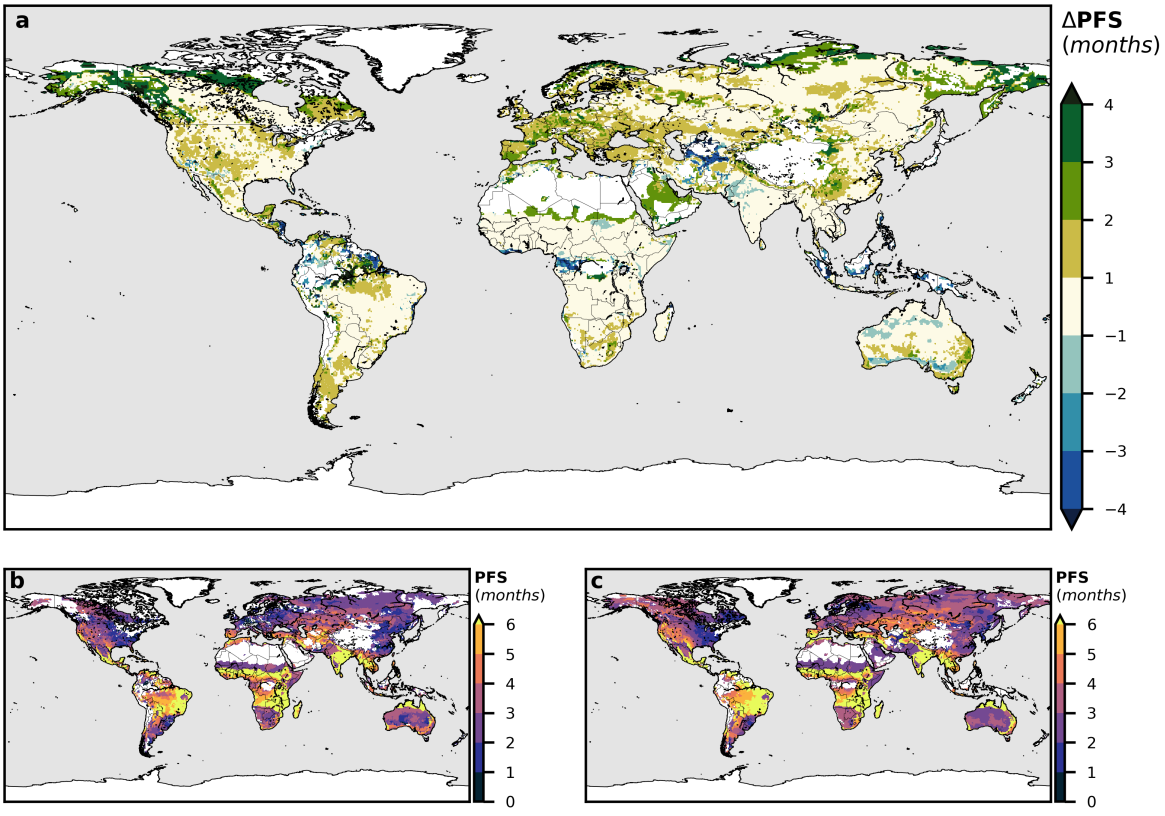


Figure 3.3: Potential Fire Season. **a**, Future minus present Potential Fire Season Length ($PFSL$) difference in months ($\Delta PFSL$). **b**, Present Potential Fire Season. **c**, Future Potential Fire Season.

3.3.2 Future fire-climate classification

A future fire-climate classification map is derived by applying the thresholds obtained in the present fire-climate classification to future climatology variables from multiple Coupled Model Intercomparison Project Phase 5 (CMIP5) Global Circulation Model (GCM) outputs, considering the RCP8.5 scenario (the worst-case climate change scenario of the CMIP5). Two contrasting approaches can be taken for analysing future fire activity, one that considers quick vegetation adaptation to the new climatic conditions, and another that does not. These two approaches clearly diverge in the boreal regions, where the biome (mainly taiga) is strongly conditioned by the low temperatures and where future temperature changes at the end of the 21st century will have a greater amplitude. It is expected that the boreal forest of these areas will not be immediately replaced by a temperate mixed forest where the average annual temperature exceeds the range of values typical of the taiga biome. Terrestrial vegetation compositional and structural change could occur during the 21st century where vegetation disturbance is accelerated or amplified by human activity, but equilibrium states may not be reached until the 22nd century or beyond [231].

Based on the assumption that during the future period (2070-2099) the vegetation will not be fully adapted to the new climatic conditions, and since the present Köppen-Geiger

USC UNIVERSIDADE DE SANTIAGO DE COMPOSTELA

climate classification (on which we base our Tr, Ar, Te and Bo categories) closely corresponds to the different existent biomes [201], we analyse only the projected changes in the specific fire-climate classification variables, maintaining the general division of Tropical, Arid, Temperate and Boreal regions as is in present climate conditions. The future fire-climate classification is shown in Figure 3.2c.

We note that we determine future fire activity from relationships of the latter with the present climate; however these relationships might not be stationary. Our approach does not contemplate possible future changes in precipitation frequency if they are not noticeable in monthly precipitation amounts. Areas with rising incidence of extreme precipitation events due to global warming [232] may experience an increase in monthly precipitation but a decrease in rainy days, which may lead us to consider the conditions there less favorable for fire activity than they actually will be.

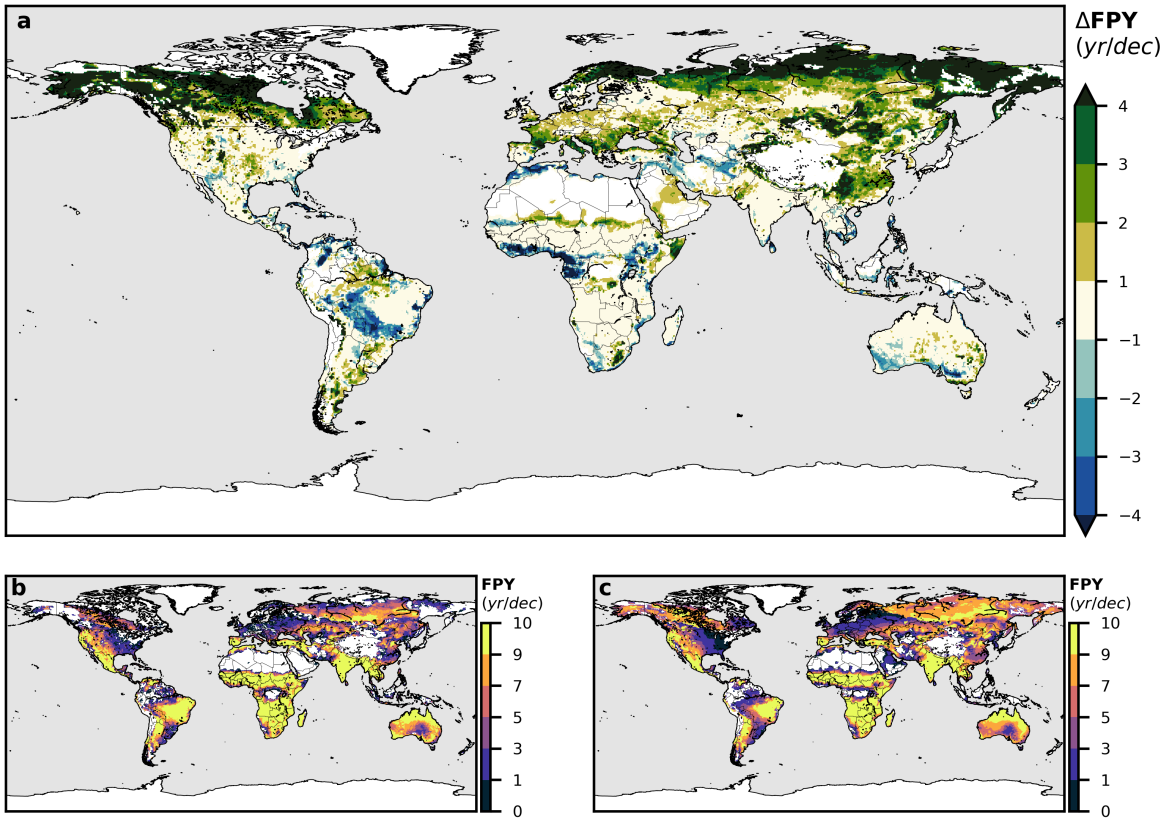


Figure 3.4: Fire Prone Years. **a**, Future minus present number of years with at least one month classified as fire-prone per decade (ΔFPY). **b**, Present fire-prone years per decade. **c**, Future fire-prone years per decade.

3.3.3 Future changes in global fire activity

Modelled future fire-prone regions experience significant variations with respect to the present (Figure 3.2b,c). Due to global warming, the Bo-hs fire class pertaining to boreal forests would spread over a larger area, reaching most of Northern Scandinavia and undergoing

a southward and northward expansion in Canada, Alaska and Russia. This category may experience a percentual expansion of 47.0% according to our results. This expansion is more accentuated for the combination of the highest recurrence subcategories Bo-hs-r and Bo-hs-o, reaching a value of 111.5%.

The conjunction of Te-dhs-r and Te-dhs-o fire classes of midlatitudes also undergoes a considerable expansion of 24.5% in area (Figure 3.2b,c). The most remarkable changes are expected in Southern China and Southern Europe. A large part of Europe transitions from a infrequent fire category to a more frequent fire category with Csa and Csb Mediterranean climates [202].

The Tr-ds fire classes with frequent fire-prone conditions in the Tropics presents less spatial changes (Figure 3.2b,c), with a spatial contraction of 6.3%. The most important differences are found in South America. Some of the climate model results considered here indicate also that some parts of the Eastern Amazon rainforest will move from a non-fire class to Tr-ds fire class, as other studies have suggested [145].

The Arid fire-prone classes Ar-fl-r and Ar-fl-o would increase its area by 5.0%. Projected changes in the extent of this class are very sensitive to changes in annual precipitation, conducive to vegetation and fuel reduction or increment, thus there is significant uncertainty in the proximity of desert regions (Figure 3.2c).

Clearer conclusions can be drawn from the PFSL and FPY calculation (Figure 3.3 and 3.4). The number of months meeting the set of conditions in Table 3.1 yields the estimated PFSL (Figure 3.3b), and the number of years with at least one month meeting the thresholds, the FPY. In the boreal regions, we obtain a general lengthening of the PFS. The PFS of these areas is conditioned by temperature, so the amplified warming of Artic zones [233] is expected to make the FS longer. Notwithstanding, in certain parts of Eastern Asia, the intense warming is counterbalanced by an increase of the precipitation in certain warm months (see Supplementary Figures S3.21 and S3.22), leading to a slight shortening of our estimated PFS. There is evidence, however, that temperature increases may lead to drier fuels in the future despite the precipitation increase, thus augmenting fire-risk, as some investigations have shown for Canada [136]. Our results agree in general with several other studies that have previously pointed towards an increase of the FSL in boreal areas [141, 142, 234], even when some suggest a more pronounced lengthening in more northerly latitudes [141, 142].

In terms of the frequency of years with fire-prone conditions, the conclusions are even clearer. A general increase of the FPY is observed, especially for northerly latitudes, where the differences reach values of more than +4 years per decade (Figure 3.4a). This possible increase in fire activity in boreal areas may result in significant peatland combustion and a release of the large quantities of soil carbon that they store into the atmosphere [235]. These greenhouse gas emissions may create a positive feedback loop, leading to a further increase in temperature, which in turn will enhance boreal wildfire incidence and more peatland burning. Of the total global area covered by peatlands, 19.7% is classified as recurrent fire-prone regions at present, a percentage that may increase to 43.2% in the period 2070-2099 according to our results (Figure 3.5).

The Te-dhs fire class, corresponding to temperate climates, would also experience a general lengthening of the PFS (Figure 3.3). A future precipitation decline may be especially significant in Southern Europe (Supplementary Figure S3.21), associated with an increased anticyclonic circulation yielding more stable conditions [237], while the temperature raise would be quite homogeneous among all Te-dhs fire-climate class areas. The FS drought intensification around

USC UNIVERSIDADE

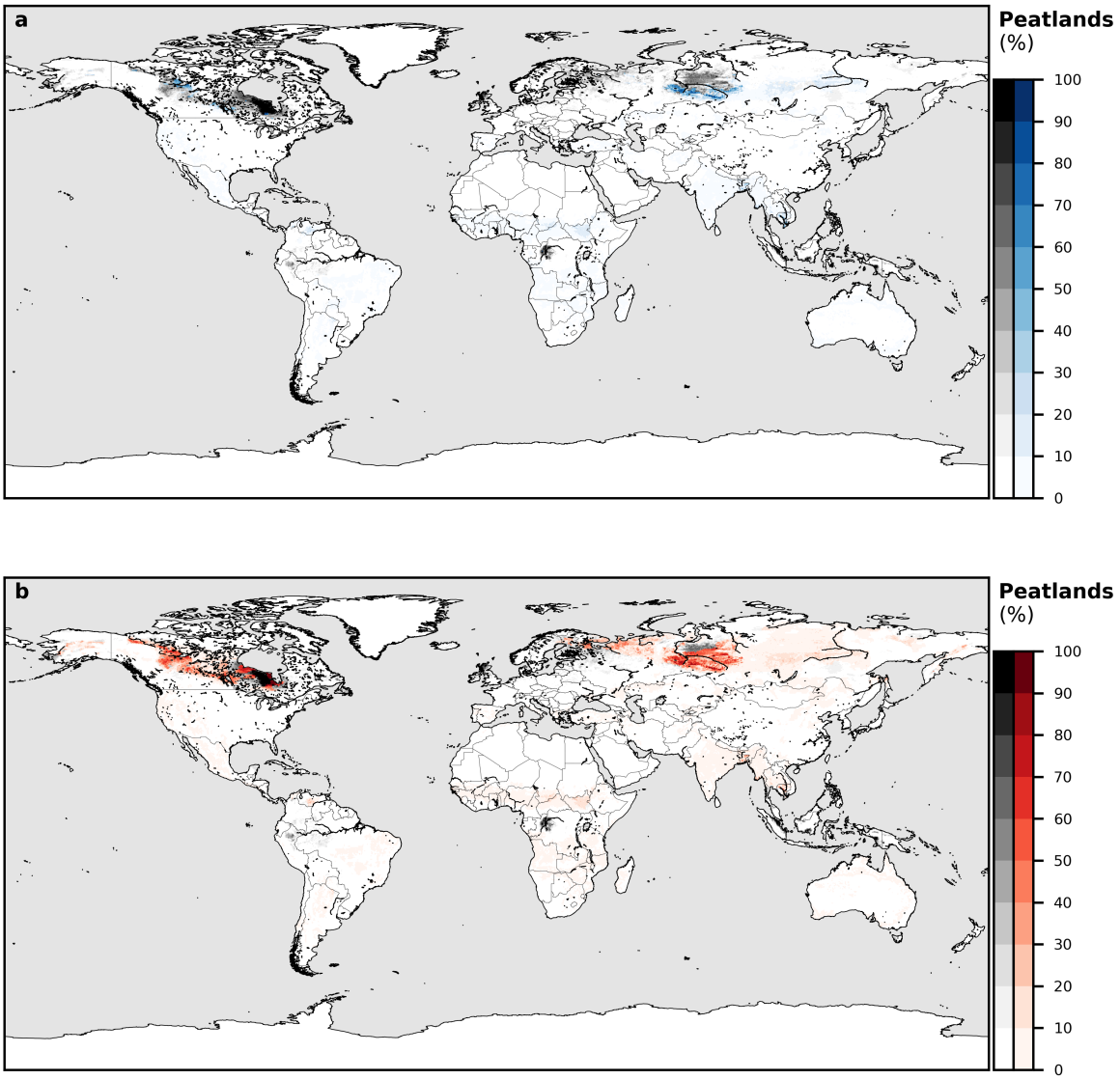


Figure 3.5: Global peatland extent expressed as land cover percent. **a**, Peatland extent coinciding with present (1996-2016) recurrent fire-prone regions (in blue). **b**, Peatland extent coinciding with future (2070-2099) recurrent fire-prone regions (in red). In both panels, the peatland cover not coinciding with recurrent fire-prone regions is represented in grey colors. Data for global peatland cover were obtained from Melton *et al.* [236].

the Mediterranean, together with the general warming (Supplementary Figure S3.21), would lead to a lengthening of the PFS of around 2 months (Figure 3.3a), but summer months could also experience this precipitation decline (Supplementary Figure S3.22), meaning that the FS would be more severe. The Western US, which has already experienced over the last decades the lengthening of the FS [135] and the increase of large fires [238] and extreme wildfire weather [156, 159] due to climate change, may also experience a FS lengthening by the end of the 21st century. Some authors [141, 239, 147] have studied projected fire future changes from other points of view (occurrence of very large fires, wildfire potential, etc.), finding also a general increase of fire severity by the end of the century in some of these Te-dhs fire regions.

The interannual recurrence of fire-prone conditions will significantly increase in countries like France, Italy or Eastern China (Figure 3.4).

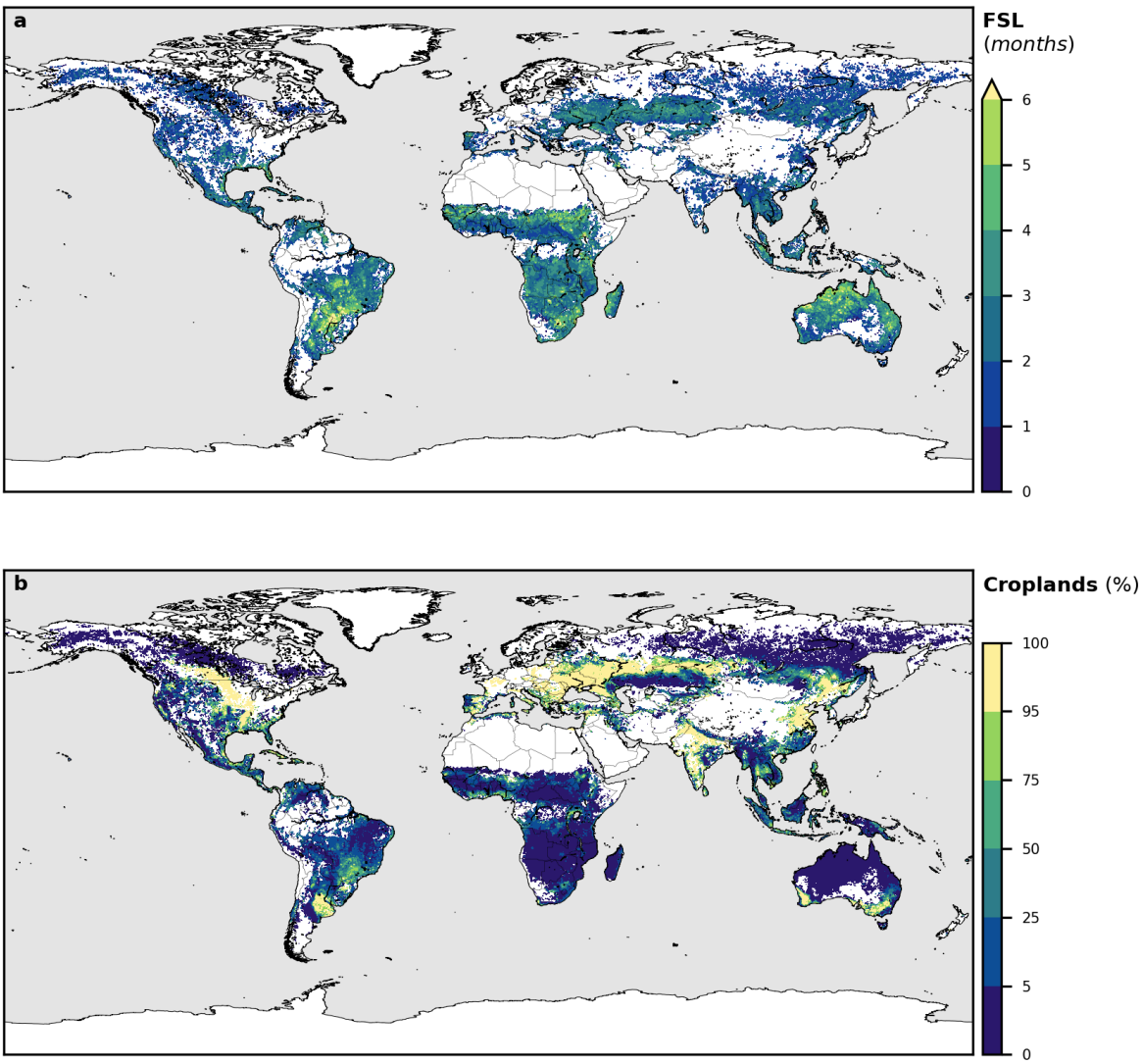
The PFSL of the Tropical Tr-ds fire-climate class presents slight differences between present and future values (Figure 3.3). Some areas of the Northern African savanna may experience a shortening of the PFS, while Southern Africa shows a lengthening. A dipole pattern of wetting in tropical Eastern Africa and drying in Southern Africa [240] could be the reason of these future changes. There is a contrasted influence of ENSO in present African fire patterns [241], which suggests that the future pattern of precipitation variations in Central Africa maybe associated with ENSO future changes under climate change conditions [242]. Although the quantification of ENSO changes in a warmer climate is still an issue that continues to be investigated, an expansion and strengthening of ENSO teleconnections is confirmed by some authors [243, 244]. The general increase in precipitation along all seasons in the western equatorial Africa would lead to a significant decrease in the recurrence of interannual fire-prone conditions (Figure 3.4a).

3.4 Conclusions

Our results show that fire-prone areas in Temperate and especially Boreal climates, are projected to undergo the most significant expansion and lengthening of the potential fire season at the end of the XXI century driven by rising temperatures. In the Tropics, little change is expected in these respects. Notwithstanding, global warming is likely to make fire risk more severe mostly everywhere, and in particular in some regions such as Mediterranean Europe and the Eastern Amazon, where an important decrease in precipitation is also predicted during the PFS. More favourable fire conditions will potentially increment fire activity and burned area in many places. In others, especially in the Tropics, increasing suppression efforts and a cease to agricultural and pastoral practices like vegetation clearing by fire, replaced by more intensive farming, could counteract the impact of a warmer climate. A reduction of these human caused fires in the Tropics could bring global burned area down [12], despite rising trends elsewhere, given the vast contribution of Tropical fires to burned area at the global scale (Figure 3.1).

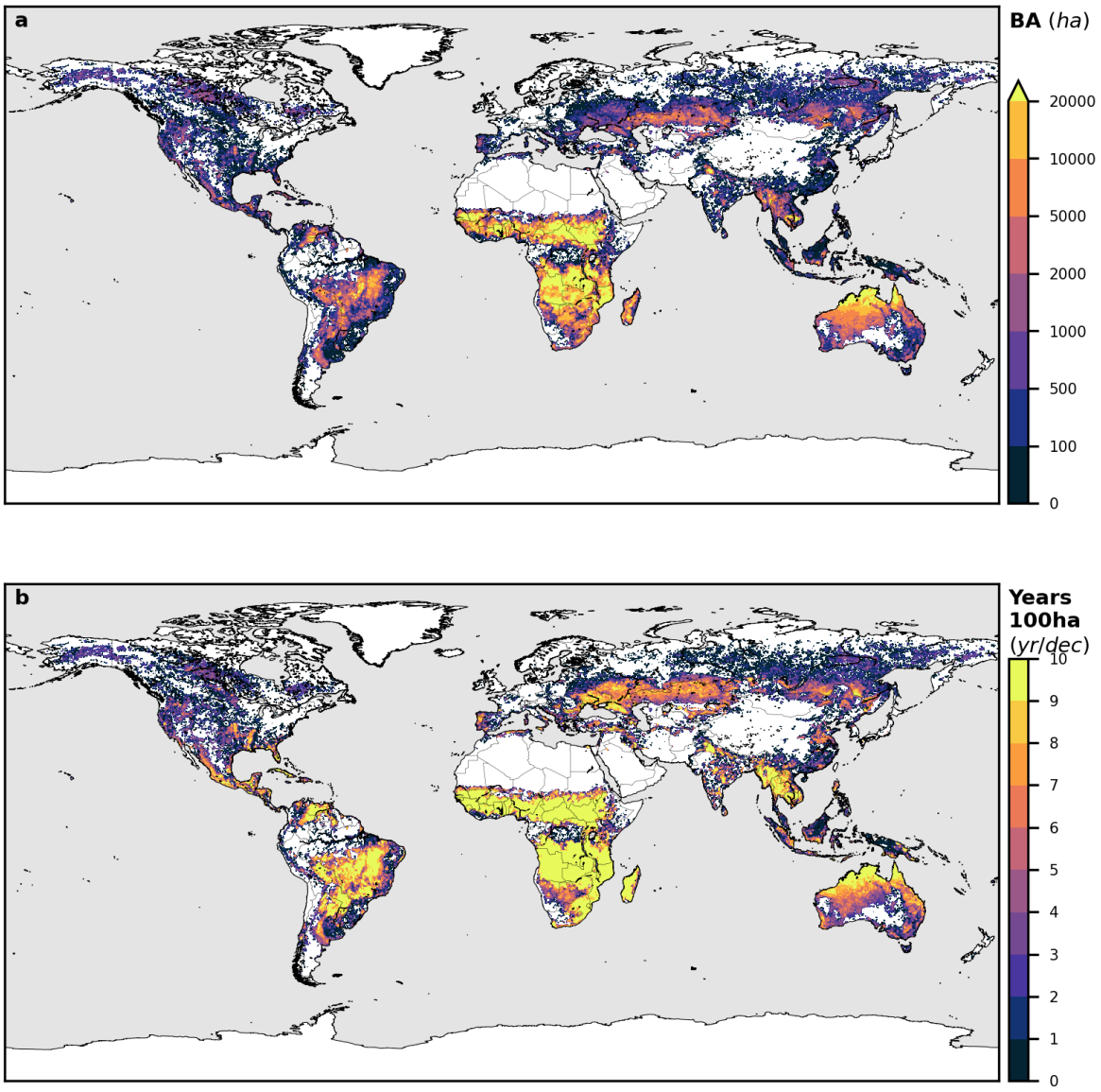
USC UNIVERSIDADE DE SANTIAGO DE COMPOSTELA

Supplementary Figures



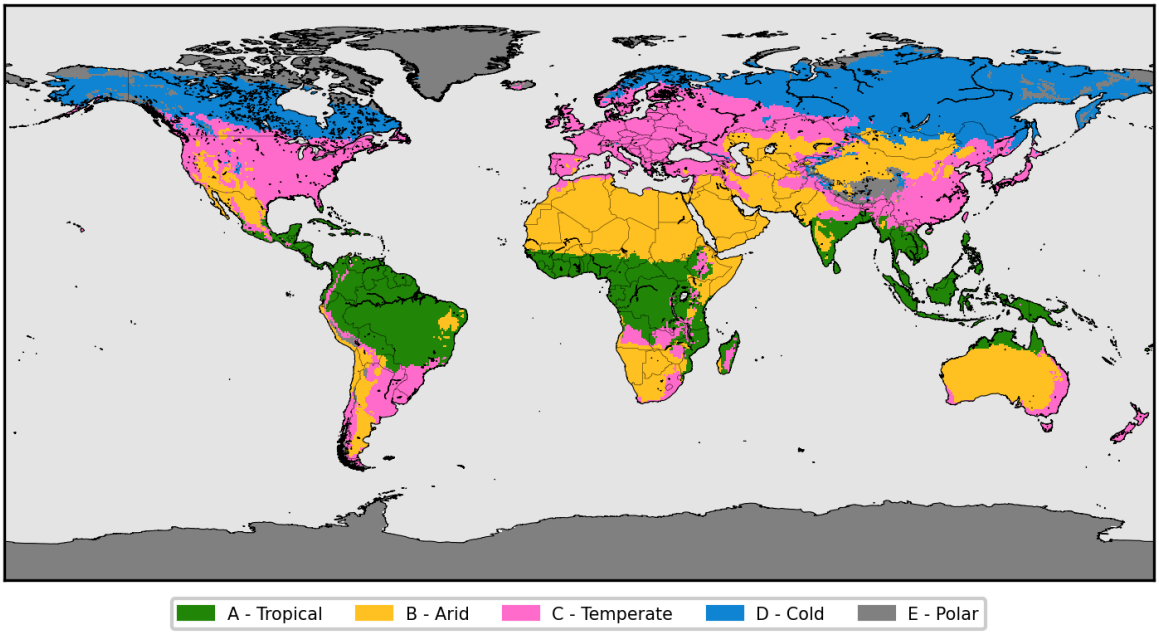
Supplementary Figure S3.1: **a**, Fire season length. **b**, Percentage of mean annual burned area (BA) corresponding to cropland land cover from GFED4 data.

USC
UNIVERSIDADE DE SANTIAGO DE COMPOSTELA



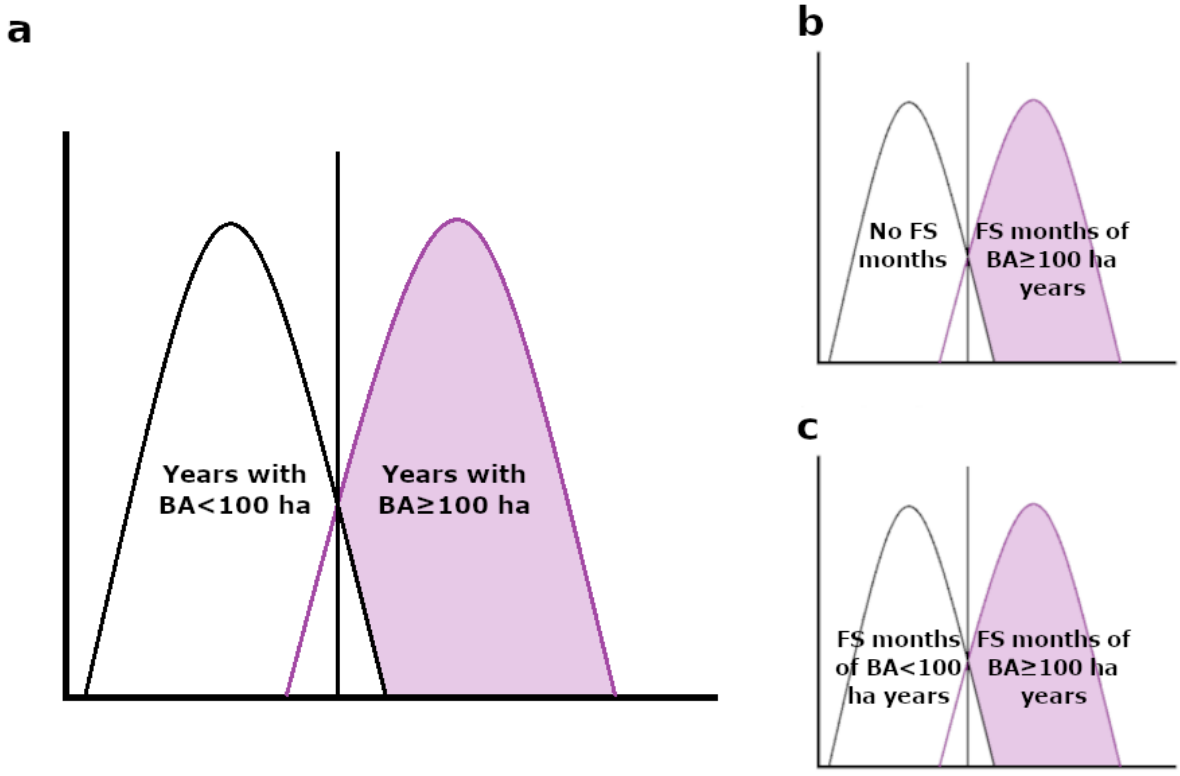
Supplementary Figure S3.2: **a**, Mean annual burned area. **b**, Number of years with an annual burned area >100ha per decade.

USC UNIVERSIDADE DE SANTIAGO DE COMPOSTELA



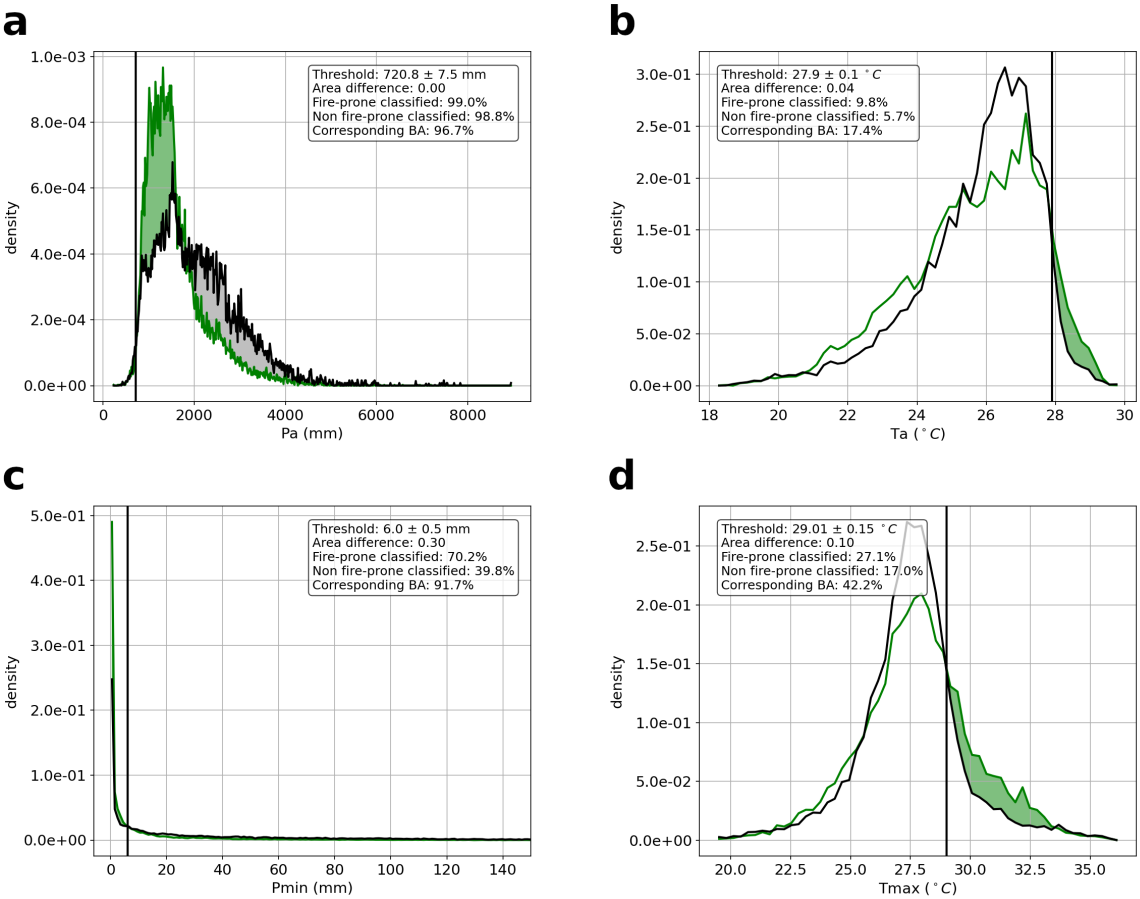
Supplementary Figure S3.3: World general climate classification. Based on the Köppen-Geiger classification but modifying the C-D category threshold to delimit the boreal forest ecoregion.

USC
UNIVERSIDADE DE SANTIAGO DE COMPOSTELA



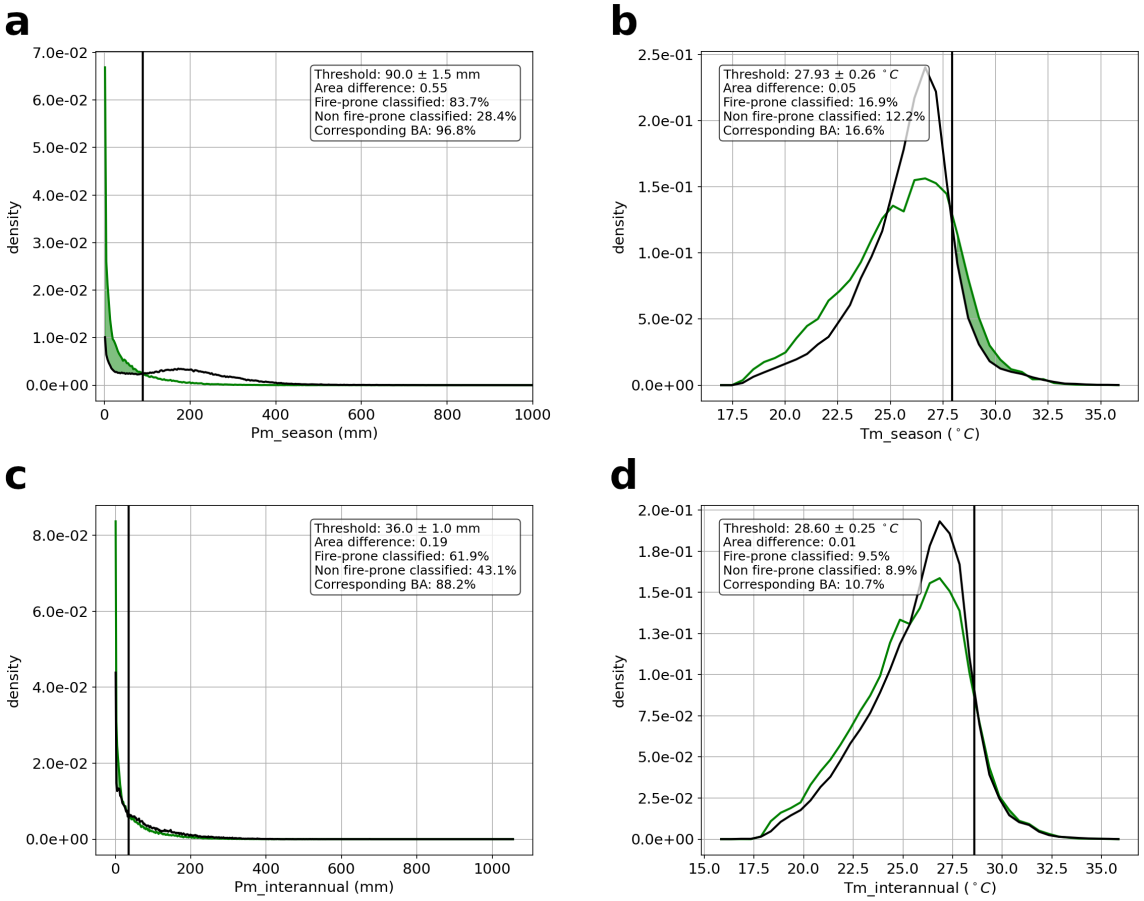
Supplementary Figure S3.4: Statistical distributions scheme. **a**, Annual variables (Pa, Ta, Pmin and Tmax) are split into values for $BA \geq 100$ha years and values for $BA < 100$ha years, all grid cells within the same main climate class are considered. Monthly variables (Pm and Tm) are used for two different comparisons: **b** seasonal and **c** interannual. The monthly seasonal distribution (**b**) compares the FS months of the $BA \geq 100$ha years against the months that are not part of a FS. For cells with no fire incidence, there is no FS, and all months are included. All grid cells within the same main climate class are considered. The interannual distribution (**c**) compares the FS months of years with $BA \geq 100$ha against the FS months of years with $BA <$ 100ha for cells with some fire incidence within the same main climate class. The thresholds are selected automatically for each distribution at the value that maximizes the area enclosed between the density function of the points with high fire activity and the density function of the points with low or no fire activity.

USC UNIVERSIDADE DE SANTIAGO DE COMPOSTELA



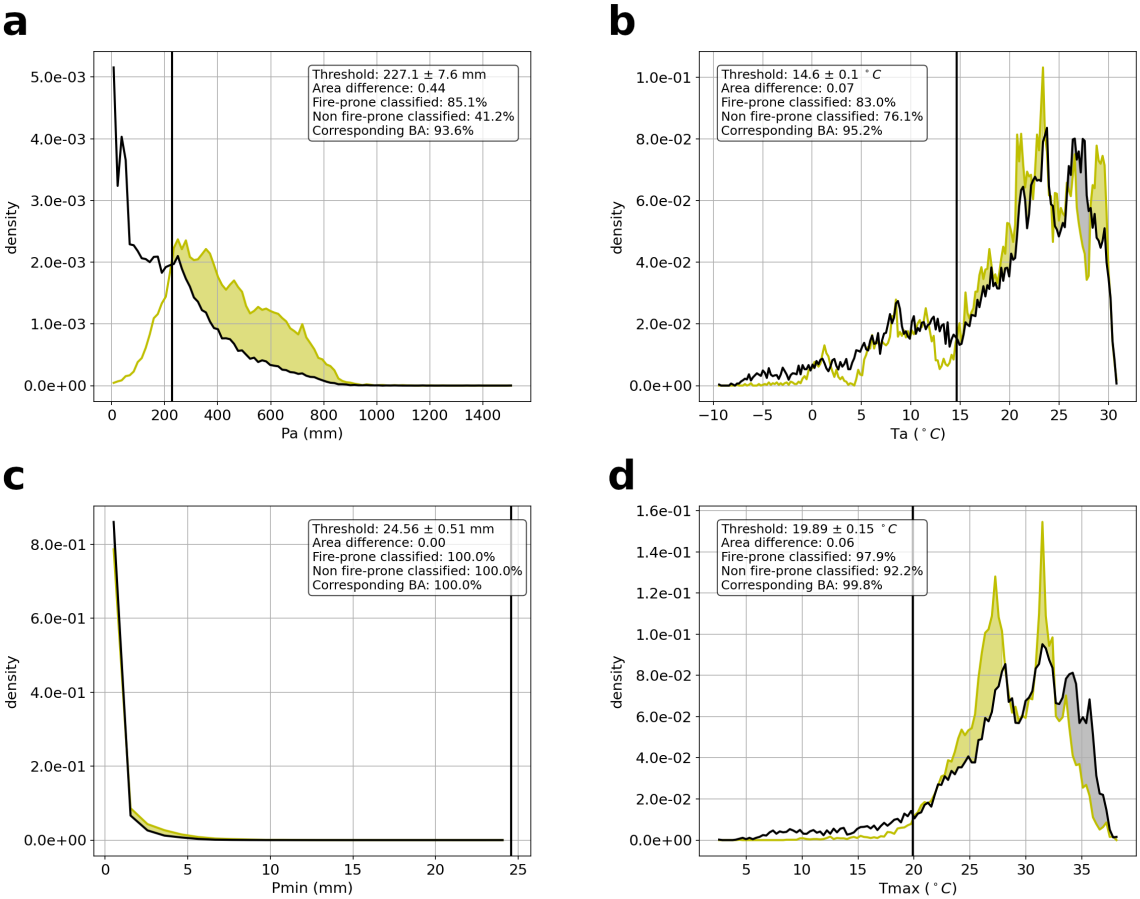
Supplementary Figure S3.5: Tropical statistical distributions for annual variables. Annual precipitation - Pa (**a**), annual mean temperature - Ta (**b**), precipitation of the driest month - Pmin (**c**) and temperature of the hottest month - Tmax (**d**). Green density functions represent values for cells and years with $BA \geq 100$ha, and black density functions represent values for cells and years with $BA < 100$ha. The thresholds are indicated through black vertical lines. The text box shows the value of the threshold and its uncertainty, the value of the area difference between fire and non-fire points, the percentage of fire points meeting the threshold, the percentage of non-fire points meeting the threshold and the percentage of burned area associated with the fire points that meet the threshold. The area difference is proportional to the difference between the percentage of fire and non-fire points. The uncertainty in the obtained threshold is the size of the x-axis discretization used in the calculation.

USC
UNIVERSIDADE DE SANTIAGO DE COMPOSTELA



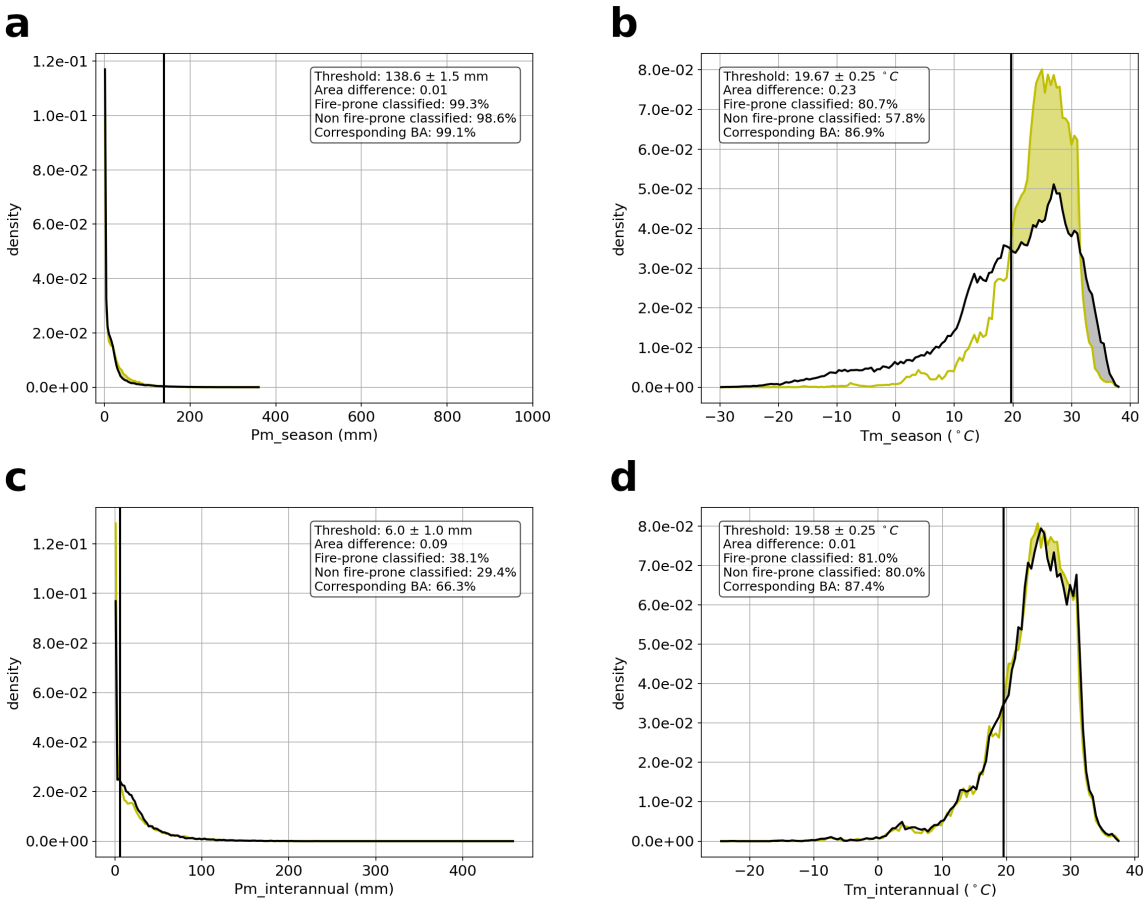
Supplementary Figure S3.6: Tropical statistical distributions for monthly variables. Monthly precipitation and temperature seasonal distributions (**a**, **b**) and interannual distributions (**c**, **d**). The thresholds are indicated through black vertical lines. In the seasonal distributions, green density functions represent the FS months of the $BA \geq 100$ha years, and black density functions represent the months out of the FS. In the interannual distributions, green density functions represent the FS of the $BA \geq 100$ha years, and black density functions represent the FS of the $BA < 100$ha years. The thresholds are indicated through black vertical lines. The text box shows the value of the threshold and its uncertainty, the value of the area difference between fire and non-fire points, the percentage of fire points meeting the threshold, the percentage of non-fire points meeting the threshold and the percentage of burned area associated with the fire points that meet the threshold. The area difference is proportional to the difference between the percentage of fire and non-fire points. The uncertainty in the obtained threshold is the size of the x-axis discretization used in the calculation.

USC UNIVERSIDADE DE SANTIAGO DE COMPOSTELA



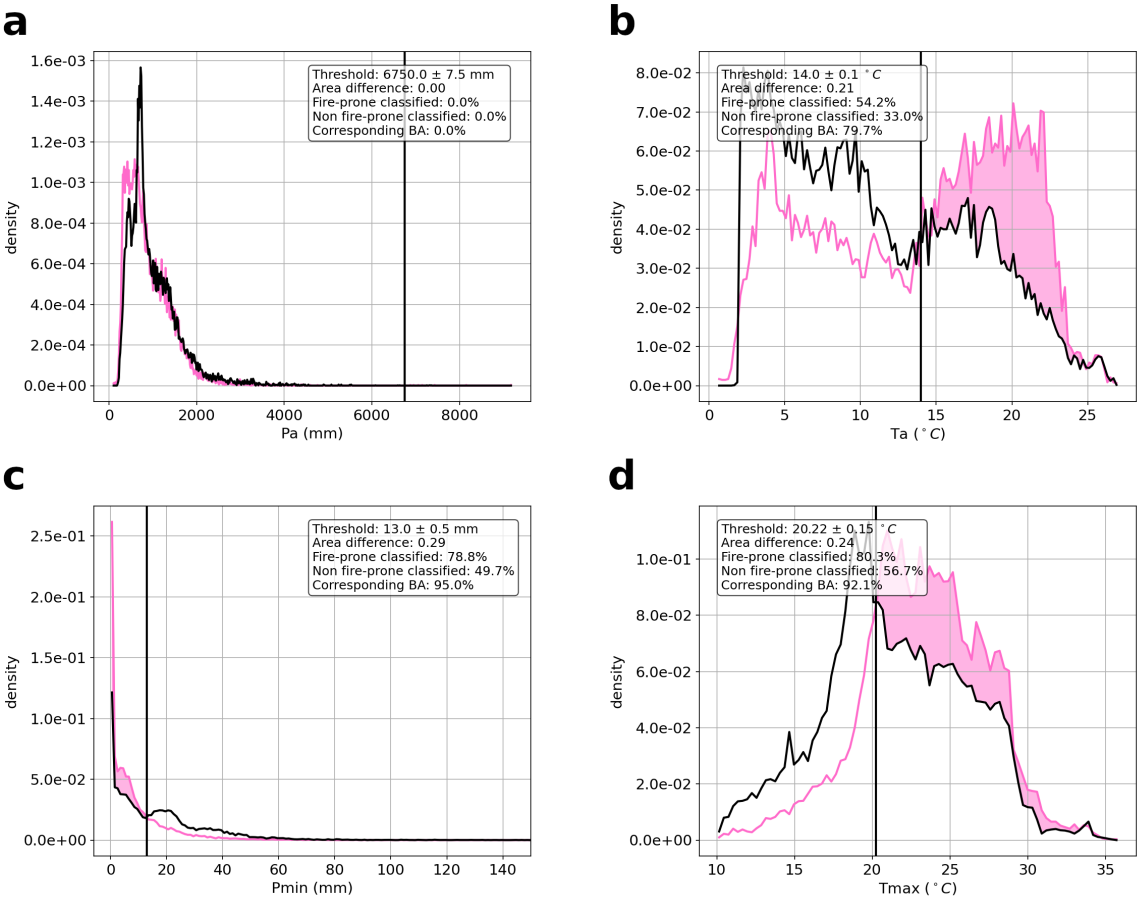
Supplementary Figure S3.7: Arid statistical distributions for annual variables. Annual precipitation - Pa (**a**), annual mean temperature - Ta (**b**), precipitation of the driest month - Pmin (**c**) and temperature of the hottest month - Tmax (**d**). Yellow density functions represent values for cells and years with $BA \geq 100$ha, and black density functions represent values for cells and years with $BA < 100$ha. The thresholds are indicated through black vertical lines. The text box shows the value of the threshold and its uncertainty, the value of the area difference between fire and non-fire points, the percentage of fire points meeting the threshold, the percentage of non-fire points meeting the threshold and the percentage of burned area associated with the fire points that meet the threshold. The area difference is proportional to the difference between the percentage of fire and non-fire points. The uncertainty in the obtained threshold is the size of the x-axis discretization used in the calculation.

USC
UNIVERSIDADE DE SANTIAGO DE COMPOSTELA



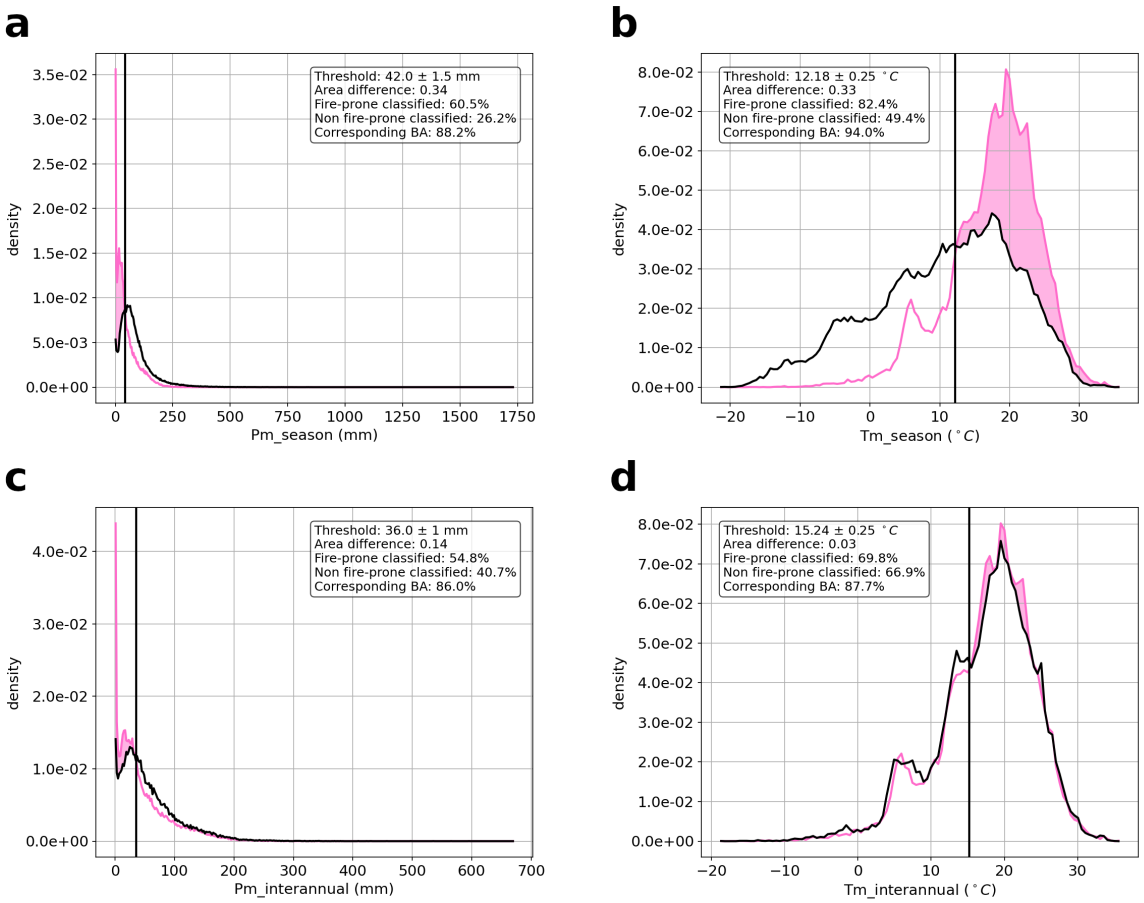
Supplementary Figure S3.8: Arid statistical distributions for monthly variables. Monthly precipitation and temperature seasonal distributions (**a**, **b**) and interannual distributions (**c**, **d**). The thresholds are indicated through black vertical lines. In the seasonal distributions, yellow density functions represent the FS months of the $BA \geq 100$ha years, and black density functions represent the months out of the FS. In the interannual distributions, yellow density functions represent the FS of the $BA \geq 100$ha years, and black density functions represent the FS of the $BA < 100$ ha years. The thresholds are indicated through black vertical lines. The text box shows the value of the threshold and its uncertainty, the value of the area difference between fire and non-fire points, the percentage of fire points meeting the threshold, the percentage of non-fire points meeting the threshold and the percentage of burned area associated with the fire points that meet the threshold. The area difference is proportional to the difference between the percentage of fire and non-fire points. The uncertainty in the obtained threshold is the size of the x-axis discretization used in the calculation.

USC UNIVERSIDADE DE SANTIAGO DE COMPOSTELA



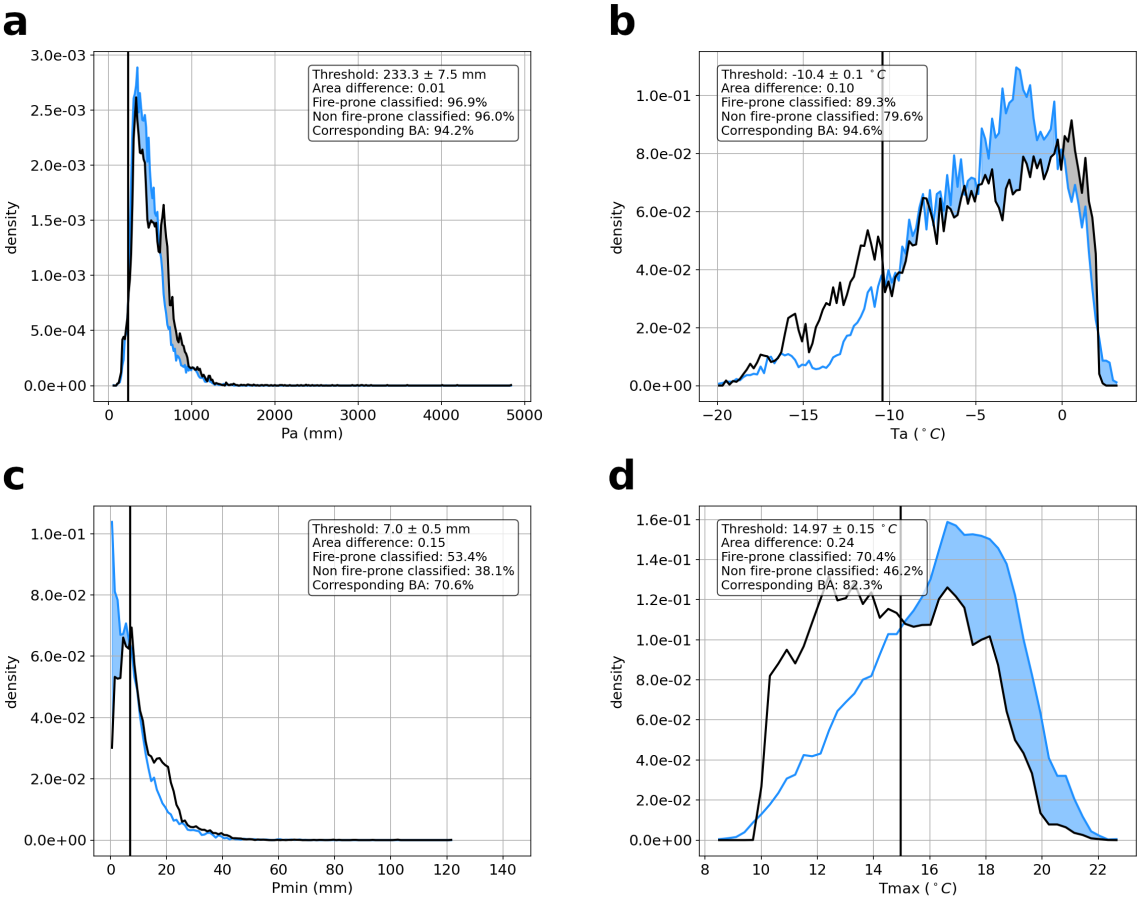
Supplementary Figure S3.9: Temperate statistical distributions for annual variables. Annual precipitation - Pa (**a**), annual mean temperature - Ta (**b**), precipitation of the driest month - Pmin (**c**) and temperature of the hottest month - Tmax (**d**). Pink density functions represent values for cells and years with $BA \geq 100$ha, and black density functions represent values for cells and years with $BA < 100$ha. The thresholds are indicated through black vertical lines. The text box shows the value of the threshold and its uncertainty, the value of the area difference between fire and non-fire points, the percentage of fire points meeting the threshold, the percentage of non-fire points meeting the threshold and the percentage of burned area associated with the fire points that meet the threshold. The area difference is proportional to the difference between the percentage of fire and non-fire points. The uncertainty in the obtained threshold is the size of the x-axis discretization used in the calculation.

USC
UNIVERSIDADE DE SANTIAGO DE COMPOSTELA



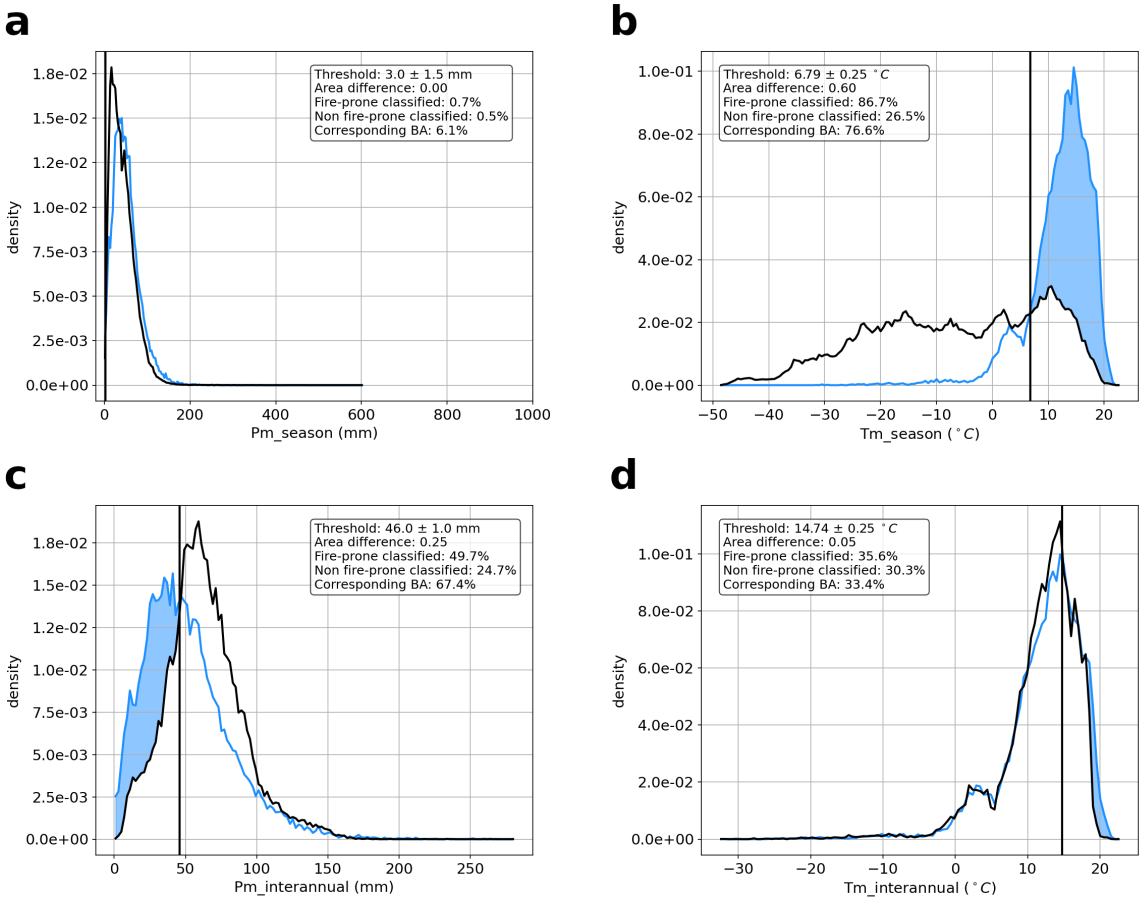
Supplementary Figure S3.10: Temperate statistical distributions for monthly variables. Monthly precipitation and temperature seasonal distributions (**a**, **b**) and interannual distributions (**c**, **d**). The thresholds are indicated through black vertical lines. In the seasonal distributions, pink density functions represent the FS months of the $BA \geq 100$ha years, and black density functions represent the months out of the FS. In the interannual distributions, pink density functions represent the FS of the $BA \geq 100$ha years, and black density functions represent the FS of the $BA < 100$ha years. The thresholds are indicated through black vertical lines. The text box shows the value of the threshold and its uncertainty, the value of the area difference between fire and non-fire points, the percentage of fire points meeting the threshold, the percentage of non-fire points meeting the threshold and the percentage of burned area associated with the fire points that meet the threshold. The area difference is proportional to the difference between the percentage of fire and non-fire points. The uncertainty in the obtained threshold is the size of the x-axis discretization used in the calculation.

USC UNIVERSIDADE DE SANTIAGO DE COMPOSTELA



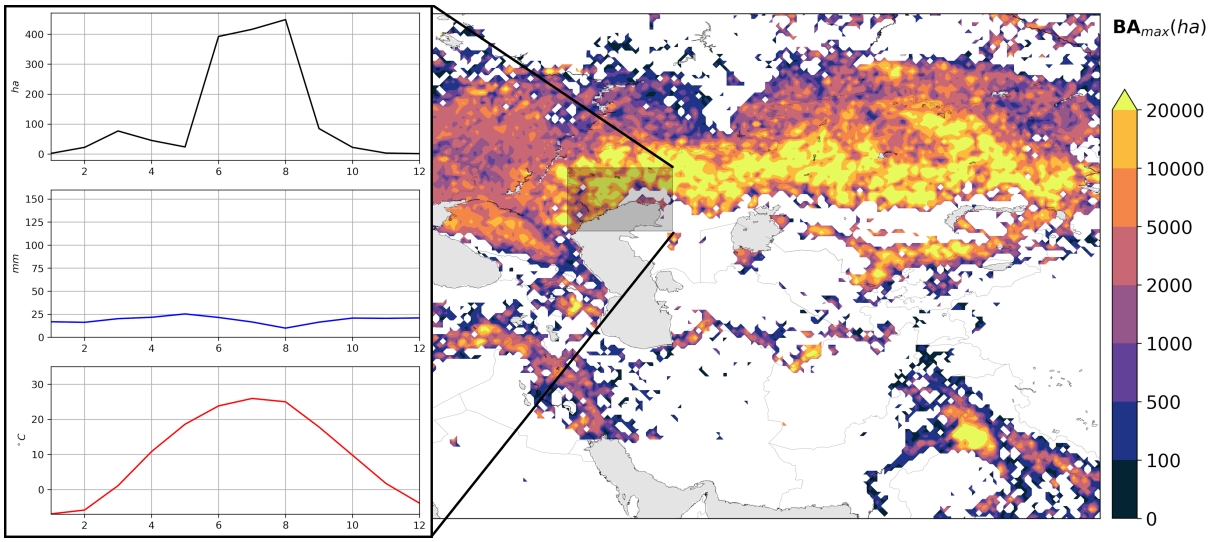
Supplementary Figure S3.11: Boreal statistical distributions for annual variables. Annual precipitation - Pa (**a**), annual mean temperature - Ta (**b**), precipitation of the driest month - Pmin (**c**) and temperature of the hottest month - Tmax (**d**). Blue density functions represent values for cells and years with $BA \geq 100$ha, and black density functions represent values for cells and years with $BA < 100$ha. The thresholds are indicated through black vertical lines. The text box shows the value of the threshold and its uncertainty, the value of the area difference between fire and non-fire points, the percentage of fire points meeting the threshold, the percentage of non-fire points meeting the threshold and the percentage of burned area associated with the fire points that meet the threshold. The area difference is proportional to the difference between the percentage of fire and non-fire points. The uncertainty in the obtained threshold is the size of the x-axis discretization used in the calculation.

USC
UNIVERSIDADE DE SANTIAGO DE COMPOSTELA

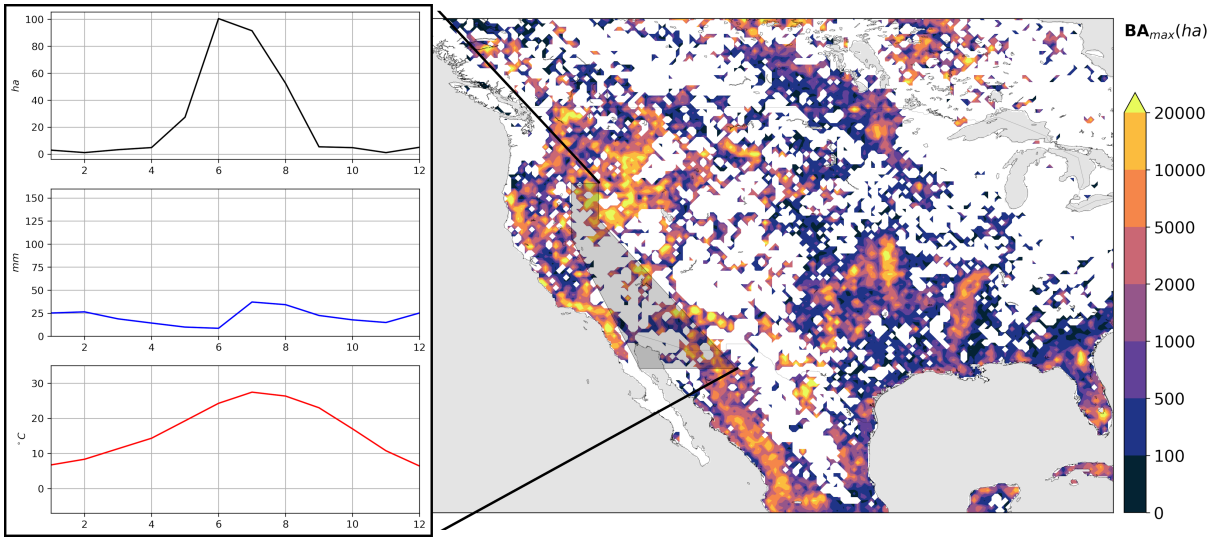


Supplementary Figure S3.12: Boreal statistical distributions of monthly variables. Monthly precipitation and temperature seasonal distributions (**a**, **b**) and interannual distributions (**c**, **d**). The thresholds are indicated through black vertical lines. In the seasonal distributions, blue density functions represent the FS months of the $BA \geq 100$ha years, and black density functions represent the months out of the FS. In the interannual distributions, blue density functions represent the FS of the $BA \geq 100$ha years, and black density functions represent the FS of the $BA < 100$ha years. The thresholds are indicated through black vertical lines. The text box shows the value of the threshold and its uncertainty, the value of the area difference between fire and non-fire points, the percentage of fire points meeting the threshold, the percentage of non-fire points meeting the threshold and the percentage of burned area associated with the fire points that meet the threshold. The area difference is proportional to the difference between the percentage of fire and non-fire points. The uncertainty in the obtained threshold is the size of the x-axis discretization used in the calculation.

USC UNIVERSIDADE DE SANTIAGO DE COMPOSTELA

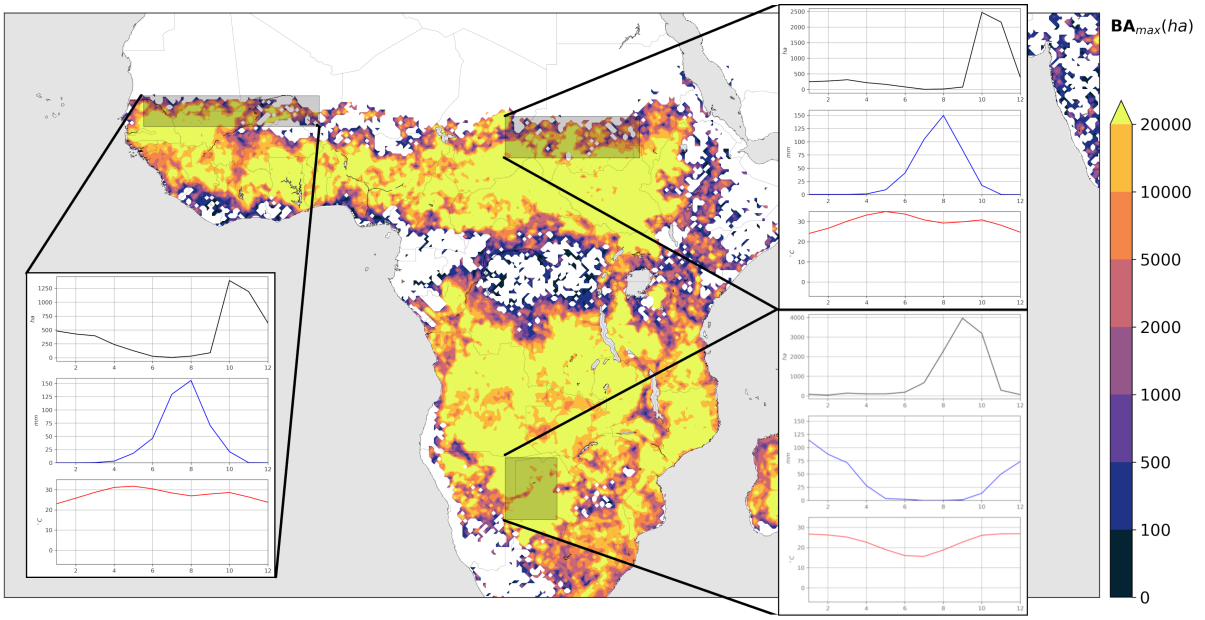


Supplementary Figure S3.13: Mean monthly values for Asian arid fire-prone regions (*BAmax* > 0ha). Mean monthly burned area in black, precipitation in blue and 2m air temperature in red.

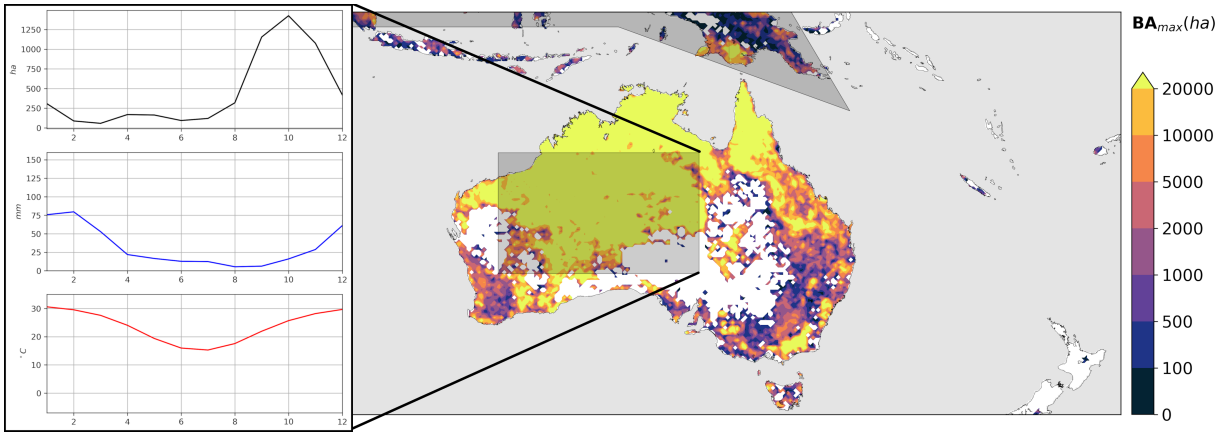


Supplementary Figure S3.14: Mean monthly values for North American arid fire-prone regions (*BAmax* > 0ha). Mean monthly burned area in black, precipitation in blue and 2m air temperature in red.

USC
UNIVERSIDADE DE SANTIAGO DE COMPOSTELA

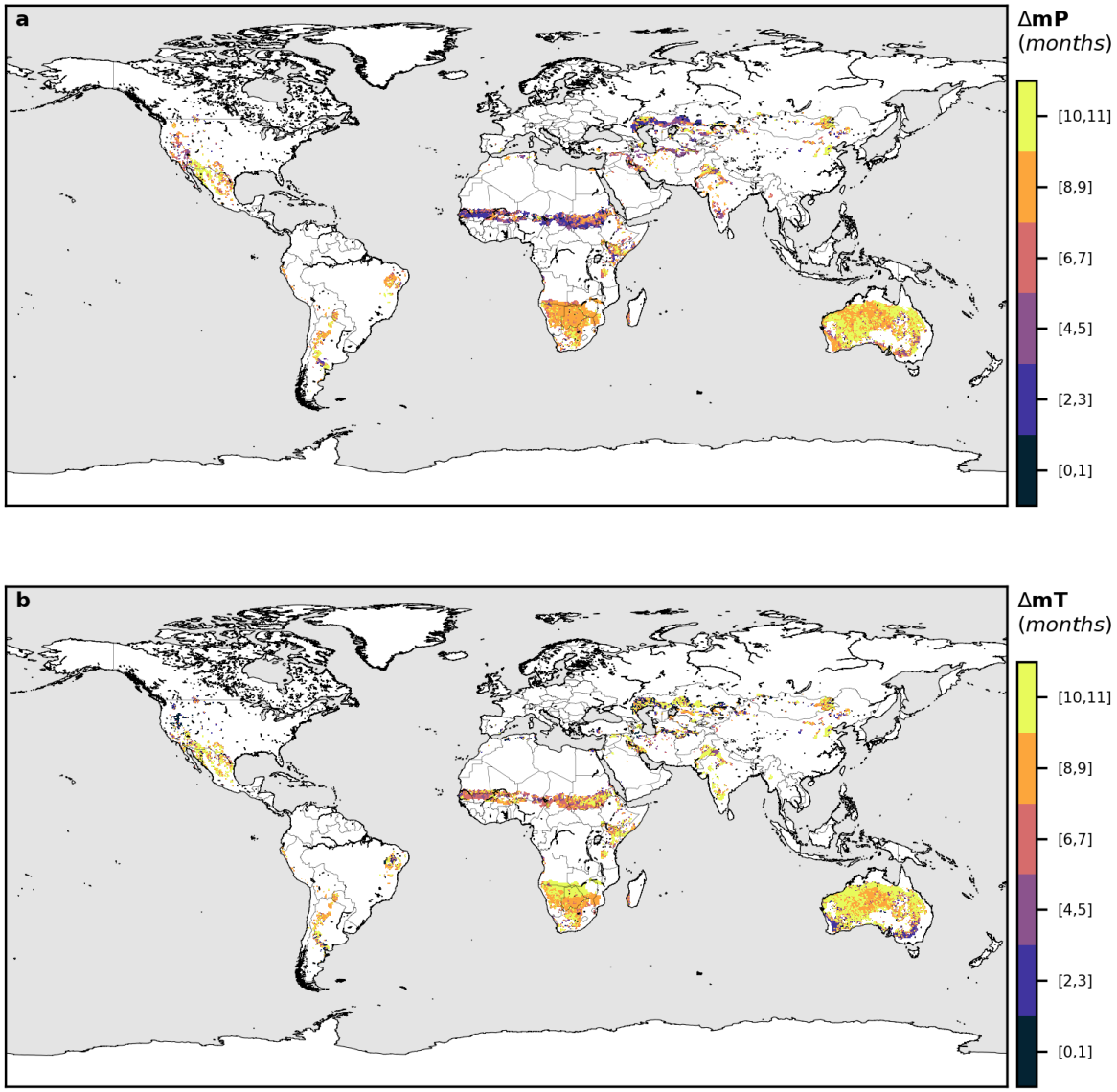


Supplementary Figure S3.15: Mean monthly values of African fire-prone arid regions ($BAmax > 0$ha). Mean monthly burned area in black, mean monthly precipitation in blue and mean monthly 2m air temperature in red.



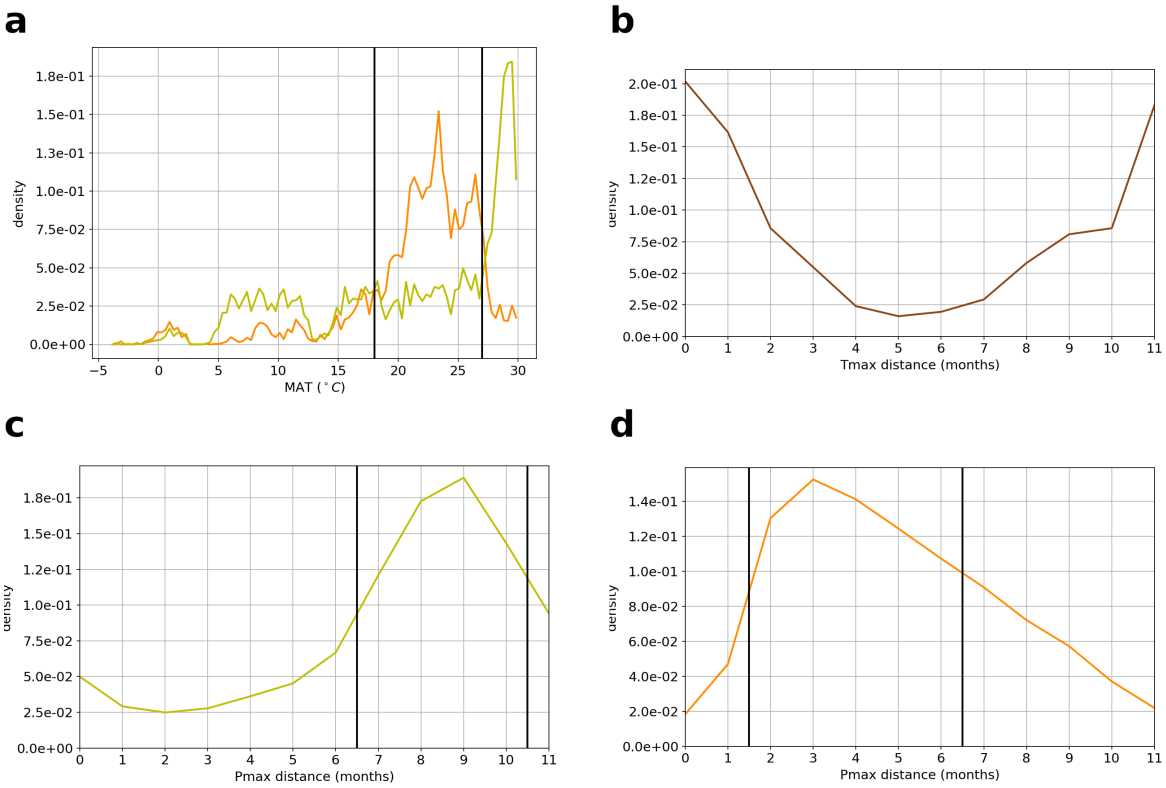
Supplementary Figure S3.16: Mean monthly values for Australian arid fire-prone regions ($BAmax > 0$ha). Mean monthly burned area in black, mean monthly precipitation in blue and mean monthly 2m air temperature in red.

USC UNIVERSIDADE DE SANTIAGO DE COMPOSTELA



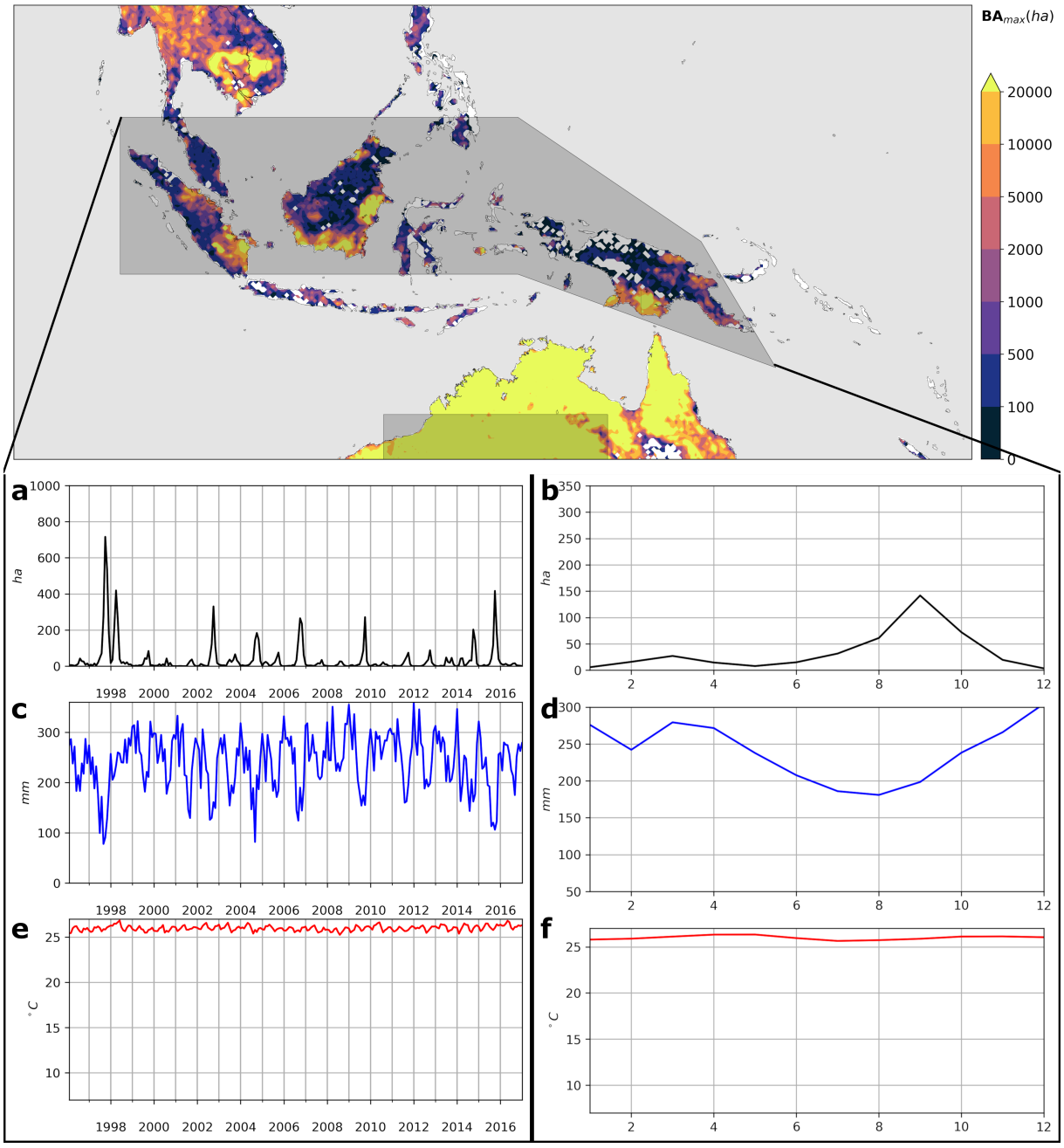
Supplementary Figure S3.17: Months from the month with highest burned area. **a**, Time period in months between the month with most burned area and the wettest month (ΔmP). **b**, Time period in months between the month with most burned area and the hottest month (ΔmT).

USC
UNIVERSIDADE DE SANTIAGO DE COMPOSTELA



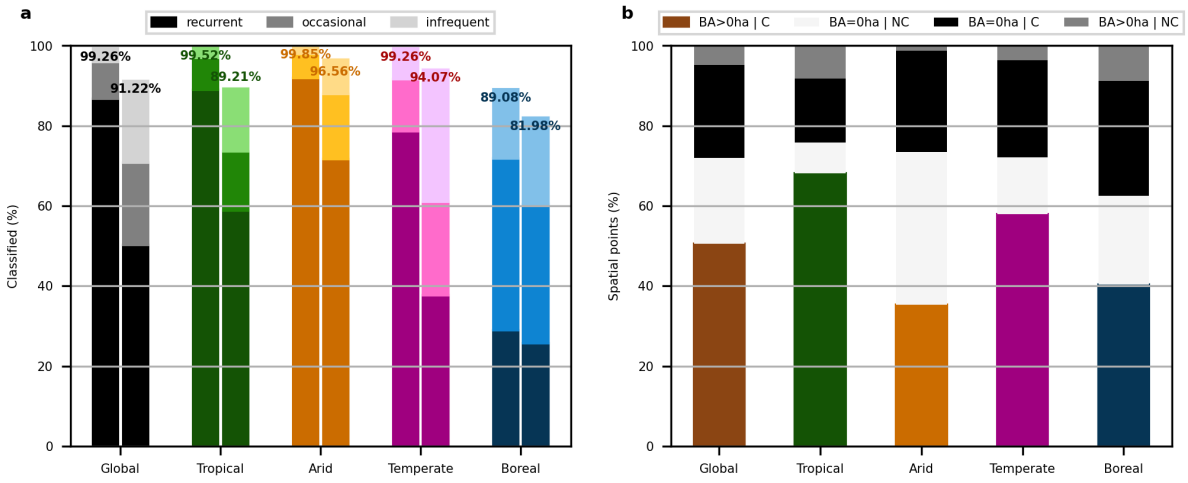
Supplementary Figure S3.18: Auxiliar statistical distributions for arid climates. **a**, MAT probability density function of arid fire-prone points ($BAmax \geq 0$ha) with $\Delta mP > 6$, i.e. with more than 6 months in between the month with most burned area and the wettest month (yellow) and with $\Delta mP \leq 6$ values (orange). **b**, For points with $MAT < 18.5°C$, probability density function of the distance in months between fire season months and the hottest month (brown). **c,** For points with $18.5°C \leq MAT < 27.5°C$, probability density function of the distance in months between fire season months and the wettest month (yellow). **d**, For points with $MAT \geq 27.5°C$, probability density function of the distance in months between fire season months and the wettest month (orange).

USC UNIVERSIDADE DE SANTIAGO DE COMPOSTELA



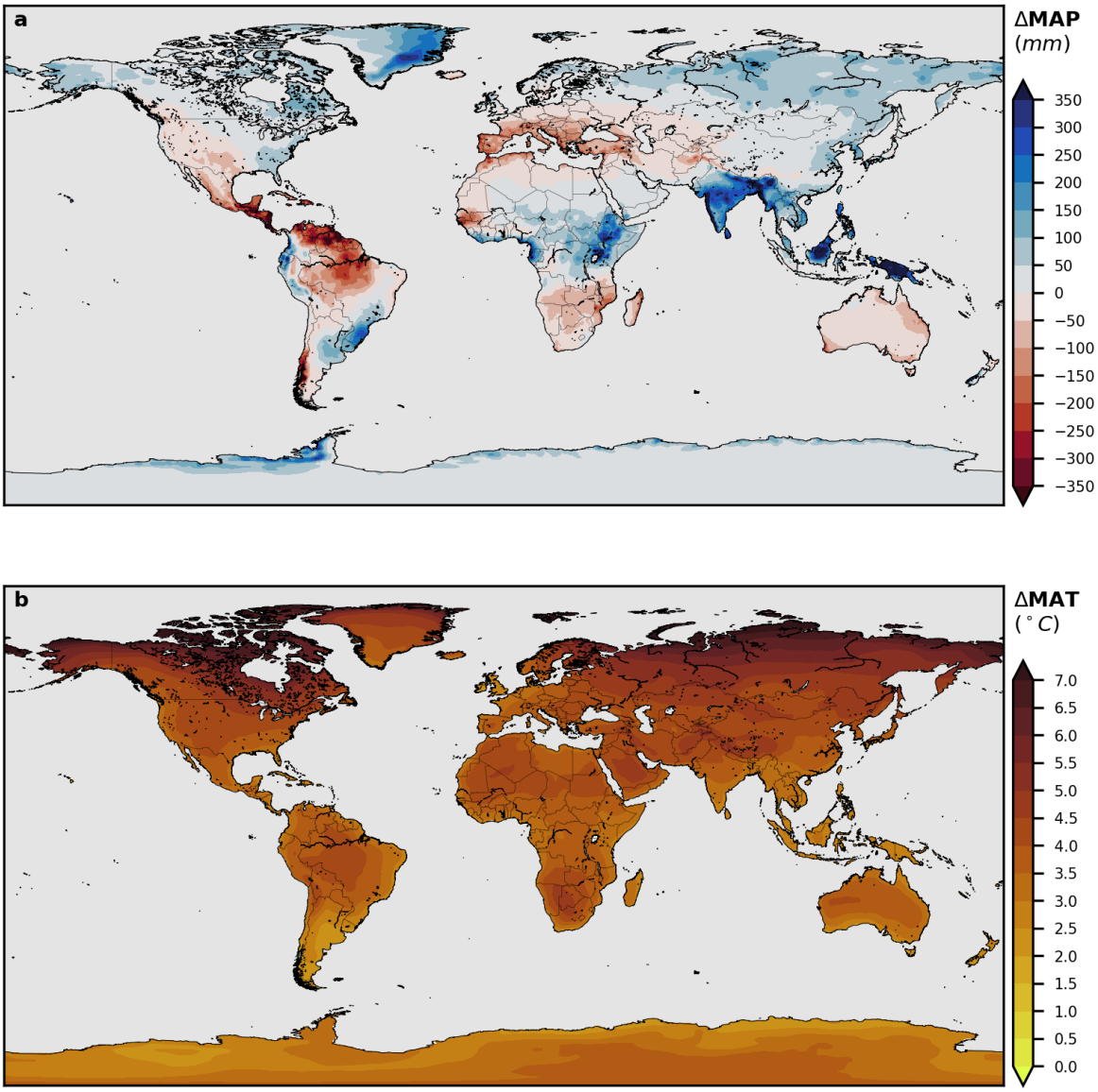
Supplementary Figure S3.19: Monthly values for South-eastern maritime Asia arid fire-prone regions. 1996-2016 time series of mean monthly values (**a**, **c**, **e**) and the mean annual cycles (**b**, **d**, **f**) of burned area (**a**, **b**, in black), precipitation (**c**, **d**, in blue) and 2m air temperature (**e**, **f** in red) for the Malay Archipelago fire-prone region (*BAmax* > 0ha).

USC
UNIVERSIDADE DE SANTIAGO DE COMPOSTELA



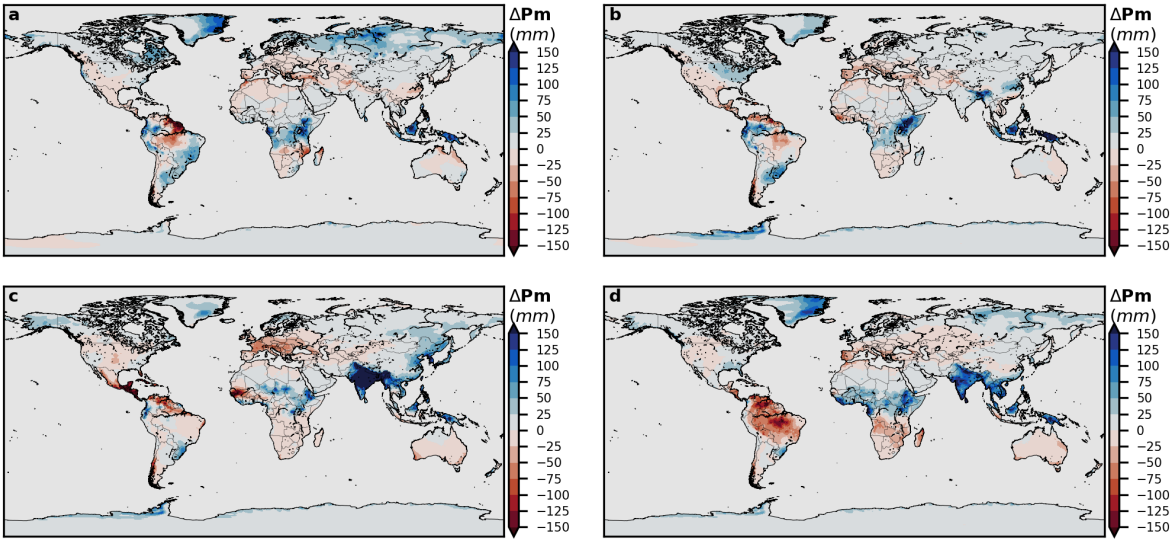
Supplementary Figure S3.20: Validation data of the fire-climate classification. a Percentage of global mean annual burned area observed at cells classified as fire-prone (left bars) and percentage of grid cells with non-zero burned area classified as fire-prone (right bars). b Percentage of: classified (color) and non-classified (black) points with non-zero observed burned area and classified (grey) and non-classified (white) with zero observed burned area (quantification of Figure 3.2a of the main text).

USC UNIVERSIDADE DE SANTIAGO DE COMPOSTELA

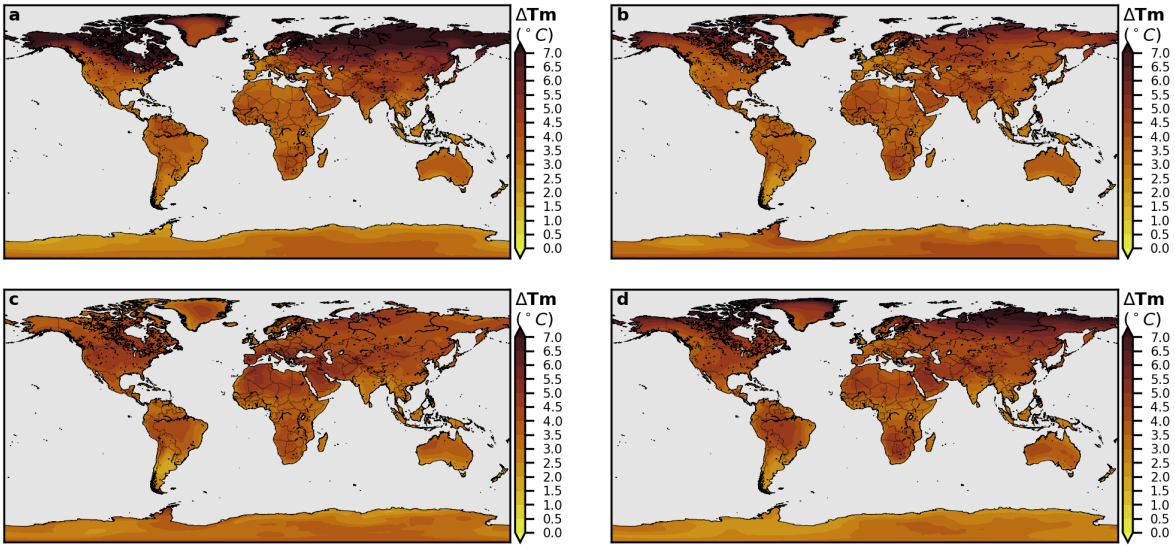


Supplementary Figure S3.21: Future changes in annual mean precipitation and temperature. **a**, Difference between 2070-2099 MAP and 1996-2016 MAP (ΔMAP). **b**, Difference between 2070-2099 MAT and 1996-2016 MAT (ΔMAT).

USC
UNIVERSIDADE DE SANTIAGO DE COMPOSTELA



Supplementary Figure S3.22: Future changes in precipitation by season. Difference between 2070-2099 and 1996-2016 mean monthly precipitation for the DJF season (**a**), MAM season (**b**), JJA season (**c**) and SON season (**d**).



Supplementary Figure S3.23: Future changes in temperature by season. Difference between 2070-2099 and 1996-2016 mean monthly temperature for the DJF season (**a**), MAM season (**b**), JJA season (**c**) and SON season (**d**).

USC UNIVERSIDADE DE SANTIAGO DE COMPOSTELA

USC
UNIVERSIDADE
DE SANTIAGO
DE COMPOSTELA

Chapter 4

The influence of climate change on wildfire behaviour in the Iberian Peninsula

* The results from this chapter are under review as Senande-Rivera, M.[1], Insua-Costa, D.[2] & Miguez-Macho, G.[1]. The influence of climate change on wildfire behaviour in the Iberian Peninsula. Under review at *Science of the Total Environment*.
There is an available preprint at SSRN: `http://dx.doi.org/10.2139/ssrn.4421371`.

[1] CRETUS, Non-linear Physics Group, Universidade de Santiago de Compostela, Galicia, Spain
[2] Hydro-Climate Extremes Lab (H-CEL), Ghent University, Ghent, Belgium

4.1 Introduction

The 6th IPCC Assessment Report (AR6) [245] determines that the likely range of human-induced change in global surface temperature in 2010–2019 relative to 1850–1900 is 0.8°C to 1.3°C (due to increases in greenhouse gas concentration and aerosols, or land-use changes), while the likely range of the change attributable to natural forcing is only –0.1°C to +0.1°C. Global increases in fire risk were linked to ongoing climate change [38, 36, 140, 158, 13], but the complex interactions between the effects of climate, vegetation and humans on fire activity involve that these changes are spatially and temporally heterogeneous [160]. When attributing extreme weather events to present climate change, the atmospheric response to anthropogenic forcings can be interpreted as a combination of a thermodynamic and a dynamic component [246]. Regarding wildfires, the thermodynamic component would be associated with the increase in atmospheric water demand (caused by the increased water-holding capacity of a warmer atmosphere), which leads to a general fuel moisture reduction [247, 149]. The dynamic component would correspond to the change in the frequency of fire-prone weather patterns, such as those leading to heat waves or droughts [69, 40]. Since wildfires are not strictly a meteorological event, an additional vegetation-related component must be included. Climate change and atmospheric CO2 fertilization are enhancing vegetation growth [248] and, together with human-induced land-use changes, this may increase fuel loads [146, 249].

USC UNIVERSIDADE DE SANTIAGO

While fire activity is augmenting in regions like the Western United States [149] or Australia [150], observed burned area and number of fires have diminished in recent decades in

Mediterranean Europe [250], in contrast to the increase in extreme fire weather conditions for this region [251] which is expected to further intensify in the future [147, 139]. This observed decrease in burned area is less pronounced in the Iberian Peninsula [250], where some recent extreme events (such as the 2017 and the 2022 fire seasons) have been on an unprecedented scale [152, 76].

To understand whether climate change may currently be intensifying extreme wildfires in the Iberian Peninsula, we have quantified the increase on the rate of spread attributable to the thermodynamic component of climate change for all wildfires between 2001 and 2021 with a burned area greater than 500 ha. In addition, we analysed how enhanced vegetation growth may have influenced the spread of these wildfires. The comparison between these two contributions is also analysed for a future scenario of intermediate emissions. Due to the remaining uncertainties in atmospheric circulation changes induced by global warming [252], we do not quantify the possible dynamic component of climate change influencing fire spread.

4.2 Methods

4.2.1 Fire and climate data

We created a database of wildfires with a burned area greater than 500 ha between 2001 and 2021 for the Iberian Peninsula by combining data from a Portuguese (ICNF) and a Spanish (MITECO) public institution. The database contains information about the location, date of ignition and burned area of 1364 wildfires.

Present climate data were obtained from the ERA5 database [129], the fifth generation ECMWF (European Centre for Medium-Range Weather Forecasts) reanalysis for the global climate, which combines model data with observations. For analysing the climate change thermodynamic influence on fire behaviour, we used the Coupled Model Intercomparison Project Phase 6 CMIP6 historical, pre-industrial and future projections from 5 general circulation models (GCMs): MPI-ESM1-2-HR, EC-Earth3, CESM2-WACCM, MRI-ESM2-0 and NorESM2-MM. The pre-industrial control simulation (piControl) is performed under conditions chosen to be representative of the period prior to the onset of large-scale industrialization, with 1850 being the reference year. We used the ”middle of the road” Shared Socio-economic Pathway SSP2-4.5, with an intermediate emissions pathway that leads to a nominal 4.5 $\mathrm{W \cdot m^{-2}}$ radiative forcing level by 2100 [253, 254]. For each model, we only consider the main ensemble member (r1i1p1f1). For analysing the vegetation component, we used 8 GMCs: ACCESS-ESM1-5, BCC-CSM2-MR, CMCC-ESM2, CanESM5, EC-Earth3-Veg, IPSL-CM6A-LR, MPI-ESM1-2-LR and NorESM2-LM. Apart from piControl, historical and SSP2-4.5 experiments, we also used the hist-noLu experiment: a historical simulation that is identical to the CMIP6 historical concentration-driven simulation, except that land use is held constant with pre-industrial values [255]. This experiment allows us to quantify the influence of land-use changes in wildfire behaviour. There is no equivalent experiment for future scenarios (i.e. future-emissions simulations but using historical land-use data), so the land-use contribution cannot be identified when analysing the influence of projected vegetation growth on fire rate of spread.

USC UNIVERSIDADE DE SANTIAGO DE COMPOSTELA

4.2.2 Rate of spread calculation

Fire rate of spread (ROS) is computed using the spread component equations of the 2016 version of the United States National Fire Danger Rating System (NFDRS2016), which is based on the Rothermel's surface fire spread model [94]. These equations were obtained by applying the conservation of energy principle to a unit volume of fuel, ahead of a steadily advancing fire in a homogeneous fuel bed [163]. The model needs 6 inputs: the moisture content of dead fuels, the moisture content of live fuels, the Keetch-Byram Drought Index, surface wind speed, terrain slope and some structure-related fuel properties (specified in different fuel models). The NFDRS2016 equations also include an energy release term, which quantifies the heat per unit area released by the fire [163].

The moisture contents of dead fuels (DFMC) were obtained with the simple time-lag model developed by Mandel [168] based on the Van Wagner and Pickett equations [170] for the Canadian Fire Weather Index. This model considers a fuel particle that exchanges water with the environment depending on atmospheric conditions, with 2m temperature, total precipitation and relative humidity as input variables, and it was run hourly.

Live fuel moisture contents (LFMC) were calculated through the Growing Season Index [174], which considers daylength, vapor pressure deficit and minimum temperatures to predict foliar phenology. We tested the performance of this index by comparing the resulting moisture contents with some in-situ observations of live fuel moisture contents in Spain [256] (Supplementary Figure S4.1).

The Keetch-Byram Drought Index (KBDI) [257] is used to represent increased fuel availability as drought progresses [163]. This index considers daily total precipitation, daily maximum temperature and mean annual precipitation.

The fuel models used in this study are the 1988 and 2016 NFDRS fuel models [163]. These models are descriptions of different representative fuel types, in terms of morphologic characteristics (see Table S4.1 for a brief summary). For each wildfire, we obtain the rate of spread for each of the different fuel models. We also obtain a fuel-averaged ROS by first grouping the results into broader fuel categories (grass, grass/shrub, brush, timber litter and slash), and then averaging the results for these five categories.

Surface wind speed is directly obtained from climatological data, and the slope factor is neglected in this study, since it is not affected by climate change.

4.2.3 Attribution method

For each of the 1364 analysed wildfires we obtain one factual rate of spread obtained from ERA5 reanalysis climate data, and several counterfactual rates of spread. We analysed two counterfactual periods (pre-industrial and 2070-2099 SSP2-4.5) and two different components (the thermodynamic component of climate change and the vegetation growth component). We used five GCMs for analysing the thermodynamic component and eight GCMs for the vegetation component. Therefore, we compute 27 different rates of spread for each wildfire.

Counterfactual rates of spread for the thermodynamic component experiment are obtained by perturbing the thermodynamic variables of the factual ERA5 dataset. Ten perturbed climate datasets are needed: five representing pre-industrial conditions (one for each GCM) and five representing 2070-2099 conditions (according to the SSP2-4.5 scenario). Inspired by the pseudo-global-warming approach (Brogli 2023, Schar 1996), counterfactual datasets are

USC UNIVERSIDADE DE COMPOSTELA

obtained by perturbing the thermodynamic variables of the factual dataset according to the following expression:

$$X_{counterfactual} = X_{factual} + \left(X^{GCM}_{counterfactual} - X^{GCM}_{factual} \right) \tag{4.1}$$

Here, $X_{counterfactual}$ indicates a value of the counterfactual dataset for a given location and time, $X_{factual}$ is the corresponding value of the factual dataset (ERA5), $X^{GCM}_{counterfactual}$ is the corresponding monthly value averaged over the counterfactual period of each GCM and $X^{GCM}_{factual}$ is the corresponding monthly value averaged over a 30-year centred window in the historical period of each GCM. Since CMIP6 historical data extends up to 2014, we use the future scenario of intermediate emissions (SSP2-4.5) to cover the entire period we are analysing (2001-2021). The $\left(X^{GCM}_{counterfactual} - X^{GCM}_{factual} \right)$ anomaly, that was obtained from monthly data, is then interpolated in time to daily data.

Since we focus on the thermodynamic component of climate change, no dynamics-dependent variables such as surface wind speed or total precipitation are perturbed. We only perturb temperature-related variables (2m temperature, daily maximum temperature and daily minimum temperature and 2m dew point temperature).

From each climate dataset we first compute the dead and live fuel moisture content, DFMC and LFMC, together with the Keetch-Byram Drought Index KBDI. These are the three inputs to the ROS computation that are affected by the perturbation of the thermodynamic variables. Then we calculate the ROS of each wildfire event from factual and counterfactual data, obtaining a reference value corresponding to factual conditions, plus five values (one for each GCM) for pre-industrial conditions, and five values (again, one for each GCM) for 2070-2099 SSP2-4.5 conditions.

The vegetation growth component of the impact of climate change is quantified by simply perturbing the total fuel load of each fuel model. We first obtain a greening/browning factor by dividing the mean annual net primary production (NPP) of the counterfactual period by the mean annual NPP of the corresponding 30-year centred window in the historical period (extended with SSP2-4.5 data). We then multiply the total fuel amount of each fuel model by this factor. We assume that this addition or reduction of fuel load occurs while keeping the amount of fuel per volume (bulk density) constant, hence an idealized approach. This assumption implies that our results (when analysing the vegetation growth component) must be considered as a maximum potential change of the rate of spread.

We note that the calculation of the ROS is non-linear for all the components discussed above; therefore, the fully perturbed experiment, in which all variables are changed simultaneously (all thermodynamic variables in one case and vegetation growth related in another), does not yield a ROS that is the sum of the partial changes from each of the different contributions. Nevertheless, we can assess the relative importance of each variable toward the full change in ROS with the separation method.

USC UNIVERSIDADE DE SANTIAGO DE COMPOSTELA

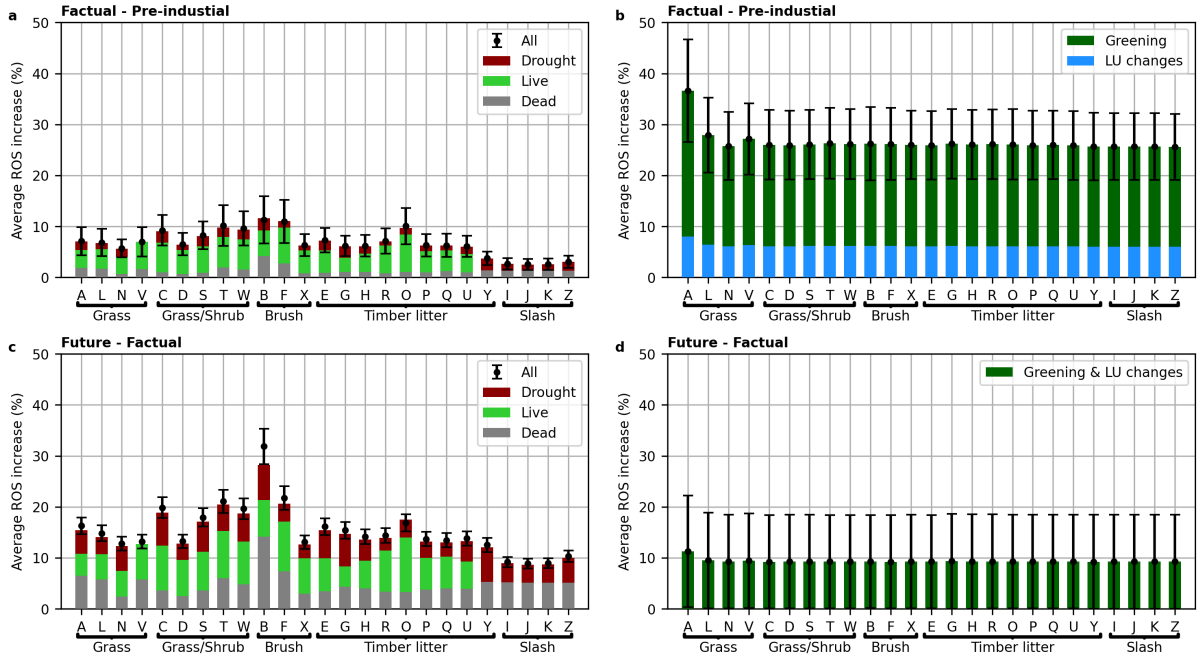


Figure 4.1: Average ROS increase by contribution. For each fuel model, average ROS increase of all wildfires with a burned area greater than 500 ha between 2001 and 2021 for the Iberian Peninsula, **a**, considering the thermodynamic component (divided into dead fuel, live fuel and fuel addition by drought factors) between pre-industrial and present conditions, **b** considering the vegetation growth component (divided into greening and land-use change factors) between pre-industrial and present conditions, **c** considering the thermodynamic component (divided into dead fuel, live fuel and fuel addition by drought factors) between present and 2070-2099 conditions (under SSP2-4.5 scenario) and **d** considering the vegetation growth component between present and 2070-2099 conditions (under SSP2-4.5 scenario). Black dots depict the mean values for changes obtained perturbing all factors simultaneously, and error bars indicate the standard deviation between different GCMs outputs. The corresponding ROS distributions are shown in Supplementary Figures S4.2 and S4.3.

4.3 Results and discussion

4.3.1 The role of the different factors

The average ROS of the 1364 analysed wildfires increases in a range from 2.6% to 11.3% by the thermodynamic component of climate change from pre-industrial conditions, depending on the fuel model considered (Figure 4.1a). Fuel structures consisting of live and dead fuels exhibit the largest increases, since differences in live fuel moisture show a more important influence than dead fuels or the fuel addition with drought (Figure 4.1a). Fuel load increases due to the greening effect and land use changes may have had an even stronger influence (25.6%-36.6%) from pre-industrial conditions (Figure 4.1b). If the analysed wildfires occurred under climate conditions corresponding to those projected by the SSP2-4.5 scenario for the end of the 21st century, the average ROS would augment by 8.9%-31.9% due to the direct (thermodynamic) effect of climate change (Figure 4.1c), which represents a larger increment than that between pre-industrial and present conditions. However, for the SSP2-4.5 future scenario the influence

of the vegetation growth component (Figure 4.1d) seems to be much more limited than its contribution to the speed up of the rate of spread between the pre-industrial and the present period (Figure 4.1b), and it is also smaller than the direct influence of the temperature increase (Figure 4.1c).

Tables S4.2 to S4.5 show the p-value of the null-hypothesis test when comparing the means of the different ROS distributions. For most fuel models and GCMs, a significant contribution of the thermodynamic component between pre-industrial and present conditions is obtained. Non-significant values are found exclusively for slash-type fuel models when considering the thermodynamic component between pre-industrial and present conditions, and for some other fuel models when using the EC-Earth3 GCM (Table S4.2). For the vegetation growth component between present and 2070-2099 conditions, three of eight fuel models show non-significant results (Table S4.5).

Considering the changes in the direct thermodynamic component, the ROS increase would be greater between the present and future conditions than between past and present conditions. This is in line with the fact that the projected temperature increase for the end of the century is also expected to overcome the actual temperature increase since pre-industrial conditions (Supplementary Figure S4.4). In contrast, the changes due to alterations in the vegetation growth component show an opposite pattern, since present-future ROS increases are less pronounced than past-present increases. This is due to the fact that vegetation greening is controlled by several factors like atmospheric CO2 fertilization, vegetation-related climatic factors (changes in temperature or precipitation that enhance vegetation growth), nitrogen deposition and land-use changes [248, 128], so the combined effect of these factors could lead to a nonlinear relation between vegetation greening and global warming. In fact, in semi-arid or low productive regions (like the south of the Iberian Peninsula), the combined effect of warming and precipitation reduction could enhance the water deficit and counterbalance the effect of CO2 fertilization in vegetation productivity [248, 128]. This could explain why the future influence of the vegetation component on the ROS increase is reduced compared to the past-present increase. Nevertheless, the vegetation growth component results present much uncertainty, both for the assumptions we have made in the methodology (we assume that the fuel load increase is proportional to the net primary production increase and that the fuel bulk density is not modified) and for the GCM discrepancies.

4.3.2 Spatial and temporal patterns

By analysing the wildfire events separately, a clear spatial pattern emerges for the thermodynamic component, with large differences in the ROS increase among events (Figure 4.2). Wildfires in the north of Portugal and the south of Galicia (hereinafter NW region) show the most significant increases of ROS both for the past-present and present-future comparisons, with up to 50% rate of spread increases (Figures 4.2a and 4.2c). This NW region is responsible for a large amount of burned area in Europe in recent decades [258], being one of the few regions in Mediterranean Europe that does not show a decreasing trend in burned area since 1980 [250].

To understand the causes behind this spatial pattern of the thermodynamic component, we calculated the expected ROS increase for all points in the domain and all days of the analysed period, regardless of whether a wildfire had taken place or not. A similar pattern arises in this comparison, with the north of Portugal and the south of Galicia displaying the

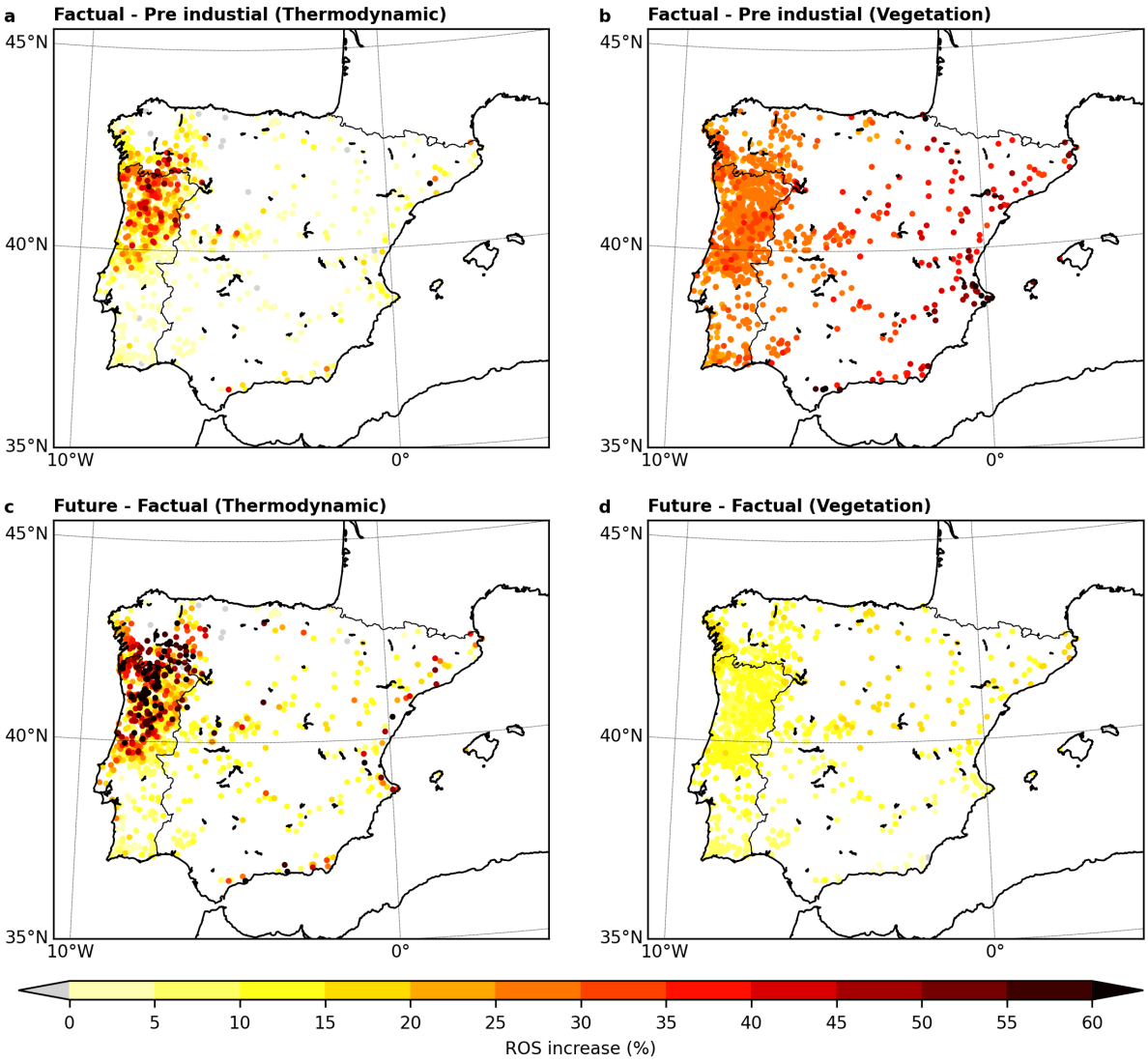


Figure 4.2: ROS increase by event. Fuel model-averaged ROS increase of each wildfire with a burned area greater than 500 ha between 2001 and 2021 for the Iberian Peninsula, **a** considering the thermodynamic component between pre-industrial and present conditions, **b** considering the vegetation growth component between pre-industrial and present conditions, **c** considering the thermodynamic component between present and 2070-2099 conditions (under SSP2-4.5 scenario) and **d** considering the vegetation growth component between present and 2070-2099 conditions (under SSP2-4.5 scenario).

most significant increases (Figure 4.3a). We split this thermodynamic component into the three different contributions considered in our methodology (dead fuel moisture, live fuel moisture and fuel addition by drought) in Supplementary Figures S4.5, S4.6 and S4.7, finding that the spatial distribution in Figure 4.3a develops from the combination of the spatiotemporal patterns of the three different contributions, with live fuels as the dominant factor (Supplementary Figure S4.6). In the NW region the three contributions are temporally synchronised, with the maximum partial ROS increase at the end of the summer (from August to October, see Supplementary Figures S4.5, S4.6 and S4.7), leading to an amplification of the total ROS increase during a time

of the year with high fire activity. In the south of the Iberian Peninsula the three contributions do not present their maximum ROS increases in the same months, mainly because the ROS growth due to the live fuel moisture contribution is nearly null during the summer (Supplementary Figure S4.6). Summers in the south of the Iberian Peninsula are very dry and hot, with vapor pressure deficits generally exceeding 4100 Pa (Supplementary Figure S4.8), a value that is sufficient to force complete stomatal closure [174] leading to a total curing of herbaceous live fuels and to minimum moisture content values of woody live fuels. Beyond this value, changes in vapor pressure deficit do not influence live fuel moisture anymore. In the south of the Iberian Peninsula the maximum ROS growth is thus found during autumn or spring months (Figure 4.3c). The ROS increase between present and SSP2-4.5 future conditions is much more pronounced and robust (Figure 4.4), and the region where the maximum ROS increase occurs during non-summer months is expected to expand north-ward (Figure 4.4c). The north-east of the Iberian Peninsula presents the most significant ROS increases for this period along with the NW region (Figure 4.4).

The vegetation growth component influence in ROS increase is much more spatially homogeneous (Figures 4.2b,d), with a spatial pattern that depends on the distribution of the net primary production increase (Supplementary Figure S4.9). However, our methodology presents an important constrain when analysing this vegetation component in fuel limited regions. Apart from increasing the fuel load, the increased vegetation growth could also enhance fuel continuity [249, 146] or modify fuel structures [148], and this could imply that vegetation growth influence in ROS increase could be underestimated in semi-arid regions where fire activity is more limited by fuel continuity [27].

4.3.3 Event-scale analysis

The direct influence of temperature increase in the wildfires' rate of spread (thermodynamic component) is very uneven among different events. We can determine the number of events in which climate change has significantly influenced the rate of spread by using a T-test for the null hypothesis that the factual ROS value of each wildfire is equal to the mean of the counterfactual ROS values (one value per GCM). Between 52.3% and 75.6% of the 1364 analysed wildfires (depending on the considered fuel model) have experienced a significant augmentation in the rate of spread due to the increase in temperature since the pre-industrial period (Table S4.6). Up to 2.5% of the wildfires have experienced a significant ROS decrease (Table S4.6). These decreases are associated with the rise of the minimum temperature at the end of winter (Figure 4.3e), which can enhance photosynthesis and anticipate the start of the vegetation growing season, leading to enhanced live fuel moisture. For the remaining events (between 24.4% and 45.0%), the thermodynamic influence of climate change on the rate of spread is non-significant when comparing present against pre-industrial conditions. When using the 2070-2099 SSP2-4.5 conditions as counterfactual data instead of those of the pre-industrial period, the number of events that undergo a significant ROS increase is much higher (above 85%), with less than 13% of the events showing a non-significant result (Table S4.7).

4.3.4 Energy released to the atmosphere

In an analogous way to the rate of spread, the heat per unit area that a wildfire releases to the atmosphere is also influenced by fuel dryness and fuel load changes. The magnitude of the

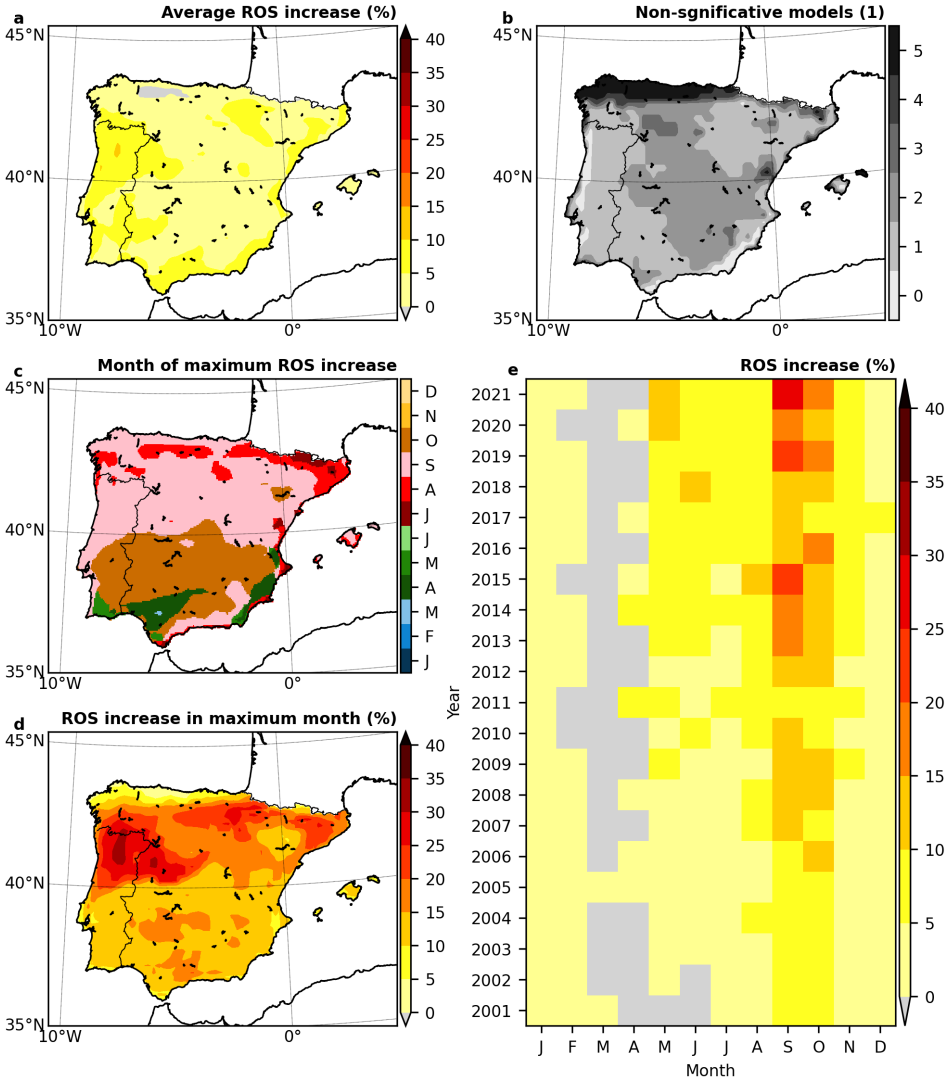


Figure 4.3: Expected ROS increase between pre-industrial and present conditions for all-points. Considering the thermodynamic component between pre-industrial and present conditions, **a** mean annual ROS increase, **b** number of non-significant (p-value>0.05) model outputs for the mean annual ROS increase, **c** month of the year with the largest ROS increase, **d** average ROS increase during the month with the largest ROS increase and **e** average ROS increase by year and month of the year.

energy release increase is similar to that of the rate of spread when considering the vegetation growth component, both for the present-past (25.7%-26.2%) and for the future-present (9.3%) comparison (Supplementary Figure S4.10). The average energy released by the 1364 analysed wildfires has been increased by 3.5% to 10.8% by the thermodynamic component of climate change from pre-industrial conditions (Supplementary Figure S4.10), a similar range of values than that of the rate of spread increase (Figure 4.1a). However, dead fuel moisture changes became the main contribution in the energy release results, since heavier fuels (100-hour and 1000-hour time-lag fuels) play a more important role in the calculation of the energy released [163]. A greater amount of heat released per unit area means that wildfires have a greater

capacity to modify atmospheric conditions, which favours atmosphere-fire coupling processes such as pyroconvection.

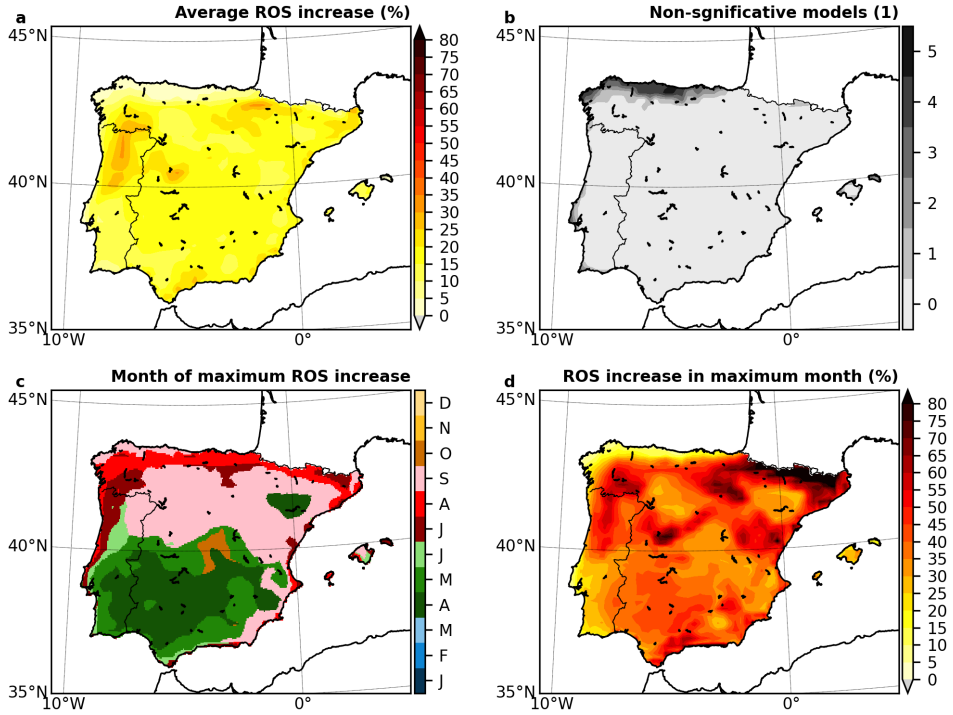


Figure 4.4: Expected ROS increase between pre-industrial and present conditions for all-points. Considering the thermodynamic component between pre-industrial and present conditions, **a** mean annual ROS increase, **b** number of non-significant (p-value>0.05) model outputs for the mean annual ROS increase, **c** month of the year with the largest ROS increase, **d** average ROS increase during the month with the largest ROS increase and **e** average ROS increase by year and month of the year.

4.4 Conclusions

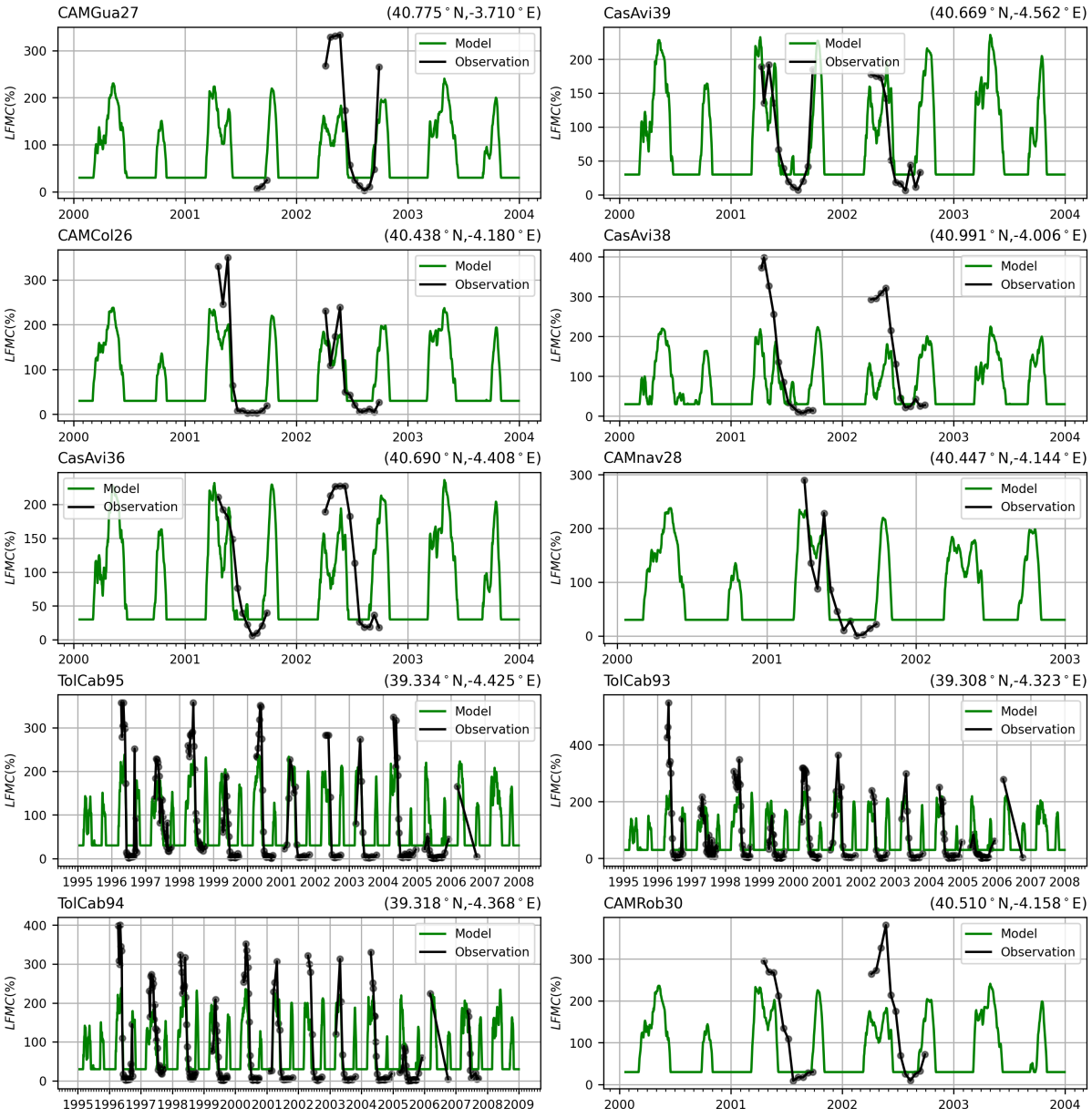
We find that the current rate of spread of wildfires in the present 2001-2021 period in the Iberian Peninsula has increased since pre-industrial times in between 2.6% and 11.3% on average due to the influence of climate change on temperature. This growth in the rate of spread is significant in more than 50% of the events. The most sensitive region to these ROS increases is the north of Portugal and the south of Galicia, which is in fact the region with the highest fire activity at present. These changes have a very uneven spatial and temporal distribution, determined by how the different factors conditioning the rate of spread react to the temperature increase at each time of the year and each location. Further ROS increases (8.9%-31.9%) are expected by the end of the 21st century according to an intermediate-emissions scenario (SSP2-4.5). We find similar increases for the heat per unit area released by wildfires, implying that the fire-atmosphere coupling may be intensifying.

Climate change also modifies vegetation growth, and in examining how this alteration influences the ROS of wildfires, we encounter that it may have had an even greater intensifying

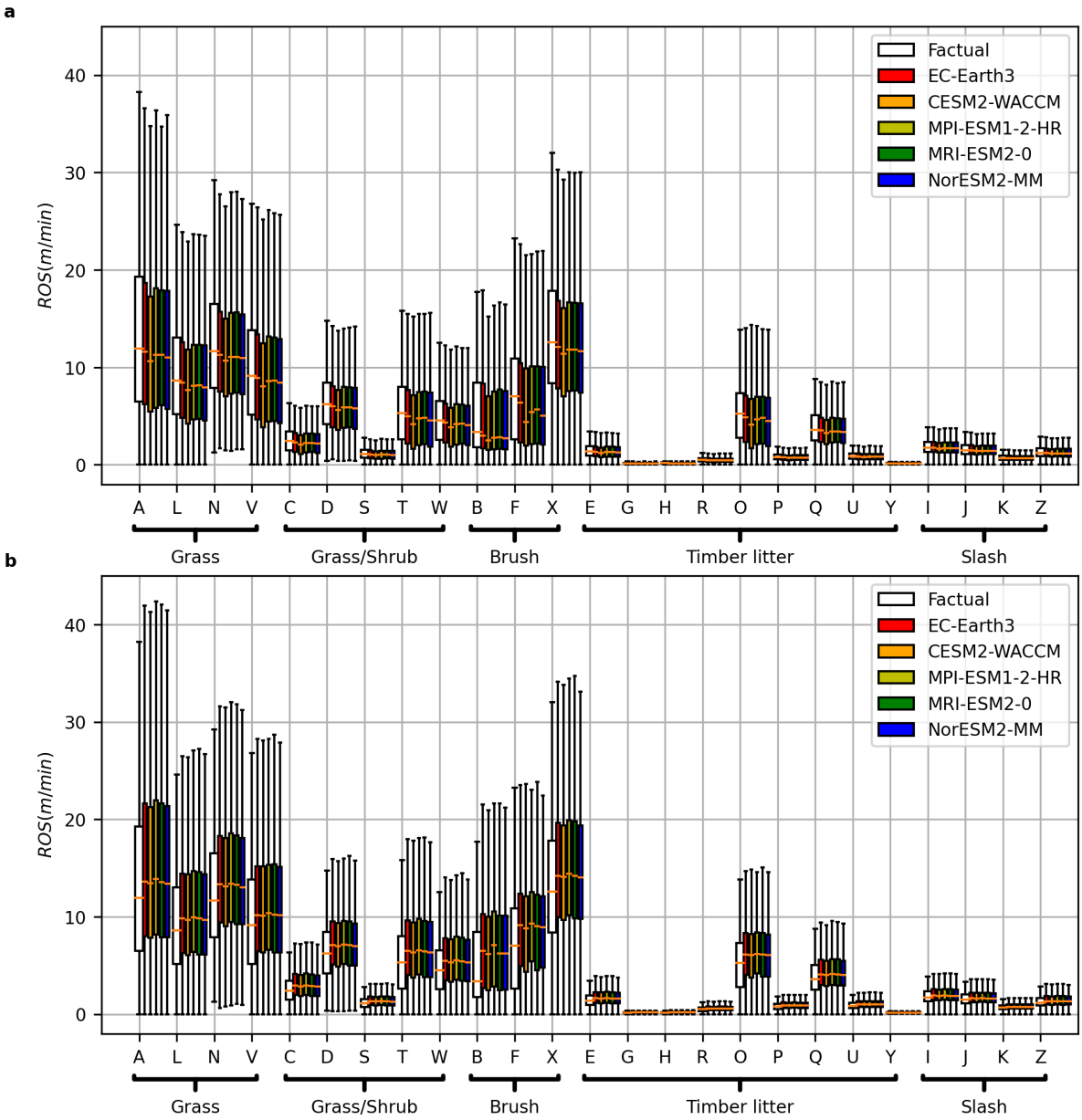
effect than that of temperature since the pre-industrial period. However, our results indicate that ROS increases in the in the future will be mainly driven by the projected temperature rise, rather than by the enhanced vegetation growth.

USC
UNIVERSIDADE DE SANTIAGO DE COMPOSTELA

Supplementary Figures

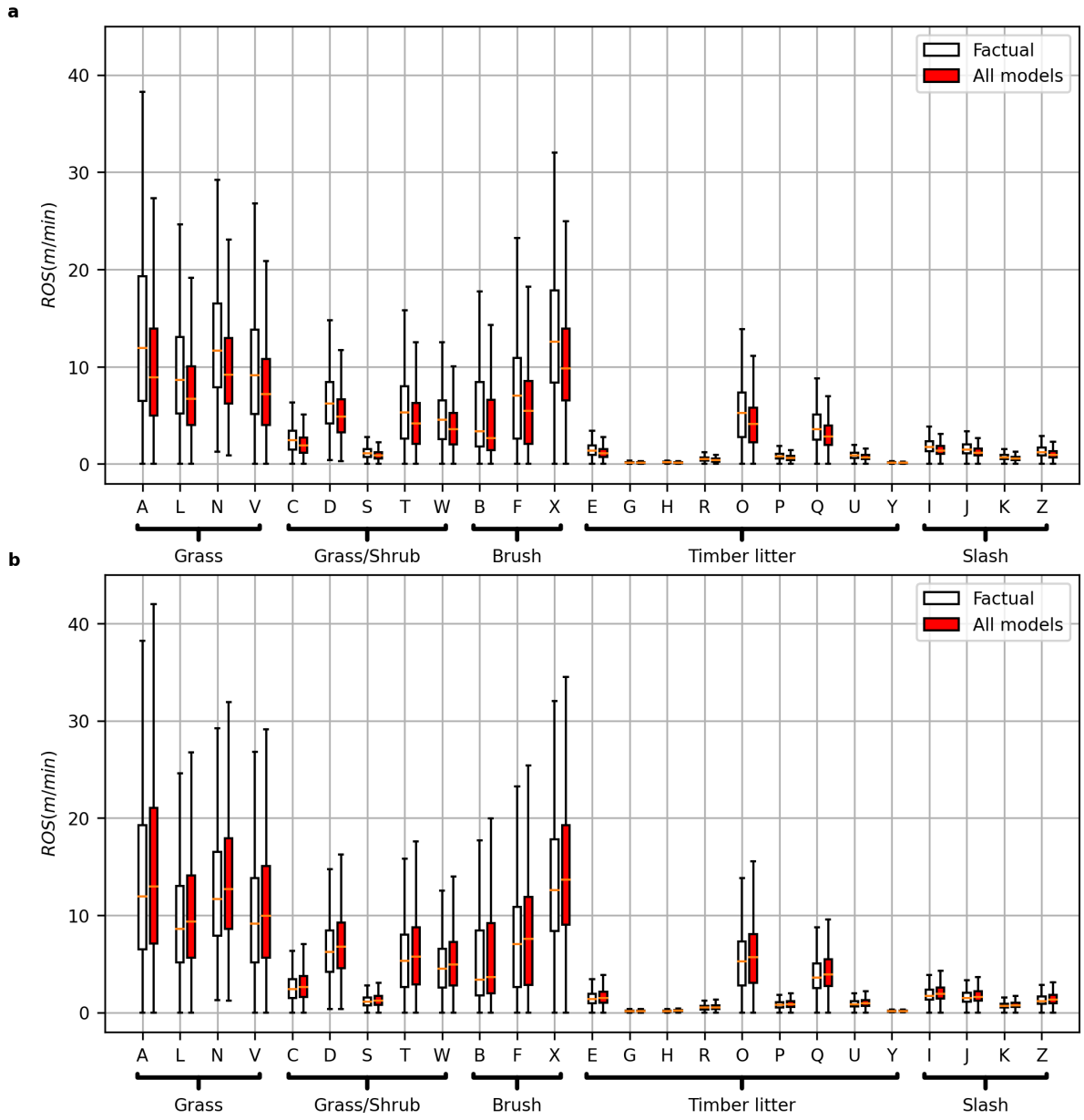


Supplementary Figure S4.1: Comparison of modelled (green) and observed (black) herbaceous live fuel moistures. Observed data is obtained from Yebra et al. (2019) [256], using all the available stations in the Iberian Peninsula with more than 10 observations of grass type species.



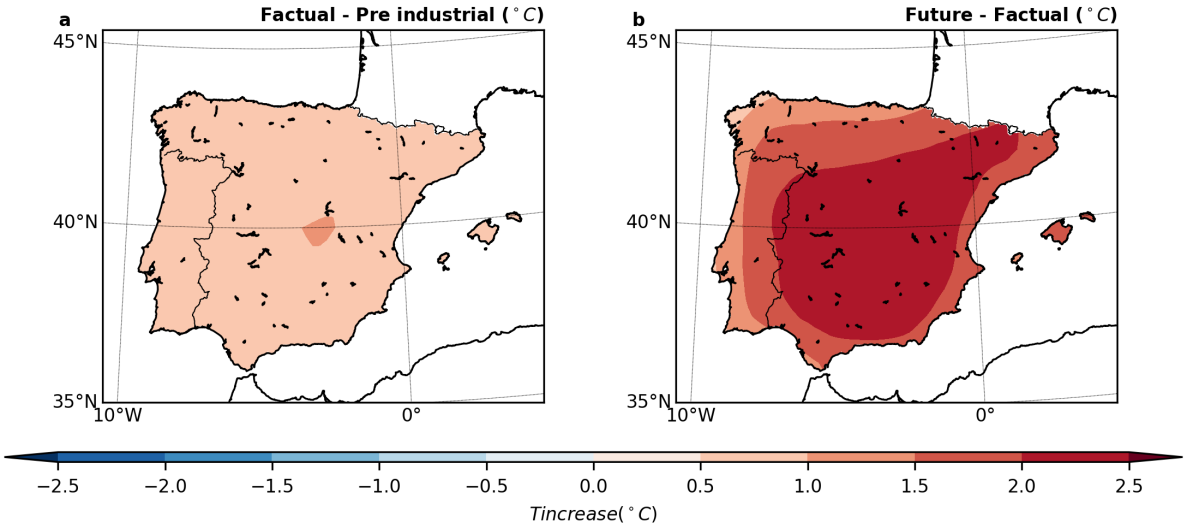
Supplementary Figure S4.2: For each fuel model, boxplot representation of the ROS distribution of all wildfires with a burned area greater than 500 ha between 2001 and 2021 for the Iberian Peninsula. White boxplots represent factual data (obtained from ERA5) and coloured boxplots represent the thermodynamic component counterfactual data for **a** pre-industrial conditions and **b** 2070-2099 conditions (under SSP2-4.5 scenario). Different colours indicate different GCM outputs.

USC UNIVERSIDADE DE SANTIAGO DE COMPOSTELA



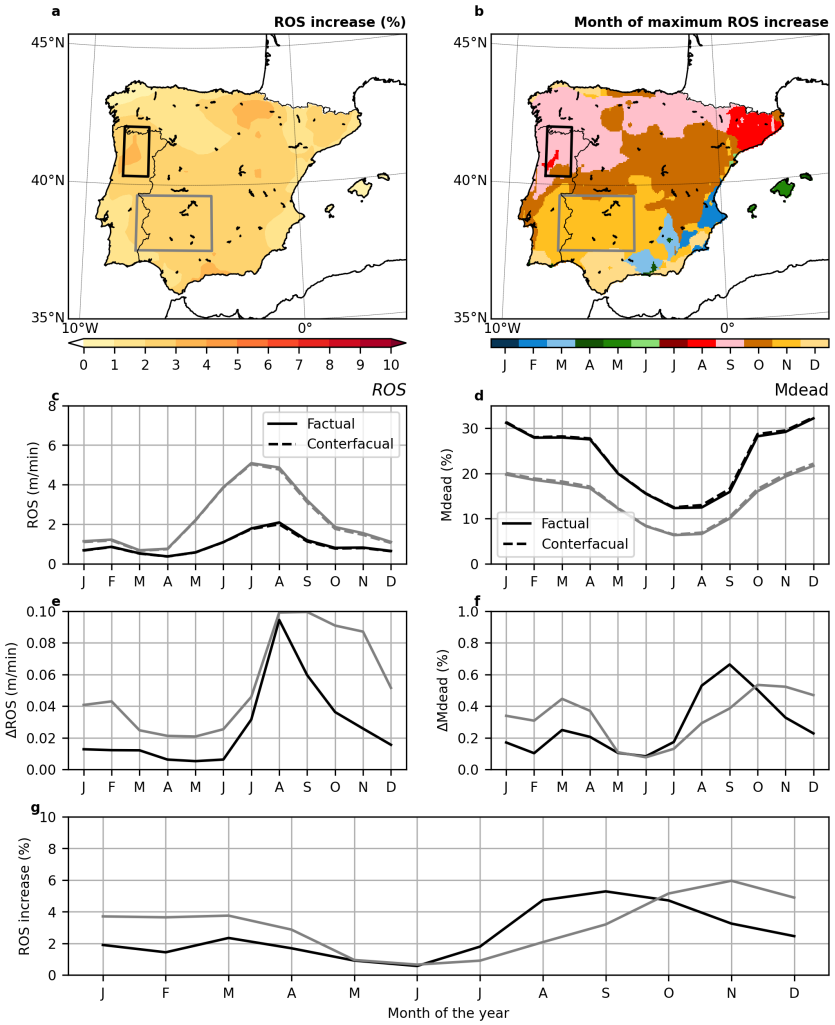
Supplementary Figure S4.3: For each fuel model, boxplot representation of the ROS distribution of all wildfires with a burned area greater than 500 ha between 2001 and 2021 for the Iberian Peninsula. White boxplots represent factual data (obtained from ERA5) and red boxplots represent the vegetation growth component counterfactual data for **a** pre-industrial conditions and **b** 2070-2099 conditions (under SSP2-4.5 scenario).

USC
UNIVERSIDADE DE SANTIAGO DE COMPOSTELA

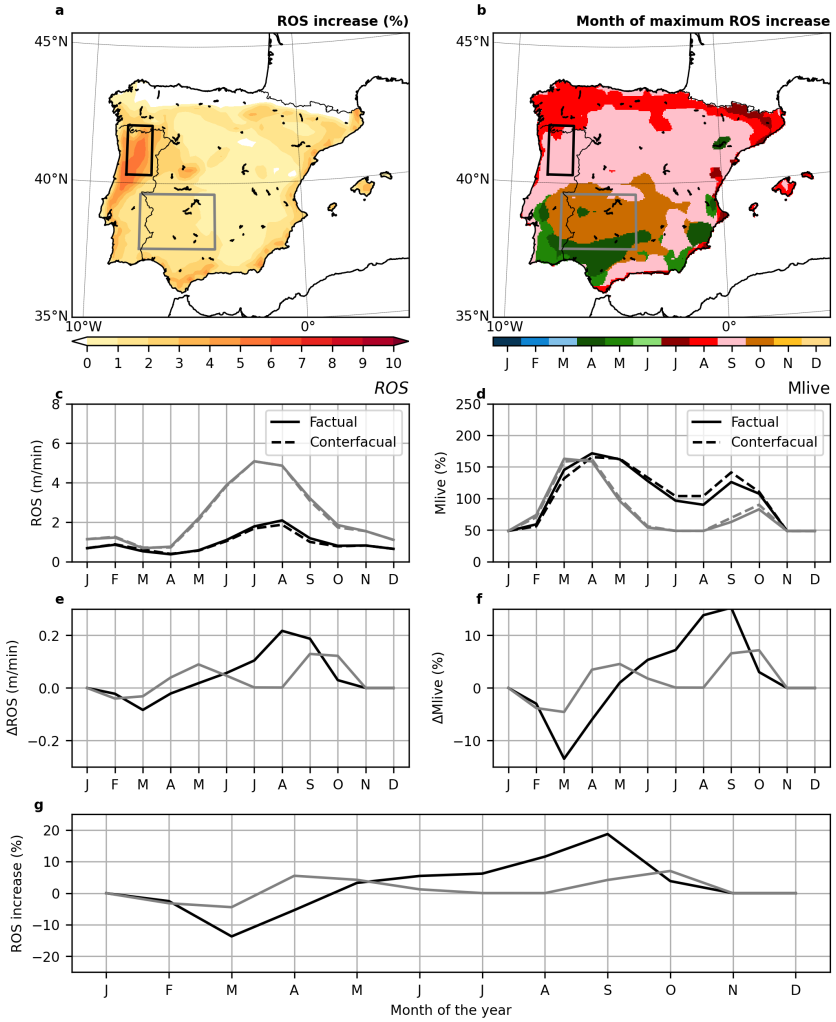


Supplementary Figure S4.4: Mean annual temperature increase between **a** pre-industrial and present conditions and between **b** 2070-2099 conditions (under SSP2-4.5 scenario) and present, averaged for all models (MPI-ESM1-2-HR, EC-Earth3, CESM2-WACCM, MRI-ESM2-0 and NorESM2-MM).

USC UNIVERSIDADE DE SANTIAGO DE COMPOSTELA

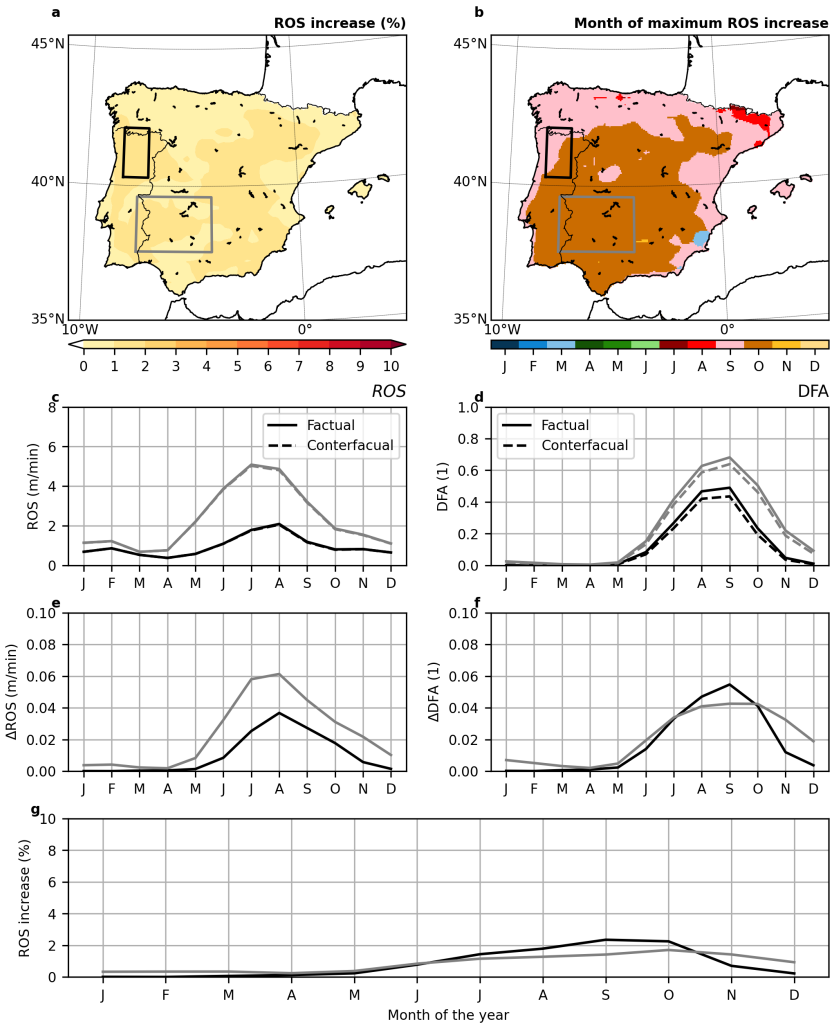


Supplementary Figure S4.5: Considering only the contribution of dead fuel moisture in the thermodynamic component between pre-industrial and present conditions, **a** mean annual ROS increase and **b** month of the year with the largest ROS increase. For the grey and black rectangles displayed in the two maps, **c** average ROS values by month of the year, **d** average dead fuel moisture values by month of the year, **e** average ROS difference by month of the year (with positive values indicating a ROS increase from pre-industrial to present conditions), **f** average dead fuel moisture difference by month of the year (with positive values indicating a fuel dryness increase from pre-industrial to present conditions), and **g** average ROS increase by month of the year. Black (grey) lines in **c**, **d**, **e**, **f** and **g** correspond to black (grey) rectangles in **a** and **b**.



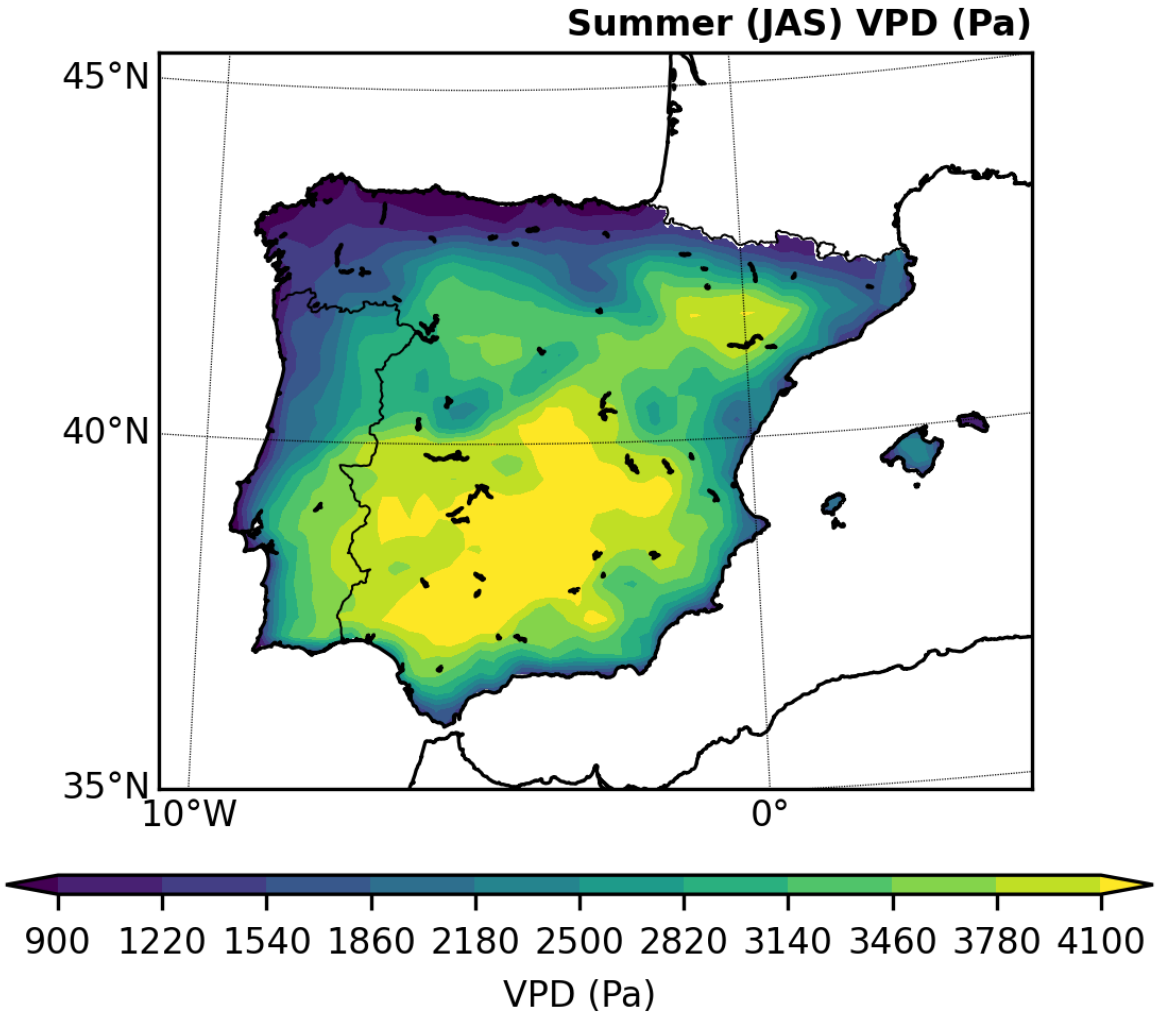
Supplementary Figure S4.6: Considering only the contribution of live fuel moisture in the thermodynamic component between pre-industrial and present conditions, **a** mean annual ROS increase and **b** month of the year with the largest ROS increase. For the grey and black rectangles displayed in the two maps, **c** average ROS values by month of the year, **d** average live fuel moisture values by month of the year, **e** average ROS difference by month of the year (with positive values indicating a ROS increase from pre-industrial to present conditions), **f** average live fuel moisture difference by month of the year (with positive values indicating a fuel dryness increase from pre-industrial to present conditions), and **g** average ROS increase by month of the year. Black (grey) lines in **c**, **d**, **e**, **f** and **g** correspond to black (grey) rectangles in **a** and **b**.

USC
UNIVERSIDADE DE SANTIAGO DE COMPOSTELA



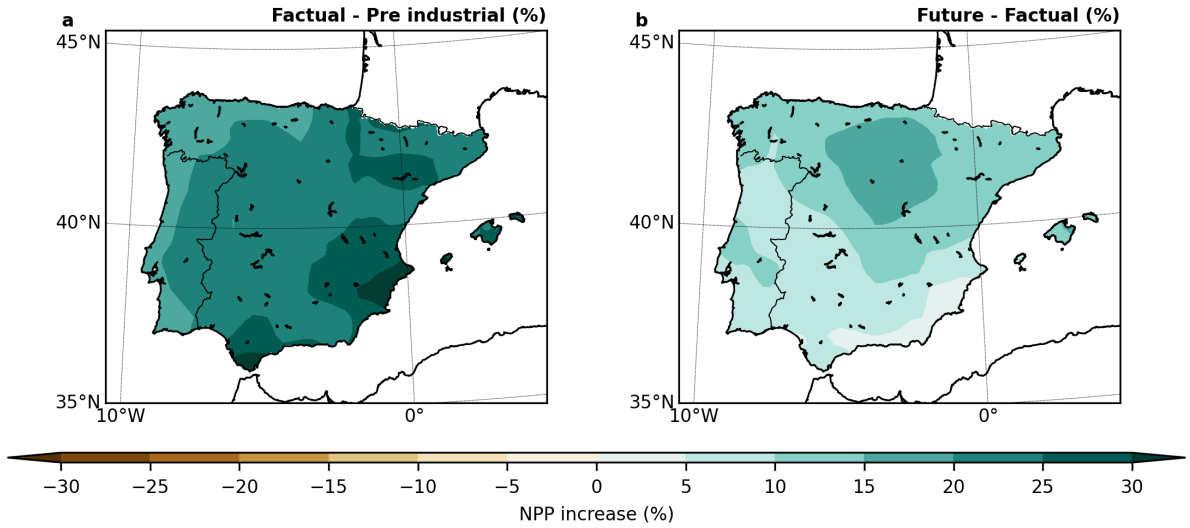
Supplementary Figure S4.7: Considering only the contribution of drought fuel addition in the thermodynamic component between pre-industrial and present conditions, **a** mean annual ROS increase and **b** month of the year with the largest ROS increase. For the grey and black rectangles displayed in the two maps, **c** average ROS values by month of the year, **d** average drought factor (values between 0 and 1 with 0 indicating no-drought conditions) by month of the year, **e** average ROS difference by month of the year (with positive values indicating a ROS increase from pre-industrial to present conditions), **f** average drought factor difference by month of the year (with positive values indicating drought intensification from pre-industrial to present conditions), and **g** average ROS increase by month of the year. Black (grey) lines in **c**, **d**, **e**, **f** and **g** correspond to black (grey) rectangles in **a** and **b**.

USC
UNIVERSIDADE DE SANTIAGO DE COMPOSTELA



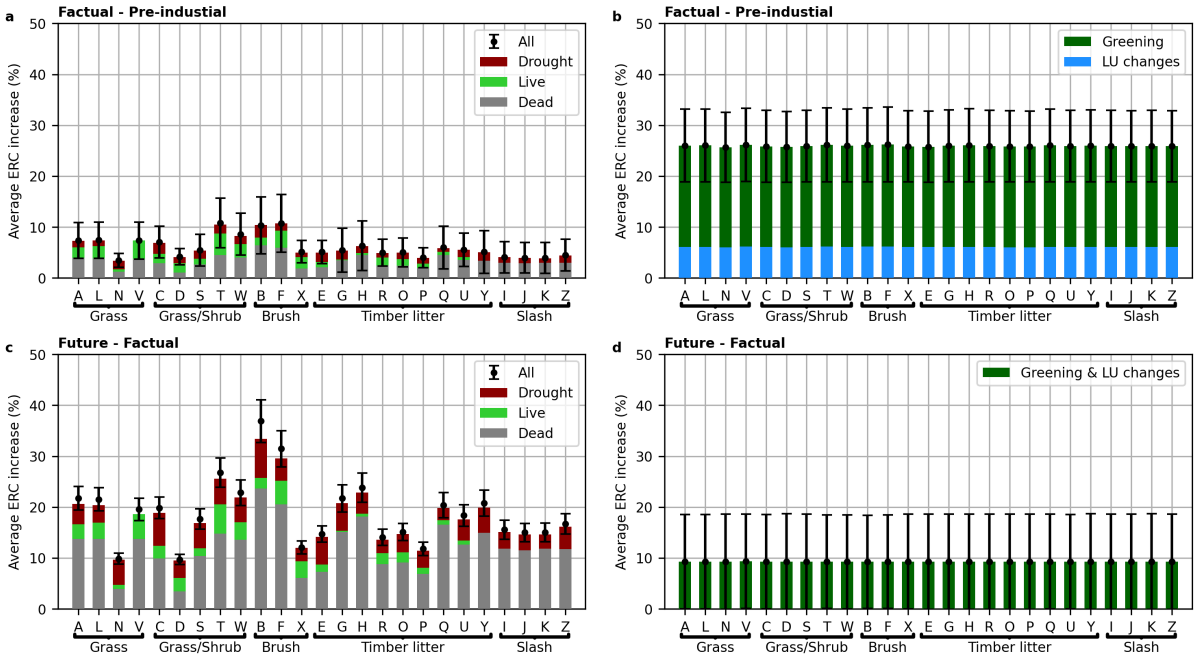
Supplementary Figure S4.8: Multi-year (2001-2021) summer (July-August-September) average of the daily maximum vapor pressure deficit (VPD).

USC UNIVERSIDADE DE SANTIAGO DE COMPOSTELA



Supplementary Figure S4.9: Mean annual net primary productivity increase between **a** pre-industrial and present conditions and between (**b** 2070-2099 conditions (under SSP2-4.5 scenario) and present, averaged for all models (ACCESS-ESM1-5, BCC-CSM2-MR, CMCC-ESM2, CanESM5, EC-Earth3-Veg, IPSL-CM6A-LR, MPI-ESM1-2-LR and NorESM2-LM).

USC
UNIVERSIDADE DE SANTIAGO DE COMPOSTELA



Supplementary Figure S4.10: Average energy released increase by contribution. For each fuel model, average Energy Release Component (ERC) increase of all wildfires with a burned area greater than 500 ha between 2001 and 2021 for the Iberian Peninsula, **a** considering the thermodynamic component (divided in dead fuels, live fuel and de drought addition factor) between pre-industrial and present conditions, **b** considering the vegetation growth component (divided in greening and land-use changes) between pre-industrial and present conditions, **c** considering the thermodynamic component (divided in dead fuels, live fuel and de drought addition factor) between present and 2070-2099 conditions (under SSP2-4.5 scenario) and **d** considering the vegetation growth component between present and 2070-2099 conditions (under SSP2-4.5 scenario). Error bars indicate the standard deviation between different GCMs outputs. The corresponding ROS distributions are shown in Supplementary Figures S4.2 and S4.3.

USC
UNIVERSIDADE DE SANTIAGO DE COMPOSTELA

Supplementary Tables

Supplementary Table S4.1: Fuel model descriptions

Fuel		Description
Grass	A	Western grasses annual
	L	Western grasses perennial
	N	Sawgrass
	V	Grass
Grass/Shrub	C	Pine-grass savanna
	D	Southern rough
	S	Tundra
	T	Sagebrush-grass
	W	Grass-shrub
Brush	B	California chaparral
	F	Intermediate brush
	X	Brush
Timber litter	E	Hardwood litter (winter)
	G	Short needle (heavy dead)
	H	Short needle (normal dead)
	R	Hardwood litter (summer)
	O	High pocosin
	P	Southern pine plantation
	Q	Alaskan black spruce
	U	Western pines
	Y	Timber litter
Slash	I	Heavy slash
	J	Intermediate slash
	K	Light slash
	Z	Slash

USC UNIVERSIDADE DE SANTIAGO DE COMPOSTELA

Supplementary Table S4.2: T-test p-values for the comparison between factual and the thermodynamic component pre-industrial ROS samples of all wildfires with a burned area greater than 500 ha between 2001 and 2021 for the Iberian Peninsula. The null hypothesis is that the 2 samples (factual and counterfactual) have identical average values. Shaded cells indicate non-significant values (p-value>0.05).

Fuel		EC-Earth3	CESM2-WACCM	MPI-ESM1-2-HR	MRI-ESM2-0	NorESM2-MM
Grass	A	0.25	0.00	0.02	0.03	0.01
	L	0.20	0.00	0.02	0.02	0.00
	N	0.07	0.00	0.01	0.01	0.00
	V	0.25	0.00	0.03	0.04	0.00
Grass/ Shrub	C	0.02	0.00	0.00	0.00	0.00
	D	0.05	0.00	0.00	0.01	0.00
	S	0.02	0.00	0.00	0.00	0.00
	T	0.09	0.00	0.00	0.00	0.00
	W	0.04	0.00	0.00	0.00	0.00
Brush	B	0.23	0.00	0.00	0.00	0.00
	F	0.07	0.00	0.00	0.00	0.00
	X	0.09	0.00	0.01	0.02	0.00
Timber litter	E	0.04	0.00	0.00	0.00	0.00
	G	0.04	0.00	0.00	0.00	0.00
	H	0.05	0.00	0.00	0.00	0.00
	R	0.05	0.00	0.00	0.00	0.00
	O	0.02	0.00	0.00	0.00	0.00
	P	0.07	0.00	0.00	0.01	0.00
	Q	0.13	0.00	0.01	0.02	0.00
	U	0.07	0.00	0.00	0.01	0.00
	Y	0.25	0.00	0.00	0.01	0.01
Slash	I	0.66	0.01	0.09	0.12	0.10
	J	0.69	0.02	0.10	0.14	0.11
	K	0.69	0.02	0.11	0.14	0.11
	Z	0.57	0.01	0.09	0.13	0.10

USC UNIVERSIDADE DE SANTIAGO DE COMPOSTELA

Supplementary Table S4.3: T-test p-values for the comparison between factual and the thermodynamic component future (2070-2099 according to SSP2-4.5) ROS samples of all wildfires with a burned area greater than 500 ha between 2001 and 2021 for the Iberian Peninsula. The null hypothesis is that the 2 samples (factual and counterfactual) have identical average values. Shaded cells indicate non-significant values (p-value>0.05).

Fuel		EC-Earth3	CESM2-WACCM	MPI-ESM1-2-HR	MRI-ESM2-0	NorESM2-MM
Grass	A	0.00	0.00	0.00	0.00	0.00
	L	0.00	0.00	0.00	0.00	0.00
	N	0.00	0.00	0.00	0.00	0.00
	V	0.00	0.00	0.00	0.00	0.00
Grass/ Shrub	C	0.00	0.00	0.00	0.00	0.00
	D	0.00	0.00	0.00	0.00	0.00
	S	0.00	0.00	0.00	0.00	0.00
	T	0.00	0.00	0.00	0.00	0.00
	W	0.00	0.00	0.00	0.00	0.00
Brush	B	0.00	0.00	0.00	0.00	0.00
	F	0.00	0.00	0.00	0.00	0.00
	X	0.00	0.00	0.00	0.00	0.00
Timber litter	E	0.00	0.00	0.00	0.00	0.00
	G	0.00	0.00	0.00	0.00	0.00
	H	0.00	0.00	0.00	0.00	0.00
	R	0.00	0.00	0.00	0.00	0.00
	O	0.00	0.00	0.00	0.00	0.00
	P	0.00	0.00	0.00	0.00	0.00
	Q	0.00	0.00	0.00	0.00	0.00
	U	0.00	0.00	0.00	0.00	0.00
	Y	0.00	0.00	0.00	0.00	0.00
Slash	I	0.00	0.00	0.00	0.00	0.00
	J	0.00	0.00	0.00	0.00	0.00
	K	0.00	0.00	0.00	0.00	0.00
	Z	0.00	0.00	0.00	0.00	0.00

USC UNIVERSIDADE DE SANTIAGO DE COMPOSTELA

Supplementary Table S4.4: T-test p-values for the comparison between factual and the vegetation growth component future (2070-2099 according to SSP2-4.5) ROS samples of all wildfires with a burned area greater than 500 ha between 2001 and 2021 for the Iberian Peninsula. The null hypothesis is that the 2 samples (factual and counterfactual) have identical average values. Shaded cells indicate non-significant values (p-value>0.05).

Fuel		ACCESS-ESM1-5	BCC-CSM2-MR	CMCC-ESM2	CanESM5
Grass	A	0.00	0.00	0.00	0.00
	L	0.00	0.00	0.00	0.00
	N	0.00	0.00	0.00	0.00
	V	0.00	0.00	0.00	0.00
Grass/ Shrub	C	0.00	0.00	0.00	0.00
	D	0.00	0.00	0.00	0.00
	S	0.00	0.00	0.00	0.00
	T	0.00	0.00	0.00	0.00
	W	0.00	0.00	0.00	0.00
Brush	B	0.00	0.00	0.00	0.00
	F	0.00	0.00	0.00	0.00
	X	0.00	0.00	0.00	0.00
Timber litter	E	0.00	0.00	0.00	0.00
	G	0.00	0.00	0.00	0.00
	H	0.00	0.00	0.00	0.00
	R	0.00	0.00	0.00	0.00
	O	0.00	0.00	0.00	0.00
	P	0.00	0.00	0.00	0.00
	Q	0.00	0.00	0.00	0.00
	U	0.00	0.00	0.00	0.00
	Y	0.00	0.00	0.00	0.00
Slash	I	0.00	0.00	0.00	0.00
	J	0.00	0.00	0.00	0.00
	K	0.00	0.00	0.00	0.00
	Z	0.00	0.00	0.00	0.00

USC UNIVERSIDADE DE SANTIAGO DE COMPOSTELA

Supplementary Table S4.4: Continued.

Fuel		EC-Earth3-Veg	IPSL-CM6A-LR	MPI-ESM1-2-LR	NorESM2-LM
Grass	A	0.00	0.00	0.00	0.00
	L	0.00	0.00	0.00	0.00
	N	0.00	0.00	0.00	0.00
	V	0.00	0.00	0.00	0.00
Grass/ Shrub	C	0.00	0.00	0.00	0.00
	D	0.00	0.00	0.00	0.00
	S	0.00	0.00	0.00	0.00
	T	0.00	0.00	0.00	0.00
	W	0.00	0.00	0.00	0.00
Brush	B	0.00	0.00	0.00	0.00
	F	0.00	0.00	0.00	0.00
	X	0.00	0.00	0.00	0.00
Timber litter	E	0.00	0.00	0.00	0.00
	G	0.00	0.00	0.00	0.00
	H	0.00	0.00	0.00	0.00
	R	0.00	0.00	0.00	0.00
	O	0.00	0.00	0.00	0.00
	P	0.00	0.00	0.00	0.00
	Q	0.00	0.00	0.00	0.00
	U	0.00	0.00	0.00	0.00
	Y	0.00	0.00	0.00	0.00
Slash	I	0.00	0.00	0.00	0.00
	J	0.00	0.00	0.00	0.00
	K	0.00	0.00	0.00	0.00
	Z	0.00	0.00	0.00	0.00

USC UNIVERSIDADE DE SANTIAGO DE COMPOSTELA

Supplementary Table S4.5: T-test p-values for the comparison between factual and the vegetation growth component future (2070-2099 according to SSP2-4.5) ROS samples of all wildfires with a burned area greater than 500 ha between 2001 and 2021 for the Iberian Peninsula. The null hypothesis is that the 2 samples (factual and counterfactual) have identical average values. Shaded cells indicate non-significant values (p-value>0.05).

Fuel		ACCESS-ESM1-5	BCC-CSM2-MR	CMCC-ESM2	CanESM5
Grass	A	0.54	0.00	0.00	0.00
	L	0.60	0.00	0.00	0.00
	N	0.52	0.00	0.00	0.00
	V	0.62	0.00	0.01	0.00
Grass/ Shrub	C	0.59	0.00	0.00	0.00
	D	0.54	0.00	0.00	0.00
	S	0.56	0.00	0.00	0.00
	T	0.65	0.01	0.01	0.00
	W	0.62	0.00	0.00	0.00
Brush	B	0.68	0.02	0.03	0.00
	F	0.65	0.01	0.01	0.00
	X	0.57	0.00	0.00	0.00
Timber litter	E	0.55	0.00	0.00	0.00
	G	0.44	0.00	0.00	0.00
	H	0.49	0.00	0.00	0.00
	R	0.55	0.00	0.00	0.00
	O	0.61	0.00	0.00	0.00
	P	0.52	0.00	0.00	0.00
	Q	0.56	0.00	0.00	0.00
	U	0.50	0.00	0.00	0.00
	Y	0.40	0.00	0.00	0.00
Slash	I	0.46	0.00	0.00	0.00
	J	0.46	0.00	0.00	0.00
	K	0.47	0.00	0.00	0.00
	Z	0.51	0.00	0.00	0.00

USC UNIVERSIDADE DE SANTIAGO DE COMPOSTELA

Supplementary Table S4.5: Continued.

Fuel		EC-Earth3-Veg	IPSL-CM6A-LR	MPI-ESM1-2-LR	NorESM2-LM
Grass	A	0.00	0.20	0.53	0.00
	L	0.00	0.20	0.56	0.00
	N	0.00	0.06	0.35	0.00
	V	0.00	0.28	0.69	0.00
Grass/ Shrub	C	0.00	0.16	0.54	0.00
	D	0.00	0.07	0.42	0.00
	S	0.00	0.10	0.46	0.00
	T	0.00	0.29	0.68	0.00
	W	0.00	0.22	0.62	0.00
Brush	B	0.00	0.47	0.83	0.00
	F	0.00	0.30	0.72	0.00
	X	0.00	0.11	0.49	0.00
Timber litter	E	0.00	0.09	0.44	0.00
	G	0.00	0.02	0.26	0.00
	H	0.00	0.04	0.33	0.00
	R	0.00	0.09	0.48	0.00
	O	0.00	0.18	0.61	0.00
	P	0.00	0.06	0.41	0.00
	Q	0.00	0.12	0.49	0.00
	U	0.00	0.05	0.36	0.00
	Y	0.00	0.01	0.13	0.00
Slash	I	0.00	0.03	0.22	0.00
	J	0.00	0.03	0.23	0.00
	K	0.00	0.03	0.24	0.00
	Z	0.00	0.05	0.28	0.00

USC UNIVERSIDADE DE SANTIAGO DE COMPOSTELA

Supplementary Table S4.6: Percentage of total number of wildfire events where a significant increase, a significant decrease or a non-significant change in the rate of spread was found. The statistical significance is based on the p-value (p-value>0.05) of a T-test for the null hypothesis that the mean of the counterfactual ROS sample (using different GCMs) is equal to the factual ROS. The counterfactual sample corresponds to the thermodynamic component of the comparison between the present and the pre-industrial conditions.

Fuel		Significant (%)	Significant increase (%)	Significant decrease (%)	Non-significant (%)
Grass	A	64.54	63.30	1.25	32.75
	L	62.93	61.68	1.25	34.36
	N	75.60	73.41	2.20	24.40
	V	52.31	50.92	1.39	44.98
Grass/ Shrub	C	74.07	71.65	2.42	25.71
	D	72.01	69.52	2.49	27.99
	S	74.21	71.79	2.42	25.71
	T	66.67	65.49	1.17	30.62
	W	68.86	67.62	1.25	28.28
Brush	B	62.12	61.03	1.10	34.87
	F	61.98	60.88	1.10	35.02
	X	69.67	67.25	2.42	30.26
Timber litter	E	74.29	71.87	2.42	25.64
	G	73.92	71.72	2.20	26.01
	H	71.06	69.16	1.90	28.72
	R	67.91	65.42	2.49	32.01
	O	69.67	67.40	2.27	30.26
	P	69.52	67.03	2.49	30.40
	Q	65.93	64.10	1.83	33.19
	U	70.77	68.86	1.90	29.01
	Y	70.62	70.62	0.00	29.30
Slash	I	65.42	65.42	0.00	34.51
	J	64.84	64.84	0.00	35.09
	K	64.98	64.98	0.00	34.95
	Z	68.06	68.06	0.00	31.87

USC UNIVERSIDADE DE SANTIAGO DE COMPOSTELA

Supplementary Table S4.7: Percentage of total number of wildfire events where a significant increase, a significant decrease or a non-significant change in the rate of spread was found. The statistical significance is based on the p-value (p-value>0.05) of a T-test for the null hypothesis that the mean of the counterfactual ROS sample (using different GCMs) is equal to the factual ROS. The counterfactual sample corresponds to the thermodynamic component of the comparison between the present and the 2070-2099 SSP2-4.5 conditions.

Fuel		Significant (%)	Significant increase (%)	Significant decrease (%)	Non-significant (%)
Grass	A	93.77	92.89	0.88	6.23
	L	93.19	92.31	0.88	6.81
	N	97.22	95.53	1.68	2.78
	V	90.62	89.52	1.10	9.38
Grass/ Shrub	C	96.63	94.95	1.68	3.37
	D	96.85	95.02	1.83	3.15
	S	97.29	95.53	1.76	2.71
	T	92.09	91.21	0.88	7.91
	W	93.48	92.60	0.88	6.52
Brush	B	87.33	86.59	0.73	12.67
	F	90.40	89.52	0.88	9.60
	X	95.97	94.21	1.76	4.03
Timber litter	E	97.22	95.46	1.76	2.78
	G	97.58	95.90	1.68	2.42
	H	96.48	95.09	1.39	3.52
	R	96.04	94.21	1.83	3.96
	O	93.63	91.87	1.76	6.37
	P	96.48	94.65	1.83	3.52
	Q	94.58	93.41	1.17	5.42
	U	96.41	94.95	1.47	3.59
	Y	97.66	97.66	0.00	2.34
Slash	I	96.41	96.41	0.00	3.59
	J	96.26	96.26	0.00	3.74
	K	96.34	96.34	0.00	3.66
	Z	97.22	97.22	0.00	2.78

USC UNIVERSIDADE DE SANTIAGO DE COMPOSTELA

Chapter 5

Analysis of the atmospheric risk of deep pyroconvection in Europe

* The results from this chapter have already been published as Senande-Rivera, M.[1], Insua-Costa, D.[1] & Miguez-Macho, G.[1]. Towards an atmosphere more favourable to firestorm development in Europe. *Environmental Research Letters* **17** 094015 (2022). https://doi.org/10.1088/1748-9326/ac85ce.

[1] CRETUS, Non-linear Physics Group, Universidade de Santiago de Compostela, Galicia, Spain

5.1 Introduction

The study of pyroconvection has been gaining attention during the last decades, especially in North America and Australia, due to certain catastrophic firestorm events such as the Colorado Hayman Fire in 2002 [98] or the Canberra fires in 2003 [102]. In Europe, the case that raised the alarm about the risks of deep pyroconvection was the destructive Pedrógão Grande fire in 2017 in Portugal [259]. Nevertheless, the environmental controls on deep pyroconvection are still not entirely clear and, in particular, there are uncertainties about the atmospheric conditions conducive to the development of this phenomenon. The limited number of firestorm records, as these events are conditioned by the existence of a fire burning large amounts of fuel, has hampered the study of deep pyroconvection.

Pyroconvective events are associated with large and intense fires [260] caused by interactions between the fire, the local terrain and critical fire weather [100]. Some studies have identified deep flaming (i.e. fires that exhibit sustained and intense flaming over a large spatial area) as a necessary factor for the development of deep pyroconvection [261, 262].

In addition to high fire intensity, an environment characterised by atmospheric instability is required [260]. Several authors have related the presence of pyroconvective events to an inverted-V atmospheric profile [98, 263, 264], consisting of a dry and unstable lower layer overlaid by a relatively moist middle troposphere. However, upper- and mid-tropospheric conditions also seem to play an important role in the development of deep pyroconvection [105, 260].

USC DE COMPOSTELA

Another issue that has been debated in recent years is the role that the moisture released by the fire may have on the convection process. Some authors claim that the fire-released moisture can constitute a large part of the water content in the fire plume [265], having a significant impact on the development of pyroconvection [103]. However, other studies point to fire-released sensible heat and midlevel moisture entrainment as much more relevant contributors [105, 264, 266, 267]. Lareau and Clements [268] measured the relative importance of these factors by comparing the ambient lifted condensation level with the height of the base of pyroCu clouds, finding that the moisture release during combustion is of secondary importance in the convective process.

The uncertainties in the understanding of the environmental controls on the development of deep pyroconvection explain why there is still no standard indicator for pyroconvection risk. The Haines index [269, 270], which identifies unstable and dry lower-tropospheric profiles, has been used in different pyroconvective studies, sometimes in combination with a near-surface fire weather index [97, 271]. However, some authors suggest that the Haines index has limited utility to identify the most extreme pyroconvective events [105, 261]. More conventional atmospheric instability indexes, like the convective available potential energy (CAPE), were also tested [265], although several pyroconvective events have been shown to be associated with little or no CAPE [98, 260].

The first objective of this study is to identify the atmospheric conditions that enable firestorm formation and to select a set of meteorological indices and thresholds that can detect days with a high risk of deep pyroconvection. For this we have conducted an experiment based on idealised numerical simulations of fires spreading under different atmospheric profiles. Once we determine the atmospheric conditions favourable for deep pyroconvection, we create a map of the risk of firestorm development in Europe for the period 1980–2018. We then assess the trend in the risk of storm-dominated fires in Europe under a changing climate from different CORDEX (Coordinated Regional Climate Downscaling Experiment) regional climate model (RCM) simulations for the European domain (EURO-CORDEX), considering the RCP8.5, RCP4.5 and RCP2.6 emissions scenario.

5.2 Methods

To analyse fire behaviour under different controlled fuel and atmospheric settings, we conduct idealized numerical simulations with the fire–atmosphere coupled model WRF-Fire [96], which combines the Advanced research Weather Research and Forecasting Model (WRF-ARW) [179] with a semi-empirical fire spread model [96]. This model has been previously tested in real wildfire case studies [272, 273], even with pyroconvective characteristics [103, 274].

The computational domain is 60 km wide in the x and y directions and the grid spacing is set to 100 m in the fire grid and 1 km in the atmospheric grid with open boundary conditions. The vertical dimension of the domain expands up to 16 km with 60 vertical levels. The microphysics scheme used is the New Thompson et al. [275], the radiation scheme is the RRTMG (Rapid Radiative Transfer Model for General Climate Models) [276], the surface layer scheme used is the revised MM5 surface layer scheme [277] and the planetary boundary layer parameterisation scheme is the Mellor–Yamada Nakamishi and Niino Level 2.5 [278]. Convection and cloud formation are explicitly resolved at this resolution without the need for a cumulus parameterisation scheme. Simulations are initialized with a single 400 m radius fire

at the centre of the domain, in flat terrain, and atmospheric conditions form a single vertical profile.

To ensure that our model configuration is able to correctly simulate pyroconvection, we have performed a validation using real cases in Europe. We searched for satellite images of cumulus clouds possibly formed by the convection associated with a fire (see Supplementary Figure S5.1) and tested the performance of our model setup in simulating these cases. As shown in Supplementary Figure S5.2, the model is able to simulate a cloud in all cases except for one (see Supplementary Figure S5.2 and Table S5.1).

The idealised runs are initialized with selected real-case atmospheric profiles of wind, temperature and moisture, corresponding to the 100 d of highest fire risk per year during the 2010–2019 period registered at each of the six locations indicated in Supplementary Figure S5.3. The atmospheric vertical data for running the model is obtained from the ERA5 database, that is the fifth generation ECMWF (European Centre for Medium-Range Weather Forecasts) reanalysis for the global climate [129], which combines model data with observations from across the world. The six locations were selected in representation of the regions with the highest incidence of fires among the southern European countries, as shown in Supplementary Figure S5.3. The fire season in these areas is the summer, characterised by being dry and warm [1], and they are generally associated with temperate dry and hot summer (Csa) or temperate dry and warm summer (Csb) climates according to the Köppen–Geiger classification [203]. The locations in Spain and Turkey are dry enough to be classified as semiarid climate (see Table S5.2). The altitudes of the selected points vary between 163 and 1096 meters above sea level (see Table S5.2), which modulates the severity of summer temperatures. The Mediterranean region owes its dry summer to the poleward displacement of the subtropical high during that time of the year. The particularities of the orography and the position to the west or east of the basin condition the different wind regimes at the different sites. However, the lack of precipitation and cloudiness is common to all of them in this season.

For each of the atmospheric profiles (a total of 6000), we perform a suite of paired experiments of an ideal fire spreading through different fuel categories, five in total, from lower to higher fuel load. These fuel characteristics are the same for the different fuel load experiments associated with each selected profile, they do not depend on the site of the profile. A moisture content of 8% is also set to constant in all cases. This moisture content is representative of the high fire activity conditions in the Mediterranean region, where just 12% of the cumulative burned area is associated with fuel moisture contents higher than 10% for late summer and 11% for early summer fires [279]. Each pair of fuel load experiments consists of a control run with interaction between fire and atmosphere and a simulation in which the sensible and latent heat fluxes from the fire are turned off (uncoupled simulation). We assess the role of fire–atmosphere feedbacks by comparing the two experiments.

We first examine how the produced vertical drafts interact with fire characteristics. In particular, we analyse downdraft intensity, now just as an indicator of the existence of pyroconvection, but also of the presence of a strong coupling between the atmosphere and the fire, as it is well known that strong downdrafts behind the head of the fire line can intensify fire spread [280]. According to the results of our simulations, we show in Figure 5.1a that the strongest downdraft speeds, higher than around 8 $m \cdot s^{-1}$, are associated with the presence of clouds formed by pyroconvection. The intensity of these downdrafts is well correlated with the intensification of surface winds (Figure 5.1b), and these stronger winds can multiply the area affected by the fire (Figure 5.1c). Strong vertical drafts are also related to the maximum height

USC UNIVERSIDADE

reached by fire smoke, indicating that when the vertical wind speeds are powerful enough, fire smoke can be easily injected into the stratosphere (Figure 5.1d). Similar relations between the fire properties in Figure 5.1 and updraft maximum speeds are found (Supplementary Figure S5.4), given that strong downdrafts are always associated with strong updrafts.

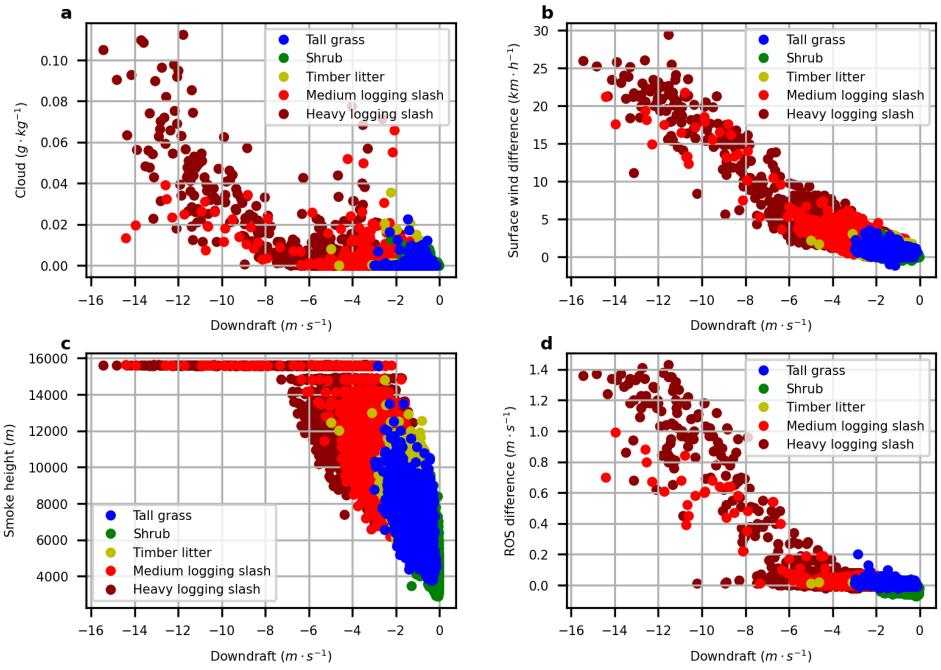


Figure 5.1: Storm downdraft influence on fire properties. Lower troposphere (1000 m) downdraft maximum speed against: **a** cloud water mixing ratio averaged for the simulation domain, **b** 10 m maximum wind difference between coupled and uncoupled fire–atmosphere simulation, **c** burned area increase fraction in 8 h from uncoupled to coupled fire–atmosphere simulation and **d** maximum fire smoke height (up to 16 km). Each colour represents a different fuel category.

Figure 2(a) shows that strong vertical drafts appear only for high fuel loads, above 6 $kg \cdot m^{-2}$ (sensible and latent heat fluxes are directly proportional to the fuel load [96]) and for unstable conditions, with the occurrence spiking when the K-index surpasses about 25°C. This index is calculated from air temperatures and dew point temperatures, and it estimates the atmospheric static stability as a combination of 850–500 hPa thermal lapse rate, 850 hPa moisture and a measure of thickness of moist layer [281]:

$$K = (T_{850} - T_{500}) - T_{d850} - (T_{700} - T_{d700}) \tag{5.1}$$

where T is the air temperature and T_d is the dew point temperature of the pressure level indicated by the subscript in hectopascals. High values of the K-index (>26°C) are associated with environments where thunderstorms are likely to occur [282]. We tested other instability indices, but all show a lower correlation with downdraft intensity (Supplementary Figures S5.5 and S5.6). The reason why the K-index yields a higher correlation with downdraft intensity may be related to the fact that it does not only consider lower tropospheric conditions, but it includes 850 hPa and 700 hPa moisture measures. In addition, it is not based on lifting an unperturbed

surface parcel in an environment that is being modified by a fire.

Favourable meteorological conditions for the spread of a fire are also necessary for the existence of deep pyroconvection [260]. These conditions, apart from enabling the ignition and spread of the fire, are also positively correlated with fuel dryness, which allows for more of the available fuel to be consumed, favouring the release of more sensible heat. In this study we quantify fire risk through the widely used Canadian Fire Weather Index [169] (FWI), developed by the Canadian Forestry Service. The FWI consists of six components: three subindexes representing fuel moisture, two subindexes representing rate of spread and fuel consumption, and a final index representing fire intensity as energy output rate per unit length of fire front.

For analysing future pyroconvective risk trends we used data from CORDEX RCM simulations for the (EURO-CORDEX), conducted at 0.11° resolution (EUR-11). From the different combinations of RCMs and General Climate Models (GCMs) available, we used those that provide the needed variables to calculate the FWI and K-index: COSMO-crCLIM-v1-1 and RCA4 RCMs and EC-EARTH, HadGEM2-ES, MPI-ESM-LR and NorESM1-M GCMs. We use the RCP8.5, RCP4.5 and RCP2.6 greenhouse gas concentration model outputs for the future projections. The Representative Concentration Pathway [198, 199] RCP8.5 assumes a scenario in which greenhouse gas emissions continue to increase throughout the 21st century, producing a radiative forcing of 8.5 $W \cdot m^{-2}$ by 2100. The RCP 4.5 scenario stabilizes radiative forcing at 4.5 $W \cdot m^{-2}$ in the year 2100 without ever exceeding that value [283]. The RCP2.6 scenario is representative of the literature on mitigation scenarios aiming to limit the increase of global mean temperature to 2°C [284].

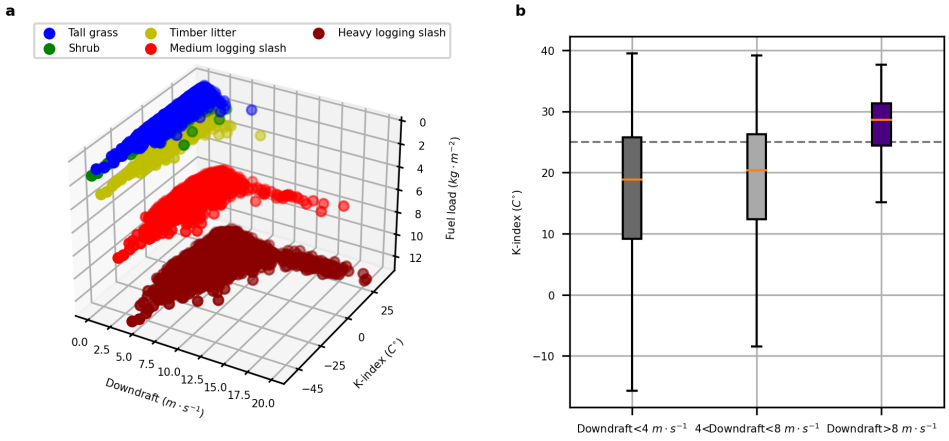


Figure 5.2: Conditions for firestorm development. **a**, Three-dimensional representation of lower troposphere (1000 m) downdraft maximum speed, K-index values and fuel load, with each colour representing a different fuel category. **b**, Relation between downdraft intensity and K-index, represented by a boxplot for each downdraft intensity interval.

5.3 Results and discussion

5.3.1 Present firestorm risk in Europe

We consider a day to have atmospheric risk of deep pyroconvection if it combines a high fire risk at the surface with high atmospheric instability, conditions that are met when certain FWI

and K-index thresholds are surpassed simultaneously. We set the K-index threshold at 25°C, a value that according to our simulations is exceeded by almost 75% of events with downdraft intensities greater than 8 $m \cdot s^{-1}$, but only by 25% of events with weaker downdrafts of less than 8 $m \cdot s^{-1}$ (Figure 5.2b). 8 $m \cdot s^{-1}$ and above are the downdraft wind speed values that we found suggestive of pyroconvection in our simulations, as discussed earlier. To define a surface fire risk threshold, we use the 90th percentile of the FWI values for the period from 1990 to 2019 at each grid cell. As shown in Supplementary Figure S5.7, for most fire-prone areas in Europe fires occur on days with FWI around the 90th percentile. In regions where this 90th percentile corresponds to a very low fire weather index, we set a minimum threshold of 11.2, which is the value that determines a moderate fire risk according to the European Forest Fire Information System, integrated in the EU Copernicus Program. Supplementary Figure S5.8 shows the FWI threshold used for each grid cell from ERA5 reanalysis data.

Figure 5.3a shows the present atmospheric firestorm risk in Europe, obtained by calculating from ERA5 reanalysis data the days per year with both a FWI and a K-index value above the selected thresholds. The Balkan Peninsula, Turkey, eastern Hungary, Italy and northeastern Spain are the regions that present a highest frequency in the occurrence of favourable atmospheric conditions for deep pyroconvection development, with up to 20 d per year of high atmospheric firestorm risk (Figure 5.3a). Maps of the number of days per year with each of the indexes (FWI and K-index) above the selected thresholds are shown separately in Supplementary Figure S5.9. In southern Europe, the atmospheric risk of pyroconvection is concentrated in the summer months, because this is when the highest fire risk at the surface is registered in combination with an also high atmospheric instability. Around the Mediterranean, atmospheric instability is generally maximum in summer, although some regions, such as the Iberian Peninsula, present a distribution that is more bimodal with peaks in spring and autumn, but maintaining elevated values in summer as well (Supplementary Figure S5.10).

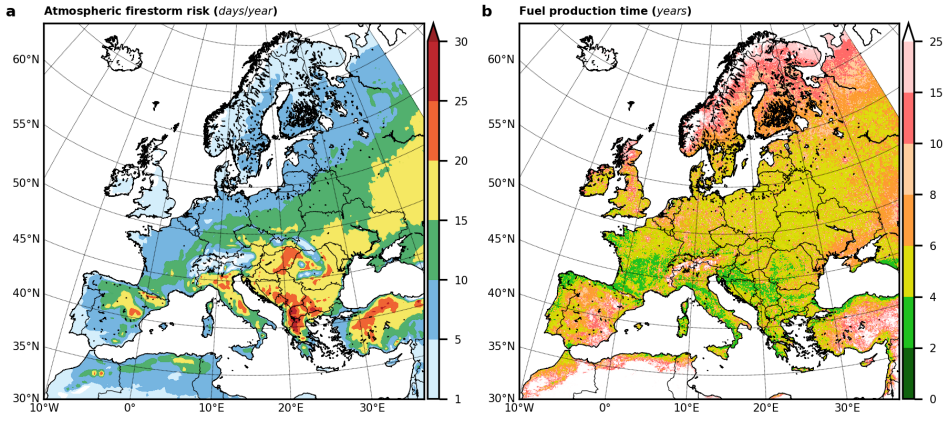


Figure 5.3: Present distribution of firestorm risk. **a**, Number of days per year with both a FWI and a K-index value above the selected thresholds, averaged from 1980-2018 ERA5 reanalysis data. **b**, Minimum number of years required for the accumulation of 6 $kg \cdot m^{-2}$ of fuel load according to the average annual dry matter productivity (DMP) in the 1999-2019 period generated by the Global Land Service of Copernicus, derived from SPOT-VGT and PROBA-V imagery combined with meteorological data from ECMWF.

Finally, for the atmospheric risk of pyroconvection to materialize into an actual firestorm, in addition to ignition of course, there must be sufficient fuel to burn. The characteristics of the

vegetation cover are very diverse across the European continent, so the amount of available fuel also varies from one region to another. Supplementary Figure S5.9 shows an estimate of dry matter productivity (DMP), representing the overall growth rate or dry biomass of vegetation. The areas with the highest productivity are the northwest of the Iberian Peninsula, the half south of France, and most of Italy and the western Balkans. In these regions, it takes only between 2 and 4 years (Figure 5.3b) to generate a 6 $kg \cdot m^{-2}$ amount of vegetation biomass, which is the fuel load threshold shown to be associated with a considerable increase in the intensity of pyroconvection in our idealized experiment results in Figure 5.2a. Some of these regions with potentially high fuel loads, such as central Italy and the Balkans, also have many days per year with high atmospheric risk of pyroconvection, thus the odds of firestorm occurrence multiply. In contrast, there are regions with such low DMP that it may be difficult for fuel to accumulate there to an amount sufficient for pyroconvection to develop, even when the atmospheric risk is high, as is the case of most of Spain and Turkey. These areas need a period of more than 15 years to generate the fuel load of 6 $kg \cdot m^{-2}$.

Most of the real cases of pyroconvection identified to carry out the validation of the model configuration occurred on days that meet the thresholds identified in this study. Specifically, as shown in Table S5.1, only one event took place on a day with a K-index lower that the threshold (with a value of 22.21 °C, when the threshold is 25 °C), and only another event occurred on a day with a FWI below the threshold (with a value of 46.61 and a threshold of 49.33). These experiments support the reliability of the results shown in Figure 5.3.

5.3.2 Future trends under different climate change scenarios

We estimate future trends in pyroconvection risk from EURO-CORDEX model results considering the RCP8.5 scenario [198]. Our calculations indicate that the number of days with high fire risk at the surface (FWI above the threshold set from present data, as discussed earlier and shown in Supplementary Figure S5.8) will increase significantly across southern Europe, especially in the Iberian Peninsula and southern France (Figure 5.4a), and also in northern Africa, moving from between 30 and 40 d per year at the present (1980–2018) to more than 60 d per year in the 2070–2098 period (Supplementary Figure S5.12), which represents a percentage increase of nearly 100%. This increase in fire risk is already appreciable at the present and has been shown to be related to human-induced climate change [137].

Less pronouncedly growing values are obtained for atmospheric instability and with a different spatial pattern (Figure 5.4b). The fastest increasing trends are found in Italy and Northern Europe, while Portugal, Spain and Turkey show less significant results. For the Mediterranean region, unstable atmospheres are already quite frequent at the present, more so than in the northern countries, and this spatial pattern will be maintained in the future, although slightly attenuated (Supplementary Figure S5.13). Some studies have previously assessed the possible influence of climate change on atmospheric static stability, finding a general increase in the number of unstable environments derived from the predicted rise in surface temperature and low-level tropospheric humidity [285, 286, 287].

To analyse the meteorological risk of firestorms and its future trend, we now consider the number of days in which high fire risk conditions at the surface and high atmospheric instability coincide. Figure 4(c) shows that the occurrence of favourable firestorm environments will increase in southern Europe, especially in the northeast of the Iberian Peninsula. As shown in the time series, this positive trend is mainly driven by the growing fire risk in Portugal and

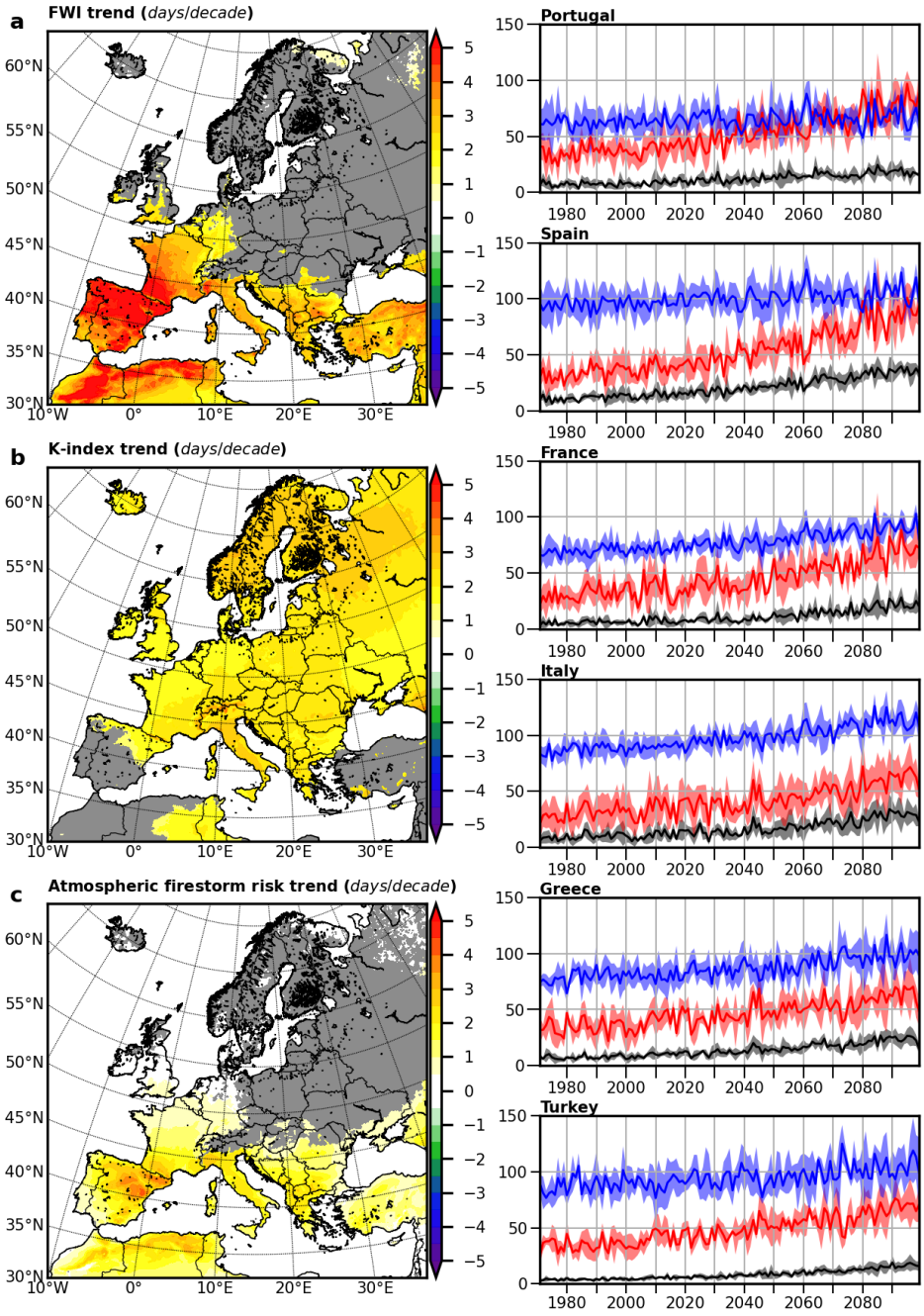


Figure 5.4: Future trends in fire risk, atmospheric instability and firestorm risk according to RCP8.5 scenario. Trend in number of days per decade with **a** FWI **b** K-index and **c** both FWI and K-index values above the selected thresholds (see text), according to different EURO-CORDEX models under the RCP8.5 scenario for the 1970–2098 period. Grey shaded regions indicate that at least one of the models presents a non-significant result (p-value>0.05) or a trend with an opposite-sign. Country-averaged time series for the number of days per year with high FWI (red), high K-index (blue) and both FWI and K-index high values (grey) are also shown, indicating the standard deviation between model outputs by the line width.

USC
UNIVERSIDADE DE SANTIAGO DE COMPOSTELA

Spain, whereas in France, Italy, Greece and Turkey, the firestorm trend is supported by both increased atmospheric instability and fire risk.

The rise in deep pyroconvection risk is more accentuated in places that already have a higher risk at the present (Figures 5.3a and Figure 5.4c), such as the eastern Iberian Peninsula, northern Algeria, northern Italy and the Balkan Peninsula. In these regions the annual number of days with high firestorm risk will double, moving from around 15 d per year in the 1980–2018 period, to more than 30 d per year by the end of the 21st century (Supplementary Figure S5.14).

In addition to the worst-case RCP8.5 scenario we have considered an intermediate scenario in which emissions peak in 2040 and then decline (RCP4.5) [48], and a scenario that requires that CO2 emissions start declining by 2020 and go to zero by 2100 (RCP 2.6) [49]. For the RCP4.5 scenario, the positive trends of fire risk, atmospheric instability and firestorm risk are also significant although less pronounced than for the RCP8.5 scenario (Supplementary Figure S5.15). Firestorm risk increases at a rate similar to that of the worst-case RCP8.5 scenario until the 2050s, stabilizing afterwards (supplementary videos 1 and 2). For the RCP2.6 scenario we observe that although atmospheric instability shows significant increases, the risk of deep pyroconvection remains very stable throughout the 21st century (Supplementary Figure S5.16). We only find a significant positive trend in the firestorm risk in the east of the Iberian Peninsula and in the south of the Balkan Peninsula (Supplementary Figure S5.16). This implies that the atmospheric firestorm risk increase can still be controlled with emission reduction policies compatible with keeping the global temperature rise below 2 °C by 2100.

The trends shown in Figure 5.4 and Supplementary Figures S5.15 and S5.16 were obtained by linear regressions. The data from the different models were treated independently, and the final result shown in each figure corresponds to the mean of the results from each model output. To quantify the statistical significance of each trend, the p-value is used in the context of null hypothesis testing. In Figures 5.4 and Supplementary Figures S5.15 and S5.16, grey shaded regions indicate that one of the model outputs presents a non-significant result (p-value$>$0.05) or that at least one of the model outputs shows an opposite-sign trend. The results shown in Figure 5.4c are robust to changes in the set of thresholds. In Supplementary Figures S5.17 and S5.18 we show how for different FWI thresholds (from the 80th to the 95th percentile) and different K-index thresholds (from 22.5 °C to 30 °C) the firestorm risk trend undergoes only very slight variations.

5.3.3 An ongoing process

We use the 1980–2018 ERA5 reanalysis data to check whether the trends determined by climate models for the 1970–2098 period are already noticeable at the present. Significant positive trends in the number of days with high fire risk are already observed for the Iberian Peninsula, France and the region north of the Black Sea and the Caucasus, covering Moldova, Ukraine and southwestern Russia (Supplementary Figure S5.19a), a wide swath of land where the values surpass those projected by the EURO-CORDEX models for the future (Figure 5.4), but with a greater interannual variability. The pronounced positive trend in the fire risk index in this region north of the Black Sea is related to the fact that this area has experienced the highest summer temperature increase in Europe during the 1979–2019 period (Supplementary Figure S5.20), which has also been accompanied by a decrease in precipitation and relative humidity (Supplementary Figures S5.21, S5.22 and S5.23).

USC UNIVERSIDADE DE SANTIAGO DE COMPOSTELA

Regarding atmospheric instability, Central Europe and the central and eastern

Mediterranean regions show the largest increases (Supplementary Figure S5.19b). This is mainly due to a steepening of the lapse rate between the 850 hPa and 500 hPa levels and a rising of the 850 hPa dew point temperature (Supplementary Figures S5.24 and S5.25). In Greece, Turkey and southern Italy, the trend is further enhanced by a decrease in the 700 hPa dew point depression (Supplementary Figure S5.26).

Finally, the risk of deep pyroconvection has been increasing in eastern Spain, most of inland France, Western Turkey and the large region north of the Black Sea (Supplementary Figure S5.19c). This result is consistent with the projections shown in Supplementary Figure S5.24 for western Europe, but not so for the east. The significant discrepancies in the region north of the Black Sea are due to the aforementioned large positive trend in fire risk index associated with summer temperatures increases of up to 5 °C and a pronounced decrease in the total summer precipitation in the 1980–2018 period (Supplementary Figure S5.23), which models do not capture properly.

5.4 Conclusions

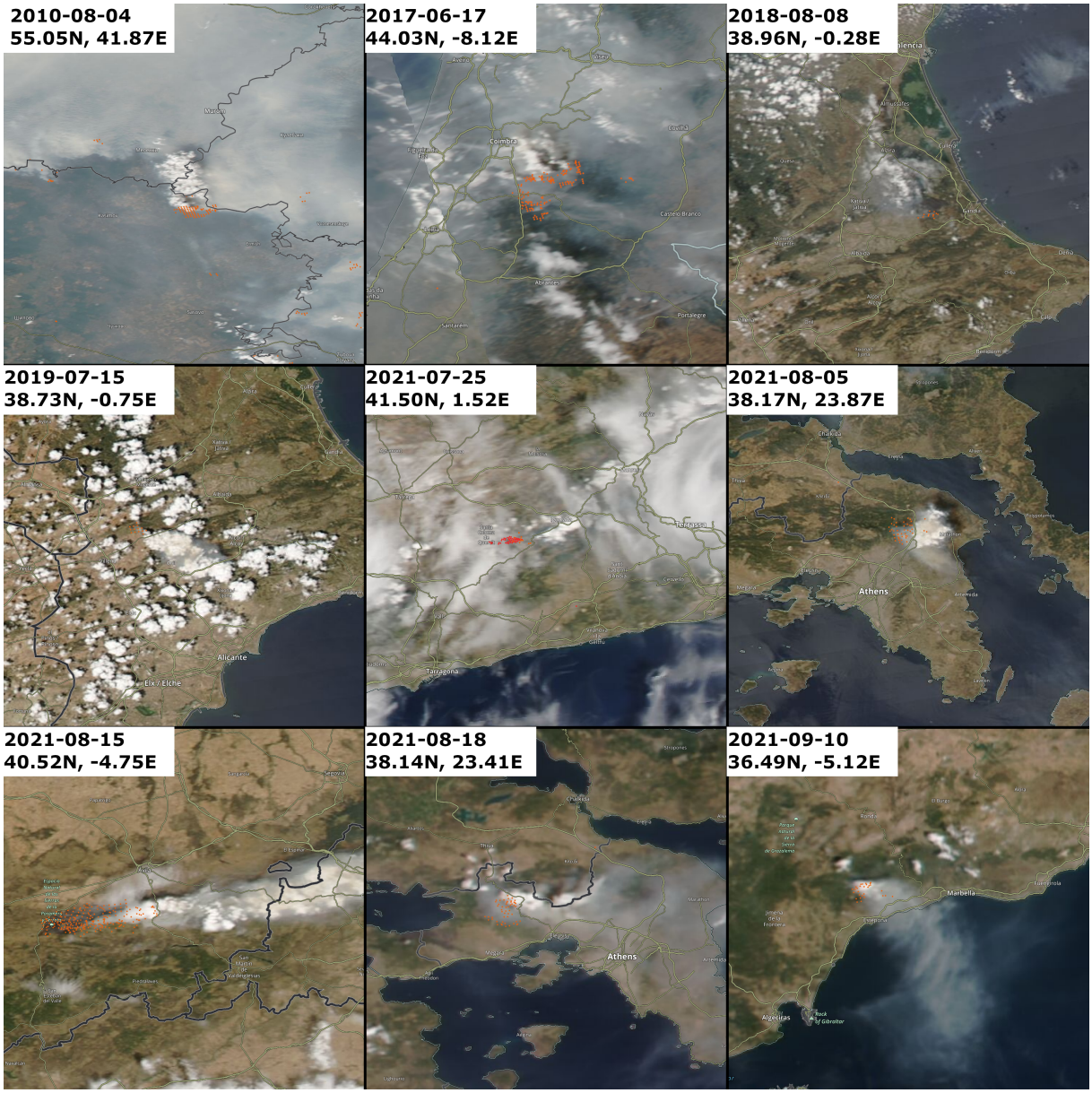
We have found that two of the three factors that determine deep pyroconvection risk, namely fire risk at the surface and atmospheric instability, will augment significantly in Europe during the 21st century. The spatial pattern of the increase in these two factors is uneven, but the number of days with high fire risk and sufficient atmospheric instability will have the greatest growth in the western Mediterranean region, where these changes are already noticeable at the present.

For the development of firestorms, a high fuel load is needed in addition. Fuel load is determined by the amount and structure of vegetation, but also by its dryness. While fuel dryness is increasing due to climate change, vegetation is the only variable influencing fire behaviour that we can manage [288]. The European landscape has been completely modified by humans, especially in the Mediterranean basin where truly wild environments no longer exist [289]. Although fuel reduction strategies are growingly being used in Southern Europe [289], the amount of fuel has been building up in the last decades due to different processes such as rural depopulation [290], the decrease of farming activities or reforestations [288] and the CO2 fertilization effect on vegetation [291, 248, 128]. Fire prevention strategies more focused on fuel management and policies that prevent rural abandonment can help to mitigate the effects of climate change on the incidence of firestorm events.

It should be mentioned that this is a study to determine the risk of deep pyroconvection on a broad temporal and spatial scale. This has required some assumptions when identifying the environmental controls on this process, which can be much more complex, especially on a more local scale. Regarding future projections, although we have used different emission scenarios, it is evident that there are still sources of uncertainty related to possible changes in human activity in terms of fuel management or fire ignitions.

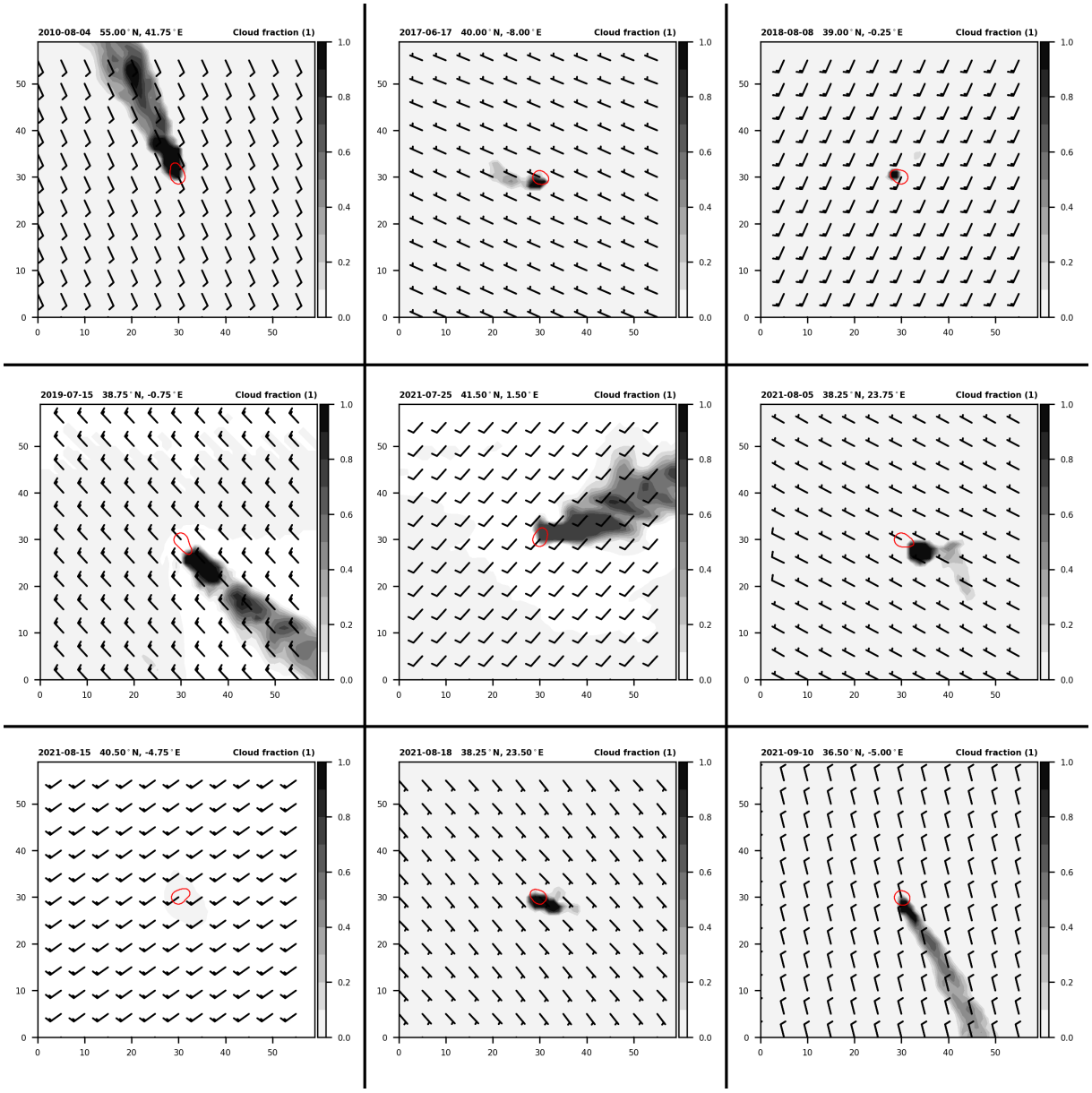
USC
UNIVERSIDADE DE SANTIAGO DE COMPOSTELA

Supplementary Figures



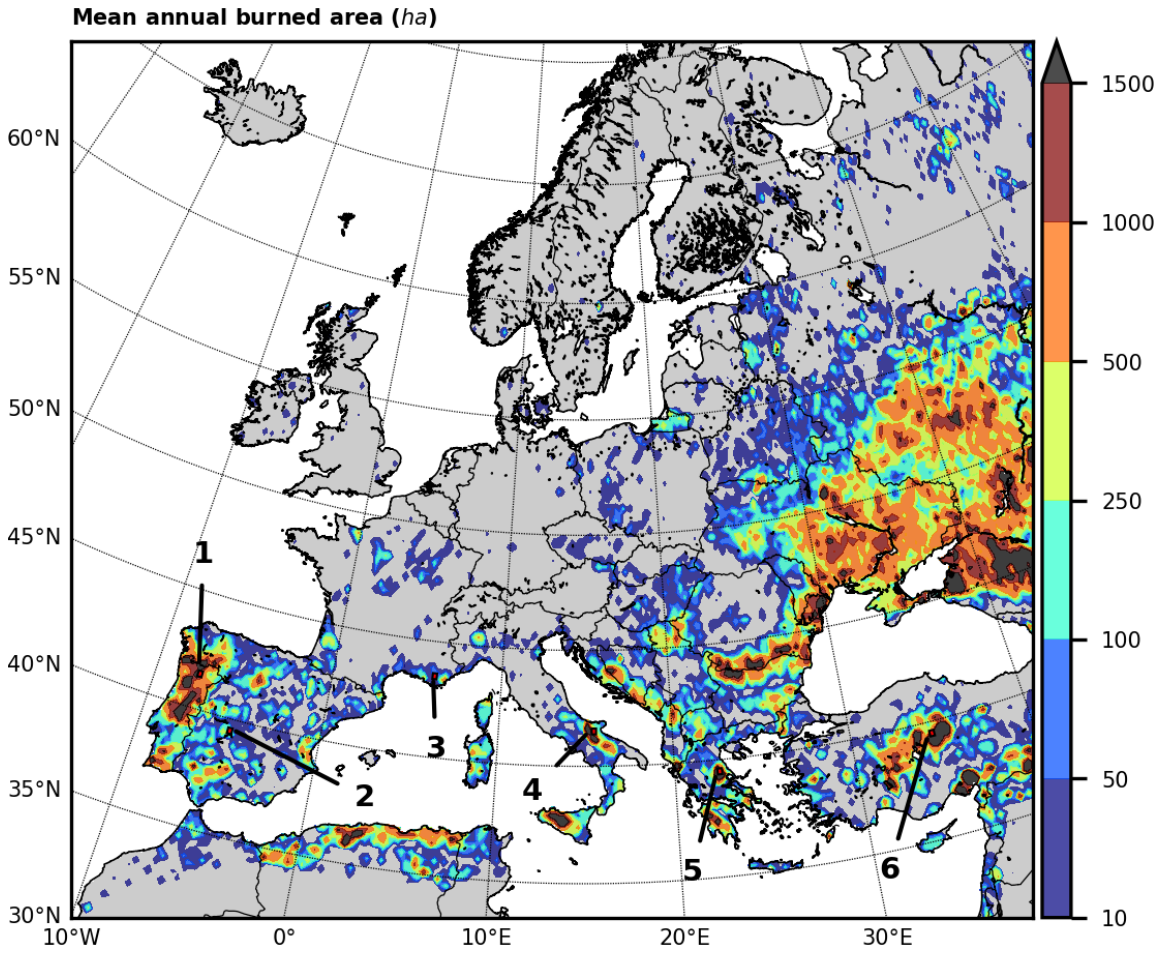
Supplementary Figure S5.1: Satellite images of clouds possibly associated with pyroconvection. All images are from NASA's Worldview service, obtained from the Moderate Resolution Imaging Spectroradiometer (MODIS) instrument abroad the Aqua satellite, unless the image corresponding to 2021-08-18, obtained from the Visible Infrared Imaging Radiometer Suite instrument abroad the NOAA-20 satellite. Fire and thermal anomalies observed by the satellite are indicated as red and orange points. We acknowledge the use of imagery from the NASA Worldview application (https://worldview.earthdata.nasa.gov), part of the NASA Earth Observing System Data and Information System (EOSDIS).

USC
UNIVERSIDADE DE SANTIAGO DE COMPOSTELA



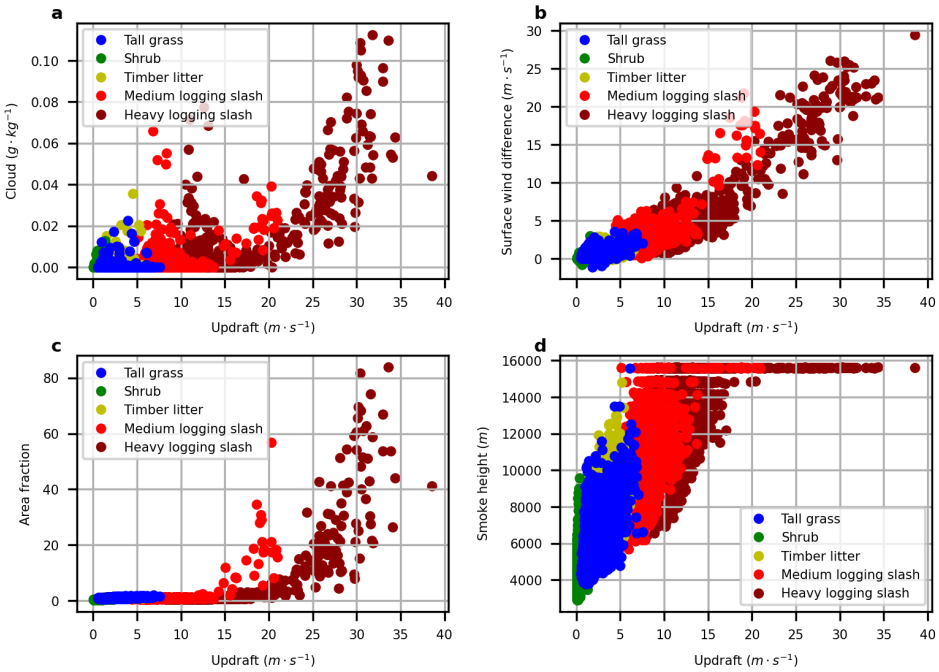
Supplementary Figure S5.2: Cloud fraction outputs of the idealized simulations for validation. Cloud fraction is shown in a grey scale, 850 hPa wind is indicated in barbs and the fire perimeter is indicated in red.

USC UNIVERSIDADE DE SANTIAGO DE COMPOSTELA



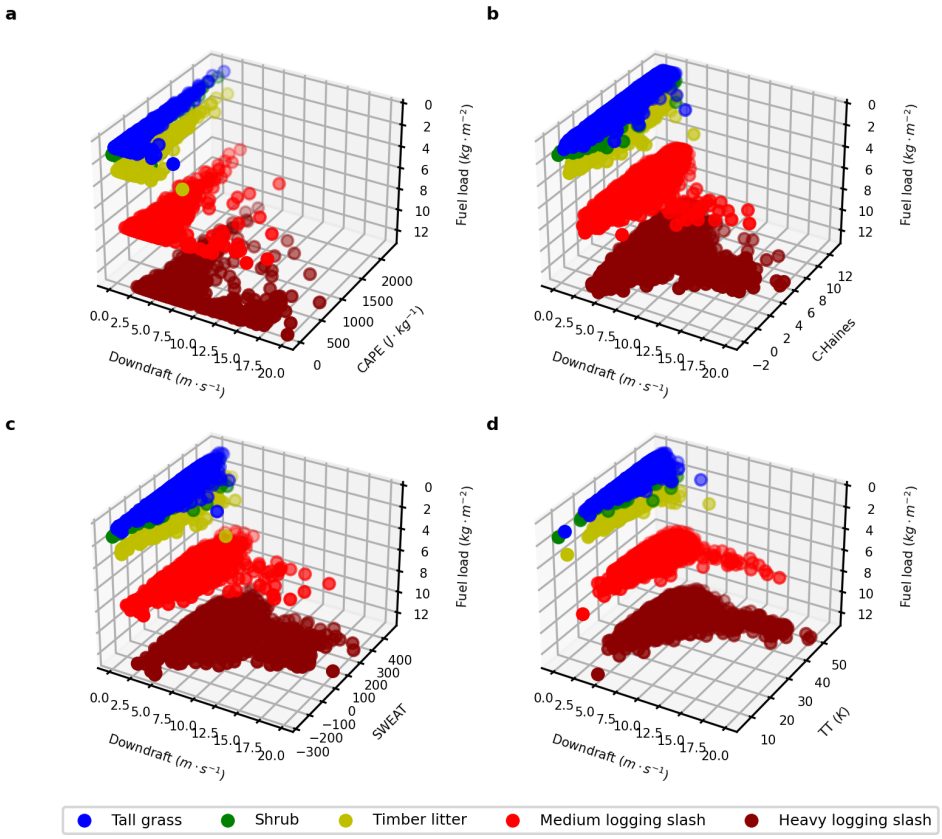
Supplementary Figure S5.3: Locations of the atmospheric vertical profiles. Grid cells ($0.25^\circ \times 0.25^\circ$) selected for obtaining the atmospheric vertical profiles for the idealized experiments marked by red dots on the mean annual burned area GFED4 data for the 1996-2016 period [190]. The selected grid cells are located in regions with high burned area values.

USC UNIVERSIDADE DE SANTIAGO DE COMPOSTELA



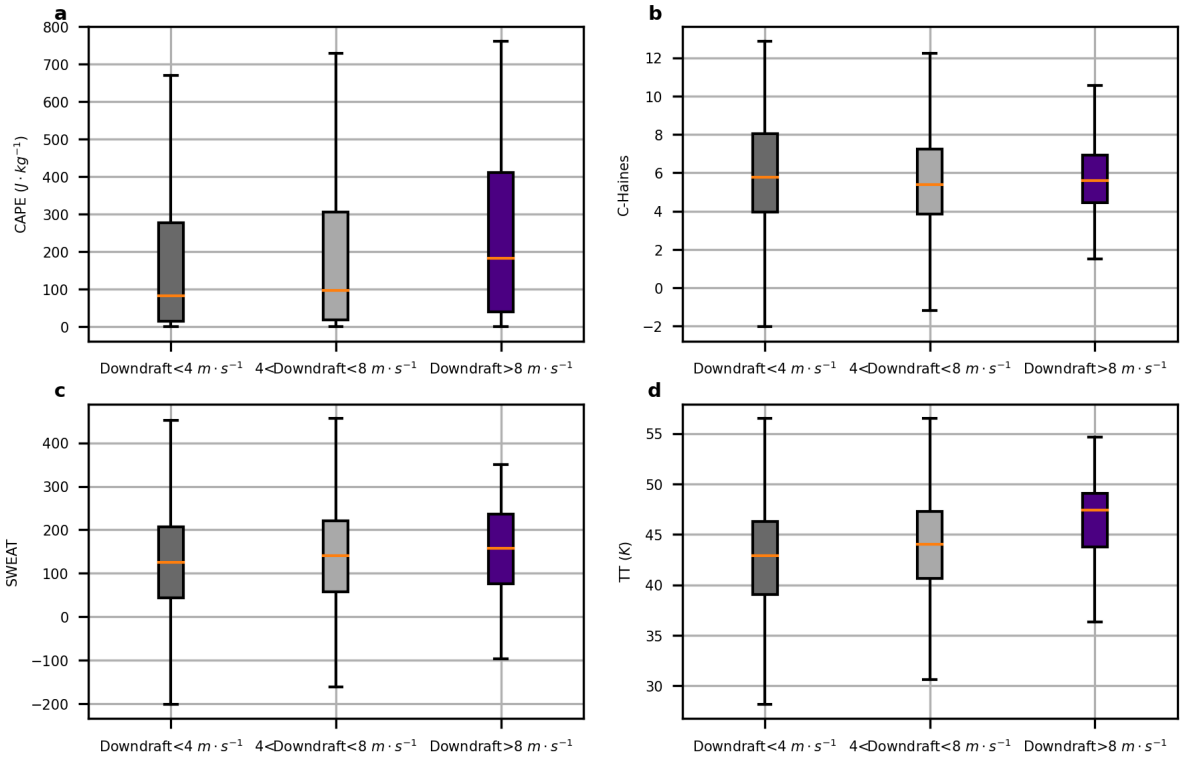
Supplementary Figure S5.4: Storm updraft influence on fire properties. Updraft maximum speed against: **a** cloud water mixing ratio averaged for the simulation domain, **b** 10 m maximum wind difference between coupled and uncoupled fire-atmosphere simulation, **c** maximum fire smoke height (up to 16 km) and **d** burned area increase fraction in 8 hours from uncoupled to coupled fire-atmosphere simulation. Each color represents a different fuel category.

USC
UNIVERSIDADE DE SANTIAGO DE COMPOSTELA

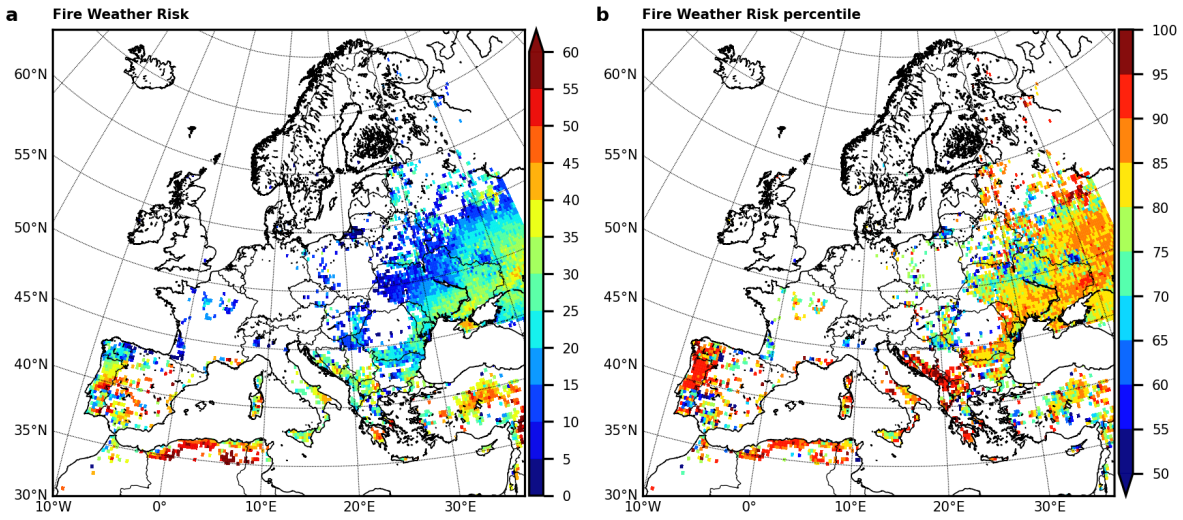


Supplementary Figure S5.5: Comparison between indexes. 3-dimensional representation of lower troposphere (1000 m) downdraft maximum speed, fuel load and: **a** Convective Available Potential Energy (CAPE), **b** Continuous Haines Index (C-Haines), **c** Severe Weather Threat Index (SWEAT) and **d** Total Totals Index (TT).

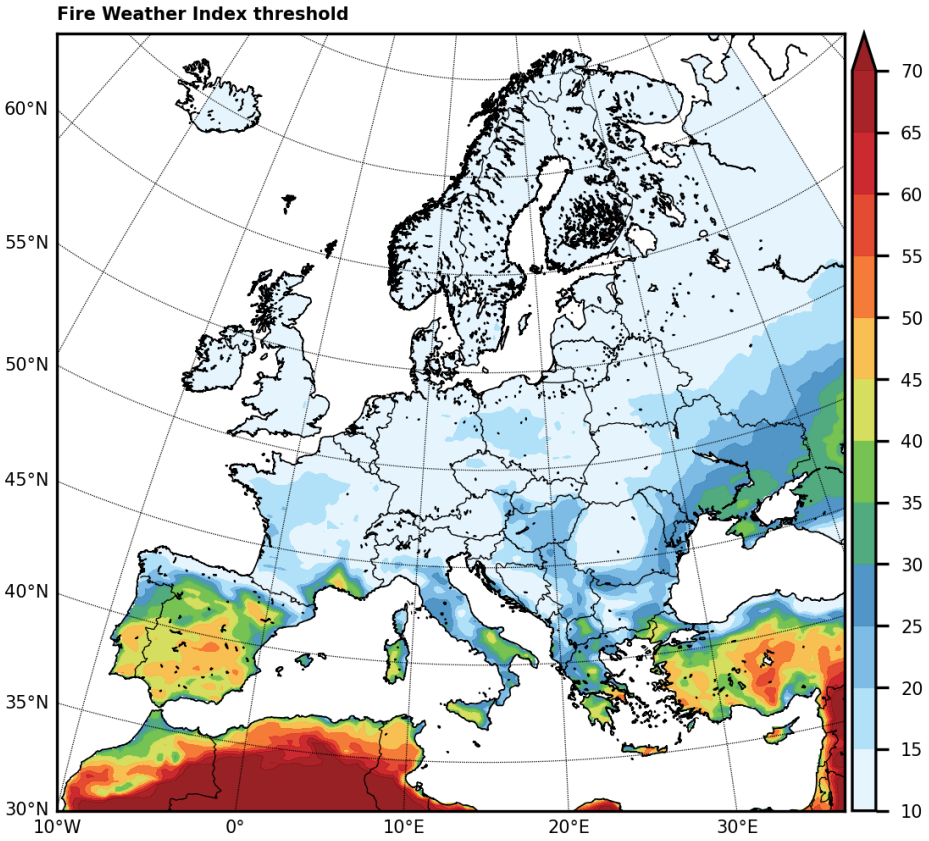
USC
UNIVERSIDADE DE SANTIAGO DE COMPOSTELA



Supplementary Figure S5.6: Boxplot comparison among indexes. Relation between downdraft intensity represented by a boxplot for each interval and: **a** Convective Available Potential Energy (CAPE), **b** Continuous Haines Index (C-Haines), **c** Severe Weather Threat Index (SWEAT) and **d** Total Totals Index (TT).

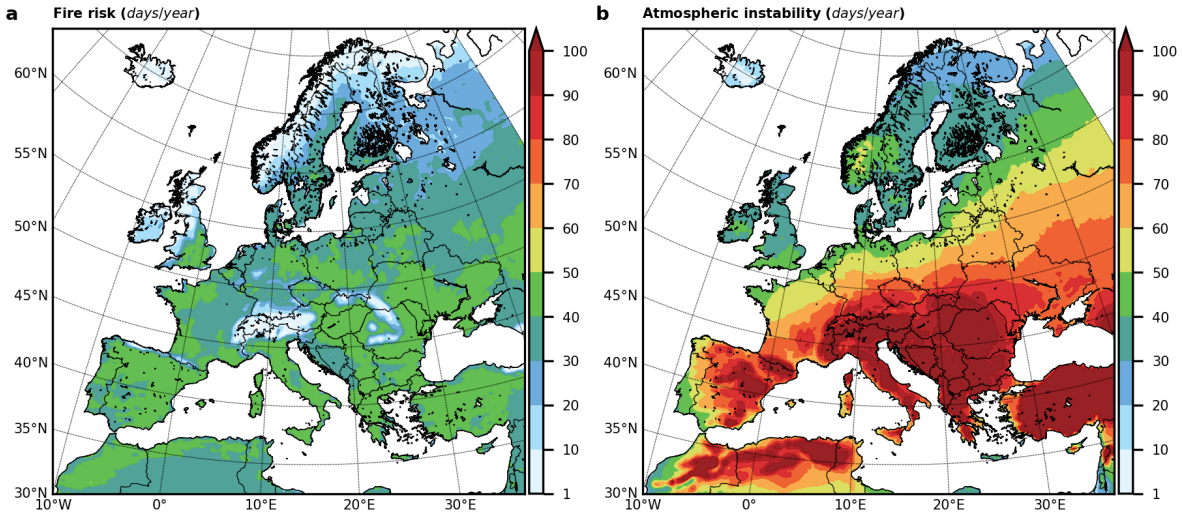


Supplementary Figure S5.7: FWI observed during fire days. **a**, Median of the FWI values on days with non-zero observed burned area during the 2001-2015 period [190]. **b**, Median of the percentiles corresponding to each of the FWI values on days with non-zero observed burned area during the 2001-2015 period.



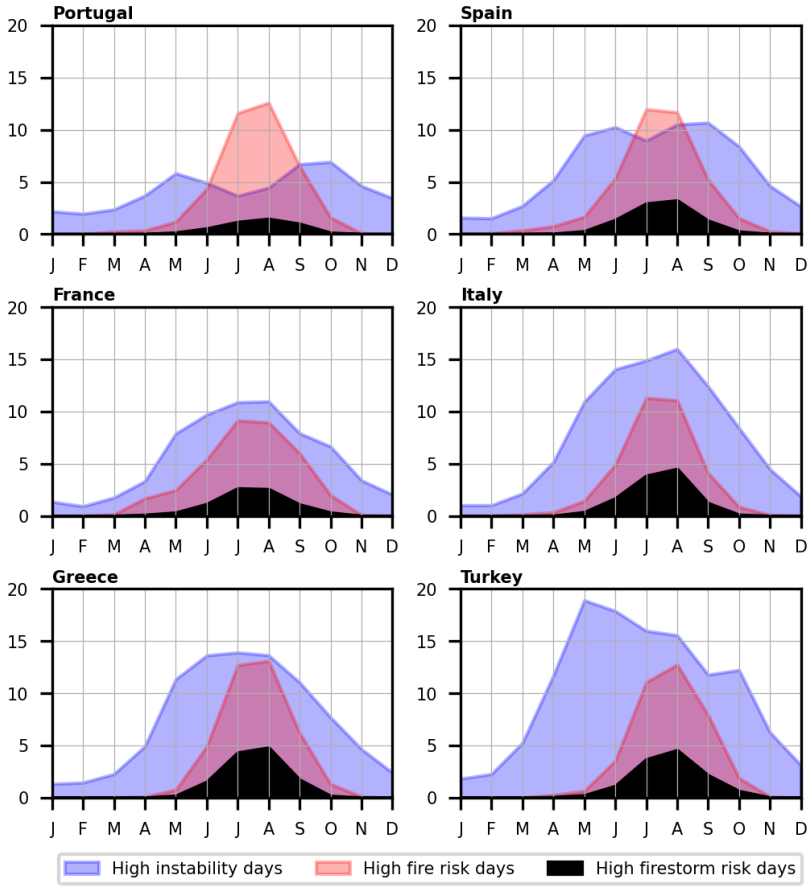
Supplementary Figure S5.8: FWI threshold. For each grid cell we combine a constant and a variable FWI threshold, where the constant threshold is 11.2 (moderate fire risk) and the variable threshold is defined for each grid cell as the 90th percentile of the FWI data from 1990 to 2019 ERA5 reanalysis data. The FWI final threshold is the maximum value between the constant and the variable threshold.

USC UNIVERSIDADE DE SANTIAGO DE COMPOSTELA



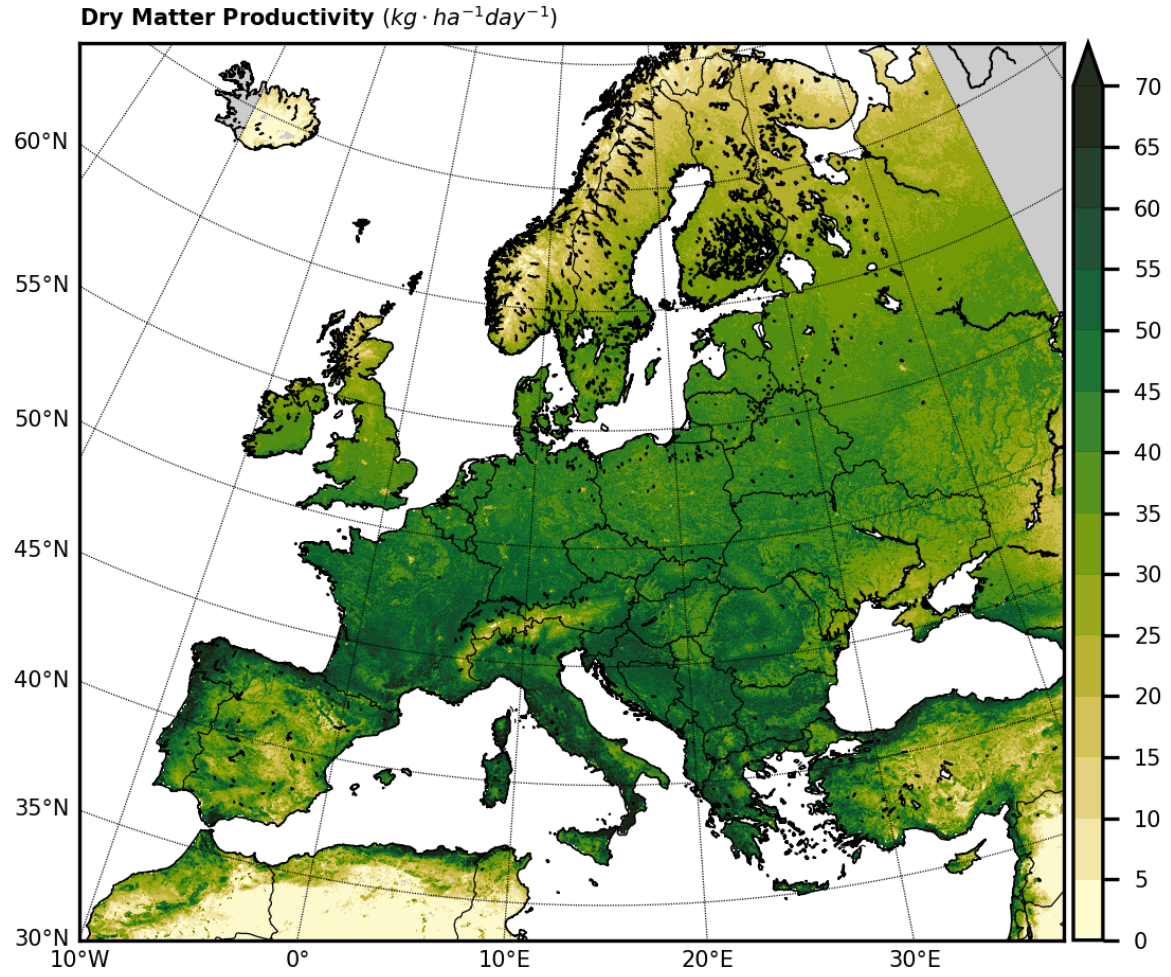
Supplementary Figure S5.9: Days with high FWI and high K-index. Number of days per year with **a** FWI and **b** K-index values above the selected threshold, averaged from 1980-2018 ERA5 reanalysis data.

USC
UNIVERSIDADE DE SANTIAGO DE COMPOSTELA

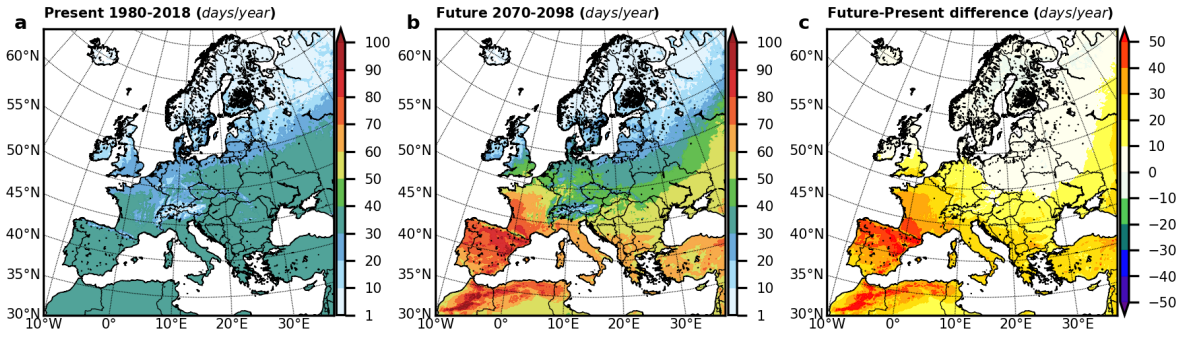


Supplementary Figure S5.10: Monthly distribution of the number of days with high values of the FWI and K-index. Monthly distribution of the number of days per year above the selected threshold with a FWI value above the selected threshold (red), a K-index value (blue) and both a FWI and K-index value above the threshold (black), averaged for the ERA5 output period 1980-2018.

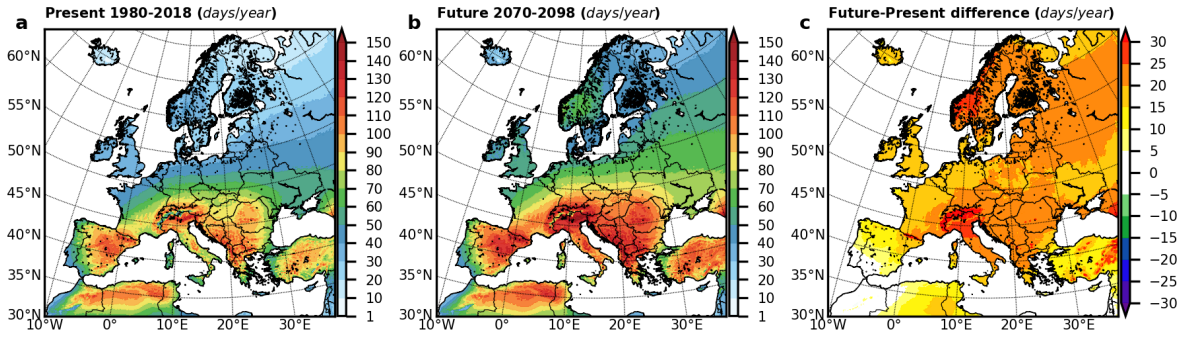
USC
UNIVERSIDADE DE SANTIAGO DE COMPOSTELA



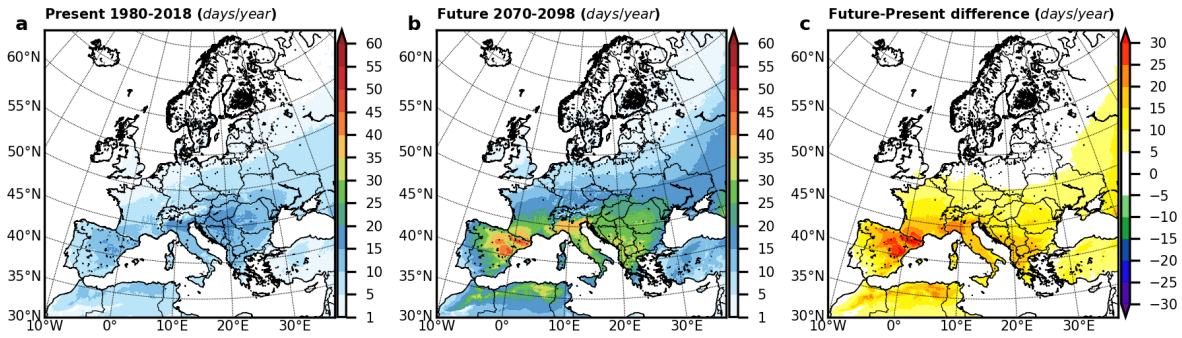
Supplementary Figure S5.11: Fuel load estimation from vegetation products. Average annual dry matter productivity (DMP) in the 1999-2019 period generated by the Global Land Service of Copernicus, derived from SPOT-VGT and PROBA-V imagery combined with meteorological data from ECMWF.



Supplementary Figure S5.12: Days with high FWI. Number of days per year with a FWI value above the selected threshold, averaged for all the EURO-CORDEX model outputs, during: **a**, 1980-2018 and **b**, 2070-2098. In **c**, the difference between the two periods is shown.

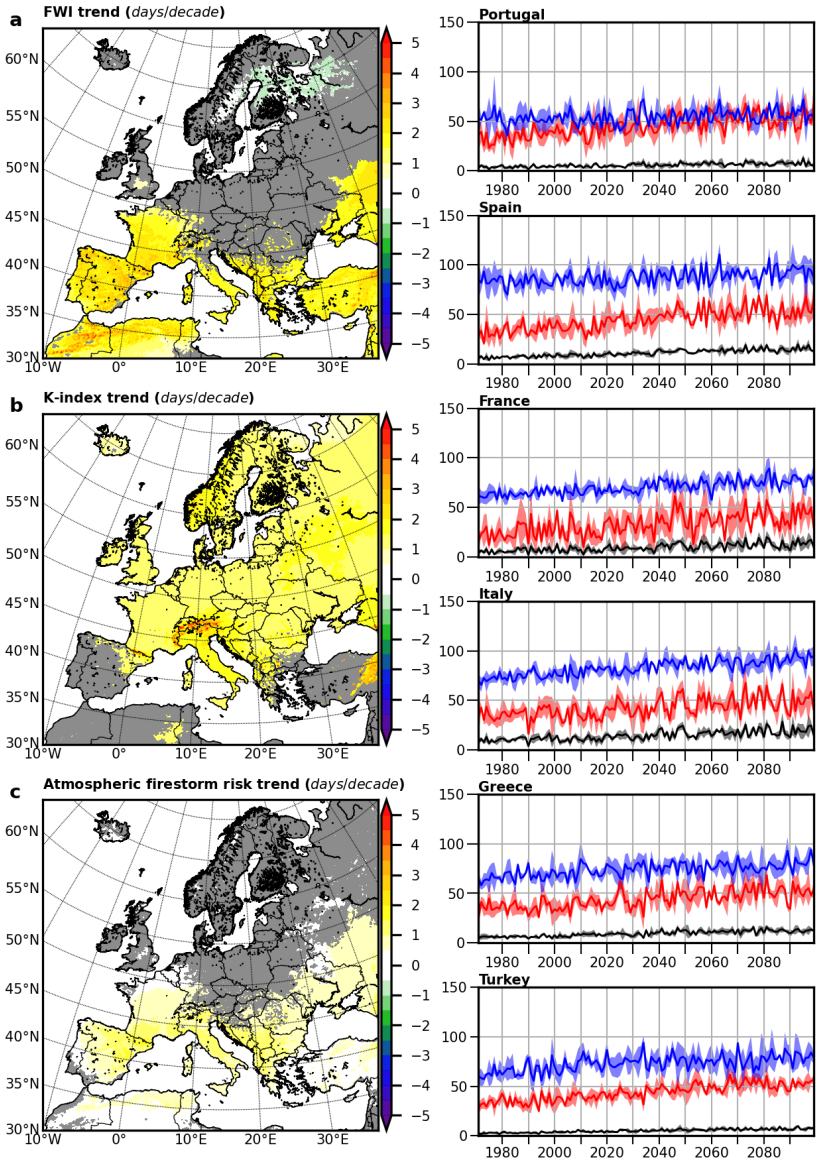


Supplementary Figure S5.13: Days with high K-index. Number of days per year with a K-index value above the selected threshold, averaged for all the EURO-CORDEX model outputs, during: **a**, 1980-2018 and **b**, 2070-2098. In **c**, the difference between the two periods is shown.



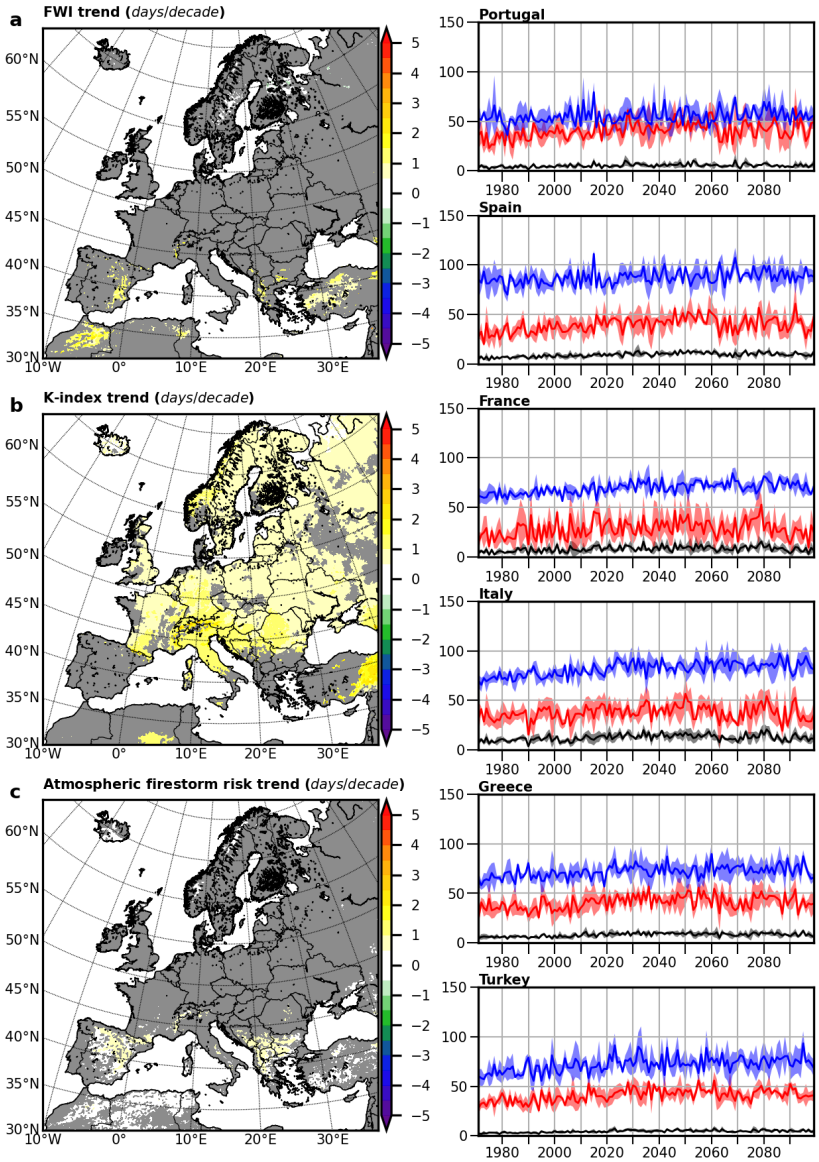
Supplementary Figure S5.14: Days with both FWI and K-index high values. Number of days per year with a FWI and a K-index value above the selected threshold, averaged for all the EURO-CORDEX model outputs, during: **a**, 1980-2018 and **b**, 2070-2098. In **c**, the difference between the two periods is shown.

USC
UNIVERSIDADE DE SANTIAGO DE COMPOSTELA



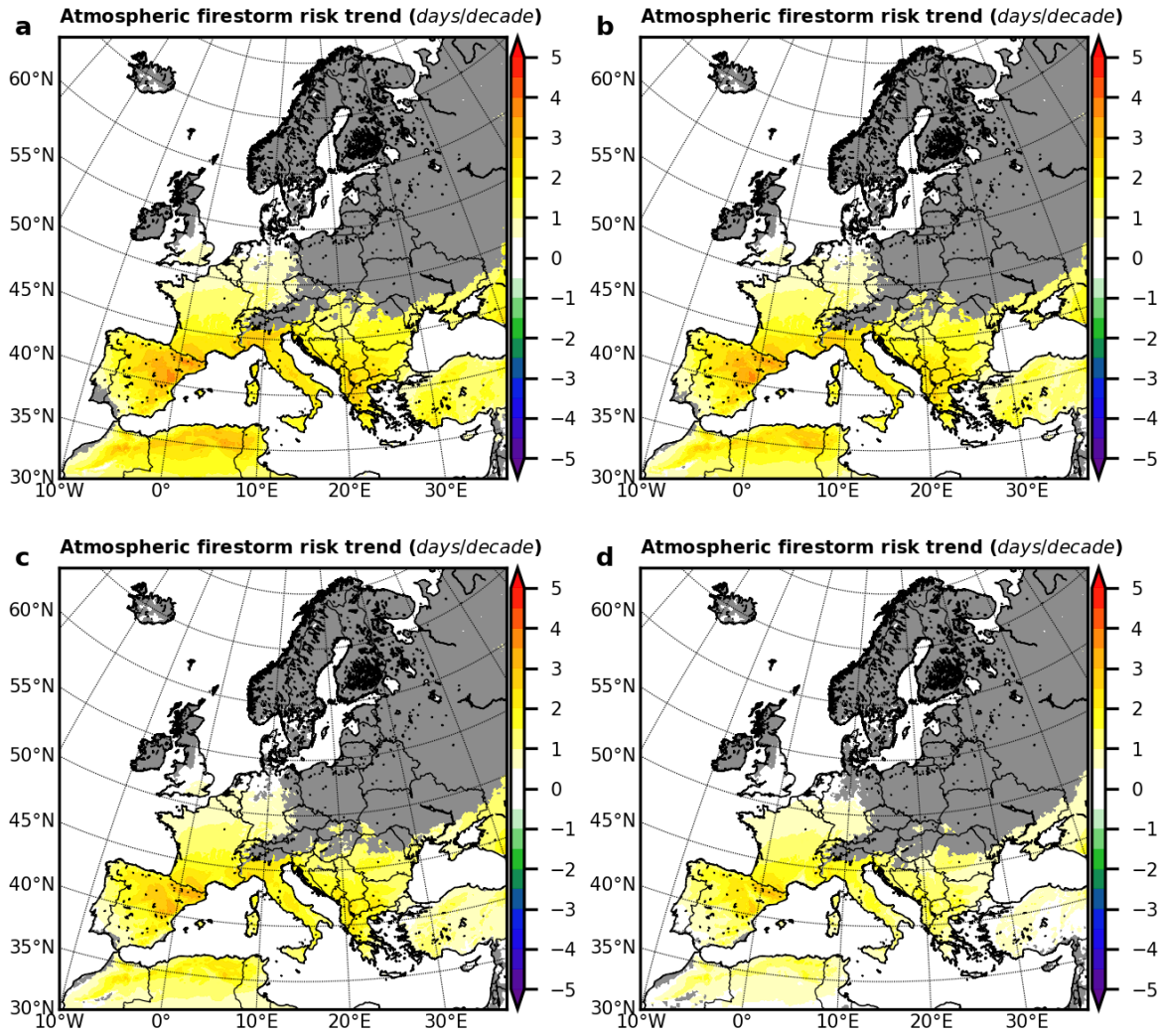
Supplementary Figure S5.15: Future trends in fire risk, atmospheric instability and firestorm risk according to RCP4.5 scenario. Trend in number of days per decade with **a** FWI **b** K-index and **c** both FWI and K-index values above the selected thresholds (see text), according to different EURO-CORDEX models under the RCP4.5 scenario for the 1970-2098 period. Grey shaded regions indicate that at least one of the models presents a nonsignificant result (p-value>0.05) or a trend with an opposite-sign. Country-averaged time series for the number of days per year with high FWI (red), high K-index (blue) and both FWI and K-index high values (grey) are also shown, indicating the standard deviation between model outputs by the line width.

USC
UNIVERSIDADE DE SANTIAGO DE COMPOSTELA



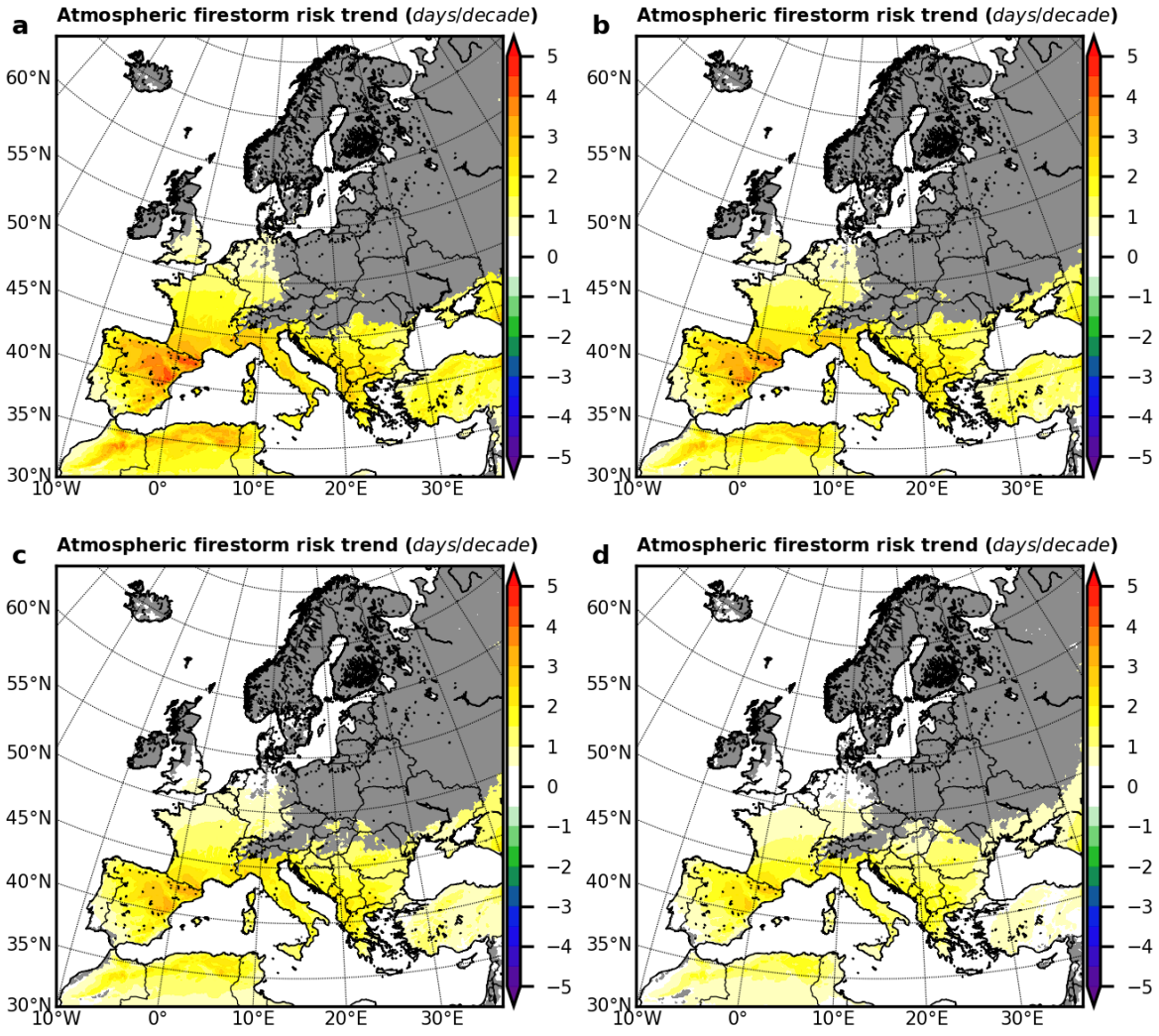
Supplementary Figure S5.16: Future trends in fire risk, atmospheric instability and firestorm risk according to RCP2.6 scenario. Trend in number of days per decade with **a** FWI **b** K-index and **c** both FWI and K-index values above the selected thresholds (see text), according to different EURO-CORDEX models under the RCP2.6 scenario for the 1970-2098 period. Grey shaded regions indicate that at least one of the models presents a nonsignificant result (p-value>0.05) or a trend with an opposite-sign. Country-averaged time series for the number of days per year with high FWI (red), high K-index (blue) and both FWI and K-index high values (grey) are also shown, indicating the standard deviation between model outputs by the line width.

USC
UNIVERSIDADE DE SANTIAGO DE COMPOSTELA



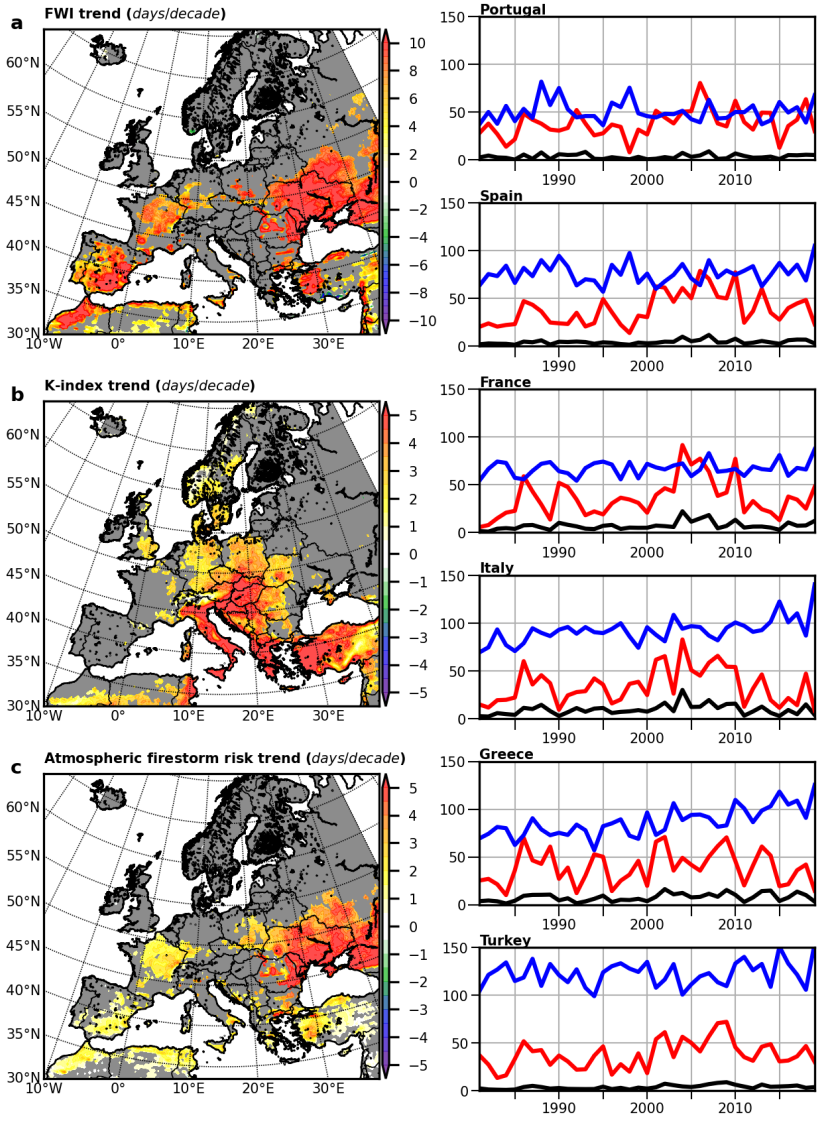
Supplementary Figure S5.17: Firestorm risk trend sensitivity to different FWI thresholds. Trend in the number of days with both FWI and K-index high values with a FWI threshold of: **a** 80th percentile, **b** 85th percentile, **c** 90th percentile (as in Figure 5 of the main text) and **d** 95th percentile of the FWI data from 1990 to 2019 for each EURO-CORDEX model output.

USC
UNIVERSIDADE DE SANTIAGO DE COMPOSTELA

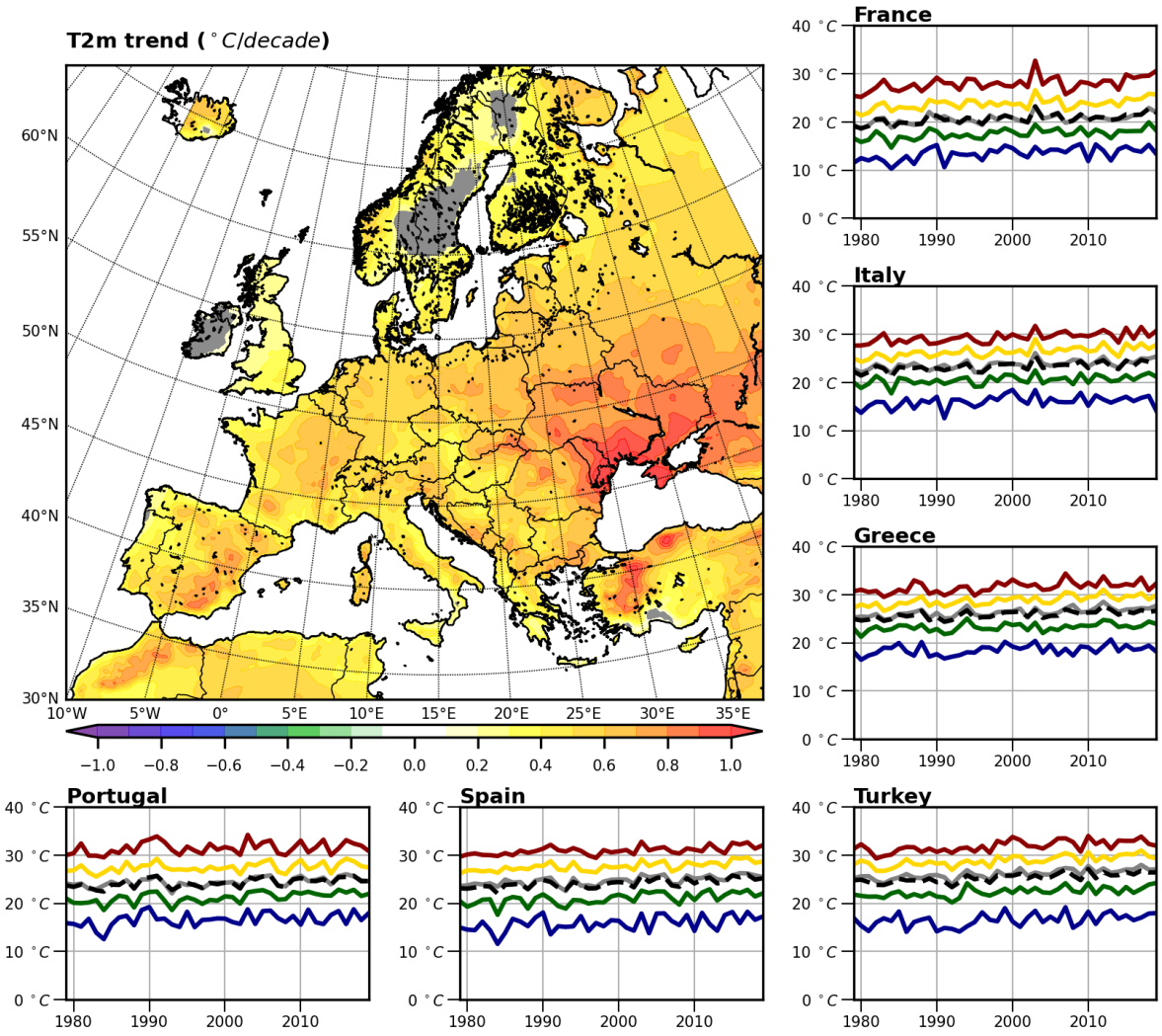


Supplementary Figure S5.18: Firestorm risk trend sensitivity to different K-index thresholds. Trend in the number of days with both FWI and K-index high values with a Kindex threshold of: **a** 20°C, **b** 22.5°C, **c** 25°C (as in Figure 5 of the main text) and **d** 27.5°C.

USC
UNIVERSIDADE DE SANTIAGO DE COMPOSTELA

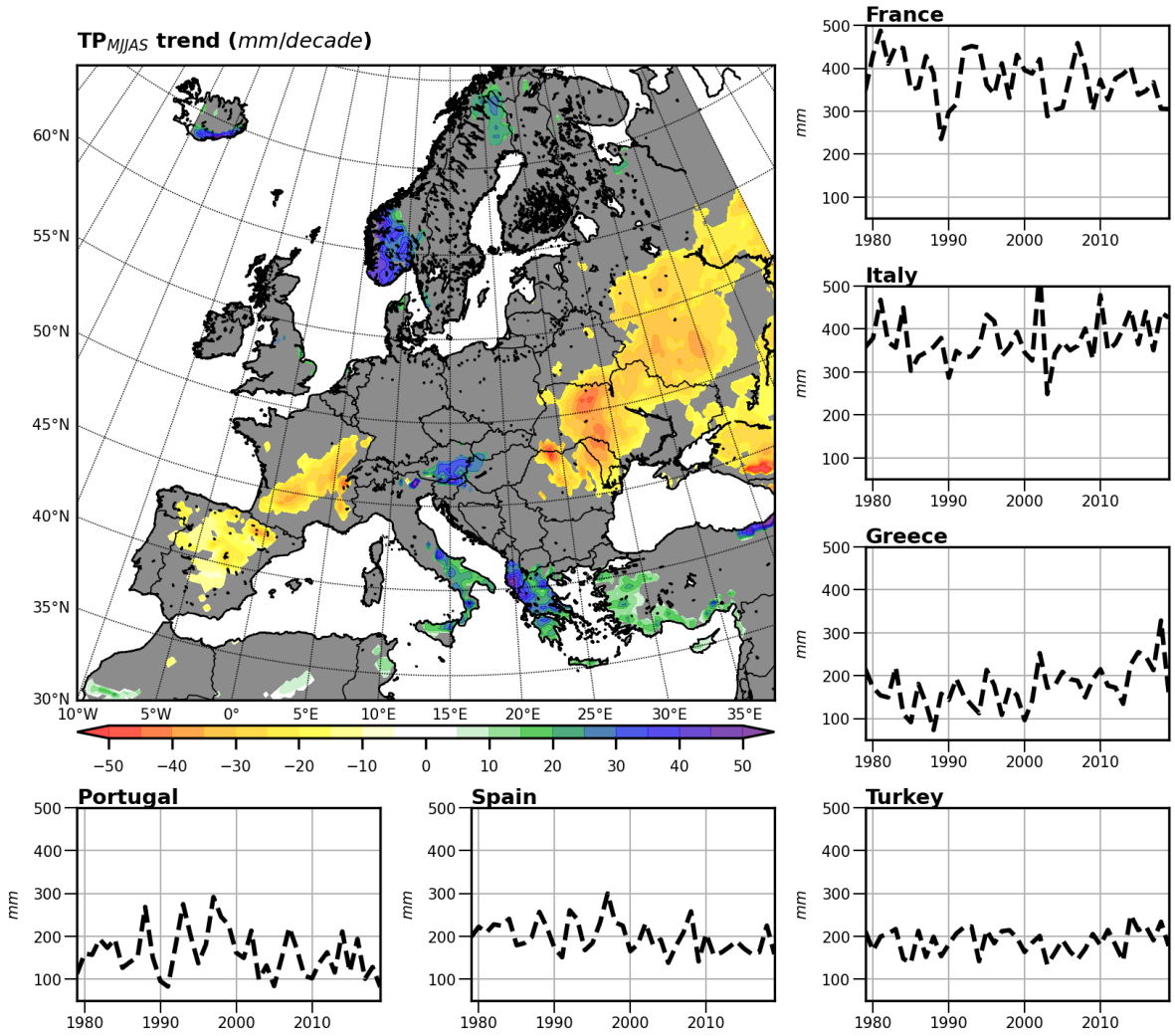


Supplementary Figure S5.19: Observed trend in fire risk, atmospheric instability and firestorm risk 1980-2018. From ERA5 reanalysis 1980-2018 period, trend in the number of days per decade with **a** FWI, **b** K-index and **c** both FWI and K-index above their threshold. Grey shaded regions indicate that the data presents a non-significant result (p-value>0.05). Country-averaged time series for the number of days per year with high FWI (red), high Kindex (blue) and both FWI and K-index high values (black) are also shown.



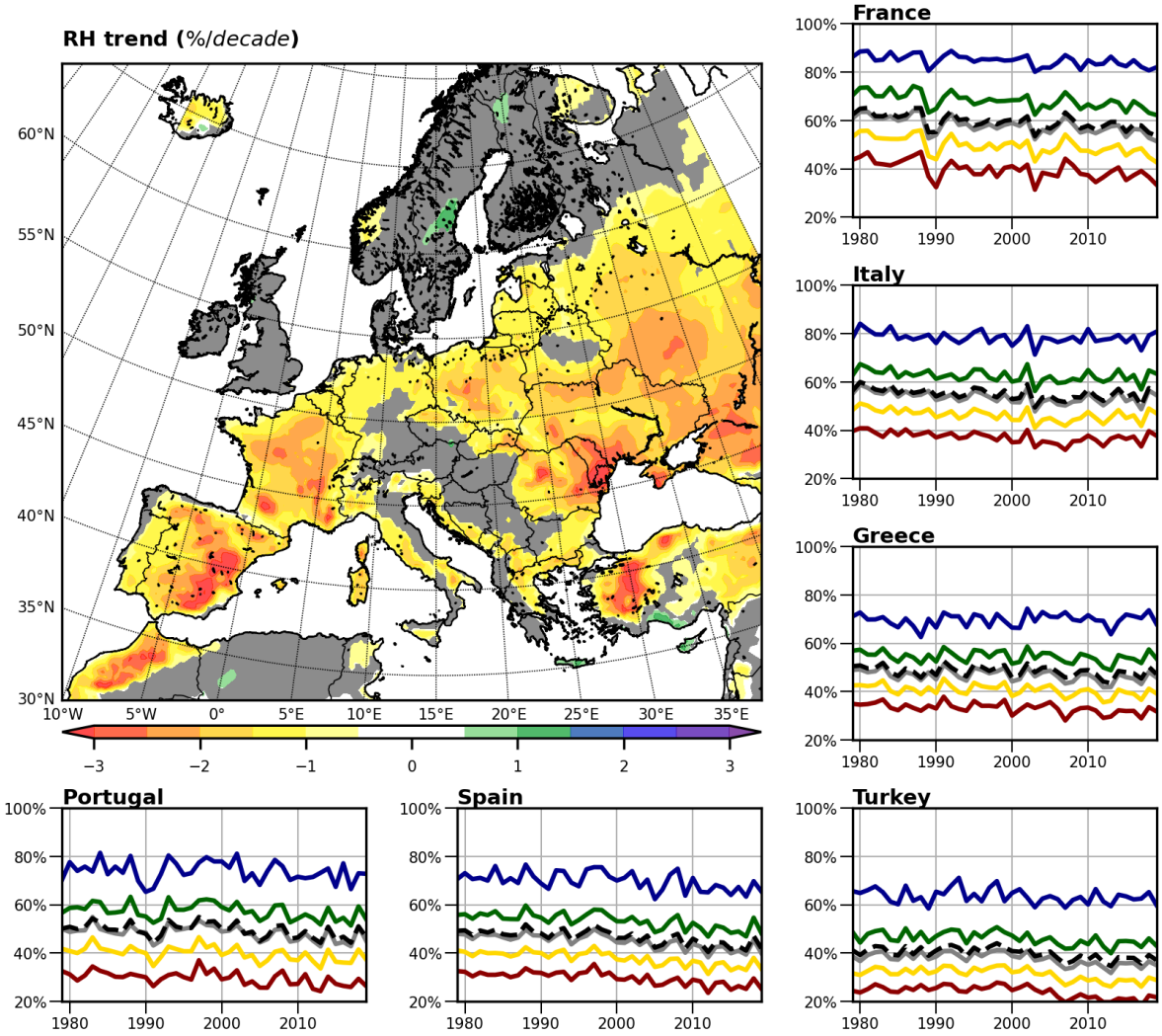
Supplementary Figure S5.20: Observed trend in summer 2m temperature for 1980-2018. Trend of the average midday 2m temperature in May, June, July, August and September according to the ERA5 reanalysis for 1980-2018. Grey shaded regions indicate a nonsignificant result (p-value>0.05). Country-averaged annual time series for 95th (red), 75th (yellow), 50th (grey), 25th (green) and 5th (blue) percentiles and mean (black dashed) of the 2m temperature values during the months of May, June, July, August and September are also shown.

USC
UNIVERSIDADE DE SANTIAGO DE COMPOSTELA



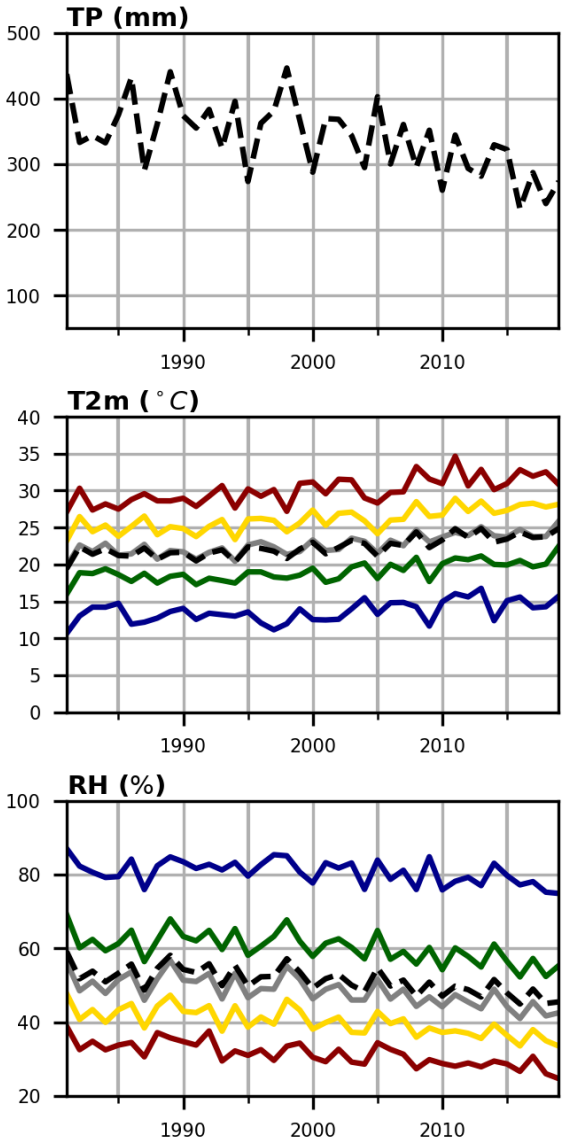
Supplementary Figure S5.21: Observed trend in summer precipitation for 1980-2018. Trend of the total precipitation accumulated in May, June, July, August and September according to the ERA5 reanalysis for 1980-2018. Grey shaded regions indicate a non-significant result (p-value>0.05). Country-averaged annual time series for the total precipitation during the months of May, June, July, August and September are also shown.

USC
UNIVERSIDADE DE SANTIAGO DE COMPOSTELA



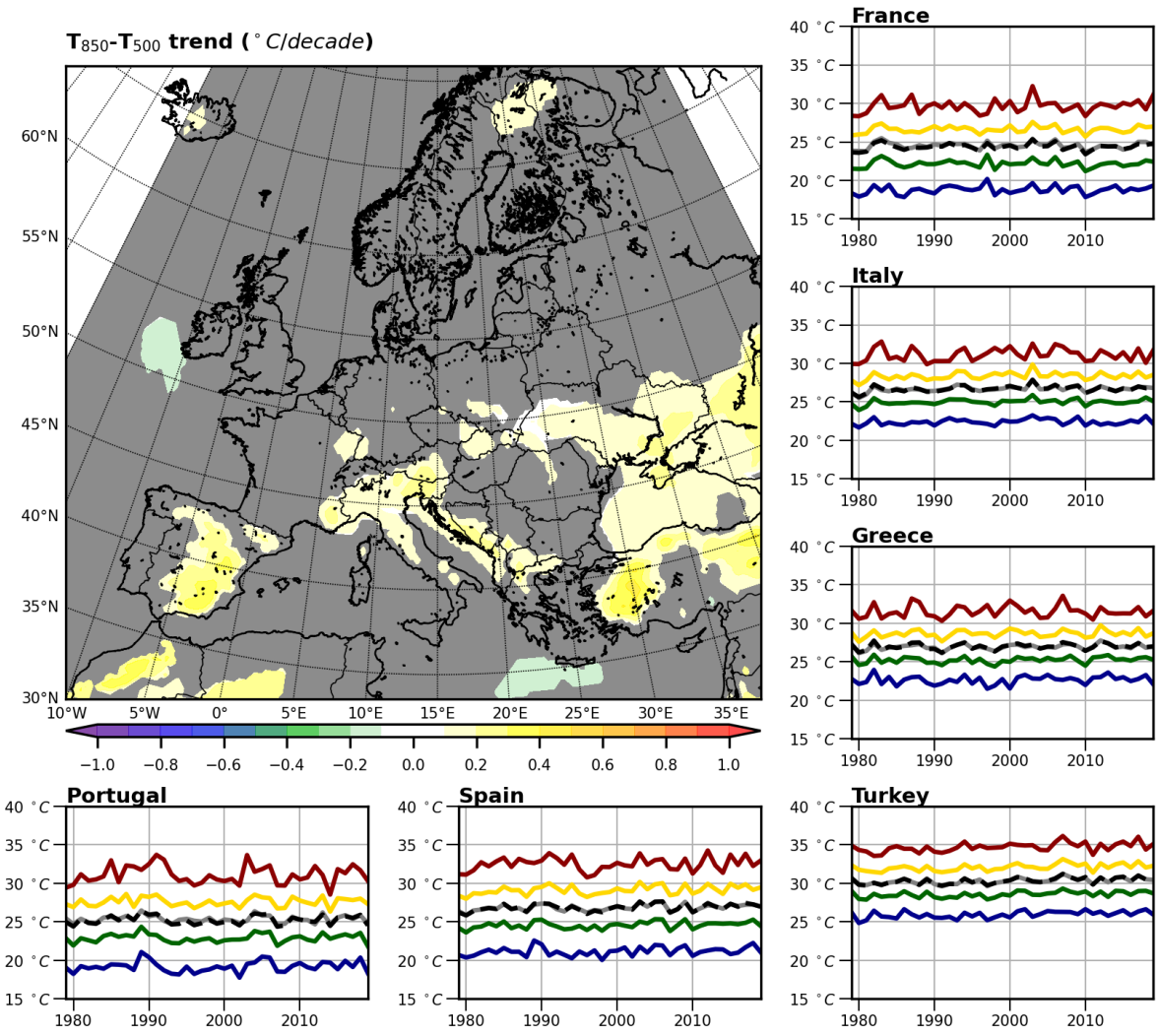
Supplementary Figure S5.22: Observed trend in summer relative humidity for 1980-2018. Trend of the average midday 2m relative humidity in May, June, July, August and September according to the ERA5 reanalysis for 1980-2018. Grey shaded regions indicate a nonsignificant result (p-value>0.05). Country-averaged annual time series for 95th (blue), 75th (green), 50th (grey), 25th (yellow) and 5th (red) percentiles and mean (black dashed) of the 2m relative humidity values during the months of May, June, July, August and September are also shown.

USC
UNIVERSIDADE DE SANTIAGO DE COMPOSTELA



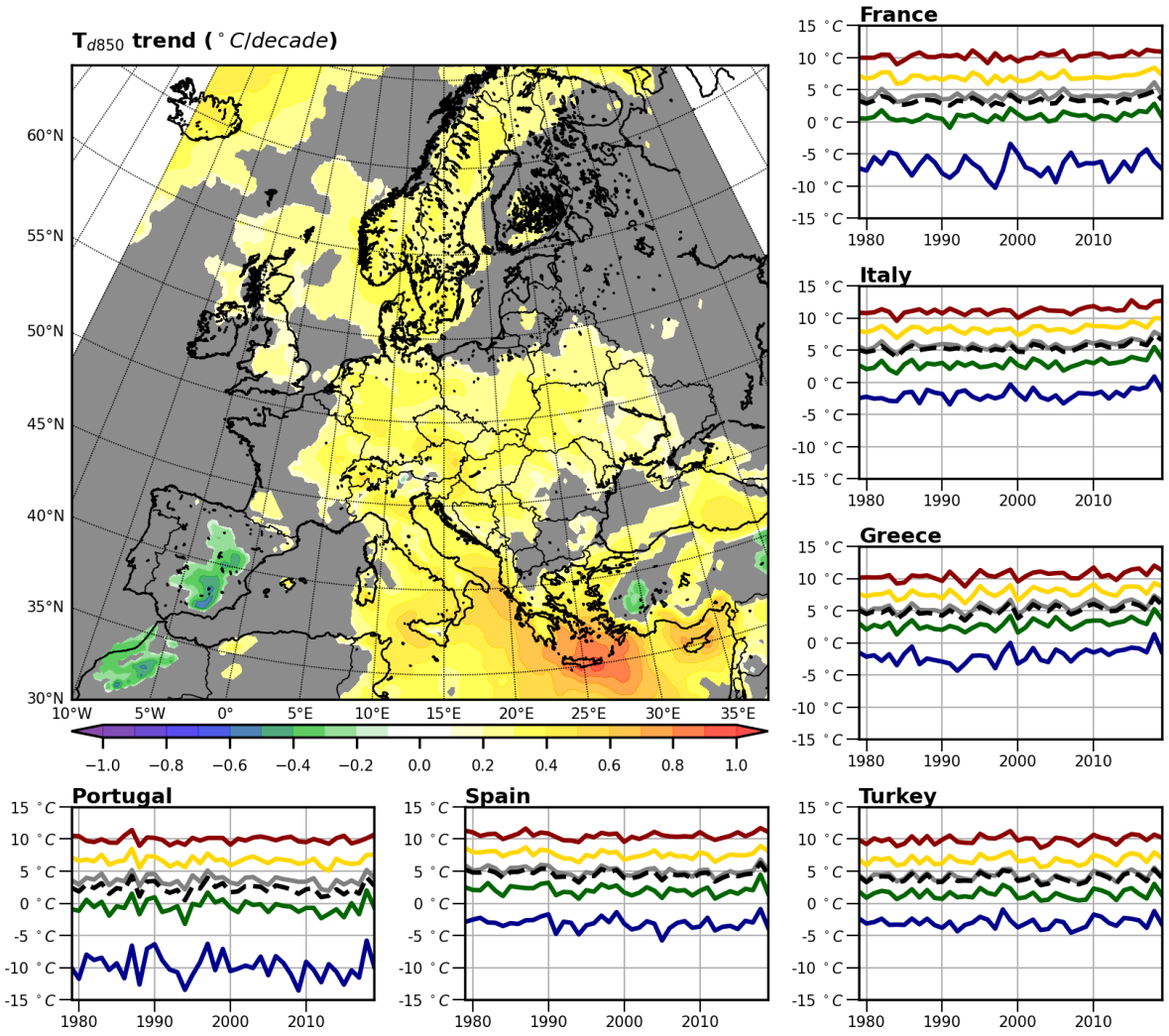
Supplementary Figure S5.23: Observed trends in Ukraine for 1980-2018. Ukraine country-averaged annual time series for total precipitation and time series for 95th (red), 75th (yellow), 50th (grey), 25th (green) and 5th (blue) percentiles and mean (black dashed) of the mean 2m temperature and relative humidity values during the months of May, June, July, August and September.

USC
UNIVERSIDADE DE SANTIAGO DE COMPOSTELA



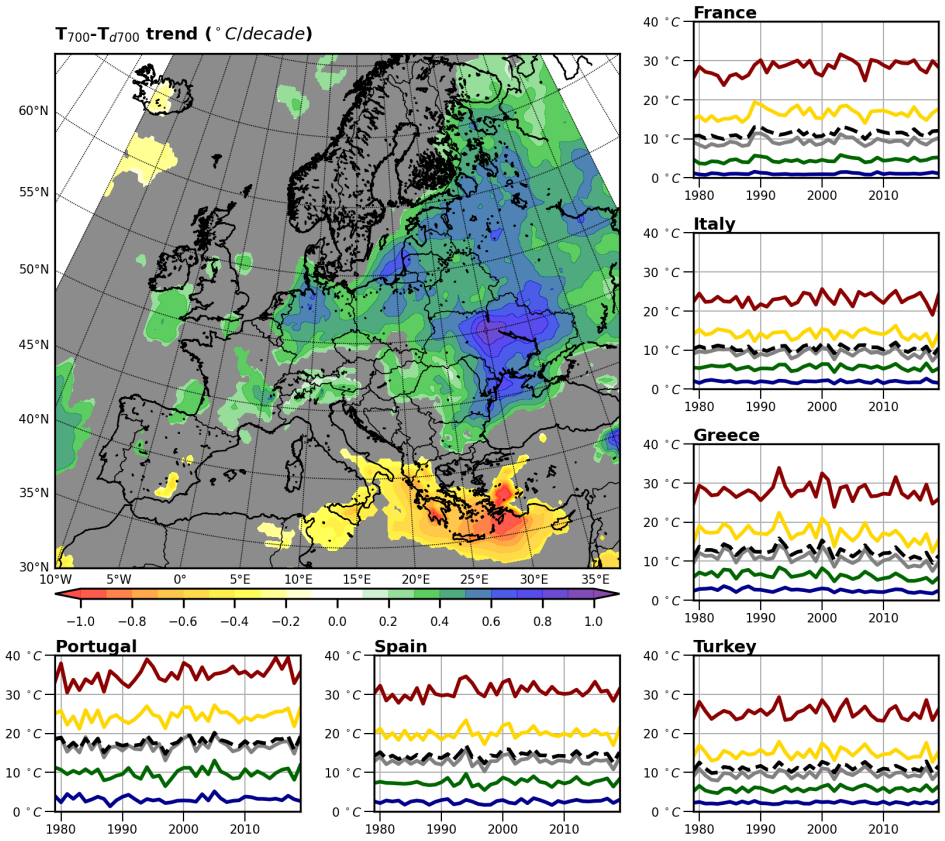
Supplementary Figure S5.24: Observed trend in temperature difference between 850 hPa and 500 hPa for 1980-2018. Trend of the average temperature difference between 850 hPa and 500 hPa in May, June, July, August and September according to the ERA5 reanalysis for 1980-2018. Grey shaded regions indicate a non-significant result (p-value>0.05). Countryaveraged annual time series for 95th (red), 75th (yellow), 50th (grey), 25th (green) and 5th (blue) percentiles and mean (black dashed) of the temperature difference between 850 hPa and 500 hPa values during the months of May, June, July, August and September are also shown.

USC
UNIVERSIDADE DE SANTIAGO DE COMPOSTELA



Supplementary Figure S5.25: Observed trend in dew point temperature at 850 hPa for 1980-2018. Trend of the mean dew point temperature at 850 hPa in May, June, July, August and September according to the ERA5 reanalysis for 1980-2018. Grey shaded regions indicate a non-significant result (p-value>0.05). Country-averaged annual time series for 95th (red), 75th (yellow), 50th (grey), 25th (green) and 5th (blue) percentiles and mean (black dashed) of the dew point temperature at 850 hPa values during the months of May, June, July, August and September are also shown.

USC
UNIVERSIDADE DE SANTIAGO DE COMPOSTELA



Supplementary Figure S5.26: Observed trend in dew point depression at 700 hPa for 1980-2018. Trend of the mean dew point depression at 700 hPa in May, June, July, August and September according to the ERA5 reanalysis for 1980-2018. Grey shaded regions indicate a non-significant result (p-value>0.05). Country-averaged annual time series for 95th (red), 75th (yellow), 50th (grey), 25th (green) and 5th (blue) percentiles and mean (black dashed) of the dew point depression at 700 hPa values during the months of May, June, July, August and September are also shown.

USC UNIVERSIDADE DE SANTIAGO DE COMPOSTELA

Supplementary Tables

Supplementary Table S5.1: Information about the outputs of the idealized simulations for validation. PyroCu indicates the creation of a cloud by the fire in at least one of the simulations. Fuels PyroCu indicates the number of fuel models for which a cloud is formed. K-index and FWI columns indicate the corresponding value of these two indexes for each case. The FWI threshold for the corresponding location is indicated in brackets.

Case	Date	Coordinates	Country	PyroCu	Fuels PyroCu	K-index (°C)	FWI (threshold)
1	2010-08-04	(55.00°N, 41.75°E)	Russia	Yes	2/5	27.90	41.06 (14.72)
2	2017-06-17	(40.00°N, -8.00°E)	Portugal	Yes	2/5	30.06	44.70 (35.36)
3	2018-08-08	(39.00°N, -0.25°E)	Spain	Yes	1/5	33.38	36.34 (29.74)
4	2019-07-15	(38.75°N, -0.75°E)	Spain	Yes	2/5	31.60	51.71 (42.31)
5	2021-07-25	(41.50°N, 1.50°E)	Spain	Yes	2/5	25.02	41.23 (28.87)
6	2021-08-05	(38.25°N, 23.75°E)	Greece	Yes	2/5	24.09	51.33 (47.20)
7	2021-08-15	(40.50°N, -4.75°E)	Spain	No	0/5	26.30	56.79 (34.49)
8	2021-08-18	(38.25°N, 23.50°E)	Greece	Yes	2/5	29.58	46.61 (49.33)
9	2021-09-10	(36.50°N, -5.00°E)	Spain	Yes	2/5	22.21	28.65 (28.35)

USC UNIVERSIDADE DE SANTIAGO DE COMPOSTELA

Supplementary Table S5.2: Information about the selected locations. Altitude and wind information is obtained directly from ERA5 database, and Köppen-Geiger climate information is obtained from Peel *et al.* [203].

Point	**Coordinates**	**Country**	**Altitude (m)**	**Climate**	**Prevailing wind**
1	(41.5°N, -7.5°E)	Portugal	626	Warm summer Mediterranean (Csb)	N and S
2	(39.5°N, -5.0°E)	Spain	682	Semiarid (BSk)	S and N-E
3	(43.5°N, 6.0°E)	France	388	Hot summer Mediterranean (Csa)	S-E and N-W
4	(41.5°N, 15.5°E)	Italy	163	Humid subtropical (Cfa)	S-E and S-W
5	(39.5°N, 22.5°E)	Greece	254	Hot summer Mediterranean (Csa)	N and S-W
6	(39.5°N, 34.5°E)	Turkey	1096	Semiarid (BSk)	E and S-W

USC UNIVERSIDADE DE SANTIAGO DE COMPOSTELA

USC
UNIVERSIDADE
DE SANTIAGO
DE COMPOSTELA

Chapter 6

Wildfire-atmosphere interactions in Galicia

Galicia and the north of Portugal is one of the most fire-active regions of Europe (Figure 6.1). The connection between wildfires and climate change has gained attention in Galician society in recent decades due to the occurrence of some extreme fire events, such as the August 2006 wildfires [258], the October 2017 Hurricane Ophelia fires [152] or the extreme 2022 fire season [76]. In this chapter we will revisit some results presented in the previous chapters with a focus on Galicia, extending some particular questions with additional analyses.

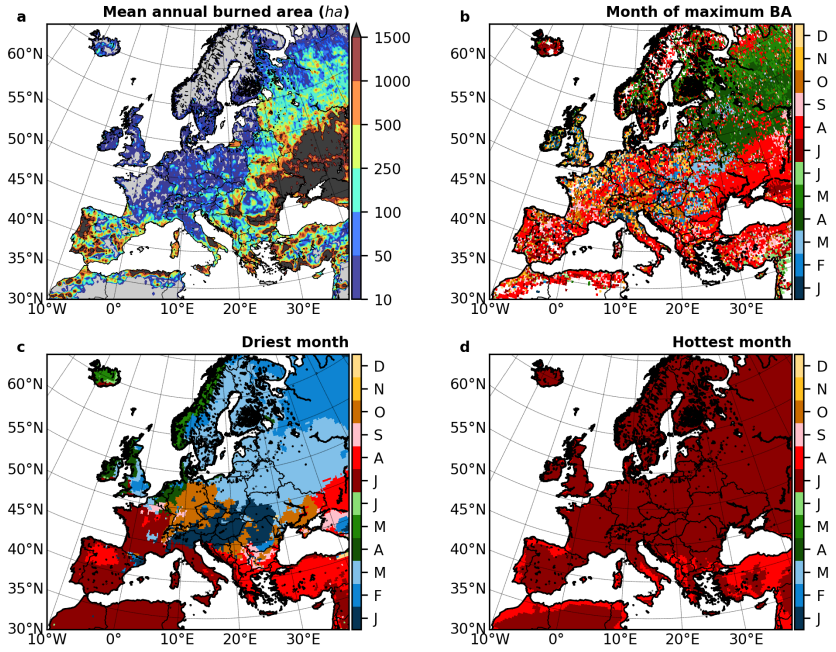


Figure 6.1: Fire activity in Europe. **a**, Mean annual burned area. **b**, Month with the maximum average burned area. **c**, Month with the minimum monthly total precipitation. **d**, Month with the maximum monthly mean temperature. Burned area data were obtained from the 1982-2018 AVHRR-LTDR Burned Area Grid product produced by the ESA Fire Climate Change Initiative (FireCCI) [292]. Climate data were obtained from ERA5 reanalysis [129].

USC
UNIVERSIDADE DE SANTIAGO DE COMPOSTELA

6.1 Climate scale

The northwest of the Iberian Peninsula is classified as a Temperate - dry and hot season fire category (Figure 3.2), characterized by a dry season coinciding with summer temperatures (Figure 6.1). Additionally, this region is also characterized by a high biomass productivity (Figure 6.2b) that leads to high fuel abundance, since this is one of the most rainy regions of Europe (along with the Alps, the Scottish Highlands, the Norwegian coast and the east coast of the Balcans, see Figure 6.2a).

According to our results, the potential fire season length in Galicia will increase by 2 months due to climate change (Figure 3.3a), moving from 2-3 months length at present to 4-5 months length by the end of the 21st century (Figure 3.3b,c). The recurrence of fire-prone conditions will also increase: 1 or 2 years more with fire-prone conditions per decade in the south of Galicia and 2 or 3 years more per decade in the north (Figure 3.4b,c).

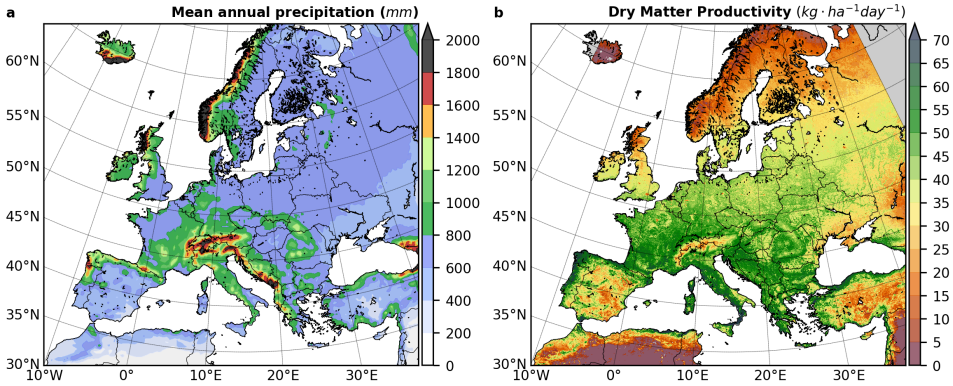


Figure 6.2: **a**, Mean annual precipitation from 1940-2022 ERA5 reanalysis [129]. **b**, Mean dry matter productivity representing the overall growth rate of vegetation, obtained from 1999-2019 data generated by the Global Land Service of Copernicus, derived from SPOT-VGT and PROBA-V imagery combined with meteorological data from ECMWF.

Although Galicia is already a fire-prone region at present, the mere increase in fire recurrence due to climate change may alter the effect of fires on climate. The release of carbon dioxide due to biomass combustion is largely neutralised after the recovery of vegetation in the fire-affected area. However, in a context of more frequent fires, vegetation may transition to structures with lower biomass load thus altering the carbon cycle, either due to natural causes (where vegetation adapts to new fire regimes) or human causes (where society reduces forest cover in order to avoid extreme fires).

Increased fire activity will also lead to climate effects through smoke emissions that can alter the radiative balance and the composition of the atmosphere. Smoke fire emissions are particularly important during extreme fire events, since it has been estimated that 2% of the fires in the Mediterranean region account for 80% of the total burned area [258]. As an example, during the October 2017 Ophelia fires in Portugal, particulate matter (PM2.5 and PM10) and carbon monoxide emissions were higher than the Portuguese anthropogenic emissions over the entire 2017 year [293].

USC UNIVERSIDADE DE SANTIAGO DE COMPOSTELA

Table 6.1: Rate of spread increase due to the thermodynamic component of climate change between pre-industrial and present conditions for the 20 most affected wildfires in Galicia between 2001 and 2021.

Date	Municipality	Province	Burned area (ha)	ROS increase (%)
2020-09-14	Manzaneda	Ourense	811	51.09
2020-09-13	Cualedro	Ourense	1310	48.78
2020-09-12	Vilar de Barrio	Ourense	505	46.81
2016-09-12	Cualedro	Ourense	1588	45.77
2015-08-30	Cualedro	Ourense	1490	45.47
2020-09-13	Vilariño de Conso	Ourense	817	44.30
2016-09-06	Oímbra	Ourense	1363	44.13
2020-09-14	A Mezquita	Ourense	520	42.96
2020-09-13	Chandrexa de Queixa	Ourense	706	39.99
2021-09-05	Ribas de Sil	Lugo	1478	37.22
2020-09-13	Lobios	Ourense	2026	30.63
2011-08-13	Carballeda de Valdeorras	Ourense	513	30.22
2016-09-05	Muíños	Ourense	747	29.29
2005-08-30	Calvos de Randín	Ourense	564	28.52
2017-08-03	Verín	Ourense	1372	27.66
2013-09-11	Negreira	A Coruña	646	26.71
2016-09-06	Entrimo	Ourense	3000	25.40
2005-08-20	Pazos de Borbén	Pontevedra	2896	24.77
2006-08-31	Quiroga	Lugo	2365	24.16
2010-08-29	Laza	Ourense	1715	23.81

6.2 Synoptic scale

According to the results shown in Chapter 4, the influence of the anthropogenic temperature increase on the rate of spread is higher in Galicia than in the rest of the Iberian Peninsula, with more than 80% of the >500 ha wildfire events between 2001 and 2021 experiencing a significant increase in the rate of spread since pre-industrial conditions, a considerably higher value than for the Iberian Peninsula as a whole (50%). This rate of spread intensification is specially important in the south of the Ourense province, an area with particularly high fire activity (Figure 4.2a). In Table 6.1 we observe that three wildfires that occurred in the province of Ourense in Septeber of 2020 were the most affected by the temperature increase since the pre-industrial period, with a percentage increase in the rate of spread of around 50%.

It has been demonstrated that climate change is affecting fire behaviour in the Iberian Peninsula. But it remains to be determined whether this increased fire rate of spread may be affecting the meteorology of the Iberian Peninsula on a synoptic scale. To determine this we have conducted a small experiment with the WRF weather model [179], in which we have evaluated the impact of the area burned by the October 2017 fires on the meteorology of the following spring (specifically the months of May and June of 2018).

Using two nested domains of 9 km and 3 km respectively, we performed 2 simulations with the WRF atmospheric model from the 15th of April of 2018 to the 30th of June of 2018, using ERA5 reanlaysis [129] as boundary and initial conditions. To ensure that the

results of the simulations do not differ from the reanalysis, we ran the simulations with a spectral nudging technique [294]. One of the two simulations (control test) is performed with monthly characteristic values of the surface albedo, Leaf Area Index (LAI) and Fraction of Absorbed Photosynthetically Active Radiation (FAPAR) already included in the model. The other simulation (burned area test) was performed by taking into account the influence of the 2017 fires in these three variables, so we change these model land inputs with the obtained anomalies from satellite observations (Figure 6.3). By comparing these two simulations we can estimate the influence of the 2017 burned area in different meteorological variables on the 2018 spring.

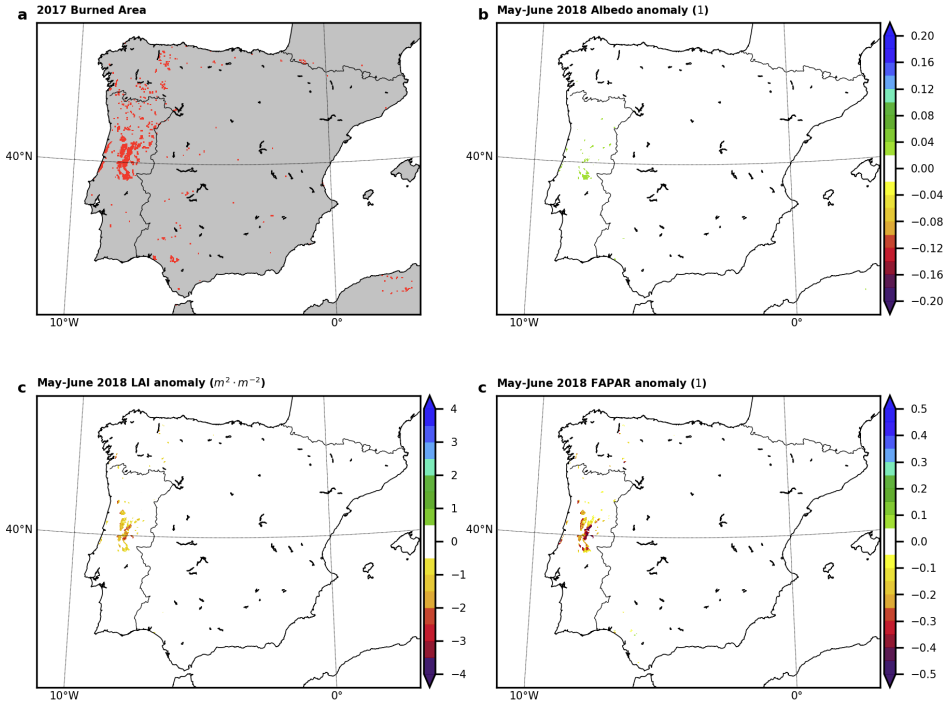


Figure 6.3: Influence of October 2017 fires in land inputs. **a**, 2017 burned area in red obtained from ESA FireCCI data [292]. **b**, Surface albedo anomaly of May-June 2018 from the May-June 1999-2019 average. **c**, Leaf Area Index (LAI) anomaly of May-June 2018 from the May-June 1999-2019 average. **d**, Fraction of Absorbed Photosynthetically Active Radiation (FAPAR) anomaly of May-June 2018 from the May-June 1999-2019 average. Surface albedo, LAI and FAPAR data were obtained from the Global Land Service of Copernicus, derived from SPOT-VGT and PROBA-V imagery combined with meteorological data from ECMWF.

The combined effect of the altered radiative balance and the changes in the soil-atmosphere fluxes leads to a noticeable increase in atmospheric surface temperature in the vicinity of the 2017 burned areas (Figure 6.4a). A reduction in the relative humidity is also observed, although its signal is not as robust as that of the temperature rise (Figure 6.4b).

Water evaporation over the continent has a very marked seasonal cycle, being predominant over the ocean water evaporation during the months of May, June, July and August in the Northern Hemisphere above 30° [81]. Some of this continental evaporation is associated with vegetation transpiration, and may become a major source of precipitation events during these months [81]. We assessed whether the reduction of vegetation due to the 2017 fires had an

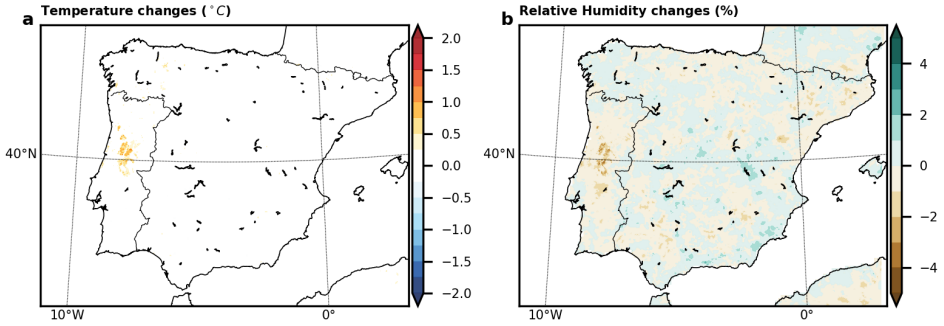


Figure 6.4: Influence of October 2017 fires in atmospheric surface variables. **a**, May-June 2018 2m air temperature average difference between the burned area test (that takes into account the 2017 burned area influence on land inputs) and the control test. **b**, May-June 2018 2m relative humidity average difference between the burned area test and the control test.

effect on precipitation in the Iberian Peninsula during the months of May and June of 2018. Although our simulations show a slight decrease in total precipitation in the burned area test (see Figure 6.5), this reduction is not robust enough to conclude that these 2017 fires have had an appreciable influence on precipitation.

The influence of fires on synoptic-scale precipitation may be limited to continental regions where the main moisture source feeding rainfall is local evapotranspiration (recycling), or to regions where the area affected by fires is even larger.

6.3 Local scale

At a local scale, the main mechanism of interaction between the wildfires and the atmosphere is pyroconvection. In Chapter 5 we show that the risk of pyroconvection is increasing due to climate change in the south of Europe. Although Galicia is not the region where this increase is most pronounced, the number of days per year with a high risk of deep pyroconvection will move from between 5 and 15 in the period 1970-2018 to between 15 and 25 in the period 2070-2099 under the RCP8.5 emissions scenario (Figure S5.14).

Deep pyroconvection events in Europe are not very frequent at the present time, not even in those areas with the highest fuel abundance, such as Galicia. However, during the 2022 summer we have been able to witness some pyroconvection events in the interior of Galicia. In particular, the events that followed the July 2022 heatwave were especially important, as they became the fires with the largest burnt area in Galicia in recent years.

On the 10th of July of 2022, a severe heatwave started in southwestern Europe, due to the flow of warm air from North Africa caused by a trough located in front of the Iberian Peninsula coast. Temperatures were especially high because of the low soil moisture content caused by the drought conditions, which results in a more efficient surface warming, as less heat is required to evaporate water from the soil. The exacerbated temperatures and the approximation of the trough caused the development of a mesoscale convective system (MSC) on the 14th of July. The mesoscale convective system resulted in a large amount of lightning, but with reduced precipitation. Some lightning strikes caused fires, which spread rapidly due to low fuel moisture. On the 17th of July, some of these fires produced pyroconvective clouds, that were

USC UNIVERSIDADE

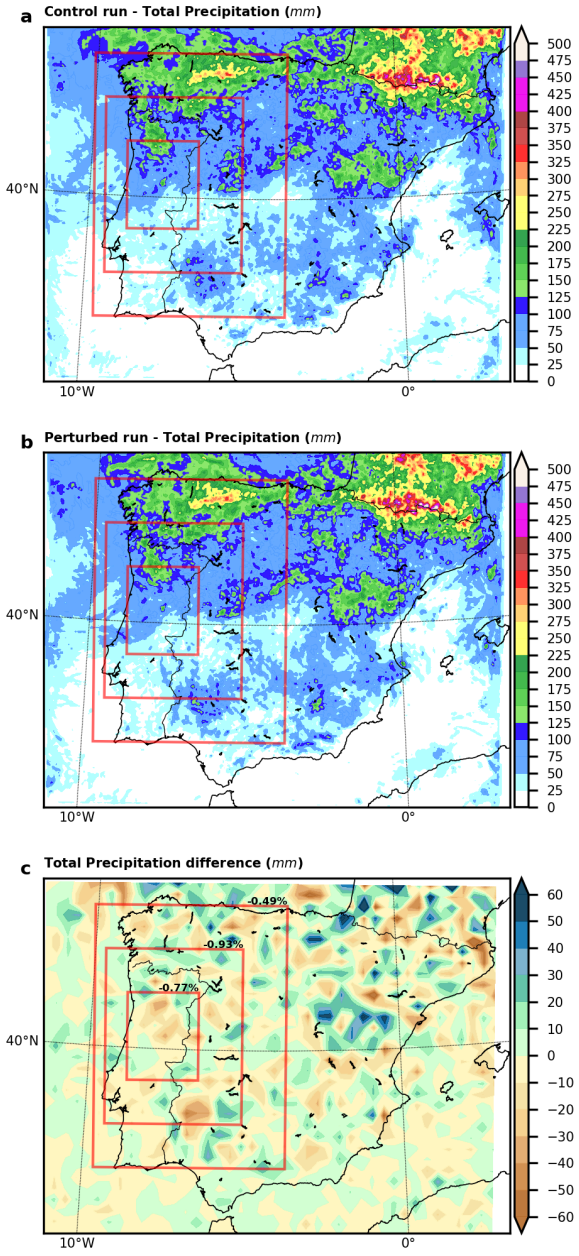


Figure 6.5: Influence of October 2017 fires in total precipitation. **a**, May-June 2018 total precipitation in the control test. **b**, May-June 2018 total precipitation in the burned area test (that takes into account the 2017 burned area influence on land inputs). **c**, May-June 2018 total precipitation difference between the burned area test and the control test, with the reduction in total precipitation for the three red-bounded regions expressed as a percentage.

observed form the NASA's Aqua satellite (Figure 6.6).

We have assessed whether the fire risk and atmospheric instability thresholds (quantified by the Fire Weather Index (FWI) and the K-index) chosen in Chapter 5 to detect pyroconvection events would be useful in this case to anticipate the occurrence of this phenomenon. We can observe in Figure 6.6 the timeseries of the FWI and the K-index for each fire observed in the satellite images. In fires 1 and 3, which are those with a clear pyroconvective cloud, the

atmospheric instability and fire risk were above the threshold at the time of cloud development (indicated by a vertical green line in the timeseries of Figure 6.6). In fire 2, atmospheric instability values are very close to the selected threshold. This fire seems to be associated with a lower pyroconvection intensity according to the satellite images (Figure 6.6).

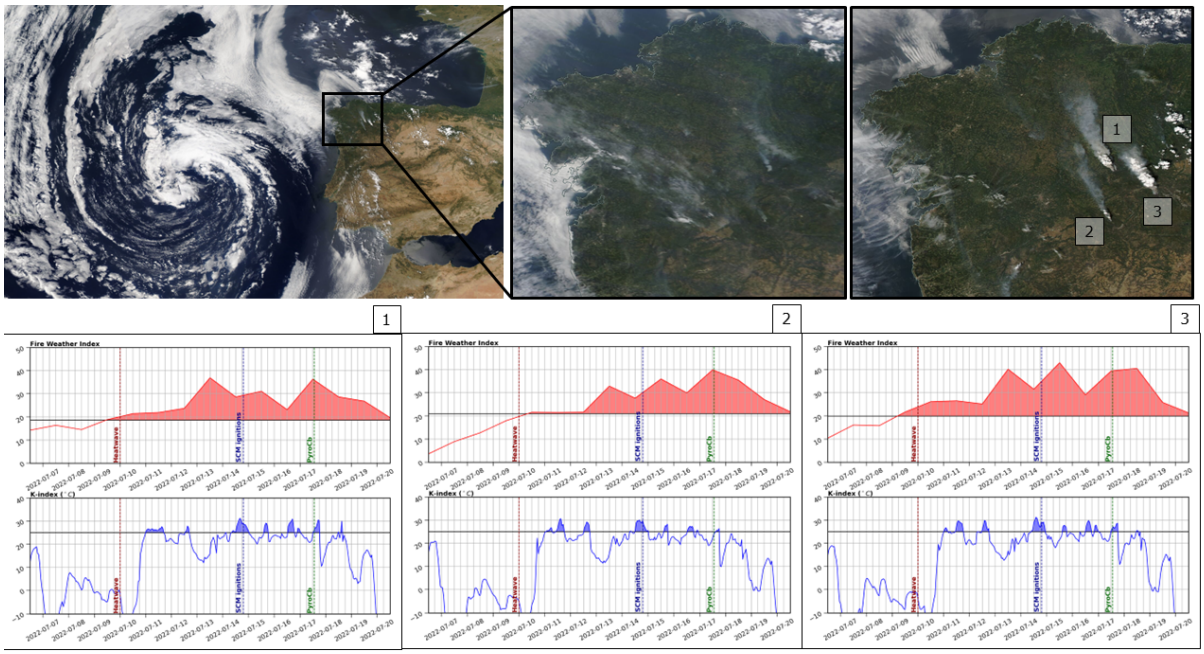


Figure 6.6: Satellite images of the trough located in front of the Iberian Peninsula coast on the 17th of July 2022 (left), and the development of different pyroconvective clouds in Galicia (middle image at 12:00h and right image at 13:30h). These images are from NASA's Worldview service, obtained from the Moderate Resolution Imaging Spectroradiometer (MODIS) instrument abroad the Aqua satellite. We acknowledge the use of imagery from the NASA Worldview application (https://worldview.earthdata.nasa.gov), part of the NASA Earth Observing System Data and Information System (EOSDIS). For each of the considered fires (labels 1, 2 and 3) we show the timeseires of the Fire Weather Index (FWI) and the K-index from ERA5 reanalysis data [129], representing the firestorm thresholds as horizontal lines.

USC
UNIVERSIDADE DE SANTIAGO DE COMPOSTELA

USC
UNIVERSIDADE
DE SANTIAGO
DE COMPOSTELA

Chapter 7

General conclusions

Throughout this thesis we have demonstrated that climate change is altering the interactions between wildfires and the atmosphere at different spatial and temporal scales.

On a global scale, climate conditions largely determine the spatial and temporal patterns of fire activity. We proved this by reproducing the global distribution of fire-prone regions through simple climatic thresholds. The association of some specific climate categories to the different fire-prone regions has allowed us to assess how the ongoing global warming will modify the present distribution of fire-prone regions and their related fire season. A general expansion of the global area with frequent fire-prone conditions is expected according to our results, specially in the boreal regions where the warming projections are more accentuated. The expected increase in fire activity in these northern regions is particularly important, as it may pose a threat to some of the Earth's most important carbon stocks. The area of carbon-rich peatlands with fire-prone conditions will increase significantly in the future according to our results, which will affect the carbon cycle by increasing the atmospheric CO_2, constituting a positive feedback on global warming. In addition to the spatial expansion of fire activity, we also show that in temperate and boreal regions the fire season will be longer. In Galicia the fire season may be increased by up to 2 months by the end of the 21st century.

We have conducted a more refined analysis to identify and quantify the physical processes that explain how climate change is altering fire behaviour in the Iberian Peninsula, by using a pseudo-global warming approach. We proved that the increased atmospheric water demand due to the temperature rise since pre-industrial times, has led to a general reduction in the moisture content of dead and live fuels, resulting in a significant increase in the rate of spread of more than 50% of the registered wildfires in the 2001-2021 period. However, the enhanced vegetation growth caused by a more carbon-rich atmosphere could potentially have a stronger impact on wildfire rate of spread than that of the increased temperature. By the end of the 21st century, the effect of temperature increase on the rate of spread is expected to become even more pronounced, while the effect of vegetation productivity is expected to become less important than that of the temperature rise. This shift evidences that the relationship of climate change with fire behaviour is driven by non-linear processes. Higher rate of spread can lead to an increase in the burned area. We have shown that vegetation disturbances in fire burned areas associated with an extreme wildfire season can have a noticeable impact on surface air temperature and relative humidity even several months after the fires, but the influence on precipitation is very limited or practically negligible in the Iberian Peninsula.

Finally, we have identified the environmental conditions that favour pyroconvection in

USC UNIVERSIDADE DE SANTIAGO DE COMPOSTELA

Europe, the process by which fires modify local atmospheric conditions, which can in turn influence fire propagation. By using a numerical fire-atmosphere coupled model, we were able to determine a set of atmospheric instability and fire risk thresholds that can determine the days with a high atmospheric risk of deep pyroconvection development. Through different regional climate change projections we proved that the number of days per year with high risk of deep pyroconvection development is increasing in the south of Europe. We could also test the performance of our thresholds in a multiple pyroconvective fire event that took place in Galicia during the 2022 summer, in which we confirm that our method would be able to identify the occurrence of pyroconvection in these events.

In general, we can conclude that wildfires will have a more important role within the Earth system due to climate change, since it was shown that fire-atmosphere interactions are intensifying at different scales.

USC
UNIVERSIDADE
DE SANTIAGO
DE COMPOSTELA

List of Figures

1.1 Schematic representation of the interactions between wildfires, humans, vegetation and the atmosphere. 24
1.2 Contribution of different forcing agents to changes in effective radiative forcing (ERF) and global surface air temperature (T) from 1750 to 2019. Data from ref. [118]. 30
1.3 Global mean surface temperature from the Temperature 12k database using different reconstruction methods. Coloured lines are the ensemble medians of each of the five reconstruction methods (Standard Calibrated Composite (SCC), Dynamic Calibrated Composite (DCC), Composite Plus Scale (CPS), Pairwise Comparison (PAI) and Generalized Additive Model (GAM)). Gray shading represents every 5th percentile of the 2500 ensemble members from all methods; the 5th and 95th percentiles are indicated by dotted lines. The fine blue line is the median latitude-band 2000-year, multi-model temperature field reconstruction from Neukom *et al.* [122], which was based on data from PAGES 2k Consortium [123]. The fine black line is instrumental data for 1900–2010 from the ERA-20C reanalysis product [124]. The inset displays an enlarged view of the past 2000 years. Adapted with permission of Springer Nature from Kaufman *et al.*, ref. [125]. 31
1.4 Historical trends of different environmental variables. **a**, 1940-2022 2 m temperature trend, **b**, 1980-2022 2 m temperature trend, **c**, 1940-2022 total column atmospheric water vapour trend, **d**, 1940-2022 2 m relative humidity trend, **e**, 1940-2022 annual precipitation trend and **f**, 1982-2020 leaf area index trend. Data for panels **a**, **b**, **c**, **d** and **e** were obtained from ERA5 reanalysis [129] and data for panel **f** were obtained from GIMMS LAI4g dataset [130]. . . 32
1.5 Global mean surface temperature anomaly for multiple models of CMIP3 [134], CMIP5 [133] and CMIP6 [132]. Historical period of each CMIP is coloured in grey. Each colour of the future projections represent a different scenario. ERA5 global mean surface temperature (1940-2020) is shown in black [129]. Temperature anomalies were obtained from ERA5 1940-2020 mean surface temperature [129]. 34

2.1 Schematic representation of a no-wind and no-slope spreading fire (**a**), a wind-driven fire (**b**) and a slope driven fire (**c**), with arrows I_x and I_z representing the horizontal and vertical term of the propagating flux. 39

USC
UNIVERSIDADE DE SANTIAGO DE COMPOSTELA

2.2 Rate of spread relations. **a**, Rate of spread decline with dead fuel moisture, expressed as a fraction between the rate of spread at different fuel moisture contents and the rate of spread at zero moisture content. **b**, Correlation of wind speeds and slope angles with identical effect on the rate of spread. Results are shown for the 13 Anderson fuel models [167], with different colours representing fuel model groups (grass, shrub, timber and slash). 42
2.3 Hurricane Ophelia near the Iberian Peninsula. **a**, Infrared satellite image of the day 2017-10-14 at 1800Z from the Meteosat Second Generation (MSG) [181] satellites, obtained from the Galician meteorological service (MeteoGalicia) website. **b**, Mean sea level pressure, 10 m wind barbs and 2 m air temperature from ERA5 reanalysis data. **b**, 2 m air temperature on 2017-10-15 at 1500Z. **c**, 2 m relative humidity on 2017-10-15 at 1500Z. Panel **b** and **c** also show the mean sea level pressure (black lines), 10 m wind speed (wind barbs) and the trajectory of the hurricane center (red line). Data for panels **b** and **c** were obatained from the first domain of the WRF-Fire simulations. 48
2.4 WRF-Fire model domain configurations used to reproduce 2017-10-15 wildfire in Nigrán, consisting of 5 models of resolutions 8100 m, 2700 m, 900 m, 300 m and 100 m. 49
2.5 Bunrned area dependence on fuel moisture content. Time series of the modelled fire burned area increase for the As Neves wildfire. Each line represents each of the simulations with different fuel moisture contents (fmc) expressed as a fraction. 50
2.6 As Neves (top) and Gondomar (bottom) fire simulation. **a**, Simulated fire burned area (in red) at instant of maximum accuracy, observed final burned area (black contour filled in grey), terrain height in white contours and 10 m wind speed in wind barbs, represented over a Google Earth image. **b**, Simulation accuracy time series (equation 2.46) in black and simulation detection time series (equation 2.46) in green. **c**, Total simulated burned area time series in red and final observed burned area in black. **d**, Time series of fire burning rate, expressed in burned area per hour ($\mathrm{ha}\cdot\mathrm{h}^{-1}$). A vertical dashed line indicates the instant of maximum accuracy in the time series. 51
2.7 As Neves fire influence on atmospheric conditions. **a**, 20 m air temperature (in °C) on 2017-10-16 at 01:00h. **b**, 200 m vertical component of wind (in $\mathrm{m}\cdot\mathrm{s}^{-1}$) on 2017-10-16 at 01:00h. **c**, Vertical cross section of the vertical component of wind (in $\mathrm{m}\cdot\mathrm{s}^{-1}$) on 2017-10-16 at 01:00h. The location of the cross section is indicated in panel **b** with a horizontal orange dashed line. **d**, Horizontal wind speed anomaly at surface originated by the fire (in $\mathrm{m}\cdot\mathrm{s}^{-1}$) on 2017-10-16 at 01:00h. The wind speed anomaly is computed by subtracting the wind intensity of the control simulation (a simulation without the fire) from the wind intensity of the fire simulation. 52

USC UNIVERSIDADE DE SANTIAGO DE COMPOSTELA

2.8 Pedrógão Grande fire simulation. **a**, Observed burned area perimeter of the fire in red and schematic representation of the actual fire spread from 14:00h to 17:00h (grey perimeter), 17:00h to 19:00h (blue perimeter) and 19:00h to 21:00h (yellow perimeter), according to ref. [184]. **b**, High cloud cover percentage in the fire simulation at 17:20h and modelled fire burned area in red. **c**, Vertical cross section of the vertical wind component in $m \cdot s^{-1}$ and horizontal wind barbs. The location of the cross section is indicated in panel **b** with a horizontal orange dashed line. **d**, Horizontal wind speed anomaly at surface originated by the fire (in $m \cdot s^{-1}$) at 18:30h. The wind speed anomaly is computed by subtracting the wind intensity of the control simulation (non-fire simulation) from the wind intensity of the fire simulation. Wind anomaly directions are indicated though horizontal arrows. 53

3.1 Burned area observations and climate drivers. **a**, 1996-2016 maximum annual burned area (*BAmax*) and monthly burned area time series for selected regions. **b** Average monthly precipitation percentage from the annual total for the fire season (PP_{FS}). **c** Average monthly temperature anomaly from the annual mean for the fire season (TA_{FS}). 57

3.2 Fire-prone region classification. **a**, With observed burned area data as a reference: Not classified (NC, white) and misclassified (C, black) areas with $BAmax = 0ha$, unclassified (NC, grey) and classified (Tr-ds, Ar-fl, Te-dhs and Bo-hs) areas with $BAmax > 0ha$. Each class is subdivided into 3 subcategories depending on the recurrence of the fire-prone conditions: recurrent (r), occasional (o) and infrequent (i). **a**, Present (1996-2016) fire-prone climatic regions. **c**, Future (2070-2099) fire-prone climatic regions with shaded grey representing a ¡75% confidence percentage, estimated as the percentage of CMIP5 Global Circulation Models (GCMs) agreeing on the result. 65

3.3 Potential Fire Season. **a**, Future minus present Potential Fire Season Length ($PFSL$) difference in months ($\Delta PFSL$). **b**, Present Potential Fire Season. **c**, Future Potential Fire Season. 67

3.4 Fire Prone Years. **a**, Future minus present number of years with at least one month classified as fire-prone per decade (ΔFPY). **b**, Present fire-prone years per decade. **c**, Future fire-prone years per decade. 68

3.5 Global peatland extent expressed as land cover percent. **a**, Peatland extent coinciding with present (1996-2016) recurrent fire-prone regions (in blue). **b**, Peatland extent coinciding with future (2070-2099) recurrent fire-prone regions (in red). In both panels, the peatland cover not coinciding with recurrent fire-prone regions is represented in grey colors. Data for global peatland cover were obtained from Melton *et al.* [236]. 70

S3.1 **a**, Fire season length. **b**, Percentage of mean annual burned area (BA) corresponding to cropland land cover from GFED4 data. 72

S3.2 **a**, Mean annual burned area. **b**, Number of years with an annual burned area >100ha per decade. 73

S3.3 World general climate classification. Based on the Köppen-Geiger classification but modifying the C-D category threshold to delimit the boreal forest ecoregion. 74

USC UNIVERSIDADE DE SANTIAGO DE COMPOSTELA

S3.4 Statistical distributions scheme. **a**, Annual variables (Pa, Ta, Pmin and Tmax) are split into values for $BA \geq 100$ha years and values for $BA < 100$ha years, all grid cells within the same main climate class are considered. Monthly variables (Pm and Tm) are used for two different comparisons: **b** seasonal and **c** interannual. The monthly seasonal distribution (**b**) compares the FS months of the $BA \geq 100$ha years against the months that are not part of a FS. For cells with no fire incidence, there is no FS, and all months are included. All grid cells within the same main climate class are considered. The interannual distribution (**c**) compares the FS months of years with $BA \geq 100$ha against the FS months of years with $BA < 100$ha for cells with some fire incidence within the same main climate class. The thresholds are selected automatically for each distribution at the value that maximizes the area enclosed between the density function of the points with high fire activity and the density function of the points with low or no fire activity. 75

S3.5 Tropical statistical distributions for annual variables. Annual precipitation - Pa (**a**), annual mean temperature - Ta (**b**), precipitation of the driest month - Pmin (**c**) and temperature of the hottest month - Tmax (**d**). Green density functions represent values for cells and years with $BA \geq 100$ha, and black density functions represent values for cells and years with $BA < 100$ha. The thresholds are indicated through black vertical lines. The text box shows the value of the threshold and its uncertainty, the value of the area difference between fire and non-fire points, the percentage of fire points meeting the threshold, the percentage of non-fire points meeting the threshold and the percentage of burned area associated with the fire points that meet the threshold. The area difference is proportional to the difference between the percentage of fire and non-fire points. The uncertainty in the obtained threshold is the size of the x-axis discretization used in the calculation. 76

S3.6 Tropical statistical distributions for monthly variables. Monthly precipitation and temperature seasonal distributions (**a**, **b**) and interannual distributions (**c**, **d**). The thresholds are indicated through black vertical lines. In the seasonal distributions, green density functions represent the FS months of the $BA \geq 100$ha years, and black density functions represent the months out of the FS. In the interannual distributions, green density functions represent the FS of the $BA \geq 100$ha years, and black density functions represent the FS of the $BA < 100$ha years. The thresholds are indicated through black vertical lines. The text box shows the value of the threshold and its uncertainty, the value of the area difference between fire and non-fire points, the percentage of fire points meeting the threshold, the percentage of non-fire points meeting the threshold and the percentage of burned area associated with the fire points that meet the threshold. The area difference is proportional to the difference between the percentage of fire and non-fire points. The uncertainty in the obtained threshold is the size of the x-axis discretization used in the calculation. 77

USC UNIVERSIDADE DE SANTIAGO DE COMPOSTELA

S3.7 Arid statistical distributions for annual variables. Annual precipitation - Pa (**a**), annual mean temperature - Ta (**b**), precipitation of the driest month - Pmin (**c**) and temperature of the hottest month - Tmax (**d**). Yellow density functions represent values for cells and years with $BA \geq 100$ha, and black density functions represent values for cells and years with $BA < 100$ha. The thresholds are indicated through black vertical lines. The text box shows the value of the threshold and its uncertainty, the value of the area difference between fire and non-fire points, the percentage of fire points meeting the threshold, the percentage of non-fire points meeting the threshold and the percentage of burned area associated with the fire points that meet the threshold. The area difference is proportional to the difference between the percentage of fire and non-fire points. The uncertainty in the obtained threshold is the size of the x-axis discretization used in the calculation. 78

S3.8 Arid statistical distributions for monthly variables. Monthly precipitation and temperature seasonal distributions (**a**, **b**) and interannual distributions (**c**, **d**). The thresholds are indicated through black vertical lines. In the seasonal distributions, yellow density functions represent the FS months of the $BA \geq 100$ha years, and black density functions represent the months out of the FS. In the interannual distributions, yellow density functions represent the FS of the $BA \geq 100$ha years, and black density functions represent the FS of the $BA < 100$ ha years. The thresholds are indicated through black vertical lines. The text box shows the value of the threshold and its uncertainty, the value of the area difference between fire and non-fire points, the percentage of fire points meeting the threshold, the percentage of non-fire points meeting the threshold and the percentage of burned area associated with the fire points that meet the threshold. The area difference is proportional to the difference between the percentage of fire and non-fire points. The uncertainty in the obtained threshold is the size of the x-axis discretization used in the calculation. 79

S3.9 Temperate statistical distributions for annual variables. Annual precipitation - Pa (**a**), annual mean temperature - Ta (**b**), precipitation of the driest month - Pmin (**c**) and temperature of the hottest month - Tmax (**d**). Pink density functions represent values for cells and years with $BA \geq 100$ha, and black density functions represent values for cells and years with $BA < 100$ha. The thresholds are indicated through black vertical lines. The text box shows the value of the threshold and its uncertainty, the value of the area difference between fire and non-fire points, the percentage of fire points meeting the threshold, the percentage of non-fire points meeting the threshold and the percentage of burned area associated with the fire points that meet the threshold. The area difference is proportional to the difference between the percentage of fire and non-fire points. The uncertainty in the obtained threshold is the size of the x-axis discretization used in the calculation. 80

USC UNIVERSIDADE DE SANTIAGO DE COMPOSTELA

S3.10Temperate statistical distributions for monthly variables. Monthly precipitation and temperature seasonal distributions (**a**, **b**) and interannual distributions (**c**, **d**). The thresholds are indicated through black vertical lines. In the seasonal distributions, pink density functions represent the FS months of the $BA \geq 100$ha years, and black density functions represent the months out of the FS. In the interannual distributions, pink density functions represent the FS of the $BA \geq 100$ha years, and black density functions represent the FS of the $BA < 100$ha years. The thresholds are indicated through black vertical lines. The text box shows the value of the threshold and its uncertainty, the value of the area difference between fire and non-fire points, the percentage of fire points meeting the threshold, the percentage of non-fire points meeting the threshold and the percentage of burned area associated with the fire points that meet the threshold. The area difference is proportional to the difference between the percentage of fire and non-fire points. The uncertainty in the obtained threshold is the size of the x-axis discretization used in the calculation. 81

S3.11Boreal statistical distributions for annual variables. Annual precipitation - Pa (**a**), annual mean temperature - Ta (**b**), precipitation of the driest month - Pmin (**c**) and temperature of the hottest month - Tmax (**d**). Blue density functions represent values for cells and years with $BA \geq 100$ha, and black density functions represent values for cells and years with $BA < 100$ha. The thresholds are indicated through black vertical lines. The text box shows the value of the threshold and its uncertainty, the value of the area difference between fire and non-fire points, the percentage of fire points meeting the threshold, the percentage of non-fire points meeting the threshold and the percentage of burned area associated with the fire points that meet the threshold. The area difference is proportional to the difference between the percentage of fire and non-fire points. The uncertainty in the obtained threshold is the size of the x-axis discretization used in the calculation. 82

S3.12Boreal statistical distributions of monthly variables. Monthly precipitation and temperature seasonal distributions (**a**, **b**) and interannual distributions (**c**, **d**). The thresholds are indicated through black vertical lines. In the seasonal distributions, blue density functions represent the FS months of the $BA \geq 100$ha years, and black density functions represent the months out of the FS. In the interannual distributions, blue density functions represent the FS of the $BA \geq 100$ha years, and black density functions represent the FS of the $BA < 100$ha years. The thresholds are indicated through black vertical lines. The text box shows the value of the threshold and its uncertainty, the value of the area difference between fire and non-fire points, the percentage of fire points meeting the threshold, the percentage of non-fire points meeting the threshold and the percentage of burned area associated with the fire points that meet the threshold. The area difference is proportional to the difference between the percentage of fire and non-fire points. The uncertainty in the obtained threshold is the size of the x-axis discretization used in the calculation. 83

S3.13Mean monthly values for Asian arid fire-prone regions ($BAmax > 0$ha). Mean monthly burned area in black, precipitation in blue and 2m air temperature in red. 84

USC UNIVERSIDADE DE SANTIAGO DE COMPOSTELA

S3.14Mean monthly values for North American arid fire-prone regions ($BAmax >$ 0ha). Mean monthly burned area in black, precipitation in blue and 2m air temperature in red. 84
S3.15Mean monthly values of African fire-prone arid regions ($BAmax > 0$ha). Mean monthly burned area in black, mean monthly precipitation in blue and mean monthly 2m air temperature in red. 85
S3.16Mean monthly values for Australian arid fire-prone regions ($BAmax > 0$ha). Mean monthly burned area in black, mean monthly precipitation in blue and mean monthly 2m air temperature in red. 85
S3.17Months from the month with highest burned area. **a**, Time period in months between the month with most burned area and the wettest month (ΔmP). **b**, Time period in months between the month with most burned area and the hottest month (ΔmT). 86
S3.18Auxiliar statistical distributions for arid climates. **a**, MAT probability density function of arid fire-prone points ($BAmax \geq 0$ha) with $\Delta mP > 6$, i.e. with more than 6 months in between the month with most burned area and the wettest month (yellow) and with $\Delta mP \leq 6$ values (orange). **b**, For points with $MAT < 18.5°C$, probability density function of the distance in months between fire season months and the hottest month (brown). **c,** For points with $18.5°C \leq MAT < 27.5°C$, probability density function of the distance in months between fire season months and the wettest month (yellow). **d**, For points with $MAT \geq 27.5°C$, probability density function of the distance in months between fire season months and the wettest month (orange). 87
S3.19Monthly values for South-eastern maritime Asia arid fire-prone regions. 1996-2016 time series of mean monthly values (**a**, **c**, **e**) and the mean annual cycles (**b**, **d**, **f**) of burned area (**a**, **b**, in black), precipitation (**c**, **d**, in blue) and 2m air temperature (**e**, **f** in red) for the Malay Archipelago fire-prone region ($BAmax > 0$ha). 88
S3.20Validation data of the fire-climate classification. a Percentage of global mean annual burned area observed at cells classified as fire-prone (left bars) and percentage of grid cells with non-zero burned area classified as fire-prone (right bars). b Percentage of: classified (color) and non-classified (black) points with non-zero observed burned area and classified (grey) and non-classified (white) with zero observed burned area (quantification of Figure 3.2a of the main text). 89
S3.21Future changes in annual mean precipitation and temperature. **a**, Difference between 2070-2099 MAP and 1996-2016 MAP (ΔMAP). **b**, Difference between 2070-2099 MAT and 1996-2016 MAT (ΔMAT). 90
S3.22Future changes in precipitation by season. Difference between 2070-2099 and 1996-2016 mean monthly precipitation for the DJF season (**a**), MAM season (**b**), JJA season (**c**) and SON season (**d**). 91
S3.23Future changes in temperature by season. Difference between 2070-2099 and 1996-2016 mean monthly temperature for the DJF season (**a**), MAM season (**b**), JJA season (**c**) and SON season (**d**). 91

USC UNIVERSIDADE DE SANTIAGO DE COMPOSTELA

4.1 Average ROS increase by contribution. For each fuel model, average ROS increase of all wildfires with a burned area greater than 500 ha between 2001 and 2021 for the Iberian Peninsula, **a**, considering the thermodynamic component (divided into dead fuel, live fuel and fuel addition by drought factors) between pre-industrial and present conditions, **b** considering the vegetation growth component (divided into greening and land-use change factors) between pre-industrial and present conditions, **c** considering the thermodynamic component (divided into dead fuel, live fuel and fuel addition by drought factors) between present and 2070-2099 conditions (under SSP2-4.5 scenario) and **d** considering the vegetation growth component between present and 2070-2099 conditions (under SSP2-4.5 scenario). Black dots depict the mean values for changes obtained perturbing all factors simultaneously, and error bars indicate the standard deviation between different GCMs outputs. The corresponding ROS distributions are shown in Supplementary Figures S4.2 and S4.3. 97

4.2 ROS increase by event. Fuel model-averaged ROS increase of each wildfire with a burned area greater than 500 ha between 2001 and 2021 for the Iberian Peninsula, **a** considering the thermodynamic component between pre-industrial and present conditions, **b** considering the vegetation growth component between pre-industrial and present conditions, **c** considering the thermodynamic component between present and 2070-2099 conditions (under SSP2-4.5 scenario) and **d** considering the vegetation growth component between present and 2070-2099 conditions (under SSP2-4.5 scenario). 99

4.3 Expected ROS increase between pre-industrial and present conditions for all-points. Considering the thermodynamic component between pre-industrial and present conditions, **a** mean annual ROS increase, **b** number of non-significant (p-value>0.05) model outputs for the mean annual ROS increase, **c** month of the year with the largest ROS increase, **d** average ROS increase during the month with the largest ROS increase and **e** average ROS increase by year and month of the year. 101

4.4 Expected ROS increase between pre-industrial and present conditions for all-points. Considering the thermodynamic component between pre-industrial and present conditions, **a** mean annual ROS increase, **b** number of non-significant (p-value>0.05) model outputs for the mean annual ROS increase, **c** month of the year with the largest ROS increase, **d** average ROS increase during the month with the largest ROS increase and **e** average ROS increase by year and month of the year. 102

S4.1 Comparison of modelled (green) and observed (black) herbaceous live fuel moistures. Observed data is obtained from Yebra et al. (2019) [256], using all the available stations in the Iberian Peninsula with more than 10 observations of grass type species. 104

USC UNIVERSIDADE DE SANTIAGO DE COMPOSTELA

S4.2 For each fuel model, boxplot representation of the ROS distribution of all wildfires with a burned area greater than 500 ha between 2001 and 2021 for the Iberian Peninsula. White boxplots represent factual data (obtained from ERA5) and coloured boxplots represent the thermodynamic component counterfactual data for **a** pre-industrial conditions and **b** 2070-2099 conditions (under SSP2-4.5 scenario). Different colours indicate different GCM outputs. . 105
S4.3 For each fuel model, boxplot representation of the ROS distribution of all wildfires with a burned area greater than 500 ha between 2001 and 2021 for the Iberian Peninsula. White boxplots represent factual data (obtained from ERA5) and red boxplots represent the vegetation growth component counterfactual data for **a** pre-industrial conditions and **b** 2070-2099 conditions (under SSP2-4.5 scenario). 106
S4.4 Mean annual temperature increase between **a** pre-industrial and present conditions and between **b** 2070-2099 conditions (under SSP2-4.5 scenario) and present, averaged for all models (MPI-ESM1-2-HR, EC-Earth3, CESM2-WACCM, MRI-ESM2-0 and NorESM2-MM). 107
S4.5 Considering only the contribution of dead fuel moisture in the thermodynamic component between pre-industrial and present conditions, **a** mean annual ROS increase and **b** month of the year with the largest ROS increase. For the grey and black rectangles displayed in the two maps, **c** average ROS values by month of the year, **d** average dead fuel moisture values by month of the year, **e** average ROS difference by month of the year (with positive values indicating a ROS increase from pre-industrial to present conditions), **f** average dead fuel moisture difference by month of the year (with positive values indicating a fuel dryness increase from pre-industrial to present conditions), and **g** average ROS increase by month of the year. Black (grey) lines in **c**, **d**, **e**, **f** and **g** correspond to black (grey) rectangles in **a** and **b**. 108
S4.6 Considering only the contribution of live fuel moisture in the thermodynamic component between pre-industrial and present conditions, **a** mean annual ROS increase and **b** month of the year with the largest ROS increase. For the grey and black rectangles displayed in the two maps, **c** average ROS values by month of the year, **d** average live fuel moisture values by month of the year, **e** average ROS difference by month of the year (with positive values indicating a ROS increase from pre-industrial to present conditions), **f** average live fuel moisture difference by month of the year (with positive values indicating a fuel dryness increase from pre-industrial to present conditions), and **g** average ROS increase by month of the year. Black (grey) lines in **c**, **d**, **e**, **f** and **g** correspond to black (grey) rectangles in **a** and **b**. 109

USC UNIVERSIDADE DE SANTIAGO DE COMPOSTELA

S4.7 Considering only the contribution of drought fuel addition in the thermodynamic component between pre-industrial and present conditions, **a** mean annual ROS increase and **b** month of the year with the largest ROS increase. For the grey and black rectangles displayed in the two maps, **c** average ROS values by month of the year, **d** average drought factor (values between 0 and 1 with 0 indicating no-drought conditions) by month of the year, **e** average ROS difference by month of the year (with positive values indicating a ROS increase from pre-industrial to present conditions), **f** average drought factor difference by month of the year (with positive values indicating drought intensification from pre-industrial to present conditions), and **g** average ROS increase by month of the year. Black (grey) lines in **c**, **d**, **e**, **f** and **g** correspond to black (grey) rectangles in **a** and **b**. 110
S4.8 Multi-year (2001-2021) summer (July-August-September) average of the daily maximum vapor pressure deficit (VPD). 111
S4.9 Mean annual net primary productivity increase between **a** pre-industrial and present conditions and between (**b** 2070-2099 conditions (under SSP2-4.5 scenario) and present, averaged for all models (ACCESS-ESM1-5, BCC-CSM2-MR, CMCC-ESM2, CanESM5, EC-Earth3-Veg, IPSL-CM6A-LR, MPI-ESM1-2-LR and NorESM2-LM). . . . 112
S4.10Average energy released increase by contribution. For each fuel model, average Energy Release Component (ERC) increase of all wildfires with a burned area greater than 500 ha between 2001 and 2021 for the Iberian Peninsula, **a** considering the thermodynamic component (divided in dead fuels, live fuel and de drought addition factor) between pre-industrial and present conditions, **b** considering the vegetation growth component (divided in greening and land-use changes) between pre-industrial and present conditions, **c** considering the thermodynamic component (divided in dead fuels, live fuel and de drought addition factor) between present and 2070-2099 conditions (under SSP2-4.5 scenario) and **d** considering the vegetation growth component between present and 2070-2099 conditions (under SSP2-4.5 scenario). Error bars indicate the standard deviation between different GCMs outputs. The corresponding ROS distributions are shown in Supplementary Figures S4.2 and S4.3. 113

5.1 Storm downdraft influence on fire properties. Lower troposphere (1000 m) downdraft maximum speed against: **a** cloud water mixing ratio averaged for the simulation domain, **b** 10 m maximum wind difference between coupled and uncoupled fire–atmosphere simulation, **c** burned area increase fraction in 8 h from uncoupled to coupled fire–atmosphere simulation and **d** maximum fire smoke height (up to 16 km). Each colour represents a different fuel category. . 126
5.2 Conditions for firestorm development. **a**, Three-dimensional representation of lower troposphere (1000 m) downdraft maximum speed, K-index values and fuel load, with each colour representing a different fuel category. **b**, Relation between downdraft intensity and K-index, represented by a boxplot for each downdraft intensity interval. 127

USC UNIVERSIDADE DE SANTIAGO DE COMPOSTELA

5.3 Present distribution of firestorm risk. **a**, Number of days per year with both a FWI and a K-index value above the selected thresholds, averaged from 1980-2018 ERA5 reanalysis data. **b**, Minimum number of years required for the accumulation of 6 $kg \cdot m^{-2}$ of fuel load according to the average annual dry matter productivity (DMP) in the 1999-2019 period generated by the Global Land Service of Copernicus, derived from SPOT-VGT and PROBA-V imagery combined with meteorological data from ECMWF. 128
5.4 Future trends in fire risk, atmospheric instability and firestorm risk according to RCP8.5 scenario. Trend in number of days per decade with **a** FWI **b** K-index and **c** both FWI and K-index values above the selected thresholds (see text), according to different EURO-CORDEX models under the RCP8.5 scenario for the 1970–2098 period. Grey shaded regions indicate that at least one of the models presents a non-significant result (p-value>0.05) or a trend with an opposite-sign. Country-averaged time series for the number of days per year with high FWI (red), high K-index (blue) and both FWI and K-index high values (grey) are also shown, indicating the standard deviation between model outputs by the line width. 130
S5.1 Satellite images of clouds possibly associated with pyroconvection. All images are from NASA's Worldview service, obtained from the Moderate Resolution Imaging Spectroradiometer (MODIS) instrument abroad the Aqua satellite, unless the image corresponding to 2021-08-18, obtained from the Visible Infrared Imaging Radiometer Suite instrument abroad the NOAA-20 satellite. Fire and thermal anomalies observed by the satellite are indicated as red and orange points. We acknowledge the use of imagery from the NASA Worldview application (https://worldview.earthdata.nasa.gov), part of the NASA Earth Observing System Data and Information System (EOSDIS). 133
S5.2 Cloud fraction outputs of the idealized simulations for validation. Cloud fraction is shown in a grey scale, 850 hPa wind is indicated in barbs and the fire perimeter is indicated in red. 134
S5.3 Locations of the atmospheric vertical profiles. Grid cells ($0.25° \times 0.25°$) selected for obtaining the atmospheric vertical profiles for the idealized experiments marked by red dots on the mean annual burned area GFED4 data for the 1996-2016 period [190]. The selected grid cells are located in regions with high burned area values. 135
S5.4 Storm updraft influence on fire properties. Updraft maximum speed against: **a** cloud water mixing ratio averaged for the simulation domain, **b** 10 m maximum wind difference between coupled and uncoupled fire-atmosphere simulation, **c** maximum fire smoke height (up to 16 km) and **d** burned area increase fraction in 8 hours from uncoupled to coupled fire-atmosphere simulation. Each color represents a different fuel category. 136
S5.5 Comparison between indexes. 3-dimensional representation of lower troposphere (1000 m) downdraft maximum speed, fuel load and: **a** Convective Available Potential Energy (CAPE), **b** Continuous Haines Index (C-Haines), **c** Severe Weather Threat Index (SWEAT) and **d** Total Totals Index (TT). 137

USC UNIVERSIDADE DE SANTIAGO DE COMPOSTELA

S5.6 Boxplot comparison among indexes. Relation between downdraft intensity represented by a boxplot for each interval and: **a** Convective Available Potential Energy (CAPE), **b** Continuous Haines Index (C-Haines), **c** Severe Weather Threat Index (SWEAT) and **d** Total Totals Index (TT). 138
S5.7 FWI observed during fire days. **a**, Median of the FWI values on days with non-zero observed burned area during the 2001-2015 period [190]. **b**, Median of the percentiles corresponding to each of the FWI values on days with non-zero observed burned area during the 2001-2015 period. 138
S5.8 FWI threshold. For each grid cell we combine a constant and a variable FWI threshold, where the constant threshold is 11.2 (moderate fire risk) and the variable threshold is defined for each grid cell as the 90th percentile of the FWI data from 1990 to 2019 ERA5 reanalysis data. The FWI final threshold is the maximum value between the constant and the variable threshold. 139
S5.9 Days with high FWI and high K-index. Number of days per year with **a** FWI and **b** K-index values above the selected threshold, averaged from 1980-2018 ERA5 reanalysis data. 140
S5.10Monthly distribution of the number of days with high values of the FWI and K-index. Monthly distribution of the number of days per year above the selected threshold with a FWI value above the selected threshold (red), a K-index value (blue) and both a FWI and K-index value above the threshold (black), averaged for the ERA5 output period 1980-2018. 141
S5.11Fuel load estimation from vegetation products. Average annual dry matter productivity (DMP) in the 1999-2019 period generated by the Global Land Service of Copernicus, derived from SPOT-VGT and PROBA-V imagery combined with meteorological data from ECMWF. 142
S5.12Days with high FWI. Number of days per year with a FWI value above the selected threshold, averaged for all the EURO-CORDEX model outputs, during: **a**, 1980-2018 and **b**, 2070-2098. In **c**, the difference between the two periods is shown. 142
S5.13Days with high K-index. Number of days per year with a K-index value above the selected threshold, averaged for all the EURO-CORDEX model outputs, during: **a**, 1980-2018 and **b**, 2070-2098. In **c**, the difference between the two periods is shown. 143
S5.14Days with both FWI and K-index high values. Number of days per year with a FWI and a K-index value above the selected threshold, averaged for all the EURO-CORDEX model outputs, during: **a**, 1980-2018 and **b**, 2070-2098. In **c**, the difference between the two periods is shown. 143

USC UNIVERSIDADE DE SANTIAGO DE COMPOSTELA

S5.15Future trends in fire risk, atmospheric instability and firestorm risk according to RCP4.5 scenario. Trend in number of days per decade with **a** FWI **b** K-index and **c** both FWI and K-index values above the selected thresholds (see text), according to different EURO-CORDEX models under the RCP4.5 scenario for the 1970-2098 period. Grey shaded regions indicate that at least one of the models presents a nonsignificant result (p-value>0.05) or a trend with an opposite-sign. Country-averaged time series for the number of days per year with high FWI (red), high K-index (blue) and both FWI and K-index high values (grey) are also shown, indicating the standard deviation between model outputs by the line width. 144
S5.16Future trends in fire risk, atmospheric instability and firestorm risk according to RCP2.6 scenario. Trend in number of days per decade with **a** FWI **b** K-index and **c** both FWI and K-index values above the selected thresholds (see text), according to different EURO-CORDEX models under the RCP2.6 scenario for the 1970-2098 period. Grey shaded regions indicate that at least one of the models presents a nonsignificant result (p-value>0.05) or a trend with an opposite-sign. Country-averaged time series for the number of days per year with high FWI (red), high K-index (blue) and both FWI and K-index high values (grey) are also shown, indicating the standard deviation between model outputs by the line width. 145
S5.17Firestorm risk trend sensitivity to different FWI thresholds. Trend in the number of days with both FWI and K-index high values with a FWI threshold of: **a** 80th percentile, **b** 85th percentile, **c** 90th percentile (as in Figure 5 of the main text) and **d** 95th percentile of the FWI data from 1990 to 2019 for each EURO-CORDEX model output. 146
S5.18Firestorm risk trend sensitivity to different K-index thresholds. Trend in the number of days with both FWI and K-index high values with a Kindex threshold of: **a** 20°C, **b** 22.5°C, **c** 25°C (as in Figure 5 of the main text) and **d** 27.5°C. . . 147
S5.19Observed trend in fire risk, atmospheric instability and firestorm risk 1980-2018. From ERA5 reanalysis 1980-2018 period, trend in the number of days per decade with **a** FWI, **b** K-index and **c** both FWI and K-index above their threshold. Grey shaded regions indicate that the data presents a non-significant result (p-value>0.05). Country-averaged time series for the number of days per year with high FWI (red), high Kindex (blue) and both FWI and K-index high values (black) are also shown. 148
S5.20Observed trend in summer 2m temperature for 1980-2018. Trend of the average midday 2m temperature in May, June, July, August and September according to the ERA5 reanalysis for 1980-2018. Grey shaded regions indicate a nonsignificant result (p-value>0.05). Country-averaged annual time series for 95th (red), 75th (yellow), 50th (grey), 25th (green) and 5th (blue) percentiles and mean (black dashed) of the 2m temperature values during the months of May, June, July, August and September are also shown. 149

USC UNIVERSIDADE DE SANTIAGO DE COMPOSTELA

S5.21 Observed trend in summer precipitation for 1980-2018. Trend of the total precipitation accumulated in May, June, July, August and September according to the ERA5 reanalysis for 1980-2018. Grey shaded regions indicate a non-significant result (p-value>0.05). Country-averaged annual time series for the total precipitation during the months of May, June, July, August and September are also shown. 150
S5.22 Observed trend in summer relative humidity for 1980-2018. Trend of the average midday 2m relative humidity in May, June, July, August and September according to the ERA5 reanalysis for 1980-2018. Grey shaded regions indicate a nonsignificant result (p-value>0.05). Country-averaged annual time series for 95th (blue), 75th (green), 50th (grey), 25th (yellow) and 5th (red) percentiles and mean (black dashed) of the 2m relative humidity values during the months of May, June, July, August and September are also shown. 151
S5.23 Observed trends in Ukraine for 1980-2018. Ukraine country-averaged annual time series for total precipitation and time series for 95th (red), 75th (yellow), 50th (grey), 25th (green) and 5th (blue) percentiles and mean (black dashed) of the mean 2m temperature and relative humidity values during the months of May, June, July, August and September. 152
S5.24 Observed trend in temperature difference between 850 hPa and 500 hPa for 1980-2018. Trend of the average temperature difference between 850 hPa and 500 hPa in May, June, July, August and September according to the ERA5 reanalysis for 1980-2018. Grey shaded regions indicate a non-significant result (p-value>0.05). Countryaveraged annual time series for 95th (red), 75th (yellow), 50th (grey), 25th (green) and 5th (blue) percentiles and mean (black dashed) of the temperature difference between 850 hPa and 500 hPa values during the months of May, June, July, August and September are also shown. . 153
S5.25 Observed trend in dew point temperature at 850 hPa for 1980-2018. Trend of the mean dew point temperature at 850 hPa in May, June, July, August and September according to the ERA5 reanalysis for 1980-2018. Grey shaded regions indicate a non-significant result (p-value>0.05). Country-averaged annual time series for 95th (red), 75th (yellow), 50th (grey), 25th (green) and 5th (blue) percentiles and mean (black dashed) of the dew point temperature at 850 hPa values during the months of May, June, July, August and September are also shown. 154
S5.26 Observed trend in dew point depression at 700 hPa for 1980-2018. Trend of the mean dew point depression at 700 hPa in May, June, July, August and September according to the ERA5 reanalysis for 1980-2018. Grey shaded regions indicate a non-significant result (p-value>0.05). Country-averaged annual time series for 95th (red), 75th (yellow), 50th (grey), 25th (green) and 5th (blue) percentiles and mean (black dashed) of the dew point depression at 700 hPa values during the months of May, June, July, August and September are also shown. 155

USC UNIVERSIDADE DE SANTIAGO DE COMPOSTELA

6.1 Fire activity in Europe. **a**, Mean annual burned area. **b**, Month with the maximum average burned area. **c**, Month with the minimum monthly total precipitation. **d**, Month with the maximum monthly mean temperature. Burned area data were obtained from the 1982-2018 AVHRR-LTDR Burned Area Grid product produced by the ESA Fire Climate Change Initiative (FireCCI) [292]. Climate data were obtained from ERA5 reanalysis [129]. 159
6.2 **a**, Mean annual precipitation from 1940-2022 ERA5 reanalysis [129]. **b**, Mean dry matter productivity representing the overall growth rate of vegetation, obtained from 1999-2019 data generated by the Global Land Service of Copernicus, derived from SPOT-VGT and PROBA-V imagery combined with meteorological data from ECMWF. 160
6.3 Influence of October 2017 fires in land inputs. **a**, 2017 burned area in red obtained from ESA FireCCI data [292]. **b**, Surface albedo anomaly of May-June 2018 from the May-June 1999-2019 average. **c**, Leaf Area Index (LAI) anomaly of May-June 2018 from the May-June 1999-2019 average. **d**, Fraction of Absorbed Photosynthetically Active Radiation (FAPAR) anomaly of May-June 2018 from the May-June 1999-2019 average. Surface albedo, LAI and FAPAR data were obtained from the Global Land Service of Copernicus, derived from SPOT-VGT and PROBA-V imagery combined with meteorological data from ECMWF. 162
6.4 Influence of October 2017 fires in atmospheric surface variables. **a**, May-June 2018 2m air temperature average difference between the burned area test (that takes into account the 2017 burned area influence on land inputs) and the control test. **b**, May-June 2018 2m relative humidity average difference between the burned area test and the control test. 163
6.5 Influence of October 2017 fires in total precipitation. **a**, May-June 2018 total precipitation in the control test. **b**, May-June 2018 total precipitation in the burned area test (that takes into account the 2017 burned area influence on land inputs). **c**, May-June 2018 total precipitation difference between the burned area test and the control test, with the reduction in total precipitation for the three red-bounded regions expressed as a percentage. 164
6.6 Satellite images of the trough located in front of the Iberian Peninsula coast on the 17th of July 2022 (left), and the development of different pyroconvective clouds in Galicia (middle image at 12:00h and right image at 13:30h). These images are from NASA's Worldview service, obtained from the Moderate Resolution Imaging Spectroradiometer (MODIS) instrument abroad the Aqua satellite. We acknowledge the use of imagery from the NASA Worldview application (https://worldview.earthdata.nasa.gov), part of the NASA Earth Observing System Data and Information System (EOSDIS). For each of the considered fires (labels 1, 2 and 3) we show the timeseires of the Fire Weather Index (FWI) and the K-index from ERA5 reanalysis data [129], representing the firestorm thresholds as horizontal lines. 165

USC UNIVERSIDADE DE SANTIAGO DE COMPOSTELA

USC
UNIVERSIDADE
DE SANTIAGO
DE COMPOSTELA

List of Tables

2.1 Input parameters for the Rothermel's rate of spread model. 43
2.2 Accuracy and detection index for the teste fuel moisture contents in As Neves and Gondomar fires. Shaded cells indicate maximum accuracy and detection index values. 49

3.1 Fire classification defining criteria. Fire-climate classes (Tr-ds, Ar-fl, Te-dhs and Bo-hs) must meet general Köppen-Geiger climate criteria (Tr, Ar, Te and Bo, in bold) and the specific fire-climate thresholds. Fire-climate classes are subdivided into three sub-classes according to the number of years classified per decade: r-reccurrent (FPY>7 years/decade), o-occasional (7>FPY>3 years/decade) and i-infrequent (3>FPY>0 years/decade). All variables are defined in Table 3.2. 60
3.2 Variable definitions 61

S4.1 Fuel model descriptions 114
S4.2 T-test p-values for the comparison between factual and the thermodynamic component pre-industrial ROS samples of all wildfires with a burned area greater than 500 ha between 2001 and 2021 for the Iberian Peninsula. The null hypothesis is that the 2 samples (factual and counterfactual) have identical average values. Shaded cells indicate non-significant values (p-value>0.05). . . 115
S4.3 T-test p-values for the comparison between factual and the thermodynamic component future (2070-2099 according to SSP2-4.5) ROS samples of all wildfires with a burned area greater than 500 ha between 2001 and 2021 for the Iberian Peninsula. The null hypothesis is that the 2 samples (factual and counterfactual) have identical average values. Shaded cells indicate non-significant values (p-value>0.05). 116
S4.4 T-test p-values for the comparison between factual and the vegetation growth component future (2070-2099 according to SSP2-4.5) ROS samples of all wildfires with a burned area greater than 500 ha between 2001 and 2021 for the Iberian Peninsula. The null hypothesis is that the 2 samples (factual and counterfactual) have identical average values. Shaded cells indicate non-significant values (p-value>0.05). 117
S4.4 Continued. 118

USC UNIVERSIDADE DE SANTIAGO DE COMPOSTELA

S4.5 T-test p-values for the comparison between factual and the vegetation growth component future (2070-2099 according to SSP2-4.5) ROS samples of all wildfires with a burned area greater than 500 ha between 2001 and 2021 for the Iberian Peninsula. The null hypothesis is that the 2 samples (factual and counterfactual) have identical average values. Shaded cells indicate non-significant values (p-value>0.05). 119
S4.5 Continued. 120
S4.6 Percentage of total number of wildfire events where a significant increase, a significant decrease or a non-significant change in the rate of spread was found. The statistical significance is based on the p-value (p-value>0.05) of a T-test for the null hypothesis that the mean of the counterfactual ROS sample (using different GCMs) is equal to the factual ROS. The counterfactual sample corresponds to the thermodynamic component of the comparison between the present and the pre-industrial conditions. 121
S4.7 Percentage of total number of wildfire events where a significant increase, a significant decrease or a non-significant change in the rate of spread was found. The statistical significance is based on the p-value (p-value>0.05) of a T-test for the null hypothesis that the mean of the counterfactual ROS sample (using different GCMs) is equal to the factual ROS. The counterfactual sample corresponds to the thermodynamic component of the comparison between the present and the 2070-2099 SSP2-4.5 conditions. 122

S5.1 Information about the outputs of the idealized simulations for validation. PyroCu indicates the creation of a cloud by the fire in at least one of the simulations. Fuels PyroCu indicates the number of fuel models for which a cloud is formed. K-index and FWI columns indicate the corresponding value of these two indexes for each case. The FWI threshold for the corresponding location is indicated in brackets. 156
S5.2 Information about the selected locations. Altitude and wind information is obtained directly from ERA5 database, and Köppen-Geiger climate information is obtained from Peel *et al.* [203]. 157

6.1 Rate of spread increase due to the thermodynamic component of climate change between pre-industrial and present conditions for the 20 most affected wildfires in Galicia between 2001 and 2021. 161

USC
UNIVERSIDADE DE SANTIAGO DE COMPOSTELA

List of publications

(I) Senande-Rivera, M., Insua-Costa, D. & Miguez-Macho, G. Spatial and temporal expansion of global wildland fire activity in response to climate change. *Nature Communications* **13**, 1208 (2022). DOI: `https://doi.org/10.1038/s41467-022-28835-2`.

Specific contribution in the publication

Designing the study, conducting the analysis, creating figures and preparing the original manuscript.

Quality indexes

Impact factor: 17.694
CiteScore: 23.2
Quartile: Q1 (6/74 in MULTIDISCIPLINARY SCIENCES)

Corresponding content in the thesis

All results from Chapter 3 (*Present global fire-prone regions and their expected alterations due to climate change*) are included in this publication, except for Figure 3.5, which was specifically created for this thesis.

(II) Senande-Rivera, M., Insua-Costa, D. & Miguez-Macho, G. The influence of climate change on wildfire behaviour in the Iberian Peninsula. Under review at *Science of the Total Environment*. Available as a preprint at SSRN: `http://dx.doi.org/10.2139/ssrn.4421371`.

Specific contribution in the publication

Designing the study, conducting the analysis, creating figures and preparing the original manuscript.

Quality indexes

Impact factor: 10.754
CiteScore: 14.1
Quartile: Q1 (26/279 in ENVIRONMENTAL SCIENCES)

Corresponding content in the thesis

All results from Chapter 4 (*The influence of climate change on wildfire behaviour in the Iberian Peninsula*) are included in this publication.

USC UNIVERSIDADE DE SANTIAGO DE COMPOSTELA

(III) Senande-Rivera, M., Insua-Costa, D. & Miguez-Macho, G. Towards an atmosphere more favourable to firestorm development in Europe. *Environmental Research Letters* **17** 094015 (2022). DOI: `https://doi.org/10.1088/1748-9326/ac85ce`.

Specific contribution in the publication

Designing the study, conducting the analysis, creating figures and preparing the original manuscript.

Quality indexes

Impact factor: 6.947
CiteScore: 9.4
Quartile: Q1 (13/94 in METEOROLOGY & ATMOSPHERIC SCIENCES), Q1 (55/279 in ENVIRONMENTAL SCIENCES)

Corresponding content in the thesis

All results from Chapter 5 (*Analysis of the atmospheric risk of deep pyroconvection in Europe*) are included in this publication. Part of the introductory text on the interactions between fires and the atmosphere on a local scale in Section 1.1.3, is also included in this publication.

USC UNIVERSIDADE DE SANTIAGO DE COMPOSTELA

Copyright Permissions

Figure 1.3. This figure was published in *Scientific Data* journal article by Springer Nature under a Creative Commons Attribution 4.0 licence (https://creativecommons.org/licenses/by/4.0/), which allows the published material to be freely shared and adapted. For further information, please refer to https://www.nature.com/sdata/oa.

Article 1. Senande-Rivera, M., Insua-Costa, D. & Miguez-Macho, G. Spatial and temporal expansion of global wildland fire activity in response to climate change. *Nature Communications* **13**, 1208 (2022). DOI: https://doi.org/10.1038/s41467-022-28835-2.

This article was published by Springer Nature under the Creative Commons Attribution 4.0 licence (https://creativecommons.org/licenses/by/4.0/) in the Nature Communications journal. No permission is therefore required. For further information, please refer to https://www.nature.com/ncomms/open-access.

Article 2. Senande-Rivera, M., Insua-Costa, D. & Miguez-Macho, G. The Influence of Climate Change on Wildfire Behaviour in the Iberian Peninsula. Under review at *Science of the Total Environment*. Available at SSRN: http://dx.doi.org/10.2139/ssrn.4421371.

This under review article will be published by Elsevier under the Creative Commons Attribution 4.0 licence (https://creativecommons.org/licenses/by/4.0/) in the Science of the Total Environment journal. No permission is therefore required. For further information, please refer to https://www.elsevier.com/journals/science-of-the-total-environment/0048-9697/open-access-options.

Article 3. Senande-Rivera, M., Insua-Costa, D. & Miguez-Macho, G. Towards an atmosphere more favourable to firestorm development in Europe. *Environmental Research Letters* **17** 094015 (2022). DOI: https://doi.org/10.1088/1748-9326/ac85ce.

This article was published by IOP Publishing under the Creative Commons Attribution 4.0 licence (https://creativecommons.org/licenses/by/4.0/) in the Environmental Research Letters journal. No permission is therefore required. For further information, please refer to https://publishingsupport.iopscience.iop.org/journals/environmental-research-letters/about-environmental-research-letters/#open-access.

USC
UNIVERSIDADE DE SANTIAGO DE COMPOSTELA

USC
UNIVERSIDADE
DE SANTIAGO
DE COMPOSTELA

Funding information

This research was supported by Xunta de Galicia through a predoctoral grant (Programa de axuda á etapa predoutoral 2019, ED481A-2019/112). Additional funding comes from CRETUS strategic partnership (AGRUP2015/02) and Agencia Estatal de Investigación (Ministerio de Ciencia e Innovación) through two different research projects: OPERMO (CGL2017-89859-R) and RIESPIRO (PID2021-128510OB-I00). All these programs are co-funded by the European Regional Development Fund (ERDF). Computation took place at CESGA (Centro de Supercomputación de Galicia).

USC
UNIVERSIDADE DE SANTIAGO DE COMPOSTELA

USC
UNIVERSIDADE
DE SANTIAGO
DE COMPOSTELA

Bibliography

[1] Senande-Rivera, M., Insua-Costa, D. & Miguez-Macho, G. Spatial and temporal expansion of global wildland fire activity in response to climate change. *Nature Communications* **13**, 1208 (2022).

[2] Senande-Rivera, M., Insua-Costa, D. & Miguez-Macho, G. The influence of climate change on wildfire behaviour in the iberian peninsula (2023). Available at SSRN 4421371.

[3] Senande-Rivera, M., Insua-Costa, D. & Miguez-Macho, G. Towards an atmosphere more favourable to firestorm development in europe. *Environmental Research Letters* **17**, 094015 (2022).

[4] Torero, J. L. An introduction to combustion in organic materials. In Belcher, C. M. (ed.) *Fire Phenomena and the Earth System*, chap. 1, 1–13 (John Wiley & Sons, Ltd, 2013).

[5] Rein, G. Smouldering fires and natural fuels. In Belcher, C. M. (ed.) *Fire Phenomena and the Earth System*, chap. 2, 15–33 (John Wiley & Sons, Ltd, 2013).

[6] Scott, A. C., Bowman, D. M., Bond, W. J., Pyne, S. J. & Alexander, M. E. *Fire on earth: an introduction* (John Wiley & Sons, Ltd, 2013).

[7] Cochrane, M. A. & Ryan, K. C. Fire and fire ecology: Concepts and principles. In Cochrane, M. A. (ed.) *Tropical Fire Ecology: Climate Change, Land Use, and Ecosystem Dynamics*, chap. 2, 25–62 (Springer Berlin Heidelberg, Berlin, Heidelberg, 2009).

[8] Rothermel, R. C. & Anderson, H. E. Fire spread characteristics determined in the laboratory. techreport 30, U.S. Department of Agriculture Forest Service (1966).

[9] Bowman, D. M. *et al.* Vegetation fires in the anthropocene. *Nature Reviews Earth & Environment* **1**, 500–515 (2020).

[10] Harrison, S., Marlon, J. & Bartlein, P. Fire in the earth system. In Dodson, J. (ed.) *Changing Climates, Earth Systems and Society*, chap. 3, 21–48 (Springer Netherlands, Dordrecht, 2010).

[11] Bowman, D. M. *et al.* Fire in the earth system. *Science* **324**, 481–484 (2009).

[12] Andela, N. *et al.* A human-driven decline in global burned area. *Science* **356**, 1356–1362 (2017).

USC UNIVERSIDADE DE SANTIAGO DE COMPOSTELA

[13] Jones, M. W. *et al.* Global and regional trends and drivers of fire under climate change. *Reviews of Geophysics* **60**, e2020RG000726 (2022).

[14] Lasslop, G. & Kloster, S. Human impact on wildfires varies between regions and with vegetation productivity. *Environmental Research Letters* **12**, 115011 (2017).

[15] Bowman, D. M. *et al.* Human exposure and sensitivity to globally extreme wildfire events. *Nature ecology & evolution* **1**, 0058 (2017).

[16] Kramer, H. A., Mockrin, M. H., Alexandre, P. M. & Radeloff, V. C. High wildfire damage in interface communities in california. *International journal of wildland fire* **28**, 641–650 (2019).

[17] Fann, N. *et al.* The health impacts and economic value of wildland fire episodes in the us: 2008–2012. *Science of the total environment* **610**, 802–809 (2018).

[18] Johnston, F. H. *et al.* Estimated global mortality attributable to smoke from landscape fires. *Environmental health perspectives* **120**, 695–701 (2012).

[19] Borchers Arriagada, N. *et al.* Unprecedented smoke-related health burden associated with the 2019–20 bushfires in eastern australia. *Medical Journal of Australia* **213**, 282–283 (2020).

[20] Doerr, S. H. & Santín, C. Global trends in wildfire and its impacts: perceptions versus realities in a changing world. *Philosophical Transactions of the Royal Society B: Biological Sciences* **371**, 20150345 (2016).

[21] Krawchuk, M. A., Moritz, M. A., Parisien, M.-A., Van Dorn, J. & Hayhoe, K. Global pyrogeography: the current and future distribution of wildfire. *PloS one* **4**, e5102 (2009).

[22] Kelley, D. I. *et al.* How contemporary bioclimatic and human controls change global fire regimes. *Nature Climate Change* **9**, 690–696 (2019).

[23] Loudermilk, E. L. *et al.* Linking complex forest fuel structure and fire behaviour at fine scales. *International Journal of Wildland Fire* **21**, 882–893 (2012).

[24] Rogers, B. M., Soja, A. J., Goulden, M. L. & Randerson, J. T. Influence of tree species on continental differences in boreal fires and climate feedbacks. *Nature Geoscience* **8**, 228–234 (2015).

[25] Pausas, J. G., Keeley, J. E. & Schwilk, D. W. Flammability as an ecological and evolutionary driver. *Journal of Ecology* **105**, 289–297 (2017).

[26] Krawchuk, M. A. & Moritz, M. A. Constraints on global fire activity vary across a resource gradient. *Ecology* **92**, 121–132 (2011).

[27] Pausas, J. G. & Paula, S. Fuel shapes the fire–climate relationship: evidence from mediterranean ecosystems. *Global Ecology and Biogeography* **21**, 1074–1082 (2012).

[28] Pausas, J. G. & Ribeiro, E. The global fire–productivity relationship. *Global Ecology and Biogeography* **22**, 728–736 (2013).

USC DE SANTIAGO

[29] Archibald, S., Lehmann, C. E., Gómez-Dans, J. L. & Bradstock, R. A. Defining pyromes and global syndromes of fire regimes. *Proceedings of the National Academy of Sciences* **110**, 6442–6447 (2013).

[30] Kelly, L. T. *et al.* Fire and biodiversity in the anthropocene. *Science* **370**, eabb0355 (2020).

[31] Harrison, S. P. *et al.* Understanding and modelling wildfire regimes: an ecological perspective. *Environmental Research Letters* **16**, 125008 (2021).

[32] He, T., Lamont, B. B. & Pausas, J. G. Fire as a key driver of earth's biodiversity. *Biological Reviews* **94**, 1983–2010 (2019).

[33] Marlon, J. R. *et al.* Climate and human influences on global biomass burning over the past two millennia. *Nature geoscience* **1**, 697–702 (2008).

[34] Marlon, J. R. *et al.* Global biomass burning: a synthesis and review of holocene paleofire records and their controls. *Quaternary Science Reviews* **65**, 5–25 (2013).

[35] Aldersley, A., Murray, S. J. & Cornell, S. E. Global and regional analysis of climate and human drivers of wildfire. *Science of the Total Environment* **409**, 3472–3481 (2011).

[36] Abatzoglou, J. T., Williams, A. P., Boschetti, L., Zubkova, M. & Kolden, C. A. Global patterns of interannual climate–fire relationships. *Global change biology* **24**, 5164–5175 (2018).

[37] Van der Werf, G. R., Randerson, J. T., Giglio, L., Gobron, N. & Dolman, A. Climate controls on the variability of fires in the tropics and subtropics. *Global Biogeochemical Cycles* **22** (2008).

[38] Jolly, W. M. *et al.* Climate-induced variations in global wildfire danger from 1979 to 2013. *Nature communications* **6**, 7537 (2015).

[39] Turco, M., Llasat, M. C., von Hardenberg, J. & Provenzale, A. Impact of climate variability on summer fires in a mediterranean environment (northeastern iberian peninsula). *Climatic Change* **116**, 665–678 (2013).

[40] Turco, M. *et al.* On the key role of droughts in the dynamics of summer fires in mediterranean europe. *Scientific reports* **7**, 1–10 (2017).

[41] Turco, M. *et al.* Skilful forecasting of global fire activity using seasonal climate predictions. *Nature communications* **9**, 1–9 (2018).

[42] Moritz, M. A. *et al.* Climate change and disruptions to global fire activity. *Ecosphere* **3**, 1–22 (2012).

[43] Van der Werf, G. R. *et al.* Global fire emissions estimates during 1997–2016. *Earth System Science Data* **9**, 697–720 (2017).

[44] Cook-Patton, S. C. *et al.* Mapping carbon accumulation potential from global natural forest regrowth. *Nature* **585**, 545–550 (2020).

USC UNIVERSIDADE DE SANTIAGO DE COMPOSTELA

[45] Bastin, J.-F. *et al.* The global tree restoration potential. *Science* **365**, 76–79 (2019).

[46] Turetsky, M. R. *et al.* Global vulnerability of peatlands to fire and carbon loss. *Nature Geoscience* **8**, 11–14 (2015).

[47] Yin, Y. *et al.* Fire decline in dry tropical ecosystems enhances decadal land carbon sink. *Nature communications* **11**, 1900 (2020).

[48] Bowring, S. P., Jones, M. W., Ciais, P., Guenet, B. & Abiven, S. Pyrogenic carbon decomposition critical to resolving fire's role in the earth system. *Nature Geoscience* **15**, 135–142 (2022).

[49] Zheng, B. *et al.* Increasing forest fire emissions despite the decline in global burned area. *Science advances* **7**, eabh2646 (2021).

[50] Zheng, B. *et al.* Record-high co2 emissions from boreal fires in 2021. *Science* **379**, 912–917 (2023).

[51] Ward, D. *et al.* The changing radiative forcing of fires: global model estimates for past, present and future. *Atmospheric Chemistry and Physics* **12**, 10857–10886 (2012).

[52] Tans, P. Global Monitoring Laboratory (GML) of the National Oceanic and Atmospheric Administration (NOAA). URL `gml.noaa.gov/ccgg/trends/`.

[53] Randerson, J. T. *et al.* The impact of boreal forest fire on climate warming. *Science* **314**, 1130–1132 (2006).

[54] Carslaw, K. *et al.* A review of natural aerosol interactions and feedbacks within the earth system. *Atmospheric Chemistry and Physics* **10**, 1701–1737 (2010).

[55] Chubarova, N., Nezval', Y., Sviridenkov, M., Smirnov, A. & Slutsker, I. Smoke aerosol and its radiative effects during extreme fire event over central russia in summer 2010. *Atmospheric Measurement Techniques Discussions* **4**, 6351–6386 (2011).

[56] Jiang, Y. *et al.* Impacts of global open-fire aerosols on direct radiative, cloud and surface-albedo effects simulated with cam5. *Atmospheric Chemistry and Physics* **16**, 14805–14824 (2016).

[57] Carter, T. S. *et al.* How emissions uncertainty influences the distribution and radiative impacts of smoke from fires in north america. *Atmospheric Chemistry and Physics* **20**, 2073–2097 (2020).

[58] Solomon, S. *et al.* On the stratospheric chemistry of midlatitude wildfire smoke. *Proceedings of the National Academy of Sciences* **119**, e2117325119 (2022).

[59] Bernath, P., Boone, C. & Crouse, J. Wildfire smoke destroys stratospheric ozone. *Science* **375**, 1292–1295 (2022).

[60] Wang, P., Solomon, S. & Stone, K. Stratospheric chlorine processing after the 2020 australian wildfires derived from satellite data. *Proceedings of the National Academy of Sciences* **120**, e2213910120 (2023).

[61] Solomon, S. *et al.* Chlorine activation and enhanced ozone depletion induced by wildfire aerosol. *Nature* **615**, 259–264 (2023).

[62] Abatzoglou, J. T., Rupp, D. E., O'Neill, L. W. & Sadegh, M. Compound extremes drive the western oregon wildfires of september 2020. *Geophysical Research Letters* **48**, e2021GL092520 (2021).

[63] Ruffault, J., Moron, V., Trigo, R. M. & Curt, T. Daily synoptic conditions associated with large fire occurrence in mediterranean france: evidence for a wind-driven fire regime. *International Journal of Climatology* **37**, 524–533 (2017).

[64] Trigo, R. M., Sousa, P. M., Pereira, M. G., Rasilla, D. & Gouveia, C. M. Modelling wildfire activity in iberia with different atmospheric circulation weather types. *International Journal of Climatology* **36**, 2761–2778 (2016).

[65] Hernandez, C., Drobinski, P. & Turquety, S. How much does weather control fire size and intensity in the mediterranean region? *Annales Geophysicae* **33**, 931–939 (2015).

[66] Urbieta, I. R. *et al.* Fire activity as a function of fire–weather seasonal severity and antecedent climate across spatial scales in southern europe and pacific western usa. *Environmental Research Letters* **10**, 114013 (2015).

[67] Aragão, L. E. *et al.* 21st century drought-related fires counteract the decline of amazon deforestation carbon emissions. *Nature communications* **9**, 536 (2018).

[68] Trigo, R. M. *et al.* Atmospheric conditions associated with the exceptional fire season of 2003 in portugal. *International Journal of Climatology: A Journal of the Royal Meteorological Society* **26**, 1741–1757 (2006).

[69] Ruffault, J. *et al.* Increased likelihood of heat-induced large wildfires in the mediterranean basin. *Scientific reports* **10**, 13790 (2020).

[70] Keeley, J. E. *et al.* Ignitions explain more than temperature or precipitation in driving santa ana wind fires. *Science advances* **7**, eabh2262 (2021).

[71] Jin, Y. *et al.* Identification of two distinct fire regimes in southern california: implications for economic impact and future change. *Environmental Research Letters* **10**, 094005 (2015).

[72] Lagouvardos, K., Kotroni, V., Giannaros, T. M. & Dafis, S. Meteorological conditions conducive to the rapid spread of the deadly wildfire in eastern attica, greece. *Bulletin of the American Meteorological Society* **100**, 2137–2145 (2019).

[73] Sharples, J. J., Mills, G. A., McRae, R. H. & Weber, R. O. Foehn-like winds and elevated fire danger conditions in southeastern australia. *Journal of Applied Meteorology and Climatology* **49**, 1067–1095 (2010).

[74] Veraverbeke, S. *et al.* Lightning as a major driver of recent large fire years in north american boreal forests. *Nature Climate Change* **7**, 529–534 (2017).

USC UNIVERSIDADE DE SANTIAGO DE COMPOSTELA

[75] Kasischke, E. S., Williams, D. & Barry, D. Analysis of the patterns of large fires in the boreal forest region of alaska. *International Journal of Wildland Fire* **11**, 131–144 (2002).

[76] Rodrigues, M. *et al.* Drivers and implications of the extreme 2022 wildfire season in southwest europe. *Science of the total environment* **859**, 160320 (2023).

[77] Fernandes, P. M., Santos, J. A., Castedo-Dorado, F. & Almeida, R. Fire from the sky in the anthropocene. *Fire* **4**, 13 (2021).

[78] Miguez-Macho, G. & Fan, Y. Spatiotemporal origin of soil water taken up by vegetation. *Nature* **598**, 624–628 (2021).

[79] Good, S. P., Noone, D. & Bowen, G. Hydrologic connectivity constrains partitioning of global terrestrial water fluxes. *Science* **349**, 175–177 (2015).

[80] Van der Ent, R. J., Savenije, H. H., Schaefli, B. & Steele-Dunne, S. C. Origin and fate of atmospheric moisture over continents. *Water Resources Research* **46** (2010).

[81] Insua-Costa, D., Senande-Rivera, M., Llasat, M. C. & Miguez-Macho, G. The central role of forests in the 2021 european floods. *Environmental Research Letters* **17**, 064053 (2022).

[82] Hernandez, C., Drobinski, P. & Turquety, S. Impact of wildfire-induced land cover modification on local meteorology: A sensitivity study of the 2003 wildfires in portugal. *Atmospheric Research* **164**, 49–64 (2015).

[83] Poon, P. K. & Kinoshita, A. M. Spatial and temporal evapotranspiration trends after wildfire in semi-arid landscapes. *Journal of hydrology* **559**, 71–83 (2018).

[84] De Sales, F., Okin, G. S., Xue, Y. & Dintwe, K. On the effects of wildfires on precipitation in southern africa. *Climate dynamics* **52**, 951–967 (2019).

[85] Saha, M. V., Scanlon, T. M. & D'Odorico, P. Suppression of rainfall by fires in african drylands. *Geophysical Research Letters* **43**, 8527–8533 (2016).

[86] Huang, X. *et al.* Smoke-weather interaction affects extreme wildfires in diverse coastal regions. *Science* **379**, 457–461 (2023).

[87] Grell, G., Freitas, S., Stuefer, M. & Fast, J. Inclusion of biomass burning in wrf-chem: impact of wildfires on weather forecasts. *Atmospheric Chemistry and Physics* **11**, 5289–5303 (2011).

[88] Lu, Z. & Sokolik, I. N. The effect of smoke emission amount on changes in cloud properties and precipitation: A case study of canadian boreal wildfires of 2007. *Journal of Geophysical Research: Atmospheres* **118**, 11–777 (2013).

[89] Graf, H.-F., Yang, J. & Wagner, T. Aerosol effects on clouds and precipitation during the 1997 smoke episode in indonesia. *Atmospheric Chemistry and Physics* **9**, 743–756 (2009).

USC DE COMPOSTELA

[90] Zhang, Y. *et al.* Notable impact of wildfires in the western united states on weather hazards in the central united states. *Proceedings of the National Academy of Sciences* **119**, e2207329119 (2022).

[91] Yu, P. *et al.* Persistent stratospheric warming due to 2019–2020 australian wildfire smoke. *Geophysical Research Letters* **48**, e2021GL092609 (2021).

[92] Khaykin, S. *et al.* The 2019/20 australian wildfires generated a persistent smoke-charged vortex rising up to 35 km altitude. *Communications Earth & Environment* **1**, 22 (2020).

[93] Kablick III, G., Allen, D. R., Fromm, M. D. & Nedoluha, G. E. Australian pyrocb smoke generates synoptic-scale stratospheric anticyclones. *Geophysical Research Letters* **47**, e2020GL088101 (2020).

[94] Rothermel, R. C. A mathematical model for predicting fire spread in wildland fuels. techreport 115, U.S. Department of Agriculture Forest Service (1972).

[95] Albini, F. A. Potential spotting distance from wind-driven surface fires. techreport 309, U.S. Department of Agriculture Forest Service (1983).

[96] Mandel, J., Beezley, J. D. & Kochanski, A. K. Coupled atmosphere–wildland fire modeling with wrf 3.3 and sfire. *Geoscientific Model Development* **4**, 591–610 (2011).

[97] Dowdy, A. J. *et al.* Future changes in extreme weather and pyroconvection risk factors for australian wildfires. *Scientific reports* **9**, 10073 (2019).

[98] Fromm, M. *et al.* The untold story of pyrocumulonimbus. *Bulletin of the American Meteorological Society* **91**, 1193–1210 (2010).

[99] Potter, B. E. Atmospheric interactions with wildland fire behaviour–ii. plume and vortex dynamics. *International Journal of Wildland Fire* **21**, 802–817 (2012).

[100] McRae, R. H., Sharples, J. J. & Fromm, M. Linking local wildfire dynamics to pyrocb development. *Natural Hazards and Earth System Science* **15**, 417–428 (2015).

[101] Dowdy, A. J., Fromm, M. D. & McCarthy, N. Pyrocumulonimbus lightning and fire ignition on black saturday in southeast australia. *Journal of Geophysical Research: Atmospheres* **122**, 7342–7354 (2017).

[102] Fromm, M., Tupper, A., Rosenfeld, D., Servranckx, R. & McRae, R. Violent pyro-convective storm devastates australia's capital and pollutes the stratosphere. *Geophysical Research Letters* **33** (2006).

[103] Cunningham, P. & Reeder, M. J. Severe convective storms initiated by intense wildfires: Numerical simulations of pyro-convection and pyro-tornadogenesis. *Geophysical Research Letters* **36** (2009).

[104] Damoah, R. *et al.* A case study of pyro-convection using transport model and remote sensing data. *Atmospheric Chemistry and Physics* **6**, 173–185 (2006).

USC UNIVERSIDADE DE SANTIAGO DE COMPOSTELA

[105] Peterson, D. A. *et al.* The 2013 rim fire: Implications for predicting extreme fire spread, pyroconvection, and smoke emissions. *Bulletin of the American Meteorological Society* **96**, 229–247 (2015).

[106] Bladon, K. D., Emelko, M. B., Silins, U. & Stone, M. Wildfire and the future of water supply. *Environmental Science & Technology* **48**, 8936–8943 (2014).

[107] Keegan, K. M., Albert, M. R., McConnell, J. R. & Baker, I. Climate change and forest fires synergistically drive widespread melt events of the greenland ice sheet. *Proceedings of the National Academy of Sciences* **111**, 7964–7967 (2014).

[108] Flanner, M. G., Zender, C. S., Randerson, J. T. & Rasch, P. J. Present-day climate forcing and response from black carbon in snow. *Journal of Geophysical Research: Atmospheres* **112** (2007).

[109] Bladon, K. D. Rethinking wildfires and forest watersheds. *Science* **359**, 1001–1002 (2018).

[110] Arrhenius, S. On the influence of carbonic acid in the air upon the temperature of the ground. *The London, Edinburgh, and Dublin Philosophical Magazine and Journal of Science* **41**, 237–276 (1896).

[111] Revelle, R. & Suess, H. E. Carbon dioxide exchange between atmosphere and ocean and the question of an increase of atmospheric co2 during the past decades. *Tellus* **9**, 18–27 (1957).

[112] Keeling, C. D. The concentration and isotopic abundances of carbon dioxide in the atmosphere. *Tellus* **12**, 200–203 (1960).

[113] Manabe, S. & Wetherald, R. T. Thermal equilibrium of the atmosphere with a given distribution of relative humidity. *Journal of Atmospheric Sciences* **24**, 241 – 259 (1967).

[114] Manabe, S. & Wetherald, R. T. The effects of doubling the co 2 concentration on the climate of a general circulation model. *Journal of Atmospheric Sciences* **32**, 3–15 (1975).

[115] Chen, D. *et al.* Framing, context, and methods. In Masson-Delmotte, V. *et al.* (eds.) *Climate Change 2021: The Physical Science Basis. Contribution of Working Group I to the Sixth Assessment Report of the Intergovernmental Panel on Climate Change*, chap. 1, 147–286 (Cambridge University Press, United Kingdom and New York, NY, USA, 2021).

[116] Marshall, J. & Plumb, R. A. *Atmosphere, ocean and climate dynamics: an introductory text* (Elsevier Academic Press, 2008).

[117] Goosse, H. *Climate system dynamics and modeling* (Cambridge University Press, 2015).

[118] Forster, P. *et al.* The earth's energy budget, climate feedbacks, and climate sensitivity. In Masson-Delmotte, V. *et al.* (eds.) *Climate Change 2021: The Physical Science Basis. Contribution of Working Group I to the Sixth Assessment Report of the Intergovernmental Panel on Climate Change*, chap. 7, 923–1054 (Cambridge University Press, United Kingdom and New York, NY, USA, 2021).

USC

[119] IPCC. Summary for policymakers. In Masson-Delmotte, V. *et al.* (eds.) *Climate Change 2021: The Physical Science Basis. Contribution of Working Group I to the Sixth Assessment Report of the Intergovernmental Panel on Climate Change*, 3–32 (Cambridge University Press, United Kingdom and New York, NY, USA, 2021).

[120] Gulev, S. *et al.* Changing state of the climate system. In Masson-Delmotte, V. *et al.* (eds.) *Climate Change 2021: The Physical Science Basis. Contribution of Working Group I to the Sixth Assessment Report of the Intergovernmental Panel on Climate Change*, chap. 2, 287–422 (Cambridge University Press, United Kingdom and New York, NY, USA, 2021).

[121] Wu, C., Krivova, N. A., Solanki, S. K. & Usoskin, I. Solar total and spectral irradiance reconstruction over the last 9000 years. *Astronomy & Astrophysics* **620**, A120 (2018).

[122] Neukom, R., Steiger, N., Gómez-Navarro, J. J., Wang, J. & Werner, J. P. No evidence for globally coherent warm and cold periods over the preindustrial common era. *Nature* **571**, 550–554 (2019).

[123] Consortium, P. A global multiproxy database for temperature reconstructions of the common era. *Scientific data* **4** (2017).

[124] Poli, P. *et al.* Era-20c: An atmospheric reanalysis of the twentieth century. *Journal of Climate* **29**, 4083–4097 (2016).

[125] Kaufman, D. *et al.* Holocene global mean surface temperature, a multi-method reconstruction approach. *Scientific data* **7**, 201 (2020).

[126] Arias, P. *et al.* Technical summary. In Masson-Delmotte, V. *et al.* (eds.) *Climate Change 2021: The Physical Science Basis. Contribution of Working Group I to the Sixth Assessment Report of the Intergovernmental Panel on Climate Change*, 33–144 (Cambridge University Press, United Kingdom and New York, NY, USA, 2021).

[127] Eyring, V. *et al.* Human influence on the climate system. In Masson-Delmotte, V. *et al.* (eds.) *Climate Change 2021: The Physical Science Basis. Contribution of Working Group I to the Sixth Assessment Report of the Intergovernmental Panel on Climate Change*, chap. 3, 423–552 (Cambridge University Press, United Kingdom and New York, NY, USA, 2021).

[128] Piao, S. *et al.* Characteristics, drivers and feedbacks of global greening. *Nature Reviews Earth & Environment* **1**, 14–27 (2020).

[129] Hersbach, H. *et al.* The era5 global reanalysis. *Quarterly Journal of the Royal Meteorological Society* **146**, 1999–2049 (2020).

[130] Cao, S. *et al.* Spatiotemporally consistent global dataset of the gimms leaf area index (gimms lai4g) from 1982 to 2020. *Earth System Science Data* **2023**, 1–31 (2023).

[131] Stuecker, M. F. *et al.* Polar amplification dominated by local forcing and feedbacks. *Nature Climate Change* **8**, 1076–1081 (2018).

USC UNIVERSIDADE DE SANTIAGO DE COMPOSTELA

[132] O'Neill, B. C. *et al.* The scenario model intercomparison project (scenariomip) for cmip6. *Geoscientific Model Development* **9**, 3461–3482 (2016).

[133] Taylor, K. E., Stouffer, R. J. & Meehl, G. A. An overview of cmip5 and the experiment design. *Bulletin of the American meteorological Society* **93**, 485–498 (2012).

[134] Meehl, G. A. *et al.* The wcrp cmip3 multimodel dataset: A new era in climate change research. *Bulletin of the American meteorological society* **88**, 1383–1394 (2007).

[135] Abatzoglou, J. T. & Williams, A. P. Impact of anthropogenic climate change on wildfire across western us forests. *Proceedings of the National Academy of Sciences* **113**, 11770–11775 (2016).

[136] Flannigan, M. *et al.* Fuel moisture sensitivity to temperature and precipitation: climate change implications. *Climatic Change* **134**, 59–71 (2016).

[137] Abatzoglou, J. T., Williams, A. P. & Barbero, R. Global emergence of anthropogenic climate change in fire weather indices. *Geophysical Research Letters* **46**, 326–336 (2019).

[138] Barbero, R., Abatzoglou, J. T., Pimont, F., Ruffault, J. & Curt, T. Attributing increases in fire weather to anthropogenic climate change over france. *Frontiers in Earth Science* **8**, 104 (2020).

[139] Calheiros, T., Pereira, M. & Nunes, J. P. Assessing impacts of future climate change on extreme fire weather and pyro-regions in iberian peninsula. *Science of The Total Environment* **754**, 142233 (2021).

[140] Ellis, T. M., Bowman, D. M., Jain, P., Flannigan, M. D. & Williamson, G. J. Global increase in wildfire risk due to climate-driven declines in fuel moisture. *Global change biology* **28**, 1544–1559 (2022).

[141] Flannigan, M. D., Krawchuk, M. A., de Groot, W. J., Wotton, B. M. & Gowman, L. M. Implications of changing climate for global wildland fire. *International journal of wildland fire* **18**, 483–507 (2009).

[142] Flannigan, M. *et al.* Global wildland fire season severity in the 21st century. *Forest Ecology and Management* **294**, 54–61 (2013).

[143] Dong, C. *et al.* The season for large fires in southern california is projected to lengthen in a changing climate. *Communications Earth & Environment* **3**, 22 (2022).

[144] Gillett, N., Weaver, A., Zwiers, F. & Flannigan, M. Detecting the effect of climate change on canadian forest fires. *Geophysical Research Letters* **31** (2004).

[145] Bedia, J. *et al.* Global patterns in the sensitivity of burned area to fire-weather: Implications for climate change. *Agricultural and Forest Meteorology* **214**, 369–379 (2015).

[146] Wu, M. *et al.* Sensitivity of burned area in europe to climate change, atmospheric co2 levels, and demography: A comparison of two fire-vegetation models. *Journal of Geophysical Research: Biogeosciences* **120**, 2256–2272 (2015).

USC

[147] Turco, M. *et al.* Exacerbated fires in mediterranean europe due to anthropogenic warming projected with non-stationary climate-fire models. *Nature communications* **9**, 3821 (2018).

[148] Teckentrup, L. *et al.* Response of simulated burned area to historical changes in environmental and anthropogenic factors: a comparison of seven fire models. *Biogeosciences* **16**, 3883–3910 (2019).

[149] Williams, A. P. *et al.* Observed impacts of anthropogenic climate change on wildfire in california. *Earth's Future* **7**, 892–910 (2019).

[150] Canadell, J. G. *et al.* Multi-decadal increase of forest burned area in australia is linked to climate change. *Nature communications* **12**, 6921 (2021).

[151] Van der Velde, I. R. *et al.* Vast co2 release from australian fires in 2019–2020 constrained by satellite. *Nature* **597**, 366–369 (2021).

[152] Turco, M. *et al.* Climate drivers of the 2017 devastating fires in portugal. *Scientific reports* **9**, 13886 (2019).

[153] Safford, H. D., Paulson, A. K., Steel, Z. L., Young, D. J. & Wayman, R. B. The 2020 california fire season: A year like no other, a return to the past or a harbinger of the future? *Global Ecology and Biogeography* **31**, 2005–2025 (2022).

[154] Kirchmeier-Young, M. C., Zwiers, F. W., Gillett, N. P. & Cannon, A. J. Attributing extreme fire risk in western canada to human emissions. *Climatic Change* **144**, 365–379 (2017).

[155] Kirchmeier-Young, M. C., Gillett, N. P., Zwiers, F. W., Cannon, A. J. & Anslow, F. Attribution of the influence of human-induced climate change on an extreme fire season. *Earth's Future* **7**, 2–10 (2019).

[156] Goss, M. *et al.* Climate change is increasing the likelihood of extreme autumn wildfire conditions across california. *Environmental Research Letters* **15**, 094016 (2020).

[157] Du, J., Wang, K. & Cui, B. Attribution of the extreme drought-related risk of wildfires in spring 2019 over southwest china. *Bulletin of the American Meteorological Society* **102**, S83–S90 (2021).

[158] Liu, Z., Eden, J. M., Dieppois, B. & Blackett, M. A global view of observed changes in fire weather extremes: uncertainties and attribution to climate change. *Climatic Change* **173**, 14 (2022).

[159] Jain, P., Castellanos-Acuna, D., Coogan, S. C., Abatzoglou, J. T. & Flannigan, M. D. Observed increases in extreme fire weather driven by atmospheric humidity and temperature. *Nature Climate Change* **12**, 63–70 (2022).

[160] Williams, A. P. & Abatzoglou, J. T. Recent advances and remaining uncertainties in resolving past and future climate effects on global fire activity. *Current Climate Change Reports* **2**, 1–14 (2016).

USC UNIVERSIDADE DE SANTIAGO DE COMPOSTELA

[161] Hantson, S. *et al.* The status and challenge of global fire modelling. *Biogeosciences* **13**, 3359–3375 (2016).

[162] Frandsen, W. H. Fire spread through porous fuels from the conservation of energy. *Combustion and Flame* **16**, 9–16 (1971).

[163] Andrews, P. L. The rothermel surface fire spread model and associated developments: A comprehensive explanation. techreport RMRS-GTR-371, U.S. Department of Agriculture Forest Service (2018).

[164] Anderson, H. E. Heat transfer and fire spread. techreport 69, U.S. Department of Agriculture Forest Service (1969).

[165] Philpot, C. W. Mineral content and pyrolysis of selected plant materials. techreport 84, U.S. Department of Agriculture Forest Service (1968).

[166] McArthur, A. The tasmanian bushfires of 7th february, 1967, and associated fire behaviour characteristics. techreport 23, Mass Fire Symposium, Camberra, Australia (1969).

[167] Anderson, H. E. Aids to determining fuel models for estimating fire behavior. techreport 122, U.S. Department of Agriculture Forest Service (1982).

[168] Mandel, J. *et al.* Recent advances and applications of wrf–sfire. *Natural Hazards and Earth System Sciences* **14**, 2829–2845 (2014).

[169] Van Wagner, C. Development and structure of the canadian forest fire weather index system. techreport 35, Canadian Forestry Service (1987).

[170] Van Wagner, C. & Pickett, T. Equations and fortran program for the canadian forest fire weather index system. techreport 33, Canadian Forestry Service (1985).

[171] Nelson Jr, R. M. Prediction of diurnal change in 10-h fuel stick moisture content. *Canadian Journal of Forest Research* **30**, 1071–1087 (2000).

[172] Ruiz-González, A. D., Vega-Hidalgo, J. A. & Álvarez-González, J. G. Construction of empirical models for predicting pinus sp. dead fine fuel moisture in nw spain. i: Response to changes in temperature and relative humidity. *International Journal of Wildland Fire* **18**, 71–83 (2009).

[173] Matthews, S. A process-based model of fine fuel moisture. *International Journal of Wildland Fire* **15**, 155–168 (2006).

[174] Jolly, W. M., Nemani, R. & Running, S. W. A generalized, bioclimatic index to predict foliar phenology in response to climate. *Global Change Biology* **11**, 619–632 (2005).

[175] Scott, J. H. & Burgan, R. Standard fire behavior fuel models: a comprehensive set for use with rothermel's surface fire spread model. techreport 153, U.S. Department of Agriculture Forest Service (2005).

[176] Holton, J. R. & Hakim, G. J. *An Introduction to Dynamic Meteorology* (Elsevier Academic Press, 2013), fifth edn.

USC

[177] Coen, J. L. *et al.* Wrf–fire: coupled weather–wildland fire modeling with the weather research and forecasting model. *Journal of Applied Meteorology and Climatology* **52**, 16–38 (2013).

[178] Muñoz-Esparza, D., Kosović, B., Jiménez, P. A. & Coen, J. L. An accurate fire-spread algorithm in the weather research and forecasting model using the level-set method. *Journal of Advances in Modeling Earth Systems* **10**, 908–926 (2018).

[179] Skamarock, W. C. *et al.* A description of the advanced research wrf model version 4. techreport 145, National Center for Atmospheric Research: Boulder, CO, USA (2019).

[180] Osher, S. & Fedkiw, R. P. *Level set methods and dynamic implicit surfaces* (Springer, New York, 2003).

[181] Schmetz, J. *et al.* An introduction to meteosat second generation (msg). *Bulletin of the American Meteorological Society* **83**, 977–992 (2002).

[182] Drusch, M. *et al.* Sentinel-2: Esa's optical high-resolution mission for gmes operational services. *Remote sensing of Environment* **120**, 25–36 (2012).

[183] Keeley, J. E. Fire intensity, fire severity and burn severity: a brief review and suggested usage. *International journal of wildland fire* **18**, 116–126 (2009).

[184] Comissão-Técnica-Independente. Análise e apuramento dos factos relativos aos incêndios que ocorreram em pedrógão grande, castanheira de pera, ansião, alvaiázere, figueiró dos vinhos, arganil, góis, penela, papilhosa da serra, oleiros e sertã, entre 17 e 24 de junho de 2017. Tech. Rep., Assembleia da República (2017).

[185] Viegas, D. *et al.* O complexo de incêndios de pedrógão grande e concelhos limítrofes, iniciado a 17 de junho de 2017. Tech. Rep., Centro de Estudos sobre Incêndios Florestais (Universidade de Coimbra) (2017).

[186] Moreira, N. *et al.* Condições meteorológicas associadas ao incêndio de pedrógão grande de 17 junho 2017. Tech. Rep., Instituto Português do Mar e da Atmosfera (IPMA) (2017).

[187] Forkel, M. *et al.* Recent global and regional trends in burned area and their compensating environmental controls. *Environmental research communications* **1**, 051005 (2019).

[188] Liu, Y., Stanturf, J. & Goodrick, S. Trends in global wildfire potential in a changing climate. *Forest ecology and management* **259**, 685–697 (2010).

[189] Pechony, O. & Shindell, D. T. Driving forces of global wildfires over the past millennium and the forthcoming century. *Proceedings of the National Academy of Sciences* **107**, 19167–19170 (2010).

[190] Giglio, L., Randerson, J. T. & Van Der Werf, G. R. Analysis of daily, monthly, and annual burned area using the fourth-generation global fire emissions database (gfed4). *Journal of Geophysical Research: Biogeosciences* **118**, 317–328 (2013).

[191] Giglio, L., Loboda, T., Roy, D. P., Quayle, B. & Justice, C. O. An active-fire based burned area mapping algorithm for the modis sensor. *Remote sensing of environment* **113**, 408–420 (2009).

USC UNIVERSIDADE DE SANTIAGO DE COMPOSTELA

[192] Copernicus climate change service (c3s). near surface meteorological variables from 1979 to 2018 derived from bias-corrected reanalysis. Copernicus Climate Change Service Climate Data Store (CDS) (2020).

[193] Weedon, G. *et al.* Creation of the watch forcing data and its use to assess global and regional reference crop evaporation over land during the twentieth century. *Journal of Hydrometeorology* **12**, 823–848 (2011).

[194] Cucchi, M. *et al.* Wfde5: bias-adjusted era5 reanalysis data for impact studies. *Earth System Science Data* **12**, 2097–2120 (2020).

[195] Harris, I., Jones, P. D., Osborn, T. J. & Lister, D. H. Updated high-resolution grids of monthly climatic observations–the cru ts3. 10 dataset. *International journal of climatology* **34**, 623–642 (2014).

[196] Schneider, U., Becker, A., Finger, P., Meyer-Christoffer, A. & Ziese, M. Gpcc full data monthly product version 2018 at 0.5°: Monthly land-surface precipitation from rain-gauges built on gts-based and historical data. Global Precipitation Climatology Centre (2018).

[197] Taylor, K. E., Stouffer, R. J. & Meehl, G. A. An overview of cmip5 and the experiment design. *Bulletin of the American meteorological Society* **93**, 485–498 (2012).

[198] Riahi, K. *et al.* Rcp 8.5—a scenario of comparatively high greenhouse gas emissions. *Climatic change* **109**, 33–57 (2011).

[199] Van Vuuren, D. P. *et al.* The representative concentration pathways: an overview. *Climatic change* **109**, 5–31 (2011).

[200] Teutschbein, C. & Seibert, J. Bias correction of regional climate model simulations for hydrological climate-change impact studies: Review and evaluation of different methods. *Journal of hydrology* **456**, 12–29 (2012).

[201] Köppen, W. *Das Geographische System der Klimate* (Gebrüder Borntraeger, Berlin, Germany, 1936).

[202] Beck, H. E. *et al.* Present and future köppen-geiger climate classification maps at 1-km resolution. *Scientific data* **5**, 1–12 (2018).

[203] Peel, M. C., Finlayson, B. L. & McMahon, T. A. Updated world map of the köppen-geiger climate classification. *Hydrology and earth system sciences* **11**, 1633–1644 (2007).

[204] Wilcock, A. A. Köppen after fifty years. *Annals of the Association of American Geographers* **58**, 12–28 (1968).

[205] Russel, R. Dry climates of the united states: I. climatic map. *University of California Publications in Geography* **5**, 1–41 (1931).

[206] Kottek, M., Grieser, J., Beck, C., Rudolf, B. & Rubel, F. World map of the köppen-geiger climate classification updated. *Meteorologische Zeitschrift* **15**, 259–263 (2006).

USC

[207] Whittaker, R. H. *Communities and ecosystems*. 167 (MacMillan, New York, USA, 1975), 2nd edn.

[208] Woodward, F. I., Lomas, M. R. & Kelly, C. K. Global climate and the distribution of plant biomes. *Philosophical Transactions of the Royal Society of London. Series B: Biological Sciences* **359**, 1465–1476 (2004).

[209] Yue, C. *et al.* Modelling the role of fires in the terrestrial carbon balance by incorporating spitfire into the global vegetation model orchidee–part 1: simulating historical global burned area and fire regimes. *Geoscientific Model Development* **7**, 2747–2767 (2014).

[210] Le Page, Y., Oom, D., Silva, J. M., Jönsson, P. & Pereira, J. M. Seasonality of vegetation fires as modified by human action: observing the deviation from eco-climatic fire regimes. *Global Ecology and Biogeography* **19**, 575–588 (2010).

[211] Hall, J. V., Loboda, T. V., Giglio, L. & McCarty, G. W. A modis-based burned area assessment for russian croplands: Mapping requirements and challenges. *Remote Sensing of Environment* **184**, 506–521 (2016).

[212] Cahoon, D. R., Stocks, B. J., Levine, J. S., Cofer, W. R. & O'Neill, K. P. Seasonal distribution of african savanna fires. *Nature* **359**, 812–815 (1992).

[213] Archibald, S., Roy, D. P., van Wilgen, B. W. & Scholes, R. J. What limits fire? an examination of drivers of burnt area in southern africa. *Global Change Biology* **15**, 613–630 (2009).

[214] Van Der Werf, G. R., Randerson, J. T., Collatz, G. J. & Giglio, L. Carbon emissions from fires in tropical and subtropical ecosystems. *Global Change Biology* **9**, 547–562 (2003).

[215] Bradstock, R. A. A biogeographic model of fire regimes in australia: current and future implications. *Global Ecology and Biogeography* **19**, 145–158 (2010).

[216] Andela, N. *et al.* Biomass burning fuel consumption dynamics in the tropics and subtropics assessed from satellite. *Biogeosciences* **13**, 3717–3734 (2016).

[217] Kull, C. & Laris, P. Fire ecology and fire politics in mali and madagascar. In Cochrane, M. (ed.) *Tropical Fire Ecology: Climate Change, Land Use and Ecosystem Dynamics*, 171–226 (Springer-Praxis, Heildelberg, 2009).

[218] Laris, P. Burning the seasonal mosaic: preventative burning strategies in the wooded savanna of southern mali. *Human Ecology* **30**, 155–186 (2002).

[219] Mbow, C., Nielsen, T. T. & Rasmussen, K. Savanna fires in east-central senegal: distribution patterns, resource management and perceptions. *Human Ecology* 561–583 (2000).

[220] Littell, J. S., McKenzie, D., Peterson, D. L. & Westerling, A. L. Climate and wildfire area burned in western us ecoprovinces, 1916–2003. *Ecological Applications* **19**, 1003–1021 (2009).

USC UNIVERSIDADE DE SANTIAGO DE COMPOSTELA

[221] Marlon, J. R. *et al.* Long-term perspective on wildfires in the western usa. *Proceedings of the National Academy of Sciences* **109**, E535–E543 (2012).

[222] Parisien, M.-A. & Moritz, M. A. Environmental controls on the distribution of wildfire at multiple spatial scales. *Ecological Monographs* **79**, 127–154 (2009).

[223] Seager, R. *et al.* Climatology, variability, and trends in the us vapor pressure deficit, an important fire-related meteorological quantity. *Journal of Applied Meteorology and Climatology* **54**, 1121–1141 (2015).

[224] Sousa, P. M., Trigo, R. M., Pereira, M. G., Bedia, J. & Gutiérrez, J. M. Different approaches to model future burnt area in the iberian peninsula. *Agricultural and Forest Meteorology* **202**, 11–25 (2015).

[225] Van Der Werf, G. R. *et al.* Continental-scale partitioning of fire emissions during the 1997 to 2001 el nino/la nina period. *Science* **303**, 73–76 (2004).

[226] Chen, Y. *et al.* A pan-tropical cascade of fire driven by el niño/southern oscillation. *Nature Climate Change* **7**, 906–911 (2017).

[227] Flannigan, M. D., Logan, K. A., Amiro, B. D., Skinner, W. R. & Stocks, B. J. Future area burned in canada. *Climatic change* **72**, 1–16 (2005).

[228] Kilpeläinen, A., Kellomäki, S., Strandman, H. & Venäläinen, A. Climate change impacts on forest fire potential in boreal conditions in finland. *Climatic Change* **103**, 383–398 (2010).

[229] Archibald, S. *et al.* Biological and geophysical feedbacks with fire in the earth system. *Environmental Research Letters* **13**, 033003 (2018).

[230] Bowman, D. M. *et al.* The human dimension of fire regimes on earth. *Journal of biogeography* **38**, 2223–2236 (2011).

[231] Nolan, C. *et al.* Past and future global transformation of terrestrial ecosystems under climate change. *Science* **361**, 920–923 (2018).

[232] Myhre, G. *et al.* Frequency of extreme precipitation increases extensively with event rareness under global warming. *Scientific reports* **9**, 16063 (2019).

[233] Pithan, F. & Mauritsen, T. Arctic amplification dominated by temperature feedbacks in contemporary climate models. *Nature geoscience* **7**, 181–184 (2014).

[234] De Groot, W. J., Flannigan, M. D. & Cantin, A. S. Climate change impacts on future boreal fire regimes. *Forest Ecology and Management* **294**, 35–44 (2013).

[235] Nelson, K., Thompson, D., Hopkinson, C., Petrone, R. & Chasmer, L. Peatland-fire interactions: A review of wildland fire feedbacks and interactions in canadian boreal peatlands. *Science of the total environment* **769**, 145212 (2021).

[236] Melton, J. R. *et al.* A map of global peatland extent created using machine learning (peat-ml). *Geoscientific Model Development* **15**, 4709–4738 (2022).

USC DE SANTIAGO

[237] Giorgi, F. & Lionello, P. Climate change projections for the mediterranean region. *Global and planetary change* **63**, 90–104 (2008).

[238] Dennison, P. E., Brewer, S. C., Arnold, J. D. & Moritz, M. A. Large wildfire trends in the western united states, 1984–2011. *Geophysical Research Letters* **41**, 2928–2933 (2014).

[239] Barbero, R., Abatzoglou, J. T., Larkin, N. K., Kolden, C. A. & Stocks, B. Climate change presents increased potential for very large fires in the contiguous united states. *International Journal of Wildland Fire* **24**, 892–899 (2015).

[240] Serdeczny, O. *et al.* Climate change impacts in sub-saharan africa: from physical changes to their social repercussions. *Regional Environmental Change* **17**, 1585–1600 (2017).

[241] Andela, N. & Van Der Werf, G. R. Recent trends in african fires driven by cropland expansion and el niño to la niña transition. *Nature Climate Change* **4**, 791–795 (2014).

[242] Dore, M. H. Climate change and changes in global precipitation patterns: what do we know? *Environment international* **31**, 1167–1181 (2005).

[243] Fasullo, J., Otto-Bliesner, B. & Stevenson, S. Enso's changing influence on temperature, precipitation, and wildfire in a warming climate. *Geophysical Research Letters* **45**, 9216–9225 (2018).

[244] Perry, S. J., McGregor, S., Gupta, A. S. & England, M. H. Future changes to el niño–southern oscillation temperature and precipitation teleconnections. *Geophysical Research Letters* **44**, 10–608 (2017).

[245] IPCC. *Climate Change 2021: The Physical Science Basis. Contribution of Working Group I to the Sixth Assessment Report of the Intergovernmental Panel on Climate Change*, vol. In Press (Cambridge University Press, Cambridge, United Kingdom and New York, NY, USA, 2021).

[246] Shepherd, T. G. *et al.* Storylines: an alternative approach to representing uncertainty in physical aspects of climate change. *Climatic change* **151**, 555–571 (2018).

[247] Clarke, H. *et al.* Forest fire threatens global carbon sinks and population centres under rising atmospheric water demand. *Nature Communications* **13**, 7161 (2022).

[248] Zhu, Z. *et al.* Greening of the earth and its drivers. *Nature climate change* **6**, 791–795 (2016).

[249] Pausas, J. G. & Keeley, J. E. Wildfires and global change. *Frontiers in Ecology and the Environment* **19**, 387–395 (2021).

[250] Turco, M. *et al.* Decreasing fires in mediterranean europe. *PLoS one* **11**, e0150663 (2016).

[251] Giannaros, T. M., Kotroni, V. & Lagouvardos, K. Climatology and trend analysis (1987–2016) of fire weather in the euro-mediterranean. *International Journal of Climatology* **41**, E491–E508 (2021).

USC UNIVERSIDADE DE SANTIAGO DE COMPOSTELA

[252] Shepherd, T. G. Atmospheric circulation as a source of uncertainty in climate change projections. *Nature Geoscience* **7**, 703–708 (2014).

[253] Riahi, K. *et al.* The shared socioeconomic pathways and their energy, land use, and greenhouse gas emissions implications: An overview. *Global environmental change* **42**, 153–168 (2017).

[254] Meinshausen, M. *et al.* The shared socio-economic pathway (ssp) greenhouse gas concentrations and their extensions to 2500. *Geoscientific Model Development* **13**, 3571–3605 (2020).

[255] Lawrence, D. M. *et al.* The land use model intercomparison project (lumip) contribution to cmip6: rationale and experimental design. *Geoscientific Model Development* **9**, 2973–2998 (2016).

[256] Yebra, M. *et al.* Globe-lfmc, a global plant water status database for vegetation ecophysiology and wildfire applications. *Scientific data* **6**, 155 (2019).

[257] Keetch, J. J. & Byram, G. M. A drought index for forest fire control. techreport 38, U.S. Department of Agriculture Forest Service (1968).

[258] San-Miguel-Ayanz, J., Moreno, J. M. & Camia, A. Analysis of large fires in european mediterranean landscapes: Lessons learned and perspectives. *Forest Ecology and Management* **294**, 11–22 (2013).

[259] Solomos, S. *et al.* Modeling and remote sensing of an indirect pyro-cb formation and biomass transport from portugal wildfires towards europe. *Atmospheric Environment* **206**, 303–315 (2019).

[260] Peterson, D. A., Hyer, E. J., Campbell, J. R., Solbrig, J. E. & Fromm, M. D. A conceptual model for development of intense pyrocumulonimbus in western north america. *Monthly Weather Review* **145**, 2235–2255 (2017).

[261] Badlan, R. L., Sharples, J. J., Evans, J. P. & McRae, R. H. Factors influencing the development of violent pyroconvection. part i: fire size and stability. *International journal of wildland fire* **30**, 484–497 (2021).

[262] McRae, R. & Sharples, J. Forecasting conditions conducive to blow-up fire events. *CAWCR Research Letters* **11**, 14–19 (2014).

[263] Tory, K. J., Thurston, W. & Kepert, J. D. Thermodynamics of pyrocumulus: A conceptual study. *Monthly Weather Review* **146**, 2579–2598 (2018).

[264] Trentmann, J. *et al.* Modeling of biomass smoke injection into the lower stratosphere by a large forest fire (part i): reference simulation. *Atmospheric Chemistry and Physics* **6**, 5247–5260 (2006).

[265] Potter, B. E. The role of released moisture in the atmospheric dynamics associated with wildland fires. *International Journal of Wildland Fire* **14**, 77–84 (2005).

USC UNIVERSIDADE DE SANTIAGO DE COMPOSTELA

[266] Luderer, G. *et al.* Modeling of biomass smoke injection into the lower stratosphere by a large forest fire (part ii): sensitivity studies. *Atmospheric Chemistry and Physics* **6**, 5261–5277 (2006).

[267] Luderer, G., Trentmann, J. & Andreae, M. O. A new look at the role of fire-released moisture on the dynamics of atmospheric pyro-convection. *International journal of wildland fire* **18**, 554–562 (2009).

[268] Lareau, N. P. & Clements, C. B. Environmental controls on pyrocumulus and pyrocumulonimbus initiation and development. *Atmospheric Chemistry and Physics* **16**, 4005–4022 (2016).

[269] Haines, D. A. A lower atmosphere severity index for wildlife fires. *National Weather Digest* **13**, 23–27 (1988).

[270] Mills, G. & L, M. Atmospheric stability environments and fire weather in australia – extending the haines index. techreport 20, Centre for Australian Weather and Climate Research (2010).

[271] Di Virgilio, G. *et al.* Climate change increases the potential for extreme wildfires. *Geophysical Research Letters* **46**, 8517–8526 (2019).

[272] Coen, J. L. & Schroeder, W. The high park fire: Coupled weather-wildland fire model simulation of a windstorm-driven wildfire in colorado's front range. *Journal of Geophysical Research: Atmospheres* **120**, 131–146 (2015).

[273] Jiménez, P. A., Muñoz-Esparza, D. & Kosović, B. A high resolution coupled fire–atmosphere forecasting system to minimize the impacts of wildland fires: Applications to the chimney tops ii wildland event. *Atmosphere* **9**, 197 (2018).

[274] Simpson, C., Sharples, J. & Evans, J. Resolving vorticity-driven lateral fire spread using the wrf-fire coupled atmosphere–fire numerical model. *Natural Hazards and Earth System Sciences* **14**, 2359–2371 (2014).

[275] Thompson, G., Field, P. R., Rasmussen, R. M. & Hall, W. D. Explicit forecasts of winter precipitation using an improved bulk microphysics scheme. part ii: Implementation of a new snow parameterization. *Monthly Weather Review* **136**, 5095–5115 (2008).

[276] Iacono, M. J. *et al.* Radiative forcing by long-lived greenhouse gases: Calculations with the aer radiative transfer models. *Journal of Geophysical Research: Atmospheres* **113** (2008).

[277] Jiménez, P. A. *et al.* A revised scheme for the wrf surface layer formulation. *Monthly weather review* **140**, 898–918 (2012).

[278] Nakanishi, M. & Niino, H. An improved mellor–yamada level-3 model: Its numerical stability and application to a regional prediction of advection fog. *Boundary-Layer Meteorology* **119**, 397–407 (2006).

USC UNIVERSIDADE DE SANTIAGO DE COMPOSTELA

[279] de Dios, V. R. *et al.* Convergence in critical fuel moisture and fire weather thresholds associated with fire activity in the pyroregions of mediterranean europe. *Science of the total environment* **806**, 151462 (2022).

[280] Sun, R., Krueger, S. K., Jenkins, M. A., Zulauf, M. A. & Charney, J. J. The importance of fire–atmosphere coupling and boundary-layer turbulence to wildfire spread. *International Journal of Wildland Fire* **18**, 50–60 (2009).

[281] Lolis, C., Bartzokas, A., Lagouvardos, K. & Metaxas, D. Intra-annual variation of atmospheric static stability in the mediterranean region: a 60-year climatology. *Theoretical and Applied Climatology* **110**, 245–261 (2012).

[282] Lolis, C. J. Climatic features of atmospheric stability in the mediterranean region (1948–2006): spatial modes, inter-monthly and inter-annual variability. *Meteorological Applications: A journal of forecasting, practical applications, training techniques and modelling* **14**, 361–379 (2007).

[283] Thomson, A. M. *et al.* Rcp4. 5: a pathway for stabilization of radiative forcing by 2100. *Climatic change* **109**, 77–94 (2011).

[284] Van Vuuren, D. P. *et al.* Rcp2. 6: exploring the possibility to keep global mean temperature increase below 2 c. *Climatic change* **109**, 95–116 (2011).

[285] Brooks, H. E. Severe thunderstorms and climate change. *Atmospheric research* **123**, 129–138 (2013).

[286] Diffenbaugh, N. S., Scherer, M. & Trapp, R. J. Robust increases in severe thunderstorm environments in response to greenhouse forcing. *Proceedings of the National Academy of Sciences* **110**, 16361–16366 (2013).

[287] Viceto, C., Marta-Almeida, M. & Rocha, A. Future climate change of stability indices for the iberian peninsula. *International Journal of Climatology* **37**, 4390–4408 (2017).

[288] Moreira, F. *et al.* Landscape–wildfire interactions in southern europe: implications for landscape management. *Journal of environmental management* **92**, 2389–2402 (2011).

[289] Moritz, M. A. *et al.* Learning to coexist with wildfire. *Nature* **515**, 58–66 (2014).

[290] Pausas, J. G. & Fernández-Muñoz, S. Fire regime changes in the western mediterranean basin: from fuel-limited to drought-driven fire regime. *Climatic change* **110**, 215–226 (2012).

[291] Kolby Smith, W. *et al.* Large divergence of satellite and earth system model estimates of global terrestrial co2 fertilization. *Nature climate change* **6**, 306–310 (2016).

[292] Chuvieco, E., Pettinari, M. & Otón, G. Esa fire climate change initiative (fire˙cci): Avhrr-ltdr burned area grid product, version 1.1. Centre of Envrionmental Data Analysis (2020).

[293] Fernandes, A. P. *et al.* Smoke emissions from the extreme wildfire events in central portugal in october 2017. *International Journal of Wildland Fire* **31**, 989–1001 (2022).

USC DE COMPOSTELA

[294] Miguez-Macho, G., Stenchikov, G. L. & Robock, A. Spectral nudging to eliminate the effects of domain position and geometry in regional climate model simulations. *Journal of Geophysical Research: Atmospheres* **109** (2004).

USC
UNIVERSIDADE DE SANTIAGO DE COMPOSTELA

USC
UNIVERSIDADE
DE SANTIAGO
DE COMPOSTELA





Wildfires are part of the Earth System since they interact with the atmosphere, the biosphere and the anthroposphere. Climate change is altering global fire activity by modifying atmospheric and vegetation conditions. As a consequence, the effects of wildfires on the atmosphere are expected to change as well. In this thesis we assess how wildfire-atmosphere interactions are being modified due to anthropogenic global warming. Using numerical models, climate projections and statistical data analysis, a significant intensification of the interactions between fires and the atmosphere at different spatio-temporal scales was found.